

Understanding Metal-Metal Bonds in Heterobimetallic Complexes and Their  
Use as Catalysts for Dinitrogen Conversion

A DISSERTATION

SUBMITTED TO THE FACULTY OF THE

UNIVERSITY OF MINNESOTA

BY

Laura J. Clouston

IN PARTIAL FULFILLMENT OF THE REQUIREMENTS

FOR THE DEGREE OF

DOCTOR OF PHILOSOPHY

Connie C. Lu, Advisor

July 2016



## Acknowledgments

I am grateful to obtain my degree from the Chemistry Department at the University of Minnesota, were I could not be surrounded by better people. I was lucky to be a part of the Lu group, where I could always find someone to talk science or have a good laugh. I would like to thank Connie for welcoming me into the group and providing me with numerous opportunities to grow as a scientist. Thanks to the rest of the Lu group, past and present, you have all taught me something valuable that I will keep with me. Thanks to Deanna for guiding me through my first two years, and to Steve, Reed and Ryan for always keeping my expectations high. Thanks to Dave, the second year crew- Matt, Bianca, JT and Sai, and Azim for keeping the lab to be a fun place to spend the majority of your time.

A special thanks to the Gagliardi group for a great collaboration, especially Varinia, who has calculated almost everything I have made or wanted to make, I have truly enjoyed working together. I am also thankful for the groups in the department that I have worked closely with, the Tonks, Tolman, Que, Ellis and Hoye groups, who have provided a wealth of advice, resources and chemicals throughout my graduate work. Thank you to Victor and Greg, who brought me in to the X-ray lab and gave me some great experiences. Thanks to Victor and Yu-Sheng and anyone else that had the pleasure of traveling to APS with me to work five straight shifts. I am also thankful to have been a part of WISE during the last five years, where I was able to make great friends. Thanks to Letitia for being the fearless leader of WISE and a great NMR director. The staff in the chemistry department have made things so easy for me- Ben, Nick, and Nancy to name a few, we are so lucky to have you. Again, thanks to everyone at Minnesota that I had the pleasure to work with.

Finally, thanks to my friends and family, some of you I have already thanked, for supporting me over the past five years. I am lucky to be surrounded by amazing people. And thanks to Chris, who joined me right at the start of this adventure, and will continue on with me to the next.

## Table of Contents

Acknowledgments.....	i
List of Figures .....	vi
List of Tables .....	xii
List of Schemes.....	xvi
List of Abbreviations .....	xvii
<b>Chapter 1</b> .....	<b>1</b>
1.1 Introduction.....	2
1.2 Modular Synthesis of Metal-Metal Compounds.....	3
1.3 Metal-Metal Bonding.....	6
1.3.1 Bonding Trends.....	8
1.3.2 Understanding Bonding through Theory .....	10
1.3.3 Spectroscopic Evidence of Multiple Bonding .....	13
1.4 In Search of Synergistic Redox and Magnetic Properties .....	14
1.5 Small molecule reactivity using multiple metals .....	17
1.6 Literature examples of N-N bond cleavage with multimetallic complexes.....	21
1.6.1 Reduction of small molecules by trigonal trimetallic clusters.....	21
1.6.2 Dinitrogen activation with heterobimetallic compounds .....	22
1.6.3 Tuning N <sub>2</sub> reduction by Co and Fe by apical ligand selection .....	25
1.7 Scope of thesis .....	27
<b>Chapter 2</b> .....	<b>29</b>
Heterobimetallic Complexes that Bond Vanadium to Iron, Cobalt and Nickel	
2.1 Overview of M-V Complexes.....	30
2.2 Introduction.....	31
2.3 Results and Discussion .....	31

2.3.1 Synthesis .....	31
2.3.2 Electrochemical and Electronic Absorption Characterization .....	33
2.3.3 X-ray Crystallography .....	37
2.3.4 NMR Spectroscopy .....	42
2.3.5 Magnetic Susceptibility and EPR Spectroscopy .....	44
2.3.6 Mössbauer Spectroscopy .....	47
2.3.7 Electronic Structure Calculations .....	48
2.4 Conclusion of M-V complexes .....	52
2.5 Experimental Section .....	52
<b>Chapter 3</b> .....	<b>60</b>
<b>Dative vs. Covalent Bonding in Trigonal Ti-M Complexes</b>	
3.1 Overview .....	61
3.2 Introduction .....	61
3.3 Results and Discussion .....	63
3.3.1 Synthesis .....	63
3.3.2 X-ray Crystallography .....	64
3.3.3 Cyclic Voltammetry .....	68
3.3.4 EPR Spectroscopy .....	71
3.3.5 Mössbauer Spectroscopy .....	74
3.3.6 Discussion .....	77
3.4 Conclusion .....	78
3.5 Experimental Section .....	79
3.5.1 General Considerations .....	79
3.5.2 Physical Methods .....	79
3.5.3 Synthetic Procedures .....	80

3.5.4 X-ray Crystallography .....	82
<b>Chapter 4</b> .....	84
Bimetallic cobalt-dinitrogen complexes: impact of the supporting metal on N <sub>2</sub> activation	
4.1 Overview.....	85
4.2 Introduction.....	86
4.3 Results and Discussion .....	87
4.3.1 Synthesis and characterization of CoTiL (1) .....	87
4.3.2 Electrochemistry of CoML series .....	90
4.3.3 Synthesis and characterization of dinitrogen adducts 2 and 3 .....	91
4.3.4 Theory .....	94
4.4 Conclusion .....	97
4.5 Experimental Section .....	98
4.5.1 General Considerations .....	98
4.5.2 Synthetic Procedures.....	99
4.5.3 X-ray crystallography .....	101
4.6 Computational Methods.....	102
4.6.1 DFT Calculations .....	102
4.6.2 Multi-reference calculations .....	103
<b>Chapter 5</b> .....	104
Understanding the Cooperation of Co–M Interactions and Ligand Hemi-lability in the Catalytic Reductive Silylation of N <sub>2</sub>	
5.1 Introduction.....	105
5.2 Catalytic reductive silylation of N <sub>2</sub> with Co heterobimetallics .....	107
5.3 Kinetic studies.....	108
5.4 Catalytic mechanism.....	110

5.4.1 Theoretical mechanistic studies .....	110
5.4.2 Electronic structure during catalysis .....	113
5.4.3 Ligand hemi-lability and Co–M interactions.....	115
5.5 Conclusion .....	121
5.6 Experimental Section .....	122
5.7 Computational Details .....	124
Bibliography .....	126
Appendix 1 .....	137
Appendix 2.....	167
Appendix 3.....	170
Appendix 4.....	192

## List of Figures

<b>Figure 1.1</b> Array of first-row transition metal-metal complexes prepared with the double-decker ligands $L^1-L^3$ ..	6
<b>Figure 1.2</b> Overlay of solid-state structures of isostructural $L^1CrM$ bimetallics shown from side ( <i>a</i> ) and top ( <i>b</i> ) views.....	7
<b>Figure 1.3</b> Formal shortness ratio (FSR) map of 21 isostructural bimetallics using the $L^1$ ligand.....	9
<b>Figure 1.4</b> Corresponding spin state map of 20 isostructural bimetallics.....	9
<b>Figure 1.5</b> Qualitative d-orbital manifolds of different metal-metal bonding regimes....	12
<b>Figure 1.6</b> Cyclic voltammograms of selected $L^1$ bimetallic complexes.....	15
<b>Figure 1.7</b> Temperature dependence of magnetic susceptibility, plotted as $\chi_M T$ versus T, of isostructural $L^2MM'Cl$ complexes.....	16
<b>Figure 1.8</b> Electronic absorption spectra of isostructural $L^2CoMCl$ bimetallics and $[L^2Co]K$ in $CH_2Cl_2$ ..	17
<b>Figure 1.9</b> Three modes of X–Y bond activation at a metal-metal bonded unit ( $M_A-M_B$ ). ..	19
<b>Figure 1.10</b> Bonding interactions between a transition metal (M) and $N_2$ in the absence and presence of a supporting metal engaged in metal-metal bonding.....	20
<b>Figure 1.11</b> Trigonal metal complex featuring a varying supporting apical ligand capable of nitrogen reduction.....	25
<b>Figure 2.1</b> Key of MV complexes organized by group number for M (vertical) and overall d-count (horizontal). ..	30
<b>Figure 2.2</b> Cyclic voltammograms of <b>1</b> – <b>4</b> in THF.....	34
<b>Figure 2.3</b> Vis-NIR spectra of complexes <b>1</b> – <b>4</b> , $[2^{ox}]PF_6$ , and $[3^{ox}]BPh_4$ in THF at rt..	36
<b>Figure 2.4</b> Solid–state structures of <b>1</b> – <b>4</b> shown at 50% thermal ellipsoid probability..	38
<b>Figure 2.5</b> Overlay of $^1H$ NMR spectra of the $(d-d)^{10}$ complexes, <b>2</b> and $[3^{ox}]BPh_4$ , in THF- $d_8$ at rt.....	43
<b>Figure 2.6</b> Temperature dependence of the effective magnetic moment, $\mu_{eff}$ , of $[2^{ox}]PF_6$ ( $\blacktriangle$ ) and <b>3</b> ( $\blacklozenge$ )..	45
<b>Figure 2.7</b> X-band EPR spectra ( $dX''/dB$ ) of $[2^{ox}]PF_6$ in frozen THF (20.0 K, frequency = 9.64 GHz, modulation to 10 G, power = 200 $\mu W$ ) and <b>3</b> in frozen toluene (13.0 K).....	46



<b>Figure 2.8</b> Zero-field Mössbauer spectra overlay of <b>2</b> (red, ×) and [ <b>2</b> <sup>ox</sup> ]PF <sub>6</sub> (black, ○) at 80 K.....	47
<b>Figure 2.9</b> Qualitative MO diagrams across the metal-vanadium series. ....	50
<b>Figure 3.1</b> Family of isolated MTiL combinations using ligand, L (left).....	61
<b>Figure 3.2</b> Solid-state structures of <b>2</b> – <b>4</b> , <b>2</b> <sup>ox</sup> and <b>4</b> <sup>ox</sup> shown at 50% thermal ellipsoid probability. ....	66
<b>Figure 3.3</b> Cyclic voltammograms of <b>2</b> – <b>4</b> in THF. ....	69
<b>Figure 3.4</b> Cyclic voltammograms of neutral d <sup>10</sup> complexes, CoTiL, FeVL and MnCrL in THF.....	70
<b>Figure 3.5</b> X-band EPR spectrum (dX''/dB) of <b>2</b> (black) in frozen toluene (20.0 K, frequency = 9.64 GHz, modulation to 10G and power = 200 μW). ....	71
<b>Figure 3.6</b> X-band EPR spectrum (dX''/dB) of <b>3</b> <sup>ox</sup> (black) in frozen THF (25.0 K, frequency = 9.64 GHz, modulation to 10G and power = 200 μW). ....	73
<b>Figure 3.7</b> X-band EPR spectrum (dX''/dB) of <b>4</b> (black) in frozen toluene (24.0 K, frequency = 9.64 GHz, modulation to 10G and power = 200 μW). ....	73
<b>Figure 3.8</b> Zero-field Mössbauer spectrum of <b>2</b> at 80 K.....	75
<b>Figure 3.9</b> Zero-field Mössbauer spectrum of <b>2</b> <sup>red</sup> at 80 K.....	76
<b>Figure 4.1</b> Series of [N <sub>2</sub> CoML] <sup>-</sup> complexes isolated using ligand L (right). ....	85
<b>Figure 4.2</b> Selected examples of cobalt-dinitrogen complexes from the literature that showcase N <sub>2</sub> activation and tuning of the metal counteraction, ligand oxidation state, and ancillary element. ....	86
<b>Figure 4.3</b> Molecular structure of <b>1</b> shown at 50% thermal ellipsoid probability. ....	90
<b>Figure 4.4</b> Cyclic voltammograms of CoML complexes collected under an atmosphere of N <sub>2</sub> (colored lines) or argon (---) in 0.4 M [ <sup>n</sup> Bu <sub>4</sub> N]PF <sub>6</sub> in THF. ....	91
<b>Figure 4.5</b> Molecular structures of <b>2</b> and <b>3</b> shown at 50% thermal ellipsoid probability.....	93
<b>Figure 4.6</b> Qualitative MO diagram showing the natural orbitals for CoTiL <sup>Me</sup> ( <b>1'</b> ) that arise from CASSCF calculations (energy ordering from DFT).....	95
<b>Figure 4.7</b> Qualitative MO diagrams of the d-orbital manifold for the [(N <sub>2</sub> )CoML] <sup>-</sup> series, where M = Al, Ti, V, Cr, and Co. In the {CoM} <sup>n</sup> descriptor, <i>n</i> is the number of valence d electrons.....	96
<b>Figure 5.1</b> Chatt/Schrock cycle for the mechanism of N <sub>2</sub> reduction to ammonia .....	106

<b>Figure 5.2</b> Isolation of a series of $[\text{N}_2\text{CoML}]^-$ complexes and their corresponding $\text{N}_2$ stretching frequencies .....	108
<b>Figure 5.3</b> Kinetic studies for CoML complexes with method 1 shown on the left and method 2 shown on the right.....	110
<b>Figure 5.4</b> Investigated mechanistic routes to the reductive silylation of $\text{N}_2$ . .....	111
<b>Figure 5.5</b> Calculated mechanism for the bimetallic mediated silylation of $\text{N}_2$ . .....	112
<b>Figure 5.6</b> Plot of the spin density values (number of unpaired electrons) located at supporting metal M (top), Co (middle) and $\text{N}_2$ (bottom) throughout the catalytic cycle. ....	114
<b>Figure 5.7</b> Decoordination of one phosphine ligand on intermediate C to $\text{C}^*$ (top) and the energy difference ( $\Delta G$ , kcal/mol) between $\text{C}^*$ and C. (bottom).....	115
<b>Figure 5.8</b> DFT optimized structures of intermediates C through $\text{D}^*$ for CoAl and CoCr .....	117
<b>Figure 5.9</b> (A) Plot of the Co–M bond distance ( $\text{\AA}$ ) in intermediates B through $\text{E}^*$ taken from the DFT geometry optimized structures (B) FSR plot for the Co–M distance; (C) Plot of the change in Co–M distance ( $\text{\AA}$ ) throughout the catalytic cycle, the difference is calculated as Co–M distance in intermediate B subtracted from the distance in each intermediate. Positive values indicate a longer Co–M distance. ....	118
<b>Figure 5.10</b> Plot of the Co–P distances ( $\text{\AA}$ ) from the DFT optimized intermediates (top) with an enlargement of the shorter distances shown below.....	119
<b>Appendix 1 Figures</b>	
<b>Figure A1.1</b> Cyclic voltammetry study of <b>2</b> . .....	137
<b>Figure A1.2</b> Cyclic voltammetry study of <b>4</b> . .....	137
<b>Figure A1.3</b> Cyclic voltammetry study of <b>3</b> . .....	138
<b>Figure A1.4</b> Vis-NIR spectra of complexes <b>1–4</b> in THF. ....	138
<b>Figure A1.5</b> $^1\text{H}$ NMR spectrum of <b>1</b> in $\text{C}_6\text{D}_6$ (500 MHz).....	139
<b>Figure A1.6</b> $^1\text{H}$ NMR spectrum of <b>2</b> in THF- $\text{d}_8$ (500 MHz). ....	139
<b>Figure A1.7</b> $^1\text{H}$ NMR spectrum of $2^{\text{ox}}[\text{PF}_6]$ in THF- $\text{d}_8$ (500 MHz). ....	140
<b>Figure A1.8</b> $^1\text{H}$ NMR spectrum of $2^{\text{ox}}[\text{BPh}_4]$ in THF- $\text{d}_8$ (400 MHz). ....	140
<b>Figure A1.9</b> $^1\text{H}$ NMR spectrum of <b>3</b> in $\text{C}_6\text{D}_6$ (500 MHz). ....	141
<b>Figure A1.10</b> $^1\text{H}$ NMR spectrum of $3^{\text{ox}}$ in THF- $\text{d}_8$ (500 MHz). ....	141

<b>Figure A1.11</b> $^1\text{H}$ NMR spectrum of <b>4</b> in $\text{C}_6\text{D}_6$ (400 MHz).....	142
<b>Figure A1.12</b> Variable temperature $^1\text{H}$ NMR spectra of <b>2</b> in toluene- $d_8$ (500 MHz). Coalescence of the methylene resonances occurs at 88 °C.....	142
<b>Figure A1.13</b> Variable temperature $^{31}\text{P}$ NMR spectra of <b>2</b> in toluene- $d_8$ (200 MHz). ..	143
<b>Figure A1.14</b> Variable temperature $^1\text{H}$ NMR spectra of <b>3<sup>ox</sup></b> in $\text{CD}_3\text{CN}$ (500 MHz). Coalescence of the methylene resonances occurs at 68 °C.....	143
<b>Figure A1.15</b> Variable temperature $^{31}\text{P}$ NMR spectra of <b>3<sup>ox</sup></b> in $\text{CD}_3\text{CN}$ (200 MHz).....	144
<b>Figure A1.16</b> Overlay of $^1\text{H}$ NMR spectra of <b>2</b> and reference complex NiAL in THF- $d_8$ . .....	145
<b>Figure A1.17</b> Spin density of FeV cation (left, $\langle S^2 \rangle_{\text{calc}} = 0.75$ ), CoV neutral (middle, $\langle S^2 \rangle_{\text{calc}} = 0.75$ ), and NiV neutral (middle, $\langle S^2 \rangle_{\text{calc}} = 2.00$ ). .....	153
<b>Figure A1.18</b> Qualitative MO diagram showing the natural orbitals for <b>2'</b> – FeVL resulting from CASSCF calculations.....	157
<b>Figure A1.19</b> Qualitative MO diagram showing the natural orbitals for <b>2<sup>ox'</sup></b> resulting from CASSCF calculations.....	158
<b>Figure A1.20</b> Qualitative MO diagram showing the natural orbitals for <b>3'</b> resulting from CASSCF calculations.....	159
<b>Figure A1.21</b> Qualitative MO diagram showing the natural orbitals for <b>3<sup>ox'</sup></b> resulting from CASSCF calculations.....	160
<b>Figure A1.22</b> Qualitative MO diagram showing the natural orbitals for <b>4'</b> resulting from CASSCF calculations.....	161
<b>Figure A1.23</b> Plot of bond order (formal versus effective, or FBO vs. EBO) against the experimentally determined formal shortness ratio ( $r$ ). .....	162
<b>Figure A1.24</b> Predicted vis-NIR spectra for NiVL( <b>4</b> ) by using different DFT functionals. .....	164
<b>Appendix 2 Figures</b>	
<b>Figure A2.1</b> $^1\text{H}$ NMR spectrum of <b>2</b> in $\text{C}_6\text{D}_6$ (500 MHz).....	167
<b>Figure A2.2</b> $^1\text{H}$ NMR spectrum of <b>2<sup>ox</sup></b> in THF- $d_8$ (500 MHz). .....	167
<b>Figure A2.3</b> $^1\text{H}$ NMR spectrum of <b>2<sup>red</sup></b> in THF- $d_8$ (500 MHz). .....	168
<b>Figure A2.4</b> $^1\text{H}$ NMR spectrum of <b>3<sup>ox</sup></b> in THF- $d_8$ (500 MHz). .....	168
<b>Figure A2.5</b> $^1\text{H}$ NMR spectrum of <b>4</b> in $\text{C}_6\text{D}_6$ (400 MHz). .....	169

<b>Figure A2.6</b> $^1\text{H}$ NMR spectrum of <b>4<sup>ox</sup></b> in THF- $d_8$ (500 MHz).....	169
--	-----

### **Appendix 3 Figures**

<b>Figure A3.1</b> $^1\text{H}$ NMR spectrum of TiL in $\text{C}_6\text{D}_6$ (500 MHz).....	170
--	-----

<b>Figure A3.2</b> $^1\text{H}$ NMR spectrum of <b>1</b> in THF- $d_8$ (500 MHz).....	171
---	-----

<b>Figure A3.3</b> $^1\text{H}$ NMR spectrum of <b>2</b> in THF- $d_8$ (500 MHz).....	171
---	-----

<b>Figure A3.4</b> $^1\text{H}$ NMR spectrum of <b>3</b> in THF- $d_8$ (500 MHz).....	172
---	-----

<b>Figure A3.5</b> IR spectra (KBr pellet) of <b>2</b> and <b>3</b> . ....	175
--	-----

<b>Figure A3.6</b> Spin densities of $\text{N}_2$ -CoML anionic species. ....	180
---	-----

<b>Figure A3.7</b> Qualitative MO diagram showing the natural orbitals for CoTiL resulting from the CASSCF calculation. ....	181
--	-----

<b>Figure A3.8</b> Qualitative MO diagram showing the natural orbitals for $\text{N}_2$ -CoTiL resulting from CASSCF calculations.....	183
--	-----

<b>Figure A3.9</b> Qualitative MO diagram showing the natural orbitals for $\text{N}_2$ -CoVL resulting from CASSCF calculations.....	185
---	-----

<b>Figure A3.10</b> Qualitative MO diagram showing the natural orbitals for $\text{N}_2$ -CoCrL resulting from CASSCF calculations.....	187
---	-----

<b>Figure A3.11</b> Qualitative molecular orbital diagram for $\text{N}_2$ -CoAIL resulting from DFT(M06-L) calculations.....	189
---	-----

<b>Figure A3.12</b> Qualitative molecular orbital diagram for $\text{N}_2$ -Co $2\text{L}$ resulting from DFT(M06-L) calculations.....	190
--	-----

### **Appendix 4 Figures**

<b>Figure A4.1</b> Kinetic plot via method 1 for CoML complexes along with their linear fit for up to 20 minutes. ....	192
--	-----

<b>Figure A4.2</b> Plot of the slope taken from the linear fit against the overall TON of the various CoML complexes to show the general correlation of initial rate and overall TON. ....	192
--	-----

<b>Figure A4.3</b> Calibration curve for the indophenol method to quantify $\text{N}(\text{SiMe}_3)_3$ .....	193
--	-----

<b>Figure A4.4</b> Combined kinetic plot for method 1 (closed markers) and 2 (open markers) showing that both methods qualitatively provide the same kinetic trend.....	193
---	-----

<b>Figure A4.5</b> $^{31}\text{P}$ NMR spectra overlay of the <i>in-operando</i> studies of CoML catalysts with 10 equivalents of reagents.....	194
---	-----

<b>Figure A4.6</b> Plot of the oxidation state for Co (top) and supporting metal M (bottom) based on the spin density located at each metal.....	195
<b>Figure A4.7</b> Plot of the spin density located at supporting metal M (top), Co (middle) and N <sub>2</sub> (bottom) throughout the catalytic cycle. ....	196
<b>Figure A4.8</b> A) Plot of the Co–M bond distance (Å) in intermediates B through E* taken from the DFT geometry optimized structures B) FSR plot for the Co–M distance and C) Plot of the change in Co-M distance (Å) throughout the catalytic cycle, the difference is calculated as Co–M distance in intermediate B subtracted from the distance in each intermediate.....	197
<b>Figure A4.9</b> Plot of the Co–P distances (Å) from the DFT optimized intermediates (top) with an enlargement of the shorter distances shown below.....	198

## List of Tables

<b>Table 1.1</b> Summary of bond order information for multiply bonded bimetallics, main configuration and EBO from CASSCF calculations. ....	11
<b>Table 1.2</b> Diamagnetic anisotropies ( $\Delta\chi$ ) for (d-d) <sup>10</sup> multiply bonded bimetallics.....	13
<b>Table 1.3</b> Summary of Mössbauer parameters for iron bimetallics with multiple bonds.	14
<b>Table 1.4</b> Comparison of group 4 metal supported Co heterobimetallic complexes that bind N <sub>2</sub> .....	23
<b>Table 1.5</b> Summary of N <sub>2</sub> bound Co and Fe complexes evaluated for the conversion of N <sub>2</sub> to NH <sub>3</sub> . .....	27
<b>Table 2.1</b> Redox potentials (V) of <b>2 - 4</b> .....	34
<b>Table 2.2</b> Vis-NIR data for <b>1 - 4</b> , [2 <sup>ox</sup> ]PF <sub>6</sub> , and [3 <sup>ox</sup> ]BPh <sub>4</sub> in THF at rt. ....	37
<b>Table 2.3</b> Geometrical parameters, including bond lengths (Å), formal shortness ratio (FSR), and angles (°), for <b>1 - 4</b> .....	39
<b>Table 2.4</b> Comparing relevant literature compounds with short metal-metal bond lengths. ....	41
<b>Table 2.5</b> Main electronic configuration of metal-vanadium complexes with formal and effective bond orders (FBO and EBO, respectively).....	49
<b>Table 2.6</b> Percentage of Metal Character (%V, %M) in metal-vanadium bonding orbitals of $\sigma$ - and $\pi$ -symmetry from CASSCF calculations.....	50
<b>Table 3.1</b> Selected structural information for structurally characterized MTiL complexes. ....	67
<b>Table 3.2</b> Redox potentials for <b>2 - 4</b> .....	69
<b>Table 3.3</b> Mössbauer parameters for Fe heterobimetallics in L, as well as other multiply bonded Fe heterobimetallics. ....	76
<b>Table 3.4</b> Crystallographic details for <b>2</b> , <b>2<sup>ox</sup></b> , <b>4</b> and <b>4<sup>ox</sup></b> .....	83
<b>Table 4.1</b> Geometrical parameters, including bond lengths (Å), formal shortness ratio (FSR), and angles (deg), for <b>1 - 3</b> , [(N <sub>2</sub> )Co <sub>2</sub> L] <sup>-</sup> and [(N <sub>2</sub> )CoAlL] <sup>-</sup> . N-N bond stretching frequencies (cm <sup>-1</sup> ) and reduction potentials (V vs Fc <sup>+</sup> /Fc) are also listed.....	89
<b>Table 4.2</b> Crystallographic Details for compounds <b>1-3</b> . ....	102
<b>Table 5.1</b> Catalytic results for the formation of N(SiMe <sub>3</sub> ) <sub>3</sub> , quantified via GC-MS.....	108

<b>Table 5.2</b> Catalytic results for the formation of N(SiMe <sub>3</sub> ) <sub>3</sub> with alternative Co based catalysts.....	121
---	-----

## Appendix 1 Tables

<b>Table A1.1</b> Calculation spreadsheet for the diamagnetic anisotropy of <b>2</b> in THF-d <sub>8</sub> . ...	146
<b>Table A1.2</b> Calculation spreadsheet for the diamagnetic anisotropy of <b>3<sup>ox</sup></b> in THF-d <sub>8</sub> .	146
<b>Table A1.3</b> Average $\Delta\chi$ and standard deviations for the two different calculation methods (uf-uf vs. uf-df) for <b>2</b> and <b>3<sup>ox</sup></b> .	147
<b>Table A1.4</b> Calculation of the energy barrier ( $\Delta G^\ddagger$ in kcal/mol) for the fluxional process equilibrating the diastereotopic methylene protons in the ligand backbone.....	147
<b>Table A1.5</b> Crystallographic details of complexes <b>1 – 4</b> .	148
<b>Table A1.6</b> Selected bond lengths and angles for comparison of DFT optimized structures using the PBE functional with experimental X-ray structures. ....	150
<b>Table A1.7</b> Calculated relative energies of various possible spin states at DFT and CASSCF levels of theory.....	151
<b>Table A1.8</b> Calculated charges at the metal centers of the ground spin state. ....	152
<b>Table A1.9</b> CASSCF Mulliken spin densities at the metal centers of the ground spin state. ....	153
<b>Table A1.10</b> Detailed CASSCF orbital analysis of <b>2'</b> - FeV neutral species.....	154
<b>Table A1.11</b> Detailed CASSCF orbital analysis of <b>2<sup>ox'</sup></b> - FeV cationic species.....	154
<b>Table A1.12</b> Detailed CASSCF orbital analysis of <b>3'</b> - CoV neutral species. ....	155
<b>Table A1.13</b> Detailed CASSCF orbital analysis of <b>3<sup>ox'</sup></b> - CoV cationic species.....	155
<b>Table A1.14</b> Detailed CASSCF orbital analysis of <b>4'</b> - NiV neutral species. ....	156
<b>Table A1.15</b> TD-DFT Excitation Energies and their MO Interpretations for <b>2</b> , FeVL neutral complex (d <sup>10</sup> ) using the M06-2X functional.....	162
<b>Table A1.16</b> TD-DFT Excitation Energies and their MO Interpretations for <b>3ox</b> , CoVL cation complex (d <sup>10</sup> ) using the M06-2X functional. ....	163
<b>Table A1.17</b> TD-DFT Excitation Energies and their MO Interpretations for <b>4</b> , NiVL neutral complex (d <sup>12</sup> ). ....	164

## Appendix 3 Tables

<b>Table A3.1</b> Selected crystallographic details for neutral CoML complexes.....	173
<b>Table A3.2</b> Selected crystallographic details for anionic CoML complexes. ....	174

<b>Table A3.3</b> Redox potentials (V) for CoML species. ....	175
<b>Table A3.4</b> Comparison of calculated and experimental bond lengths (Å) and angles (deg) for the CoTiL neutral species .....	176
<b>Table A3.5</b> Comparison of Calculated (M06-L) and Experimental Bond Lengths (Å) and Angles (deg.) for N <sub>2</sub> -CoAIL anionic species .....	176
<b>Table A3.6</b> Comparison of Calculated (M06-L) and Experimental Bond Lengths (Å) and Angles (deg.) for N <sub>2</sub> -CoVL anionic species.....	177
<b>Table A3.7</b> Comparison of Calculated (M06-L) and Experimental Bond Lengths (Å) and Angles (deg.) for N <sub>2</sub> -CoCrL anionic species. ....	177
<b>Table A3.8</b> Electronic energies at the M06-L/def2-TZVPD/SMD // M06-L/def2-TZVP level of theory. ....	178
<b>Table A3.9</b> Calculated Bond Lengths (Å) and N <sub>1</sub> -N <sub>2</sub> bond stretching frequencies (cm <sup>-1</sup> ) for ground spin-state species.....	179
<b>Table A3.10</b> Calculated spin densities, CM5 charges, and NBO analysis at the metal centers and N <sub>2</sub> molecule for ground spin-state species.....	179
<b>Table A3.11</b> Detailed CASSCF orbital analysis of CoTiL (10,10) neutral species.....	182
<b>Table A3.12</b> Detailed CASSCF orbital analysis of CoTiL (10,10) neutral species.....	182
<b>Table A3.13</b> Detailed CASSCF orbital analysis of N <sub>2</sub> -CoTiL neutral species.....	184
<b>Table A3.14</b> Detailed CASSCF orbital analysis of N <sub>2</sub> -CoVL neutral species.....	186
<b>Table A3.15</b> Detailed CASSCF orbital analysis of N <sub>2</sub> -CoCrL neutral species. ....	188
<b>Table A3.16</b> Details of $\sigma$ and $\sigma^*$ CASSCF bond orbital analysis of N <sub>2</sub> -Co <sub>2</sub> L neutral species. ....	188
<b>Table A3.17</b> Oxidation states of N <sub>2</sub> -CoML complexes with the percent of electron located on the upper Co atom in the $\sigma$ bond. ....	191

#### **Appendix 4 Tables**

<b>Table A4.1</b> Energy profile of the catalytic mechanism mediated by CoML catalysts with calculated intermediates and transition states for the bimetallic series. ....	199
<b>Table A4.2</b> List of electronic energies for CoAIL calculated at the M06-L/def2-TZVPD/SMD // M06-L/def2-TZVP level of theory.. ....	200
<b>Table A4.3</b> List of electronic energies for CoTiL calculated at the M06-L/def2-TZVPD/SMD // M06-L/def2-TZVP level of theory. ....	201



<b>Table A4.4</b> List of electronic energies for CoVL calculated at the M06-L/def2-TZVPD/SMD // M06-L/def2-TZVP level of theory. ....	202
<b>Table A4.5</b> List of electronic energies for CoCrL calculated at the M06-L/def2-TZVPD/SMD // M06-L/def2-TZVP level of theory. ....	203
<b>Table A4.6</b> Calculated Bond Lengths (Å) and N <sub>1</sub> -N <sub>2</sub> bond stretching frequencies (cm <sup>-1</sup> ). .....	204
<b>Table A4.7</b> Calculated spin densities, CM5 charges and Bond order from the NBO analysis.....	205

## List of Schemes

<b>Scheme 1.1</b> Modular synthesis of metal-metal complexes using double-decker ligands (L <sup>1</sup> –L <sup>3</sup> ) in a two-step metallation. ....	4
<b>Scheme 1.2</b> Reactions that exemplify limitations in the two-step metallation approach. ..	5
<b>Scheme 1.3</b> Reactivity of tri-iron complex (t <sup>bs</sup> L)Fe <sub>3</sub> (THF) with N <sub>2</sub> derived substrates... ..	22
<b>Scheme 1.4</b> Reactivity of a (THF)Zr(MesNP <sup>i</sup> Pr <sub>2</sub> ) <sub>3</sub> CoN <sub>2</sub> with hydrazine and hydrazine derivatives. ....	23
<b>Scheme 1.5</b> Reaction of (THF)Ti(XylNP <sup>i</sup> Pr <sub>2</sub> ) <sub>3</sub> CoN <sub>2</sub> with hydrazine.....	25
<b>Scheme 2.1</b> From monovanadium <b>1</b> , synthesis of MV complexes <b>2</b> – <b>4</b> , <b>2<sup>ox</sup></b> , and <b>3<sup>ox</sup></b> . ....	32
<b>Scheme 3.1</b> Synthetic route to isolated titanium heterobimetallic complexes .....	64
<b>Scheme 4.1</b> Synthesis of compound <b>1</b> . ....	88
<b>Scheme 4.2</b> Synthesis of compounds <b>2</b> and <b>3</b> . ....	92
<b>Scheme 5.1</b> Catalytic conditions for reductive silylation of N <sub>2</sub> with CoML bimetallic catalysts. ....	107

## List of Abbreviations

°	degree
18-crown-6	1,4,7,10,13,16-hexaoxacyclooctadecane
222-cryptand	4,7,13,16,21,24-Hexaoxa-1,10-diazabicyclo[8.8.8]hexacosane
Å	angstrom
ACN	acetonitrile
ap	apical
atm	atmosphere
avg	average
B	magnetic field
B(ArF) <sub>4</sub>	B(3,5-(CF <sub>3</sub> ) <sub>2</sub> C <sub>6</sub> H <sub>3</sub> ) <sub>4</sub>
br	broad
C	Celsius
CASPT2	complete active space second order perturbation theory
CASSCF	complete active space self-consistent field theory
cm <sup>-1</sup>	wavenumber
COD	cyclooctadiene
crypt-222	4,7,13,16,21,24-Hexaoxa-1,10-diazabicyclo[8.8.8]hexacosane
CV	cyclic voltammetry
d	doublet
D	zero-field splitting
DFT	density functional theory
E/D	rhombicity
E <sub>1/2</sub>	reduction potential
EBO	effective bond order
E <sub>pa</sub>	anodic peak potential
E <sub>pc</sub>	cathodic peak potential
EPR	electron paramagnetic resonance
eq	equatorial
Eqn	equation
equiv	equivalent
exptl	experimental
FBO	formal bond order
Fc	ferrocene
Fc <sup>+</sup>	ferrocenium cation
FSR	formal shortness ratio
<i>g</i>	anisotropic <i>g</i> factor
<b>G</b>	Gauss
<i>g</i>	gram
<i>g<sup>eff</sup></i>	effective <i>g</i> factor
h	hour

Hz	Hertz
$I$	nuclear spin quantum number
$i_{pa}$	anodic current
$i_{pc}$	cathodic current
$iPr$	isopropyl
IR	infrared
$J$	coupling constant
K	Kelvin
kcal	kilocalorie
L	liter
M	molar
m	multiplet
Me	methyl
mes	mesityl
mg	milligram
MHz	megahertz
min	minute
MO	molecular orbital
mV	millivolts
NBO	natural bond order
$nBu$	n-butyl
NIR	near infrared
nm	nanometers
NMR	nuclear magnetic resonance
Ph	phenyl
ppm	parts per million
reflns	reflections
rt	room temperature
s	second
s	singlet
$S$	spin state
SQUID	superconducting quantum interference device
t	triplet
$tBu$	tert-butyl
TD-DFT	time dependent density functional theory
THF	tetrahydrofuran
UV	ultra-violet
V	volts
Vis	visible
XAS	X-ray Absorption Spectroscopy
$\delta$	delta

$\Delta E_Q$	quadrupole splitting
$\Delta\delta$	isomer shift
$\lambda_{\max}$	maximum absorbance wavelength
$\mu_B$	Bohr magneton
$\pi$	pi
$\sigma$	sigma

# Chapter 1

## Introduction

Reproduced in part with permission from: Eisenhart, R. J.; Clouston, L. J.; Lu, C. C.,  
Configuring Bonds between First-Row Transition Metals. *Acc. Chem. Res.* **2015**, *48* (11),  
2885-2894. Copyright 2015 American Chemical Society, and Cammarota, R. C.;  
Clouston, L. J.; Lu, C. C. *Coord. Chem. Rev.* **2016**, *in press* (DOI:  
10.1016/j.ccr.2016.06.014).

## 1.1 Introduction

Fifty years have passed since the delta bond was recognized in the structure of  $[\text{Re}_2\text{Cl}_8]^{2-}$ .<sup>1</sup> Today, the field of metal-metal bonding continues to challenge our notions of chemical bonding, electronic structure, and reactivity paradigms.<sup>2,3</sup> The discovery of a quintuply bonded dichromium complex revived efforts to make and understand metal-metal bonds across the periodic table, focusing on the transition metal block to the lanthanides and actinides.<sup>4,5</sup> This is an area ripe with possibilities in part because vast numbers of different metal-metal pairings remain largely unexplored. Such explorations are motivated to uncover emergent properties that are remarkably different from the properties of the individual metals, or to develop new modes of cooperative reactivity.<sup>6,7</sup> Understanding the underlying principles that govern metal-metal bonding and dictate its electronic and chemical behavior is essential in order to rationally wield these properties and to tailor multimetallic active sites.

First-row metals are particularly attractive because they adopt a wide range of spin states and their natural abundance is relevant to sustainability. Prior to 2013, there was no example of a coordination complex with multiple bonds between different first-row transition metals. These species had only been observed spectroscopically as naked binuclear clusters in gas-phase or matrix isolation studies.<sup>8,9</sup> The poor spatial overlap of  $3d$  orbitals was believed to impede strong covalent bonding between different first-row metals. Challenging this notion, two independent reports demonstrated that Fe–Cr and Fe–V triple bonds could be stabilized with auxiliary ligands.<sup>10,11</sup>

The Lu group's recent progress in isolating metal-metal bonds with first-row transition metals range from Ti to Cu. A signature of the work is the use of double-decker ligands, which use two discrete ligand pockets to bind two different metals. These unique platforms have provided access to diverse bimetallics of exclusively first-row metals. To understand the underlying principles of metal-metal bonding and its attendant electronic structure, properties, and reactivities, isostructural bimetallics are compared, where each metal site is systematically varied.

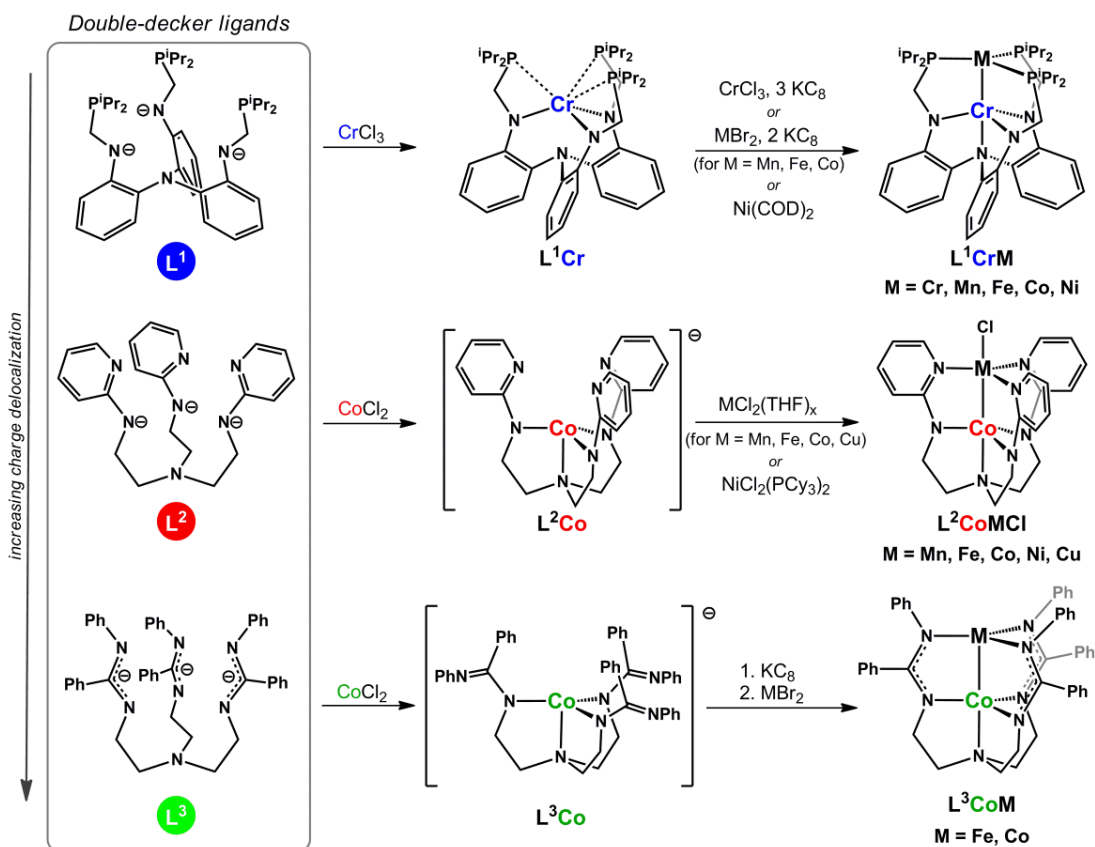
## 1.2 Modular Synthesis of Metal-Metal Compounds

Double-decker ligands, or binucleating ligands with two decks of donor atoms shown in Scheme 1.1, brace two metal atoms in proximity.<sup>12-14</sup> The ligands favor metal-metal interactions by forming 5-membered chelate rings comprising two metal centers and a 3-atom buttress. The ligands are tripodal and trianionic, where an apical amine connects the three ligand arms. The ligands can be made on multigram scale by simple elaboration of the tren backbone,  $N(C_2H_4NH_2)_3$ , or the aryl variant,  $N(o-NH_2C_6H_4)_3$ . Donor types differ across the ligands, but perhaps more importantly, so does the extent of charge delocalization. In  $L^1$ , charge is localized to the amide pocket, whereas charge is delocalized in the amidinate groups of  $L^3$ . The delocalization of charge is somewhere in the middle for the pyridylamide ligand,  $L^2$ .

The value of using double-decker ligands is debatable, as many bimetallics are generated with much simpler ligands, e.g. amido-phosphines,  $[RN-PR'_2]^-$ .<sup>15-17</sup> The latter are known to slip from bridging two metals ( $\kappa^1N, \kappa^1P$ ) to one metal ( $\kappa^2NP$ ), and thus, creating open coordination site(s) at either metal center for promoting reactivity.<sup>18</sup> In contrast, the multidenticity of ligands  $L^1-L^3$  constrains the coordination environment, locking the number and type of donors at each metal-binding site, with the only obvious open coordination site for reactivity is the apical pocket at the upper metal. One advantage is that the bimetallics obtained with ligands  $L^1-L^3$  are largely isostructural, enabling systematic comparisons to be made.

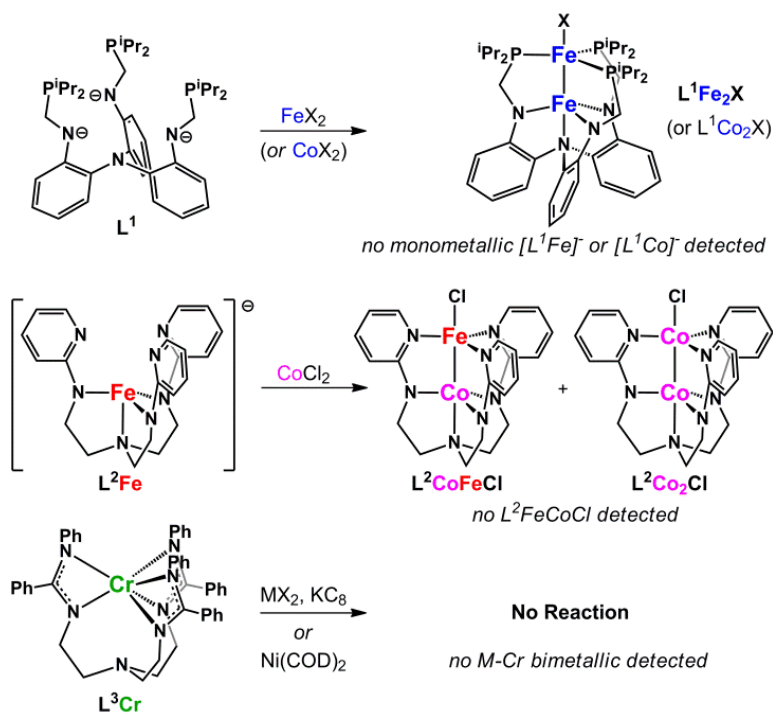
The double-decker ligands have distinct binding sites for selective installation of different metals. Many heterobimetallics were prepared by a two-step metalation, where initial metalation of the tri(amido)amine pocket provides a monometallic complex that then acts as a metalloligand in a subsequent metalation. Using the two-step procedure, diverse metal-metal pairings were achieved (Scheme 1.1).<sup>10,13,14,19-21</sup> Despite the general success of this approach, there are specific limitations, which are rationalized according to the ligand's ability to delocalize charge.





**Scheme 1.1** Modular synthesis of metal-metal complexes using double-decker ligands (L<sup>1</sup>–L<sup>3</sup>) in a two-step metalation.

The mixed amide-phosphine ligand, L<sup>1</sup>, is effective for stabilizing monometallic Ti, V, and Cr complexes. Presumably, the trianionic amide pocket is ideal for stable trivalent metals. The upper phosphine pocket is suited to late metals, including low-valent Fe, Co, and Ni often occupies this site. As a partner metal, chromium is versatile and also adept at multiple bonding.<sup>2,4,22,23</sup> A dozen (CrM)<sup>+n</sup> complexes were isolated, where M = Cr–Ni and *n* = 2–4. However, divalent metals in the L<sup>1</sup> amide pocket tend to be unstable. Attempts to singly metalate with FeX<sub>2</sub> (or CoX<sub>2</sub>) gave instead the corresponding homobimetallic (M<sub>2</sub>)<sup>+4</sup> halides (Scheme 1.2).<sup>24</sup> The lack of late metal precursors has thwarted efforts to isolate late-late heterobimetallics within this scaffold. For example, L<sup>1</sup>FeCoCl was synthesized in a metal-swapping reaction of L<sup>1</sup>Fe<sub>2</sub>Cl and CoCl<sub>2</sub>(THF)<sub>1.5</sub>.<sup>25</sup>



**Scheme 1.2** Reactions that exemplify limitations in the two-step metalation approach.

The  $L^2$  and  $L^3$  platforms have successfully been used for assembling bimetallics of the mid-to-late first-row metals, Mn to Cu. In contrast to  $L^1$ , monometallic Fe(II) and Co(II) complexes are stable with  $L^2$  and  $L^3$ . Bimetallics containing an early metal are notably absent for  $L^2$  and  $L^3$  platforms, even though V(III) and Cr(III) complexes were isolated. The V and Cr metalloligands were unreactive to further metal uptake, presumably because, in the quasi-octahedral coordination geometry at V and Cr, all six N-atoms are tightly bound to the metal.<sup>26</sup>

A subtle limitation is the lack of heterobimetallic isomers, where only the metal sites are swapped. As an example,  $L^2CoFeCl$  was formed cleanly from  $[L^2Co]K$  and  $FeCl_2$ . Attempts to prepare the  $L^2FeCoCl$  isomer from  $[L^2Fe]K$  and  $CoCl_2$ , instead produced  $L^2CoFeCl$  and  $L^2Co_2Cl$ . For labile first-row metal ions, trapping a “kinetic” heterobimetallic species appears untenable.

Figure 1.1 sums the progress in the Lu group to configure bonds across the first-row transition metal period. Half of the possible metal-metal combinations from Ti to Cu have been isolated with structural validation. The ability of these species to transfer

multiple electrons have been probed by isolating different redox states of the bimetallic core, particularly  $(MM')^{+2,+3,+4}$ .

	Ti	V	Cr	Mn	Fe	Co	Ni	Cu
Ti					• +3	• +3	• +3	
V					• +3 • +4	• +2 • +3 • +4	• +3	
Cr			• +2 • +3	• +2 • +3	• +2 • +3 • +4	• +2 • +3 • +4	• +3 • +4	
Mn					• +4	• +4		
Fe					• +3 • +4	• +2 • +3 • +4		
Co						• +2 • +3 • +4	• +4	• +3 • +4
Ni								
Cu								

**Key**

- L<sup>1</sup>
- L<sup>2</sup>
- L<sup>3</sup>

**Figure 1.1** Array of first-row transition metal-metal complexes prepared with the double-decker ligands  $L^1-L^3$ . Homometallic  $(M_2)^{+n}$  and heterometallic  $(MM')^{+n}$  species are indicated by colored boxes (in blue and yellow, respectively), with the redox state(s) of the b bimetallic core,  $+n$ , inside the box.

### 1.3 Metal-Metal Bonding

Molecular metal-metal bonding continues to be primarily characterized by X-ray crystallography, where the intermetal distance defines the metal-metal interaction. While an inverse relationship between intermetal distances and metal-metal bond order is qualitatively understood, formulating a quantitative relationship has been impossible because of complex electronic configurations, subtlety of delta bonds, and the sensitivity of intermetal distances to external factors, such as molecular charge, ligand electronics and sterics, and crystal packing forces.<sup>2</sup> Some of these complications are obviated by comparing isostructural complexes with the same ligand. Hence, the diverse bimetallics

obtained with  $L^1$  make an ideal collection for understanding how metal-metal bonding varies across the first-row transition metal period.

A counterargument is that bridging ligands intrinsically enforce short metal-metal contacts. In the case of  $L^1$ , the scaffold is flexible and accommodates a wide range of metal-metal distances (Figure 1.2). Considering just the  $L^1CrM$  complexes, the intermetal contact can differ by 0.70 Å, from 1.74 Å in  $[L^1Cr_2]K$  to 2.41 Å in  $L^1CrNi$ . The Cr–N<sub>amine</sub> distance changes by 0.4 Å, despite the constancy of the  $L^1Cr$  metalloligand. Based on these stark structural changes, any inherent bias of the ligand pales to the metal-metal interaction in determining the metal-metal bond distance.

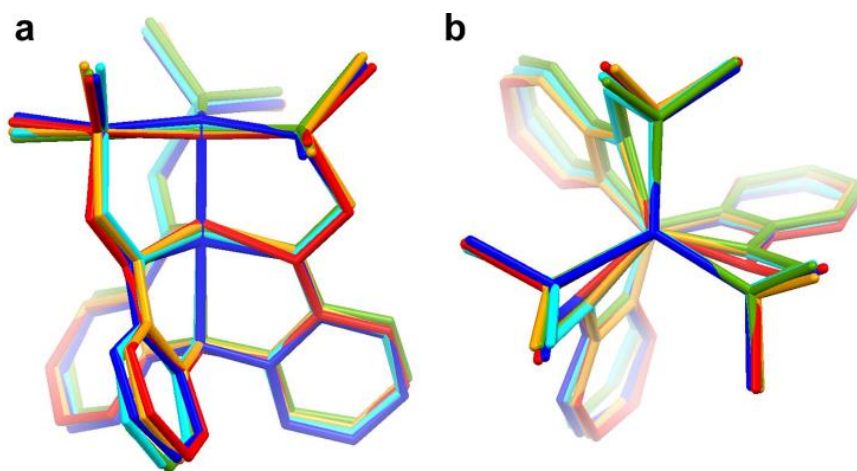


**Figure 1.2** Overlay of solid-state structures of isostructural  $L^1CrM$  bimetallics shown from side (a) and top (b) views. Methyl and H atoms were omitted for clarity. The bimetallics are  $[L^1Cr_2]K$  (red),  $L^1CrMn$  (orange),  $L^1CrFe$  (green),  $L^1CrCo$  (cyan), and  $L^1CrNi$  (blue).

Interpreting heterometallic bonding is vexing because absolute intermetal distances cannot be neatly compared. To normalize metal-metal bonding across different metals, Cotton introduced the formal shortness ratio (FSR), a quotient of the intermetal distance to the expected single-bond length.<sup>2</sup> An underlying issue is how one determines the “expected” single-bond length between any two metals. Typically, one sums the metals’ single-bond radii, a tabulated value that depends on the metallic radii and coordination number in the lattice.<sup>27</sup>

Short intermetal distances may indicate multiple bonding and correspond to FSR below unity. At the other extreme, long intermetal distances with FSR values above unity

would be considered weakly or non-interacting. The bonding interpretations were guided by experimental FSR values and theoretical calculations by Gagliardi and co-workers. While FSR values appear distinctive for the number of  $\sigma$ - and  $\pi$ -bonds, they poorly reflect the presence of delta bonds. The poor spatial overlap of  $\delta$ -symmetry d-orbitals render delta bonds weak and of minor impact to the intermetal distance. Hence, for quadruply or higher bonded bimetallics, theory is critical to gain a precise bonding picture. The M–M stretching frequencies are arguably a better experimental readout of metal-metal bond multiplicity, but such measurements can be challenging to obtain.

### 1.3.1 Bonding Trends

To extract trends in metal-metal bonding, we focus on the strictly isostructural bimetallics,  $[L^1MM]^{+,0,-}$ , which comprise twenty-one unique compounds. The shortness of the metal-metal bond (as indicated by low FSR values, Figure 1.3) depends on a combination of two factors: (1) the total  $d$ -electron count, and (2) the polarity of the metal-metal interaction, which is approximated by the difference in the two metals' group numbers, or  $\Delta N$ . Metal-metal bond multiplicity (FSR < 0.97) is observed within a small range of  $d$ -electrons (9–12), while bond polarity is better tolerated ( $\Delta N \leq 5$ ). Based on complementary theoretical calculations, FSR values near 0.9 correspond to a double metal-metal bond ( $\sigma + \pi$ ), while values close to 0.8 correspond to a triple bond ( $\sigma + 2\pi$ ). Formal quintuple bonding ( $\sigma + 2\pi + 2\delta$ ) was predicted for  $[L^1Cr_2]^-$  and  $L^1CrMn$ , which have the lowest FSR values of 0.74 and 0.78, respectively, in this series.<sup>20,28</sup> Multiply bonded bimetallics tend to be low-spin,  $S = 0$  or  $S = 1/2$  (Figure 1.4). The one exception,  $[L^1CrFe]^-$ , is  $S = 1$ , but this complex is also considered low spin, as the unpaired electrons populate degenerate  $d$ -orbitals.

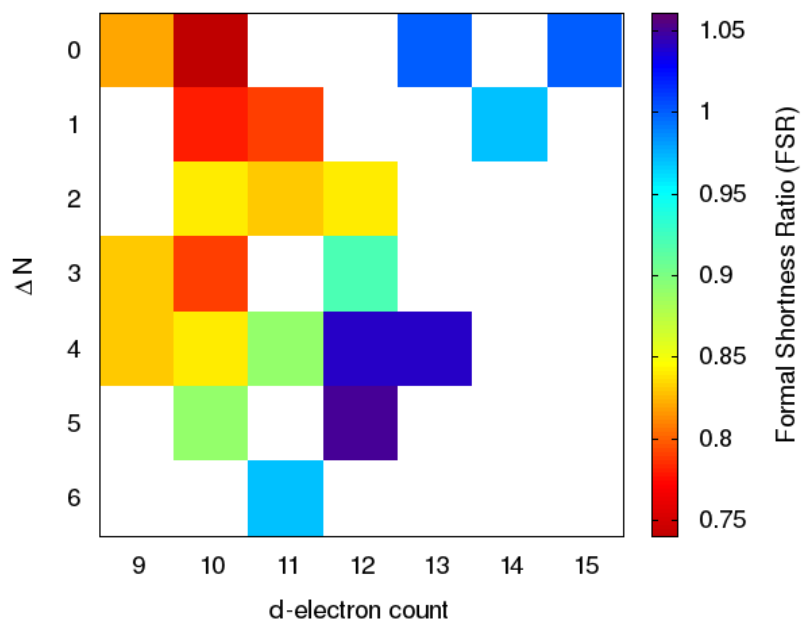


**Figure 1.3** Formal shortness ratio (FSR) map of 21 isostructural bimetallics using the  $L^1$  ligand. FSR values are plotted according to the total d-electron count and the difference in the two metal's group numbers ( $\Delta N$ ).

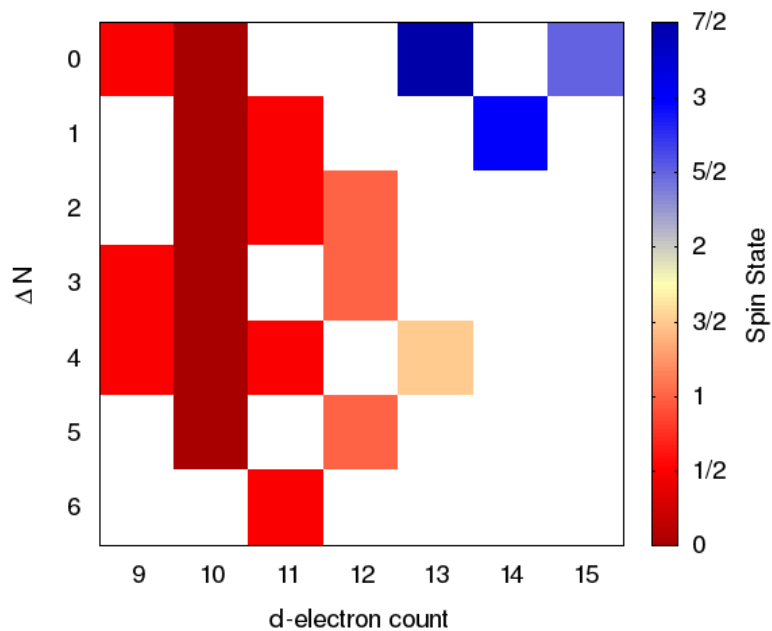


**Figure 1.4** Corresponding spin state map of 20 isostructural bimetallics.

In addition to multiply bonded bimetallics, significant metal-metal interactions are observed in two other distinct groups. The first set is a trio of late-late metal pairings,  $L^1Fe_2$ ,  $L^1Co_2$ , and  $L^1FeCo$ , where the metal elements are identical or similar ( $\Delta N = 0, 1$ ) and  $d$ -electron counts are high, from 13–15.<sup>24,29</sup> The FSR values (0.97–1.00) approximate a single metal-metal covalent bond. Notably, this trio adopts high-spin configurations,  $S = 5/2$ – $7/2$ . Also befitting this group,  $L^3Co_2$  and  $L^3CoFe$ , which have FSR values of 1.03 and 0.94, respectively, are similarly high spin.<sup>14</sup>

The remaining group comprises Ni–M bimetallics with high bond polarity ( $\Delta N = 4$ – $6$ ) and intermediate  $d$ -electron counts, 11–13. The FSR values are generally close to unity (0.98–1.05). Because of the large Ni–M bond polarity, where M is Ti–Cr, the  $d$ -electrons are primarily localized at Ni, and the interaction is aptly described as a Ni(0)→M(III) dative bond. The overall spin states, which are low to intermediate spin, simply reflect the localized spin of the M(III) center, e.g.  $S = 1/2$  Ti(III),  $S = 1$  V(III), and  $S = 3/2$  Cr(III).

### 1.3.2 Understanding Bonding through Theory

Complementary theoretical calculations by Gagliardi and co-workers have heightened our understanding of metal-metal bonding in the double-decker systems. Figure 1.5 shows the evolution of the molecular orbital diagrams across different metal-metal bonding regimes. The bond orders shown are based on the main electronic configuration, which is defined as the formal bond order (FBO). The corresponding effective bond order (EBO), which considers multiconfigurationality, is typically lower by 0.7 on average in the multiply bonded bimetallics (Table 1.1).

**Table 1.1** Summary of bond order information for multiply bonded bimetallics, main configuration and EBO from CASSCF calculations.

MM pair	d-count	FSR	% of main configuration	FBO	EBO	$\Delta(\text{FBO} - \text{EBO})$
$L^1Cr_2$	9	0.82	42	4	2.71	1.29
$[L^1Cr_2]^-$	10	0.74	60	5	3.99	1.01
$L^1MnCr$	10	0.78	55	5	3.85	1.15
$[L^1MnCr]^-$	11	0.79	64	3	2.39	0.61
$L^1FeCr$	11	0.83	58	3	2.15	0.85
$[L^1FeCr]^+$	10	0.84	55	3	2.21	0.79
$[L^1FeCr]^-$	12	0.84	60	3	2.35	0.65
$L^1CoCr$	12	0.92	60	2	1.58	0.42
$L^1FeV$	10	0.79	75	3	2.51	0.49
$[L^1FeV]^+$	9	0.83	72	3	2.42	0.58
$L^1CoV$	11	0.89	72	2	1.55	0.45
$[L^1CoV]^+$	10	0.84	75	3	2.49	0.51

The weaker ligand field associated with trigonal symmetry permits all five  $d$ -orbitals to engage in metal-metal bonding by forming  $\sigma$ ,  $2\pi$ , and  $2\delta$  molecular orbitals. Hence, 10 is a magical  $d$ -count for maximal bonding, and quintuple bonds are predicted for  $(d-d)^{10}$   $[L^1Cr_2]^-$  and  $L^1CrMn$ . The corresponding EBO values of 3.99 and 3.85, respectively, are on par with those calculated for quintuply bonded dichromium complexes.<sup>30</sup> While quintuple bonding requires a  $(d-d)^{10}$  configuration, the converse is false. For instance,  $[L^1CrFe]^+$ , which has 10  $d$ -electrons, exhibits a different electronic configuration of  $\sigma^2\pi^4(\text{Fe } d_{xy}, d_x^2-y^2)$ .<sup>4</sup> Presumably, as  $\Delta N$  increases, the energy overlap between the two metals  $\delta$ -symmetry  $d$ -orbitals worsens, resulting in non-bonding, localized  $d$ -orbitals. Even larger  $\Delta N$  results in localization of the  $\pi$ -symmetry, and eventually  $\sigma$ -symmetry,  $d$ -orbitals until all  $d$ -electrons are localized at individual metals. At this extreme,



the metal-metal interaction, if any, would be dative in nature, which is characteristic of the Ni–Cr, Ni–V, and Ni–Ti bimetallics.

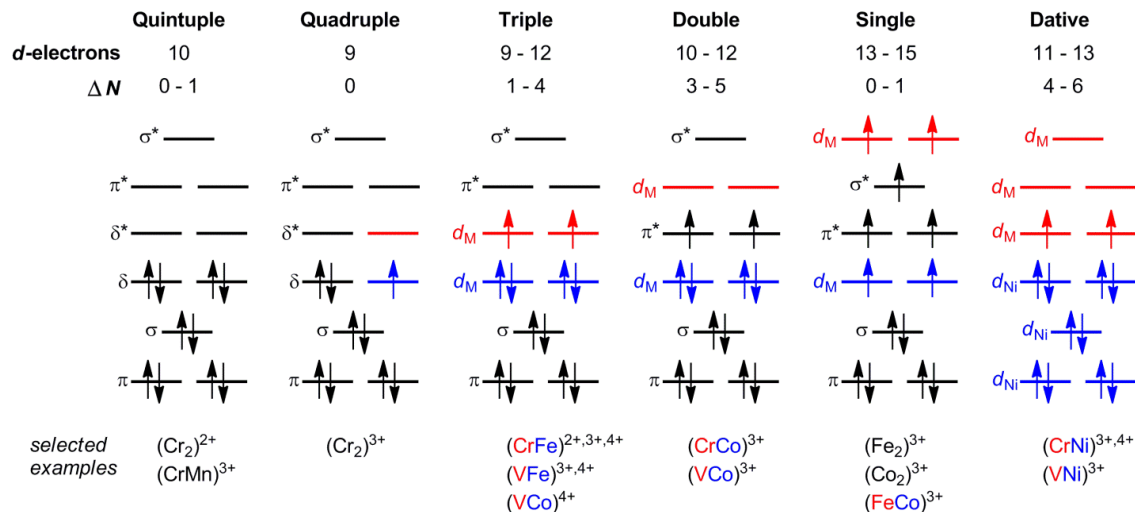


**Figure 1.5** Qualitative d-orbital manifolds of different metal-metal bonding regimes. The coloring of the energy levels and electrons denotes whether they are primarily delocalized (black) or localized (red and blue).

Delta bonding is highly sensitive to electron count. In  $(d-d)^9$  L<sup>1</sup>Cr<sub>2</sub>, the intuitive formal bond order based on the canonical manifold ( $\sigma + 2\pi + 2\delta$ ) is 4.5. The predicted FBO is lower at 4 because of localization of one  $\delta$ -symmetry *d*-orbital. By contrast,  $\pi$ -bonding is robust. Triply bonded bimetallics are the majority of multiply bonded heterobimetallics and tolerate a large range of d-counts and  $\Delta N$  (Figure 1.5). A slight increase in the number of d-electrons and/or  $\Delta N$ , however, can cost a bond order to give a formal metal-metal double bond.

In the single covalent regime, the MO diagram actually estimates a slightly higher FBO of 1.5. These bimetallics are high spin, which is rare for metal-metal complexes. The concurrence of metal-metal bonding and a high spin configuration seems counterintuitive. Electron unpairing cannot result from poor energy overlap as these complexes are homobimetallic, or a close analogue, e.g. L<sup>1</sup>FeCo. High-spin phenomenon has been described in other metal-metal systems, and there is no link to geometry, coordination number, or ligand.<sup>17,31-33</sup> However, many are homobimetallic, and all have high d-electron

counts, 13–16. Presumably, as *d*-electrons increase well above 10, electron-electron repulsion becomes a significant problem. Hence, electron unpairing alleviates electronic repulsion while providing favorable exchange interactions.

### 1.3.3 Spectroscopic Evidence of Multiple Bonding

Besides short intermetal distances, multiply bonded bimetallics should exhibit unique spectroscopic signatures. Delta bonding electrons should manifest a  $\delta \rightarrow \delta^*$  transition, which can indirectly probe the M–M bond strength.<sup>34</sup> While  $\delta^2 \rightarrow \delta\delta^*$  transitions of quadruply bonded complexes are well known, reports of  $\delta^4 \rightarrow \delta^3\delta^*$  transitions in quintuply bonded species are lacking. In  $[\text{L}^1\text{Cr}_2]^-$  and  $\text{L}^1\text{CrMn}$ , the lowest energy transitions at 675 and 1025 nm, respectively, were assigned as  $\delta^4 \rightarrow \delta^3\delta^*$  transitions.<sup>28</sup> A complementary resonance Raman study of  $[\text{L}^1\text{Cr}_2]^-$  showed a band at  $443\text{ cm}^{-1}$  that was identified by theory as a relatively pure Cr–Cr bond vibration.

Metal-metal multiple bonding can significantly perturb  $^1\text{H}$  NMR chemical shifts of protons near the multiply bonded nuclei.<sup>35</sup> The methylene protons in  $\text{L}^1$  shift downfield by as much as 3.5 ppm in the  $(d-d)^{10}$  bimetallics. The diamagnetic anisotropies ( $\Delta\chi$ ) in Table 1.2 are large, implicating multiple bonding. Unfortunately,  $\Delta\chi$  does not correlate with bond order or FSR and appears insensitive to delta bonding. Presumably,  $\Delta\chi$  relates to both FSR and bond polarity ( $\Delta\text{N}$ ), since low FSR values ( $\leq 0.84$  to maximize  $\pi$ -bonding) and bond polarization can enlarge diamagnetic anisotropy.

**Table 1.2** Diamagnetic anisotropies ( $\Delta\chi$ ) for  $(d-d)^{10}$  multiply bonded bimetallics.

Complex	FSR	$\Delta\text{N}$	$\Delta\chi$ ( $10^{-36}\text{ m}^3\text{ molecule}^{-1}$ )
$[\text{L}^1\text{Cr}_2]^-$	0.74	0	–3500
$\text{L}^1\text{CrMn}$	0.78	1	–3900
$[\text{L}^1\text{CrFe}]^+$	0.84	2	–5800
$\text{L}^1\text{VFe}$	0.79	3	–4600
$[\text{L}^1\text{VCo}]^+$	0.84	4	–4600
$\text{L}^1\text{TiCo}$	0.89	5	–3400

Nearly all the multiply bonded Fe-bimetallics exhibit large quadrupole splittings ( $\Delta E_Q = 4\text{--}6$  mm/s) by  $^{57}\text{Fe}$  Mössbauer spectroscopy (Table 1.3). Large  $\Delta E_Q$  values are rare, but they are common for iron nitride complexes with a highly covalent  $\text{Fe}\equiv\text{N}$  triple bond.<sup>36</sup> By analogy, a triply bonded  $\text{Fe}\equiv\text{M}$  core could give rise to the large  $\Delta E_Q$  values.<sup>10</sup> There are a few exceptions,  $\text{L}^1\text{TiFe}$ ,  $\text{V}(\text{}^i\text{PrNPPPh}_2)_3\text{FeBr}$ , and  $\text{V}(\text{}^i\text{PrNPPPh}_2)_3\text{Fe}(\text{PMe}_3)$ ,<sup>11</sup> which show normal  $\Delta E_Q$ . Hence, further studies are needed to understand this spectroscopic phenomenon.

**Table 1.3** Summary of Mössbauer parameters for iron bimetallics with multiple bonds.

Complex	$\delta$ (mm s <sup>-1</sup> )	$\Delta E_Q$ (mm s <sup>-1</sup> )	Avg Fe–P distance (Å)	$\Sigma \angle\text{P-M-P}$ (°)	FSR	Ref
$\text{L}^1\text{FeV}$	0.25	5.97	2.263	357.9	0.79	19
$[\text{L}^1\text{FeV}]^+$	0.25	4.04	2.295	358.9	0.84	19
$[\text{L}^1\text{FeCr}]^+$	0.18	5.86	2.268	355.9	0.84	28
$\text{L}^1\text{FeCr}$	0.25	5.92	2.264	358.2	0.83	10
$[\text{L}^1\text{FeCr}]^-$	0.29	5.2	2.244	359.5	0.84	10
$\text{L}^1\text{FeTi}$	0.35	2.64	2.286	359.9	0.83	19
$\text{V}(\text{}^i\text{PrNPPPh}_2)_3\text{FeBr}$	0.33	2.01	2.292	338.7	0.86	11
$\text{V}(\text{}^i\text{PrNPPPh}_2)_3\text{Fe}(\text{PMe}_3)$	0.19	1.85	2.217	341.1	0.86	11

#### 1.4 In Search of Synergistic Redox and Magnetic Properties

By cyclic voltammetry, a few metal-metal pairings exhibit rich redox profiles with 3 or 4 reversible one-electron transfers (Figure 1.6). For instance,  $\text{L}^1\text{CrNi}$  has three reversible events, two oxidations and one reduction at  $-1.32$ ,  $-0.18$ , and  $-2.56$  V, respectively. Comparing  $\text{L}^1\text{CrNi}$  to its individual components was possible because both monometallic  $\text{L}^1\text{Cr}$  and  $(\text{H}_3\text{L}^1)\text{Ni}$  are known. While  $(\text{H}_3\text{L}^1)\text{Ni}$  has a single reversible oxidation at  $-1.02$  V, and  $\text{L}^1\text{Cr}$  shows broad, *irreversible* features above  $-0.4$  V. Thus, the emergence of three reversible redox events for  $\text{L}^1\text{CrNi}$  is remarkable. The overall redox profile of  $\text{L}^1\text{CrNi}$  exemplifies the principle that the whole is greater than the sum of the parts.

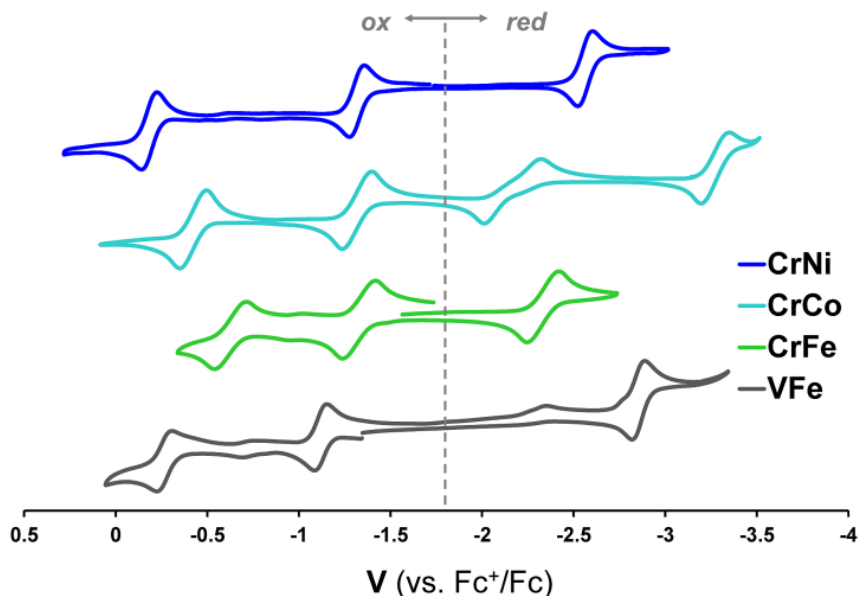


**Figure 1.6** Cyclic voltammograms of selected  $L^1$  bimetallic complexes.

The other redox-active bimetallics,  $L^1CrCo$ ,  $L^1CrFe$ , and  $L^1VFe$ , contain multiple bonds unlike datively bonded  $L^1CrNi$ . Nearly all these bimetallics have valence electrons and/or holes in localized  $d$ -orbitals. Consistent with this idea, quintuply bonded  $[L^1Cr_2]^-$  and  $L^1CrMn$ , which have highly delocalized valence electrons, exhibit fewer redox processes. Empirically, multi-electron redox processes are more favorable in heterobimetallics containing Cr, which perhaps as a mid-metal, is inherently more redox flexible than the early metals V and Ti. Consistent with this finding, substituting Cr for V results in globally harsher redox potentials in  $L^1VFe$  than in  $L^1CrFe$ . In summary, maximizing the number of accessible redox processes may correlate with localized valence electrons and/or holes, while an appropriate metal partner can favorably shift redox potentials.<sup>16</sup>

The concept that metal-metal interactions can govern magnetic behavior is demonstrated by the isostructural  $L^2MM'Cl$  systems.<sup>13,21</sup> The magnetic susceptibilities in Figure 1.7 were modeled using two individual spins that couple magnetically, but unexpectedly, the nature of the coupling, anti- versus ferromagnetic, was correlated to differences in the metal-metal interaction. In weakly interacting systems (FSR 1.03–1.09), the total unpaired spins are equivalent to  $\Delta N$  because each divalent, high-spin metal

couples antiferromagnetically. Hence,  $L^2Co_2Cl$  is  $S = 0$ ;  $L^2CoFeCl$  and  $L^2FeMnCl$  are  $S = \frac{1}{2}$ ; and  $L^2CoMnCl$  and  $L^2CoCuCl$  are  $S = 1$ . Moreover, the strength of the magnetic coupling was found to increase across the period. A surprising finding was that the ground spin state of  $L^2Fe_2Cl$ , which has an Fe–Fe bond of 2.2867(5) Å (FSR 0.98) is close to  $S = 3$ , implicating ferromagnetic coupling between the two iron centers engaged in a single metal-metal bond.

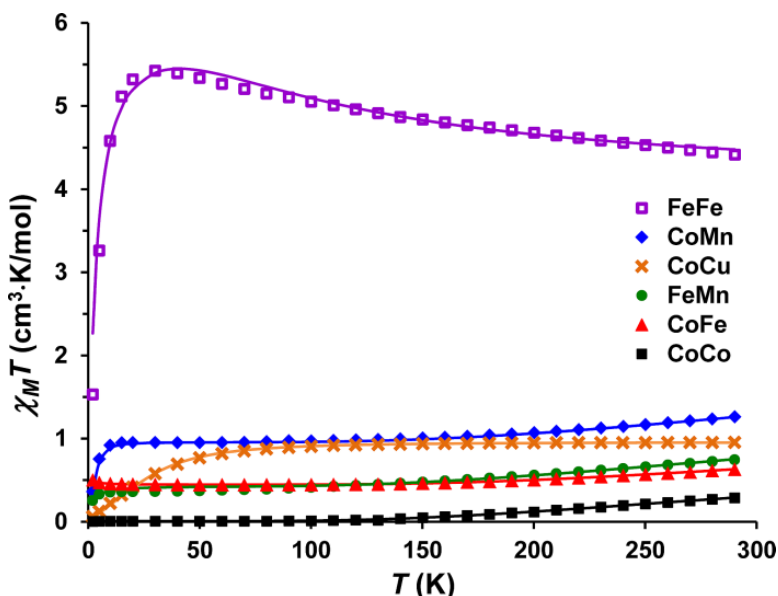


**Figure 1.7** Temperature dependence of magnetic susceptibility, plotted as  $\chi_M T$  versus  $T$ , of isostructural  $L^2MM'Cl$  complexes.

Metal-to-metal charge transfer (MMCT) is another fascinating property of multimetallic complexes that has applicability in photocatalysis. In the  $L^2CoMCl$  series, an intense band in the visible region was proposed to be a  $Co \rightarrow M$  electronic excitation, or  $Co(II)M(II) \xrightarrow{h\nu} Co(III)M(I)$  (Figure 1.8). The MMCT energy red-shifts as  $M$  is varied across the first-row period,  $M = Mn < Fe \sim Co < Ni \ll Cu$ . Based on electronegativity,  $M(II/I)$  redox couples should become more favorable across the period. Indeed, the  $Cu(II/I)$  potential in  $L^2CoCuCl$  is the mildest of all the  $M(II/I)$  redox couples, and corresponds to the lowest excitation energy.<sup>21</sup>

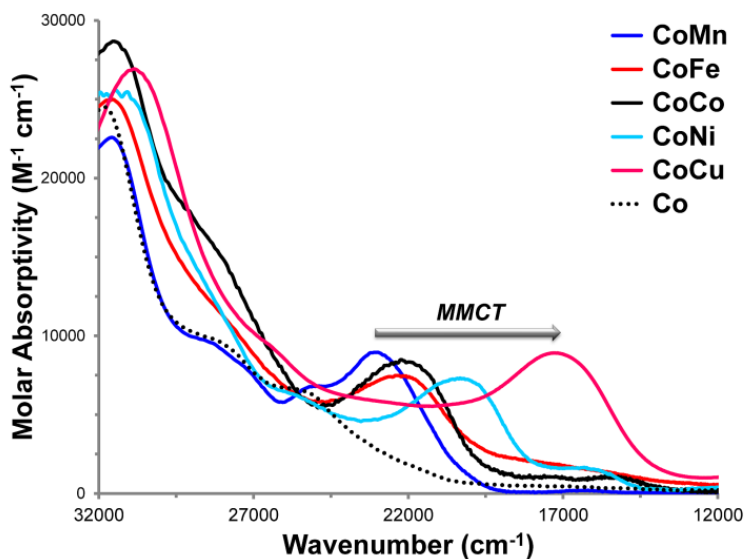


**Figure 1.8** Electronic absorption spectra of isostructural  $L^2CoMCl$  bimetallics and  $[L^2Co]K$  in  $CH_2Cl_2$ .

The electrochemical data was then used to attempt to quantify the excitation energies. If Co and M are non-interacting in the ground and excited states, then the excitation energy could be approximate to the driving force for the corresponding redox changes, or  $\Delta E = E^\circ M(II/I) - E^\circ Co(III/II)$ . For  $L^2CoMnCl$ , the excitation energy ( $\lambda_{max} = 2.85$  eV) is reasonably close to  $\Delta E$  (2.55 V), where the ratio of  $\Delta E$  to  $\lambda_{max}$  is 0.89. The ratio, however, decreases significantly across the first-row period: 0.73 (Fe), 0.70 (Co), 0.53 (Ni), and 0.27 (Cu). Presumably, the deviation is due to significant Co–M interactions in the ground state, which includes any intermetal electrostatic attraction. Hence, destabilizing the Co–M interaction costs additional energy, raising  $\lambda_{max}$  well above  $\Delta E$ . In support, the FSR of the  $L^2CoMCl$  complexes decrease across the period, from 1.09 in  $L^2CoMnCl$  to 1.03 in  $L^2CoCuCl$ , where the larger deviations correlate to the stronger Co–M interactions.

### 1.5 Small molecule reactivity using multiple metals

In addressing the problem of limited energy sources, a critical component is to catalyze challenging chemical reactions using sustainable, earth-abundant metals instead of precious metals. In particular, the multielectron conversion of small-molecule feedstocks into useful commodities is essential to the chemical industry, but inherently

difficult to mediate efficiently. This difficulty stems from the kinetic challenge of directing the simultaneous transfer of multiple electron and/or proton equivalents, so as to bypass high energy intermediates during catalysis. One strategy for replacing precious metal catalysts while maintaining multielectron redox capabilities is to couple two or more first-row transition metals in a single catalyst or active site. Cooperativity among multiple earth-abundant metals underlies numerous essential biological processes, including the reduction of  $N_2$  to ammonia.

The FeMo cofactor of nitrogenase, a cluster of 7 Fe centers and 1 Mo, supported by 9 bridging sulfides and an unusual, central carbide, facilitates  $N_2$  fixation to  $NH_3$ <sup>37-41</sup>. It has been proposed that the key intermediate that is primed to bind and reduce  $N_2$  comprises two  $Fe(\mu-H)Fe$  fragments, which together store four reducing equivalents in the cofactor. Thus, the proximity of several Fe centers in the FeMo cofactor promotes multielectron reactivity by allowing the substantial buildup and storage of electron equivalents via the cooperative stabilization of bridging hydride moieties.

In developing multimetallic catalysts for functionalizing small molecules, chemists have long sought to understand and apply the design principles underlying the function of biological enzymes. As illustrated by enzyme active sites, synthetically coupling multiple metal centers in close proximity can allow for maximal storage of electrons (e.g., in FeMo-co). However, large metal clusters, which are more difficult to synthetically assemble in the laboratory, are not prerequisites for rich redox profiles. Indeed, two first-row metals that are bonded together can promote multiple single-electron transfers.<sup>20</sup> Notably, the rich redox profile of a metal-metal bonded species may be synergistic in that it can be greater than the sum of its parts: electronic coupling of the metal centers may give rise to more accessible redox states than those of the individual constituent metals (*vide supra*).<sup>20</sup> Two metals in a metal-metal bonded unit are also in close enough proximity to engage in cooperative interactions with substrate, as is critical to stabilizing bridging hydride intermediates in nitrogenase. In short, while enzymatic active sites no doubt rely upon all metal centers and the surrounding residues to function, the key design principles of redox versatility and cooperative substrate activation by multiple proximal metal centers may be retained in a bimetallic complex featuring two metals engaged in a metal-metal bond.

The manner in which a metal-metal bonded ( $M_A-M_B$ ) complex activates a substrate with an  $X-Y$  bond can be divided broadly into three categories (Figure 1.9): (1) cooperative activation across the  $M_A-M_B$  bond in which each metal directly interacts with substrate, (2) homolysis of the  $M_A-M_B$  bond to form two metalloradical fragments that cooperatively activate substrate, and (3) activation of substrate at an active metal ( $M_A$ ) in which the supporting metal ( $M_B$ ) primarily serves to electronically tune the active metal.

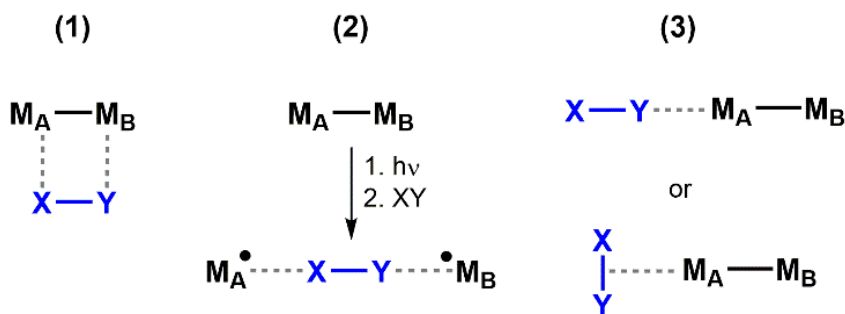


**Figure 1.9** Three modes of  $X-Y$  bond activation at a metal-metal bonded unit ( $M_A-M_B$ ).

Cooperative activation of the substrate  $X-Y$  bond across the  $M_A-M_B$  bond can occur in either a homolytic or heterolytic fashion, a distinction which typically depends on the polarity of both the  $M_A-M_B$  and  $X-Y$  bonds. Homolytic substrate activation is more common across homobimetallics and other relatively nonpolar  $M_A-M_B$  bonds. On the other hand, polar  $M_A-M_B$  bonds between disparate metals, such as the pairing of a late transition metal with an early or main-group metal, often leads to heterolytic substrate activation. Cooperative substrate activation by early-late heterobimetallics<sup>6,7,42-46</sup> has been more generally reviewed, as has the reactivity of metalloradicals formed *in situ* from metal-metal bonded precursors.<sup>47-49</sup> The main focus of this section will primarily consider the case in which a single active metal binds and activates  $N_2$ , while the supporting metal tunes the electronic coordination environment of the active metal via a metal-metal bond.

The binding of dinitrogen to a metal center is primary due to dinitrogen being a good  $\pi$ -acceptor. Hence, the dominant interaction in the  $M-N_2$  end-on binding mode is  $\pi$ -back-bonding:  $(M d_{xz}, d_{yz})^4 \rightarrow (N_2 \pi^*)^0$  (Figure 1.10).<sup>50,51</sup> A Lewis acid support (LA) will



render a transition metal more electron-deficient and weaken  $M \rightarrow N_2$   $\pi$ -back-bonding compared to a single metal center. Nevertheless, a Lewis acid support can stabilize exceedingly low metal oxidation states, e.g.  $M(-I)$ , which have greater electron-density to  $\pi$ -back-donate to  $N_2$ . This paradigm has allowed for enhanced  $N_2$  activation in  $[(N_2)FeAl]^-$  and  $[(N_2)CoAl]^-$  species via the stabilization of highly reduced  $Fe(-I)$  and  $Co(-I)$  by an  $Al(III)$  supporting Lewis acid.<sup>52</sup>

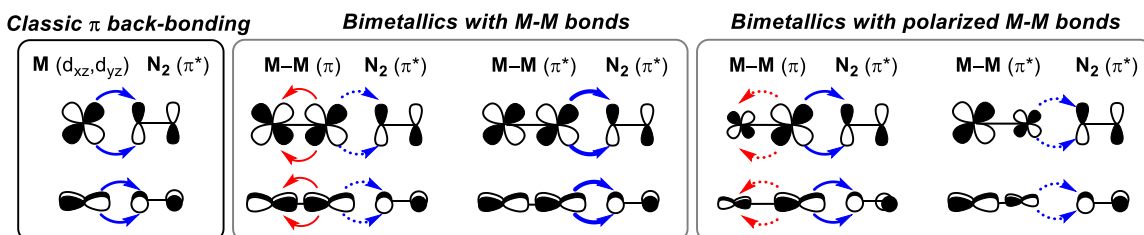


**Figure 1.10** Bonding interactions between a transition metal (M) and  $N_2$  in the absence and presence of a supporting metal engaged in metal-metal bonding. Note that the orbital depictions for the polarized  $M_B-M_A-N_2$  case presumes that the electronegativity of  $M_A$  is greater than that of  $M_B$ . Blue arrows indicate  $M_B$  donation to the  $N_2$ , while red arrows represent donation to  $M_A$ .

Moving beyond Lewis acid supports, a supporting transition metal ( $M_B$ ) is a more complex case because it can engage the “active” transition metal ( $M_A$ ) to form a covalent bond of varying bond order and polarity. Such a metal-metal interaction arises from the mixing of the d-orbitals of  $M_A$  and  $M_B$ , from which a maximum bond order of five can be achieved ( $\sigma$ , 2  $\pi$ , and 2  $\delta$  bonds). The bond order is dictated by the total d-electron count and by the energy overlap of d-orbitals at the two metals (*vide supra*).<sup>20,53</sup> Since  $\pi$ -back-donation to  $N_2$  can only occur from the  $M_A-M_B$   $\pi$  and  $\pi^*$  molecular orbitals, two limiting cases of metal-metal bonding are considered (Figure 1.10): (1) delocalized  $M-M$   $\pi/\pi^*$  orbitals arising from  $M_A$  and  $M_B$  d-orbitals of similar energies, and (2) polarized  $M-M$   $\pi/\pi^*$  orbitals from  $M_A$  and  $M_B$  d-orbitals of disparate energies. In the former case,  $\pi$ -back-donation to  $N_2$  should be more effective from the high-lying  $M-M$   $\pi^*$  orbital and less effective from the stabilized  $M-M$   $\pi$  orbital, compared to the corresponding  $\pi$ -back-donation interactions for a single metal center. Several examples of the multimetallic

activation of dinitrogen will be discussed in addition to the reactivity of N<sub>2</sub> and N<sub>2</sub> derived substrates by complexes with multimetallic cores.

## 1.6 Literature examples of N-N bond cleavage with multimetallic complexes

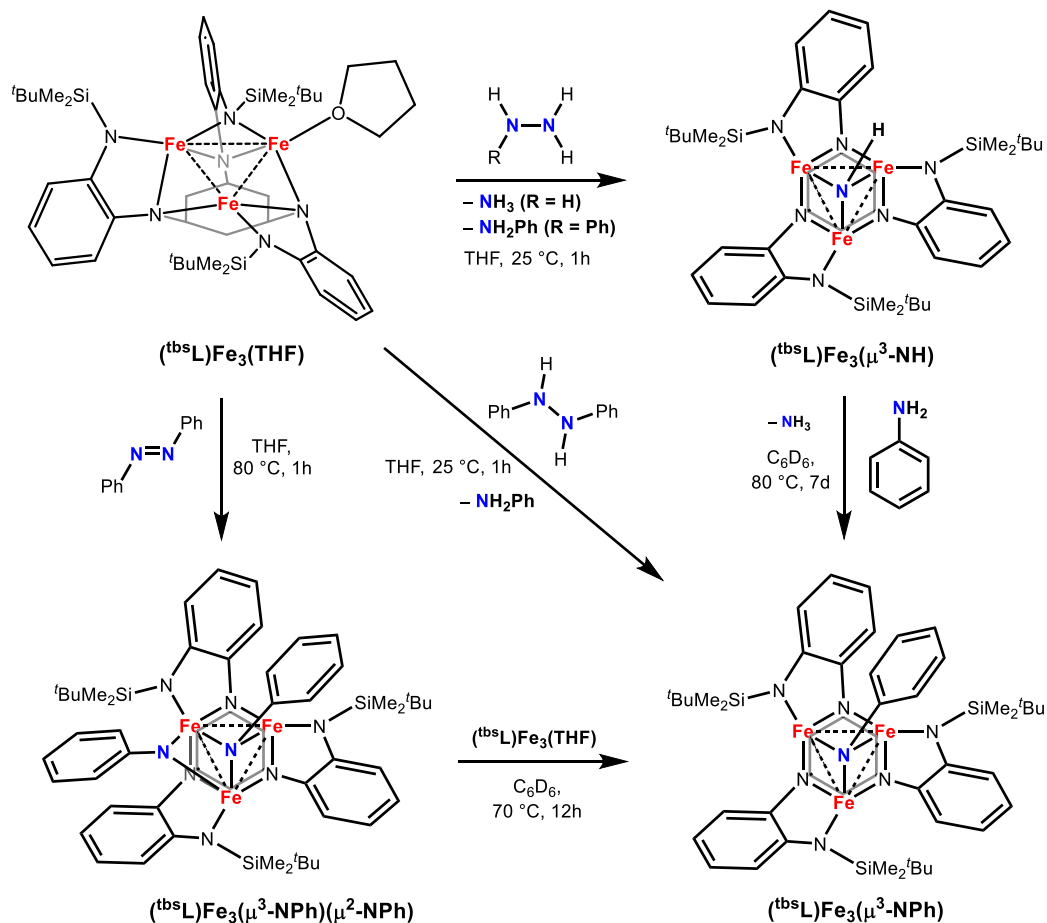
### 1.6.1 Reduction of small molecules by trigonal trimetallic clusters

The challenge of a controlled synthesis of trinuclear metal clusters was addressed by the Betley group with the use of multidentate amine ligands. A tri-iron cluster was first synthesized using the ligand CH<sub>3</sub>C(CH<sub>2</sub>NHPh-*o*-NH<sub>2</sub>)<sub>3</sub>, 1.5 equivalents of [Fe<sub>2</sub>{N(SiMe<sub>3</sub>)<sub>2</sub>}<sub>4</sub>], and 3 equivalents of a tertiary phosphine ligand.<sup>54</sup> This tri-iron complex was the beginning of a series of tri-iron complexes using variants of the multidentate amine ligand that have been shown to undergo multiple redox processes, achieve high spin ground states, and reduce small molecules.<sup>54-57</sup>

A variant of the initial tri-iron cluster was prepared by using the ligand, [1,3,5-C<sub>6</sub>H<sub>9</sub>-(NPh-*o*-NSi<sup>t</sup>BuMe<sub>2</sub>)<sub>3</sub>]<sup>6-</sup>, which increases steric bulk to mitigate the binding of multiple L (L = PR<sub>3</sub>, THF) ligands. Instead, only one THF solvent molecule binds to one Fe, and one silylamide bridges between two Fe centers, resulting in three distinct Fe coordination environments. This asymmetric tri-iron complex reacts with tetrabutylammonium azide at room temperature to form a tri-iron μ<sub>3</sub>-nitride via a two-electron oxidation of the tri-iron complex. The Fe<sub>3</sub>-nitride displayed nucleophilicity when it underwent a rapid reaction with methyl iodide to form a methyl imido complex. The use of a single ligand framework to bind three redox active iron centers provides unique control of reactivity while exploiting the redox abilities of multimetallic clusters.<sup>55</sup>

Cooperative multielectron reduction of small molecules with these tri-iron clusters was extended to the N<sub>2</sub> derivatives: hydrazine, phenyl hydrazine and azobenzene.<sup>57</sup> In these reactions, the N-N bond is cleaved, forming a tri-iron μ<sub>3</sub>-imido and releasing an equivalent of amine. The use of phenylhydrazine as a substrate demonstrated the preference to form a Fe<sub>3</sub>(μ<sub>3</sub>-NH) and releasing aniline. The Fe<sub>3</sub>(μ<sub>3</sub>-NH) was shown to be the kinetic product of the reaction, but upon heating the crude mixture, a transamination occurred, resulting in the phenylimido Fe<sub>3</sub> product, Fe<sub>3</sub>(μ<sub>3</sub>-NPh). The Fe<sub>3</sub>(μ<sub>3</sub>-NPh) could also be isolated when

symmetric 1,2-diphenylhydrazine or azobenzene was used as the substrate. However, when azobenzene was used a substrate, an intermediate was isolated prior to the formation of  $\text{Fe}_3(\mu^3\text{-NPh})$ , revealing a tri-iron bis-imido complex. The four-electron reduction of azobenzene to cleave the N=N bond demonstrates the use of multimetallic cooperativity to achieve multiple electron redox processes at mild conditions.<sup>57</sup>



**Scheme 1.3** Reactivity of tri-iron complex  $(\text{tbsL})\text{Fe}_3(\text{THF})$  with  $\text{N}_2$  derived substrates.

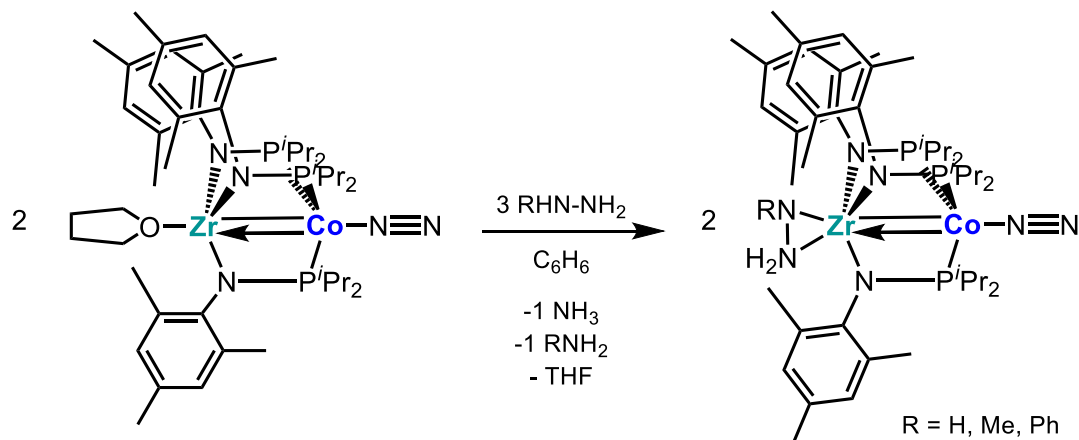
### 1.6.2 Dinitrogen activation with heterobimetallic compounds

Heterobimetallic complexes in the Thomas lab have paired Co with Ti, Zr and Hf using a mixed amide-phosphine ligand.<sup>16,58,59</sup> These M–Co bonds all feature a short metal-metal interaction and an  $\text{N}_2$  molecule bound to Co. The variation of the early metal by the

use of different group 4 metals can be seen to attenuate the activation of the N<sub>2</sub> bound to the Co. When compared to an isostructural bimetallic, the larger metal supports a more activated N<sub>2</sub> molecule bound to Co by its  $\nu_{N_2}$  (Table 1.4). It is speculated that with the larger group 4 metals a weaker interaction with Co is seen, allowing more electron density in Co to participate in  $\pi$ -backbonding to the N<sub>2</sub>. This trend can be seen in Table 1.4 where the smaller the FSR, the less activated the N<sub>2</sub>.

**Table 1.4** Comparison of group 4 metal supported Co heterobimetallic complexes that bind N<sub>2</sub>

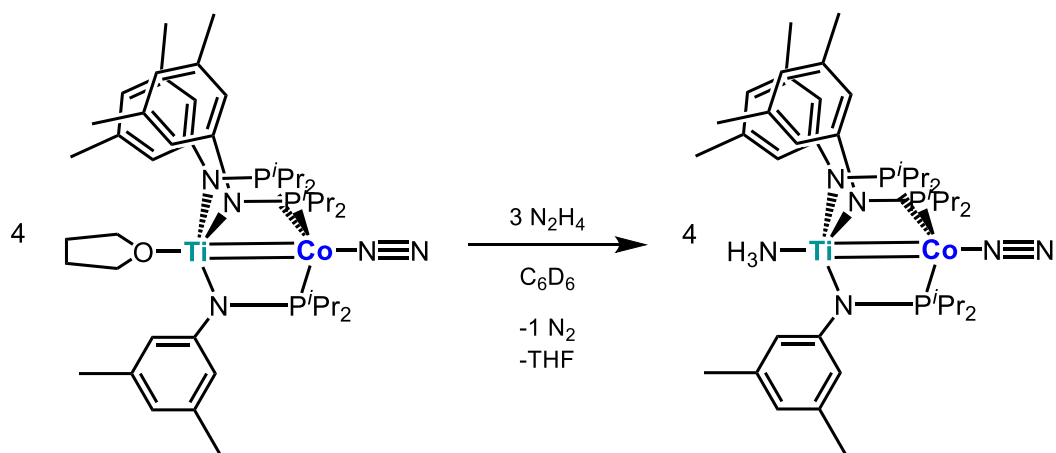
Complex	M–Co distance (Å)	FSR	$\nu_{N-N}$ (cm <sup>-1</sup> )	ref
(THF)Ti(XylNP <sup>i</sup> Pr <sub>2</sub> ) <sub>3</sub> CoN <sub>2</sub>	2.23	0.90	2084	59
(THF)Zr(XylNP <sup>i</sup> Pr <sub>2</sub> ) <sub>3</sub> CoN <sub>2</sub>	2.38	0.91	2045	60
[(THF) <sub>5</sub> Na]Zr(MesNP <sup>i</sup> Pr <sub>2</sub> ) <sub>3</sub> CoN <sub>2</sub>	2.56	0.98	2023	16
[(THF) <sub>5</sub> Na]Hf(MesNP <sup>i</sup> Pr <sub>2</sub> ) <sub>3</sub> CoN <sub>2</sub>	2.46	0.95	1992	58



**Scheme 1.4** Reactivity of a (THF)Zr(MesNP<sup>i</sup>Pr<sub>2</sub>)<sub>3</sub>CoN<sub>2</sub> with hydrazine and hydrazine derivatives.

Two of these Co heterobimetallics were used to promote the breaking of an N–N bond in hydrazine and related substrates.<sup>59,61</sup> For a Co-Zr complex, (THF)Zr(MesNP<sup>*i*</sup>Pr<sub>2</sub>)<sub>3</sub>CoN<sub>2</sub>, 1.5 equivalents of hydrazine or a hydrazine derivative, reacted with the CoZr complex to yield hydrazido complexes, with the hydrazido ligand bound side-on to the Zr (Scheme 1.4). The reaction is thought to proceed via the binding of hydrazine to Zr, followed by N–H bond cleavage which ejects an H-atom that can then cleave the N–N bond of another hydrazine substrate. If the substrate is phenylhydrazine, the CoZr complex will react with 2 equivalents of phenylhydrazine to give a 2 electron oxidized product, where a phenyl hydrazido ligand is bound side on to the Zr and phenyl amide bound to Co.<sup>61</sup>

The reactivity with hydrazine is extended from the Thomas lab by the exchange of the Zr early metal for Ti. The TiCo complex (THF)Ti(XylNP<sup>*i*</sup>Pr<sub>2</sub>)<sub>3</sub>CoN<sub>2</sub> disproportionates hydrazine to form an ammonia adduct to Ti and releases free N<sub>2</sub> (Scheme 1.5). The stoichiometric reactivity was extended to the catalytic disproportionation of hydrazine, by reacting (THF)Ti(XylNP<sup>*i*</sup>Pr<sub>2</sub>)<sub>3</sub>CoN<sub>2</sub> with excess hydrazine in diethyl ether. The catalysis had a maximum turnover of 18, and catalyst decomposition is thought to be the limiting factor in catalysis. The catalysis achieves similar turnovers with the ammonia bound complex, (NH<sub>3</sub>)Ti(XylNP<sup>*i*</sup>Pr<sub>2</sub>)<sub>3</sub>CoN<sub>2</sub>, and an N<sub>2</sub>-free complex. Azobenzene was used as a substrate to gain mechanistic insight, and was found to form the same intermediate as the reaction with 1,2-diphenylhydrazine, suggesting that the disproportionation of hydrazine proceeds through a diazene intermediate.<sup>59</sup> The catalytic ability of the TiCo demonstrates how the exchange of Zr for Ti allows for a significant change in the reactivity with a substrate.



**Scheme 1.5** Reaction of (THF)Ti(XylNP*i*Pr<sub>2</sub>)<sub>3</sub>CoN<sub>2</sub> with hydrazine.

### 1.6.3 Tuning N<sub>2</sub> reduction by Co and Fe by apical ligand selection

Low valent, trigonal Co and Fe compounds that bind N<sub>2</sub> have been isolated and studied by the Peters group for over a decade.<sup>62-66</sup> The isolated N<sub>2</sub> bound complexes act as precursors for N<sub>2</sub> functionalization to catalytic nitrogen fixation. Depending on the metal and its supporting apical ligand, varying degrees of N<sub>2</sub> activation is seen based on the ν<sub>N-N</sub>. Functionalization of N<sub>2</sub> has been shown with methyl tosylate, trimethylsilyl chloride and bis(chlorodimethylsilyl)ethane to form silyldiazendio and silylhydrazido species.<sup>62,67,68</sup> The characterization of these compounds serve as pseudo-intermediates in nitrogen fixation, and also reveal a flexible Fe-B interaction that aids in the isolation of these complexes.<sup>67,68</sup>

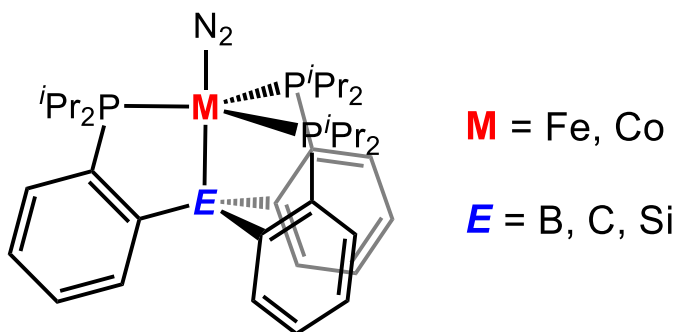


**Figure 1.11** Trigonal metal complex featuring a varying supporting apical ligand capable of nitrogen reduction.

The ability for these Fe-N<sub>2</sub> and Co-N<sub>2</sub> complexes to catalytically reduce N<sub>2</sub> to ammonia was tested, with the results summarized in Table 1.5.<sup>69-72</sup> The Co based catalysts are inferior for the production of ammonia by an order of magnitude compared to the best Fe based catalyst. However, the Co catalysts were the first well-defined, non-iron or molybdenum based systems able to convert N<sub>2</sub> to NH<sub>3</sub>.<sup>73</sup> The Fe catalysts demonstrated a wide range of activity, with the B supporting ligand generating the highest ammonia production with 64 equivalents of ammonia generated per Fe.<sup>72</sup> This high result is on par with Mo based catalysts as the best molecular systems for nitrogen fixation.<sup>74</sup> The activity of the catalysis can be predicted by the combination of the degree of N<sub>2</sub> activation and M-E flexibility.<sup>70,73</sup> The hemi-lability of the Fe-B interaction is attributed for the highest yields seen with (TPB)FeN<sub>2</sub>.<sup>70</sup>

The use of these iron model systems becomes apparent with the wealth of mechanistic studies that can be done with these molecular complexes. Recently, two reports have shed new light onto the mechanism of nitrogen reduction at an Fe metal center. While the Si supported Fe was not found to be as good of a catalyst as its C and B counterparts, it allowed for the isolation and characterization of an Fe=NNH<sub>2</sub> species, which supports two initial additions of H atoms at the distal nitrogen. The (SiP<sub>3</sub>)Fe=NNH<sub>2</sub><sup>0/+</sup> complexes are stable in solution at -78 °C, but disproportionate at rt to isolate an iron hydrazine species, (SiP<sub>3</sub>)Fe-NH<sub>2</sub>NH<sub>2</sub><sup>+</sup>, and (SiP<sub>3</sub>)FeN<sub>2</sub>.<sup>75</sup> The iron hydrazine species is able to liberate NH<sub>3</sub>, which when combined with the isolation of the Fe=NNH<sub>2</sub>, gives evidence for a combination pathway consisting of two initial distal additions followed by two proximal additions prior to N-N bond cleavage to form NH<sub>3</sub>.<sup>65,75</sup> A separate study, was able to follow the catalysis using freeze-quench <sup>57</sup>Fe Mössbauer spectroscopy, which identified (TBP)(μ-H)Fe(H)(L) where L = N<sub>2</sub> or H<sub>2</sub> as the catalyst resting state, as opposed to being a catalyst sink that was initially proposed. The (TBP)(μ-H)Fe(H)(L) was also found to be catalytically competent in optimized reaction conditions, demonstrating the importance of not only modifying the catalyst for greater yields, but also that the reaction conditions are critical as well.<sup>72</sup>

**Table 1.5** Summary of N<sub>2</sub> bound Co and Fe complexes evaluated for the conversion of N<sub>2</sub> to NH<sub>3</sub>.

Complex	E (apical ligand)	$\nu_{N-N}$ (cm <sup>-1</sup> )	NH <sub>3</sub> equiv per M	ref
(TPB)]Co(N <sub>2</sub> )	B	2089	0.8	73,76
[(TPB)]Co(N <sub>2</sub> ) <sup>-</sup>	B	1978	2.4	73
(SiP <sub>3</sub> )Co(N <sub>2</sub> )	Si	2063	<0.1	64,73
(CP <sub>3</sub> )Co(N <sub>2</sub> )	C	2057	0.1	73
(TPB)]Fe(N <sub>2</sub> )	B	2011		66
[(TPB)]Fe(N <sub>2</sub> ) <sup>-</sup>	B	1905	64	66,72
[(SiP <sub>3</sub> )Fe(N <sub>2</sub> ) <sup>-</sup>	Si	1920	4.4	65,72
(CP <sub>3</sub> )Fe(N <sub>2</sub> )	C	1992		70
[(CP <sub>3</sub> )Fe(N <sub>2</sub> ) <sup>-</sup>	C	1905	47	70,72

## 1.7 Scope of thesis

The purpose of this thesis is to describe the synthesis and characterization of heterobimetallic complexes using the mixed amide-phosphine binucleating ligand, N(*o*-(NHCH<sub>2</sub>P(<sup>*i*</sup>Pr)<sub>2</sub>)C<sub>6</sub>H<sub>4</sub>)<sub>3</sub>, that feature metal-metal bonds while exploiting the ability to change the supporting metal to tune the catalytic ability of an active Co center in the activation and reduction of dinitrogen. General characterization of heterobimetallic complexes include solid state structure, cyclic voltammetry, electronic ground state determination (EPR spectroscopy or SQUID magnetometry), NMR, Mössbauer, and UV-vis-NIR spectroscopies in combination with multi-configurational CAS calculations in collaboration with the Gagliardi group.

Chapter 2 of this thesis describes the synthesis and characterization of five isostructural heterobimetallics that pair vanadium with Fe, Co and Ni. The vanadium-metal interactions are shown to span a wide range of bonding, from triply bonded Fe-V complexes, that feature a large quadrupole splitting ( $\Delta E_Q > 4 \text{ mm s}^{-1}$ ) in their Mössbauer



spectra, to a single dative interaction between Ni and V. Chapter 3 extends the study of heterobimetallic metal-metal interactions with a series of Ti–M complexes, where M = Fe, Co and Ni. The polarized nature of the Ti–M interaction in addition to a more redox susceptible Ti(III) supporting metal toes the line between covalent and dative interactions between metals. Multiple redox members have been isolated for the three TiM combinations, aiding the identification of oxidation states in a complex Ti–M core.

A new angle is investigated in the fourth chapter, where the top Co metal is held constant, and the variation of the supporting metal is investigated in regards to the activation of dinitrogen with anionic heterobimetallics. Two anionic CoM complexes (M = V, Cr) are found to bind dinitrogen at Co, and can be evaluated along with two previously published complexes, to identify trends in N<sub>2</sub> activation by supporting metal choice. Lastly, in chapter 5, five CoM complexes are used in the catalytic reductive silylation of dinitrogen to tris(trimethylsilyl)amine. Experimental controls and kinetic studies, combined with theory, are used to identify how the supporting metal influences the catalytic ability of an active Co center. The Co–M interaction and hemi-lability of a phosphine ligand are thought to work cooperatively to allow for the turnover and formation of amine, and suggesting the right balance struck between these influences can tune a catalyst to optimal activity.

## Chapter 2

### Heterobimetallic Complexes that Bond Vanadium to Iron, Cobalt and Nickel

Reproduced with permission from: Clouston, L. J.; Bernales, V.; Cammarota, R. C.; Carlson, R. K.; Bill, E.; Gagliardi, L.; Lu, C. C., Heterobimetallic Complexes That Bond Vanadium to Iron, Cobalt, and Nickel. *Inorg. Chem.* **2015**, *54* (24), 11669-11679. Copyright 2015 American Chemical Society.

## 2.1 Overview of M-V Complexes

Zero-valent iron, cobalt, and nickel were installed into the metalloligand  $V[N(o\text{-}(\text{NCH}_2\text{P}(i\text{Pr})_2)\text{C}_6\text{H}_4)_3]$  (**1**, VL), generating the heterobimetallic trio FeVL (**2**), CoVL (**3**), and NiVL (**4**), respectively. In addition, the one-electron-oxidized analogues  $[\text{FeVL}]\text{X}$  ( $[\mathbf{2}^{\text{ox}}]\text{X}$ , where  $\text{X}^- = \text{BPh}_4$  or  $\text{PF}_6$ ) and  $[\text{CoVL}]\text{BPh}_4$  ( $[\mathbf{3}^{\text{ox}}]\text{BPh}_4$ ) were prepared. The complexes were characterized by a host of physical methods, including cyclic voltammetry, X-ray crystallography, magnetic susceptibility, electronic absorption, NMR, electron paramagnetic resonance (EPR), and Mössbauer spectroscopies. The CoV and FeV heterobimetallic compounds have short M–V bond lengths that are consistent with M–M multiple bonding. As revealed by theoretical calculations, the M–V bond is triple in **2**,  $\mathbf{2}^{\text{ox}}$ , and  $\mathbf{3}^{\text{ox}}$ , double in **3**, and dative ( $\text{Ni} \rightarrow \text{V}$ ) in **4**. The  $(d-d)^{10}$  species, **2** and  $\mathbf{3}^{\text{ox}}$ , are diamagnetic and exhibit large diamagnetic anisotropies of  $-4700 \times 10^{-36} \text{ m}^3/\text{molecule}$ . Complexes **2** and  $\mathbf{3}^{\text{ox}}$  are also characterized by intense visible bands at 760 and 610 nm ( $\epsilon > 1000 \text{ M}^{-1}\text{cm}^{-1}$ ), respectively, which correspond to an intermetal ( $\text{M} \rightarrow \text{V}$ ) charge-transfer transition. Magnetic susceptibility measurements and EPR characterization establish  $S = 1/2$  ground states for  $(d-d)^9$   $\mathbf{2}^{\text{ox}}$  and  $(d-d)^{11}$  **3**, while  $(d-d)^{12}$  **4** is  $S = 1$  based on Evans' method.

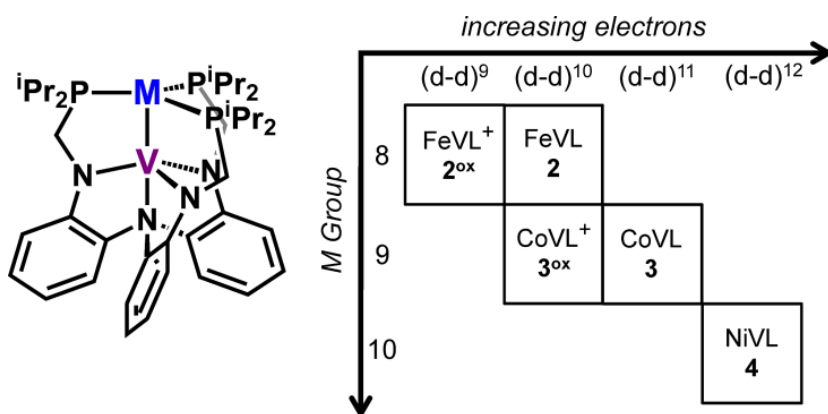


**Figure 2.1** Key of MV complexes organized by group number for M (vertical) and overall d-count (horizontal).

## 2.2 Introduction

Chemical bonding between transition metals continues to fascinate chemists because of the complex interplay of bonding, electronic structure, and reactivity.<sup>22,57,77-79</sup> Homometallic compounds dominate this area, even though the potential number of heterometallic pairings significantly outnumbers the former. A synthetic roadblock to expanding heterometallics is the inherent challenge of selectively assembling different transition-metal atoms.<sup>80</sup>

For the group 5 triad, homobimetallic complexes featuring multiple M–M bonds are known.<sup>81</sup> By contrast, group 5 heterobimetallics with multiply bonded metal atoms are rare,<sup>82</sup> although three heterobinuclear molecules, VNi, VTi, and VZr, have been generated and characterized in the gas phase.<sup>9,83</sup> By moving to trigonal ligand environments, Thomas et al. successfully prepared several FeV complexes from a common V<sup>III</sup> precursor.<sup>11</sup> The (FeV)<sup>3+/4+</sup> complexes have short Fe–V bond distances (2.0–2.1 Å) and were interpreted as triply bonded.

Using the double-decker ligand shown in Figure 2.1, we previously isolated an isostructural MCr series, where M was varied across the period from Mn to Ni.<sup>10,20,28</sup> In this paper, we demonstrate that the same ligand scaffold can stabilize an (FeV)<sup>3+</sup> complex and two other V–late metal bimetallics, (CoV)<sup>3+</sup> and (NiV)<sup>3+</sup>. Two additional redox states, (FeV)<sup>4+</sup> and (CoV)<sup>4+</sup>, were isolated. Collectively, the five-membered MV family (Figure 2.1) allows us to assess potential periodic trends in bonding, properties, and electronic structures, as elucidated by cyclic voltammetry, X-ray crystallography, magnetic susceptibility, various spectroscopies [vis–near-IR (NIR), NMR, electron paramagnetic resonance (EPR), Mössbauer], and theory.

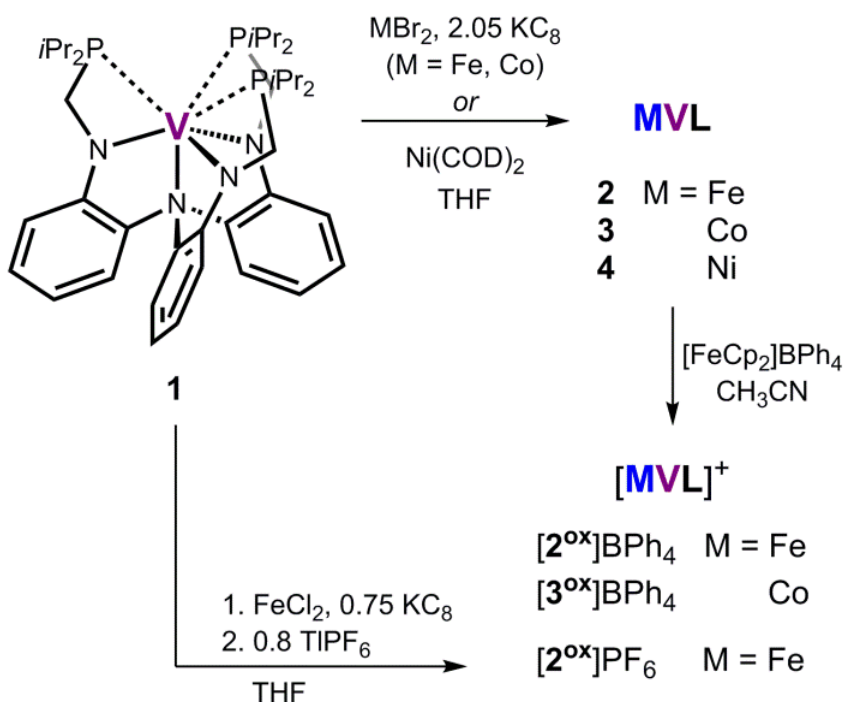
## 2.3 Results and Discussion

### 2.3.1 Synthesis

The monovanadium(III) compound, V(N(*o*-(NCH<sub>2</sub>P<sup>i</sup>Pr<sub>2</sub>)C<sub>6</sub>H<sub>4</sub>)<sub>3</sub>) (**1**, abbreviated as VL), was obtained in good yield from the reaction of VCl<sub>3</sub>(THF)<sub>3</sub> (THF = tetrahydrofuran) and the triply deprotonated ligand [N(*o*-(NCH<sub>2</sub>P<sup>i</sup>Pr<sub>2</sub>)C<sub>6</sub>H<sub>4</sub>)<sub>3</sub>]<sup>3-</sup>. Brown **1** was used as a metalloligand in a subsequent metalation to install zerovalent iron, cobalt, or nickel

(Scheme 2.1). The heterobimetallics FeVL (**2**) and CoVL (**3**) were isolated from the reactions of **1** with the corresponding  $MBr_2$  ( $M = Fe, Co$ ) and 2.05 equiv of  $KC_8$ . Complex NiVL (**4**) was produced from **1** and  $Ni(COD)_2$ , where COD = 1,5-cyclooctadiene.

The cationic counterparts  $[FeVL]BPh_4$  ( $[2^{ox}]BPh_4$ ) and  $[CoVL]BPh_4$  ( $[3^{ox}]BPh_4$ ) were isolated from the reaction of ferrocenium tetraphenylborate with **2** and **3**, respectively. Starting from **1**, an alternative synthesis of  $2^{ox}$  involves the mixing of **1**,  $FeCl_2$ , and 0.75 equiv of  $KC_8$  to generate an  $(FeV)^{4+}$  intermediate, presumably  $(Cl)FeVL$ . Specifically, only 0.75 equiv of  $KC_8$  was used to prevent any undesired overreduction to **2**. Next, chloride abstraction with  $TIPF_6$  provided  $[2^{ox}]PF_6$ . We prefer this alternative route to  $2^{ox}$  because it only involves a single redox change at the Fe center, from  $Fe^{II}$  to  $Fe^I$ . The synthesis of  $2^{ox}$  from **1**, via the intermediacy of **2**, is more complex because it requires two independent redox changes that shuttle electrons in opposite directions, first reducing  $Fe^{II}$  to  $Fe^0$  and then oxidizing  $Fe^0$  to  $Fe^I$ .



**Scheme 2.1** From monovanadium **1**, synthesis of MV complexes **2** – **4**,  $2^{ox}$ , and  $3^{ox}$ .

### 2.3.2 Electrochemical and Electronic Absorption Characterization

The cyclic voltammograms (CVs) of VL (**1**) and the heterobimetallic MV complexes are shown in Figure 2.2, with the corresponding redox potentials listed in Table 2.1. The monovanadium complex contains two quasi-reversible oxidations at  $-0.70$  and  $-0.04$  V (vs  $\text{Fc}^+/\text{Fc}$ ). In sharp contrast, the monochromium analogue showed only irreversible, ill-resolved oxidative processes.<sup>20</sup> A close analogue to **1**,  $\text{V}(\text{iPrNPPH}_2)_3$ ,<sup>11</sup> also has a different electrochemical profile with a single, reversible oxidation at  $-1.13$  V and one quasi-reversible reduction. The possibility of a ligand-based oxidation was scrutinized, but ligand-based oxidations are completely irreversible and significantly more anodic ( $E_{\text{pa}} \sim 0.50$  V). Hence, the two oxidations of **1** are tentatively assigned to the  $\text{V}^{\text{III/IV}}$  and  $\text{V}^{\text{IV/V}}$  redox couples.

The  $(\text{FeV})^{3+}$  complex **2** has three reversible one-electron redox events ( $-0.27$ ,  $-1.12$ , and  $-2.85$  V vs  $\text{Fc}^+/\text{Fc}$ ), akin to the  $(\text{FeCr})^{3+}$  analogue ( $-0.62$ ,  $-1.32$ , and  $-2.33$  V). Between  $\text{FeVL}$  and  $\text{FeCrL}$ , the most similar redox potential is the first oxidation at  $-1.12$  and  $-1.32$  V, respectively. This may suggest an  $\text{Fe}^{0/\text{I}}$  oxidation, which is more anodic for the V ancillary metal than the Cr one. Of note, the related  $\text{Fe}(\text{PMe}_3)(\text{Ph}_2\text{PN}^i\text{Pr})_3\text{V}$  compound showed two reversible oxidations at  $-0.28$  and  $-1.26$  V, which are quite close to those of **2**, where the latter was similarly proposed to be an  $\text{Fe}^{0/\text{I}}$  redox couple.<sup>11</sup> The second oxidation at  $-0.27$  V is likely the  $\text{V}^{\text{III/IV}}$  redox couple, which shifts  $+0.43$  V upon coordination of Fe.

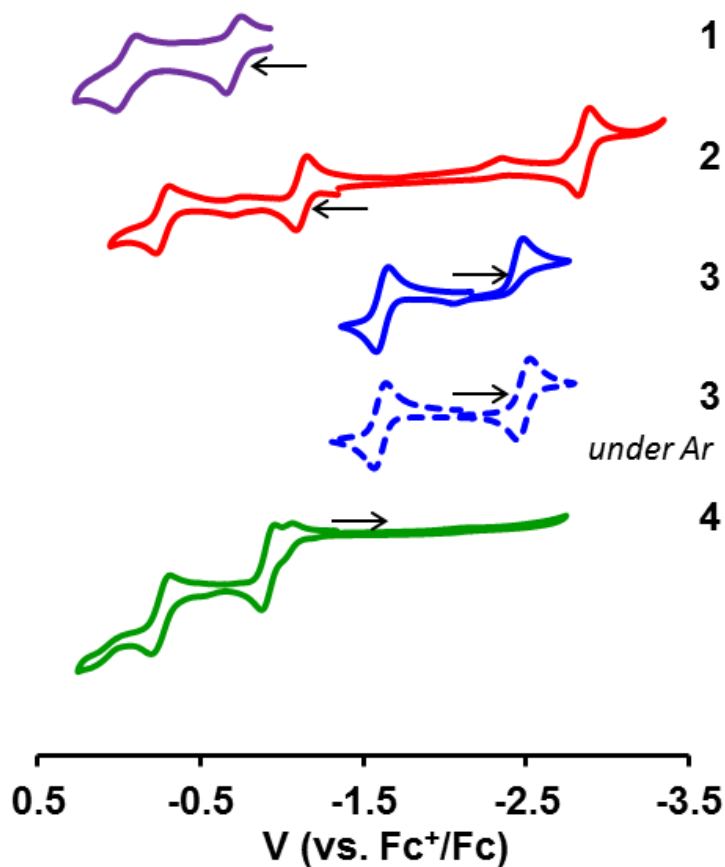


**Figure 2.2** Cyclic voltammograms of **1** – **4** in THF with 0.4 M [nBu<sub>4</sub>N]PF<sub>6</sub> electrolyte starting at zero current (scan rate of 250 mV/s for **1** and 10 mV/s for **2** – **4**; collected under N<sub>2</sub>, unless indicated otherwise). See Figures A1.1 – A1.3 for CVs at different scan rates (Appendix 1).

**Table 2.1** Redox potentials (V) of **2** - **4**.

<sup>a</sup>under argon

complex	2 <sup>nd</sup> oxidation	1 <sup>st</sup> oxidation	1 <sup>st</sup> reduction
<b>1</b>	-0.04	-0.71	n/a
<b>2</b>	-0.27	-1.10	-2.85
<b>3<sup>a</sup></b>	n/a	-1.60	-2.50
<b>4</b>	-0.31	-0.96	n/a

The CoVL complex **3** has an irreversible reduction at  $-2.50$  V under  $N_2$ , which becomes reversible under Ar. The electrochemical behavior is typical of fast binding of  $N_2$  upon reduction, which was also observed for CoCrL.<sup>20</sup> One remarkable difference between CoVL and CoCrL is that the latter shows four reversible one-electron processes under Ar, while the former exhibits only two redox events. Hence, one effect of swapping Cr for V in the CoML systems is to significantly curtail the number of redox processes. The cause of this effect is unclear. Finally, the first oxidation process of NiVL at  $-0.91$  V is typical of a  $Ni^{0/I}$  oxidation because the previously reported mononickel complex  $Ni(LH_3)$  has a comparable  $E^\circ_{1/2}$  of  $-1.02$  V. The  $V^{III/IV}$  redox couple likely accounts for the second oxidation at  $-0.25$  V.

The neutral MVL compounds are dark brown as solids, but as dilute solutions, they show different tints of brown: yellow for **2** ( $M = Fe$ ), red for **3** ( $M = Co$ ), and orange for **4** ( $M = Ni$ ). The cationic species  $[2^{ox}]PF_6$  and  $[3^{ox}]BPh_4$  are maroon ( $\lambda_{max} = 524$  nm;  $\epsilon = 3700$   $M^{-1} cm^{-1}$ ) and green ( $\lambda_{max} = 613$  nm;  $\epsilon = 2900$   $M^{-1} cm^{-1}$ ), respectively. The visible to near-infrared (vis-NIR) spectra for the full series, including VL (**1**), are shown in Figure 2.3 and summarized in Table 2.2. Monovanadium **1** has a broad band centered at 845 nm ( $\epsilon = 300$   $M^{-1} cm^{-1}$ ). A similar band is observed for NiVL (**4**) at 905 nm ( $\epsilon = 500$   $M^{-1} cm^{-1}$ ). These bands likely correspond to a d-d transition at the  $V^{III}$   $d^2$  center, and the molar absorptivities are consistent with parity-allowed d-d transitions in non-centrosymmetric molecules.



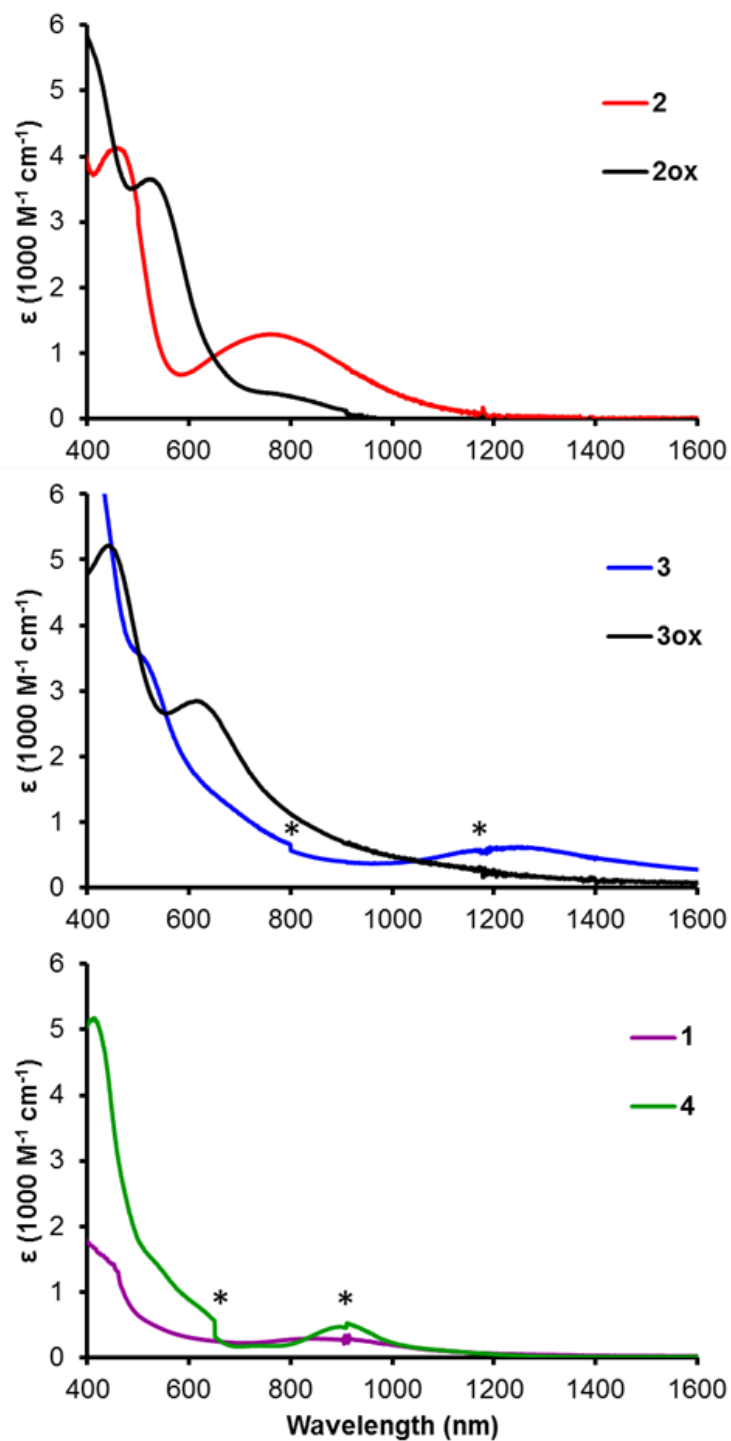


**Figure 2.3** Vis-NIR spectra of complexes **1** – **4**,  $[2^{ox}]PF_6$ , and  $[3^{ox}]BPh_4$  in THF at rt. Spectral discontinuities due to a lamp change are marked with asterisks. For an overlay plot of the full series, see Figure A1.4 (Appendix 1).

**Table 2.2** Vis-NIR data for **1** – **4**, [**2<sup>ox</sup>**]PF<sub>6</sub>, and [**3<sup>ox</sup>**]BPh<sub>4</sub> in THF at rt.

complex	$\lambda_{\text{max}}$ , nm ( $\epsilon$ , M <sup>-1</sup> cm <sup>-1</sup> )
<b>1</b>	845 (300)
<b>2</b>	464 (4100), 762 (1300)
[ <b>2<sup>ox</sup></b> ]PF <sub>6</sub>	524 (3700), 785 sh (400)
<b>3</b>	505 sh (3600), 1254 (600)
[ <b>3<sup>ox</sup></b> ]BPh <sub>4</sub>	441 (5200), 613 (2900)
<b>4</b>	410 (5200), 905 (500)

Bimetallic FeVL (**2**) and [CoVL]BPh<sub>4</sub> (**3<sup>ox</sup>**) are isoelectronic (d–d)<sup>10</sup> species, and both have intense bands ( $\epsilon > 1000 \text{ M}^{-1} \text{ cm}^{-1}$ ) at 762 and 613 nm, respectively. We propose that this electronic transition involves partial charge transfer between the two metals, M → V. In common, the highest occupied molecular orbitals (HOMOs) of these two complexes are doubly occupied  $d_{xy}$  and  $d_{x^2-y^2}$  orbitals, which are degenerate in 3-fold symmetry and are localized at the late metal, Fe, or Co (vide infra). The lowest unoccupied molecular orbital (LUMO) is  $\pi^*$  with respect to M–V bonding and has 50–60% V character. Hence, the electronic transition is proposed to be  $(M d_{xy}, d_{x^2-y^2})^4 \rightarrow (\pi_{M-V}^* d_{xz}, d_{yz})^0$ , where M is Fe or Co. Time-dependent density functional theory (TD-DFT) calculations validate the assignment of these bands as intermetal (M → V) charge transfer (vide infra). The observed blue shift from FeVL to [CoVL]<sup>+</sup> is large at  $\sim 3200 \text{ cm}^{-1}$ . The shift to higher energy may be explained by a larger stabilization of the HOMO in [CoVL]<sup>+</sup>, i.e.,  $(\text{Co } d_{xy}, d_{x^2-y^2})^4$ , relative to that in FeVL by virtue of cobalt's higher formal oxidation state, Co<sup>I</sup>, compared to Fe<sup>0</sup>. The overall cationic charge of **3<sup>ox</sup>** could further stabilize the HOMO.

### 2.3.3 X-ray Crystallography

Single-crystal X-ray diffraction studies were performed on **1–4**, [**2<sup>ox</sup>**]BPh<sub>4</sub>, and [**3<sup>ox</sup>**]BPh<sub>4</sub>. The solid-state structures are shown in Figure 2.4 with average bond distances. Individual bond distances and angles are provided in Table 2.3. Arguably, the V site is invariant throughout the series in that the average V–N<sub>amide</sub> bond lengths do not change:

from 1.95 Å in VL (**1**) to 1.96 Å in all of the neutral MVL complexes (**2–4**) to 1.93 Å in the cationic [MVL]<sup>+</sup> complexes, which is a small contraction considering the change in the charge. The constant V–N<sub>amide</sub> bond lengths suggest that the V<sup>III</sup> oxidation state is maintained throughout the series. On the other hand, the apical V–N<sub>amine</sub> bond does vary from 2.15 to 2.31 Å. The V–N<sub>amine</sub> bond length is relatively short in monovanadium **1** and NiVL, intermediate in CoVL (**3**), and long in **2**, **2**<sup>ox</sup>, and **3**<sup>ox</sup>. Of note, the V–N<sub>amine</sub> and M–V bond lengths are inversely related in that the former contracts when M–V interactions are absent or weak, and it elongates with increasing M–V multiple bonding (vide infra). A similar trend had been observed in the MCr family.<sup>20</sup>

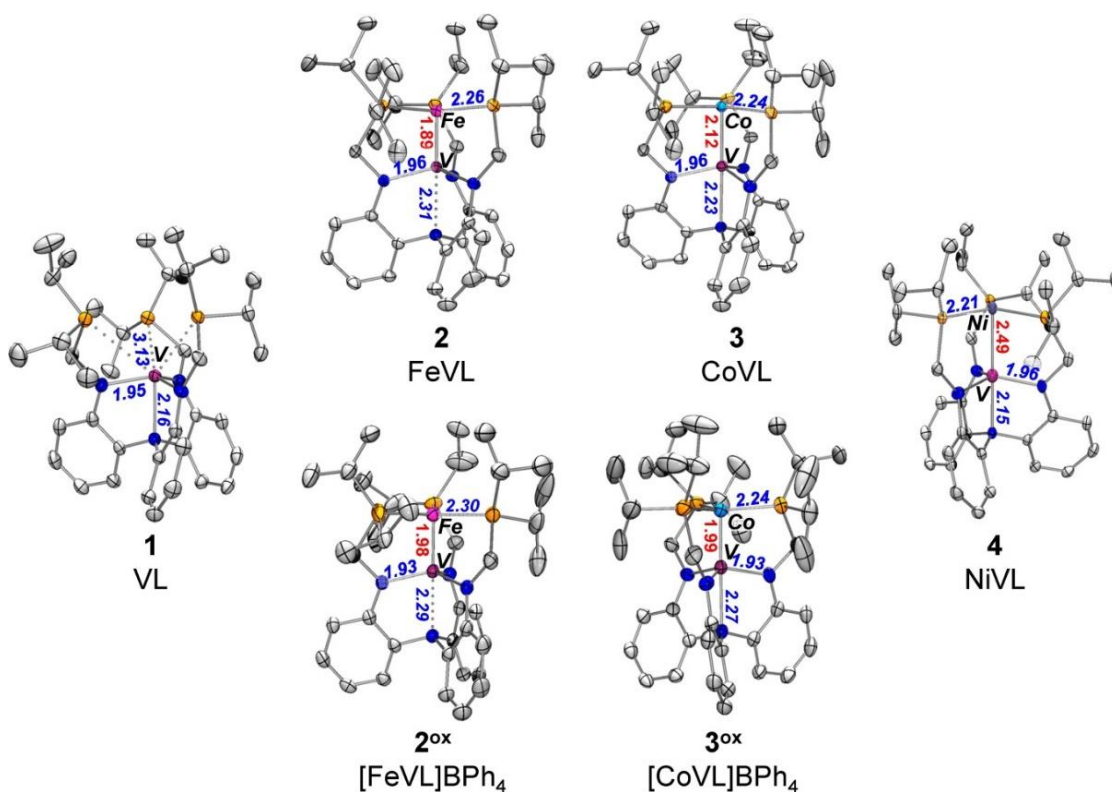


**Figure 2.4** Solid-state structures of **1** – **4** shown at 50% thermal ellipsoid probability. Hydrogen atoms, counterions and non-coordinating solvent molecules have been omitted for clarity. Average bond lengths (Å) are shown.

**Table 2.3** Geometrical parameters, including bond lengths (Å), formal shortness ratio (FSR), and angles (°), for **1** – **4**.

	<b>1</b> VL	<b>2</b> FeVL	<b>3</b> CoVL	<b>4</b> NiVL	[2 <sup>ox</sup> ]BPh <sub>4</sub> [FeVL]BPh <sub>4</sub>	[3 <sup>ox</sup> ]BPh <sub>4</sub> [CoVL]BPh <sub>4</sub>
M–V		1.8940(4)	2.1234(4)	2.4873(14)	1.9791(6)	1.9930(11)
FSR		<i>0.79</i>	<i>0.89</i>	<i>1.05</i>	<i>0.83</i>	<i>0.84</i>
		2.2585(6)	2.2315(7)	2.2051(11)	2.2829(8)	2.2356(16)
M–P		2.2599(6)	2.2317(6)	2.2051(11)	2.2992(9)	2.2448(15)
		2.2705(6)	2.2434(6)	2.2051(11)	2.3042(9)	2.2470(16)
	1.9308(13)	1.9584(17)	1.9442(18)	1.957(3)	1.933(2)	1.925(4)
V–N <sub>amide</sub>	1.9477(13)	1.9645(17)	1.9543(18)	1.957(3)	1.933(2)	1.926(4)
	1.9629(13)	1.9682(17)	1.9694(17)	1.957(3)	1.937(2)	1.926(4)
V–N <sub>amine</sub>	2.1591(12)	2.3082(16)	2.2266(17)	2.149(5)	2.293(2)	2.272(4)
M to P <sub>3</sub> -plane		–0.191	–0.032	0.130	–0.161	–0.165
V to N <sub>3</sub> -plane	0.328	0.444	0.395	0.279	0.358	0.365
		119.53(2)	120.61(3)	119.658(6)	120.46(4)	118.20(6)
P–M–P		119.54(2)	120.01(2)	119.657(6)	112.79(3)	119.92(7)
		118.80(2)	119.33(3)	119.656(6)	125.66(4)	120.29(6)
	119.83(5)	113.70(7)	114.20(8)	118.00(4)	117.22(9)	117.92(17)
N <sub>amide</sub> –V–N <sub>amide</sub>	116.25(5)	116.33(7)	117.03(8)	118.00(4)	115.39(9)	114.69(18)
	115.69(5)	115.09(7)	116.84(8)	118.00(4)	117.34(9)	116.90(17)
M–V–N <sub>amine</sub>		179.29(5)	177.67(5)	180	177.90(6)	179.60(11)

Importantly, the M–V bond distances in the bimetallic complexes can provide insight into the changing nature of the M–M bonding. The M–V bond distances are compared to other literature compounds in Table 2.4, which includes the related tri(phosphinoamide) FeV complexes reported by Thomas et al.<sup>11</sup> The formal shortness ratio (FSR) is the ratio of the observed M–V bond length to the expected M–V single bond length, which is determined by summing the two metals’ single bond radii.<sup>27</sup> Typically, a FSR value significantly lower than unity is interpreted as an indicator of multiple M–M bonding. With the exception of NiVL, all of the bimetallics in this series have FSR  $\ll$  1.

The Fe–V bond length of 1.8940(4) Å in **2** is shorter than that in [2<sup>ox</sup>]BPh<sub>4</sub> [1.9791(6) Å] and those in Thomas' Fe(PMe<sub>3</sub>)(Ph<sub>2</sub>PN<sup>i</sup>Pr)<sub>3</sub>V and FeI(Ph<sub>2</sub>PN<sup>i</sup>Pr)<sub>3</sub>V compounds (2.05 and 2.06 Å). The latter complexes, which have FSR = 0.86, were interpreted as triply bonded. The FSR value for [2<sup>ox</sup>]BPh<sub>4</sub> is slightly smaller at 0.83, and by analogy, **2**<sup>ox</sup> is interpreted as possessing an Fe–V triple bond. Curiously, the FSR value for FeVL (**2**) is 0.79, which is significantly smaller. In terms of FSR, **2** is closer to the isostructural MnCrL complex, which formally has a quintuple M–M bond (FSR = 0.78). Because only three bonding molecular orbitals (MOs),  $\sigma + 2\pi$ , were calculated for **2** (vide infra), one possible explanation is that an additional  $\delta$ -dative interaction (Fe  $\rightarrow$  V) is present to increase bonding and decrease the FSR. The Fe–V bond does expand by 0.09 Å upon oxidation of **2** to [2<sup>ox</sup>]BPh<sub>4</sub>, suggesting the loss of an electron involved in Fe–V bonding.

It is interesting to speculate why the Fe–V interactions are shorter in the present system compared to Thomas' FeV phosphinoamide complexes. One primary difference is the lack of an exogenous axial donor in **2** and [2<sup>ox</sup>]BPh<sub>4</sub>, since axial donors are well-known to elongate M–M bonds.<sup>84</sup> A more fundamental question is why does the present system enable bimetallic cores to be isolated without additional donors? Krogman and Thomas have proposed that the two-atom bridging phosphinoamide ligands enforce a relatively large M–P–N bond angle of  $\sim 109.5^\circ$  in their system (compared to  $76^\circ$  in **2**), which may promote tetrahedral coordination geometry at M, where the fourth ligand is an exogenous donor.<sup>79</sup> By contrast, the three-atom buttress of L positions the phosphine donors so that they are coplanar with M, thereby possibly discouraging the binding of an additional donor while encouraging shorter M–M interactions. Another way to view the differences between the two ligand systems is that the amide and phosphine lone pairs are more divergent in the phosphinoamide case.

**Table 2.4** Comparing relevant literature compounds with short metal-metal bond lengths.

complex	M–M bond (Å)	FSR	ref.
FeVL, <b>2</b>	1.89	0.79	this
[FeVL]BPh <sub>4</sub> , <b>2<sup>ox</sup></b>	1.98	0.83	this
FeI(Ph <sub>2</sub> PN <sup><i>i</i></sup> Pr) <sub>3</sub> V	2.06	0.86	11
Fe(PMe <sub>3</sub> )(Ph <sub>2</sub> PN <sup><i>i</i></sup> Pr) <sub>3</sub> V	2.05	0.86	11
FeCrL	1.94	0.83	10
[FeCrL] <sup>+</sup>	1.96	0.84	10,28
[FeCrL] <sup>-</sup>	1.97	0.84	10
CoVL, <b>3</b>	2.12	0.89	this
[CoVL]BPh <sub>4</sub> , <b>3<sup>ox</sup></b>	1.99	0.84	this
Co( <sup><i>i</i></sup> Pr <sub>2</sub> PNMe <sub>s</sub> ) <sub>3</sub> Zr(THF)	2.14	0.82	85
Co(PMe <sub>3</sub> )( <sup><i>i</i></sup> Pr <sub>2</sub> PNXyl) <sub>2</sub> TiCl	2.02	0.81	86
{CoI( <sup><i>i</i></sup> Pr <sub>2</sub> PNXyl) <sub>2</sub> Ti(μ-Cl) <sub>2</sub> }	2.21	0.89	86
CoTiL	2.20	0.89	87
CoCrL	2.14	0.92	20
NiVL, <b>4</b>	2.49	1.05	this
NiCrL	2.41	1.04	20

Although several CoM bimetallic complexes are known (Table 2.4), **3** and [**3<sup>ox</sup>**]BPh<sub>4</sub> are, to our knowledge, the first coordination complexes to pair V with Co. Between the Co–V pair, **3** and [**3<sup>ox</sup>**]BPh<sub>4</sub>, the Co–V bond length contracts significantly [from 2.1234(4) to 1.9930(11) Å] upon oxidation by one electron. Among CoM bimetallics, (PMe<sub>3</sub>)Co(<sup>*i*</sup>Pr<sub>2</sub>PNXyl)<sub>2</sub>TiCl has the smallest formal shortness ratio of 0.81 and was interpreted as containing a Ti–Co triple bond.<sup>86</sup> By analogy to other CoM bimetallics, the formal shortness ratios are most consistent with a double Co–V bond in **3** (FSR = 0.89) and a triple Co–V bond in [**3<sup>ox</sup>**]BPh<sub>4</sub> (FSR = 0.84).

Pyykkö and co-workers have tabulated triple- and double-bond covalent radii for many elements, including transition metals.<sup>88,89</sup> The multiple bond radii could prove useful for guiding bonding interpretations, but their utility in M–M multiple bonding has not been demonstrated. Comparing the experimental Co–V distances to the sum of the multiple-bond covalent radii, the Co–V distances of 2.12 and 1.99 Å in **3** and [**3<sup>ox</sup>**]BPh<sub>4</sub>, respectively, agree well with the calculated Co–V double- and triple-bond lengths of 2.15 and 2.02 Å, respectively. The close agreement may support our bonding interpretations in

these bimetallics. On the other hand, the Fe–V bond distances of 1.89 and 1.98 Å in **2** and [2<sup>ox</sup>]BPh<sub>4</sub>, respectively, are significantly shorter than the Fe–V triple-bond length of 2.08 Å (by 0.19 and 0.10 Å, respectively).

For each redox pair, the M–P bond lengths can be directly compared. In mononuclear coordination complexes, oxidations at the metal can be accompanied by contraction of the M–ligand bonds. However, this is not the case for either redox pair. In **3** and [3<sup>ox</sup>]BPh<sub>4</sub>, the Co–P bond distances are essentially unchanged at 2.24 Å, although the Co–V bond does significantly contract between **3** and [3<sup>ox</sup>]BPh<sub>4</sub>. Oddly, the Fe–V pair shows a small increase in the Fe–P bond lengths upon oxidation, from 2.26 Å in **2** to 2.30 Å in [2<sup>ox</sup>]BPh<sub>4</sub>. One plausible explanation is that the more electron-rich Fe center in **2** has more  $\pi$ -back-bonding donation to the phosphines than [2<sup>ox</sup>]BPh<sub>4</sub> and thereby has shorter Fe–P bonds.

#### 2.3.4 NMR Spectroscopy

The <sup>1</sup>H NMR spectra of the bimetallic complexes **2<sup>ox</sup>**, **3**, and **4** contain paramagnetically shifted resonances (Figures A1.7–A1.9 and A1.11). Complex **3** exhibited 12 proton peaks, which is consistent with a locked 3-fold symmetry, where four aryl protons, two diastereotopic methylenes, two methines, and four methyl groups are all chemically unique (Figure A1.9). Both [2<sup>ox</sup>]BPh<sub>4</sub> and [2<sup>ox</sup>]PF<sub>6</sub> show only nine proton resonances for the ligand, and the slight decrease in the number of peaks may be caused by the paramagnetic broadening of some peaks. In contrast to **3** and **2<sup>ox</sup>**, paramagnetic **1** and **4** show even fewer (six total) proton resonances that are significantly broadened (Figures A1.5 and A1.11). Because **1** and **4** both owe their paramagnetism to an  $S = 1$  V<sup>III</sup> center, it is not so surprising that their NMR spectra are qualitatively similar. The origin of the peak broadening is not clear because doubly degenerate V<sup>III</sup> spins have short electronic relaxation times.<sup>90</sup>

The (d–d)<sup>10</sup> complexes **2** and [3<sup>ox</sup>]BPh<sub>4</sub>, by virtue of their diamagnetism, yield more informative <sup>1</sup>H NMR spectra (Figure 2.5). In the spectra of **2** and **3<sup>ox</sup>**, the methylene protons are diastereotopic and are shifted downfield by 2–3 ppm compared to the free ligand. These protons are deshielded by a highly anisotropic, local magnetic field, which is induced by the circulating electrons of the M–M multiple bond. The diamagnetic

anisotropy ( $\chi_{\parallel} - \chi_{\perp}$ , or  $\Delta\chi$ ) can be calculated using the equation  $\Delta\delta = (1/3r^3)^{80}/4\pi$ ,<sup>91</sup> where  $\Delta\delta$  is the difference in the  $^1\text{H}$  NMR chemical shifts of the methylene protons in the multiply bonded bimetallic versus that of an isostructural reference complex,  $\text{NiAlL}$ , which contains a  $\text{Ni} \rightarrow \text{Al}$  dative interaction (Tables A1.1–A1.3). The remaining variables were extracted from the corresponding solid-state structures:  $r$  is the distance and  $\theta$  is the acute angle of the methylene protons relative to the center and axis of the  $\text{M}-\text{M}$  bond. The diamagnetic anisotropies of **2** and **3<sup>ox</sup>** are essentially identical at  $-4700 \times 10^{-36} \text{ m}^3/\text{molecule}$ , which are greater than that measured for  $\text{MnCrL}$  ( $-3900 \times 10^{-36} \text{ m}^3/\text{molecule}$ ).<sup>28</sup> Because the  $\text{MnCrL}$  species has the highest formal bond order, the magnitude of the diamagnetic anisotropies is not as much a consequence of bond order but of bond polarity, a phenomenon that has been observed for unsaturated organic molecules.<sup>92</sup>

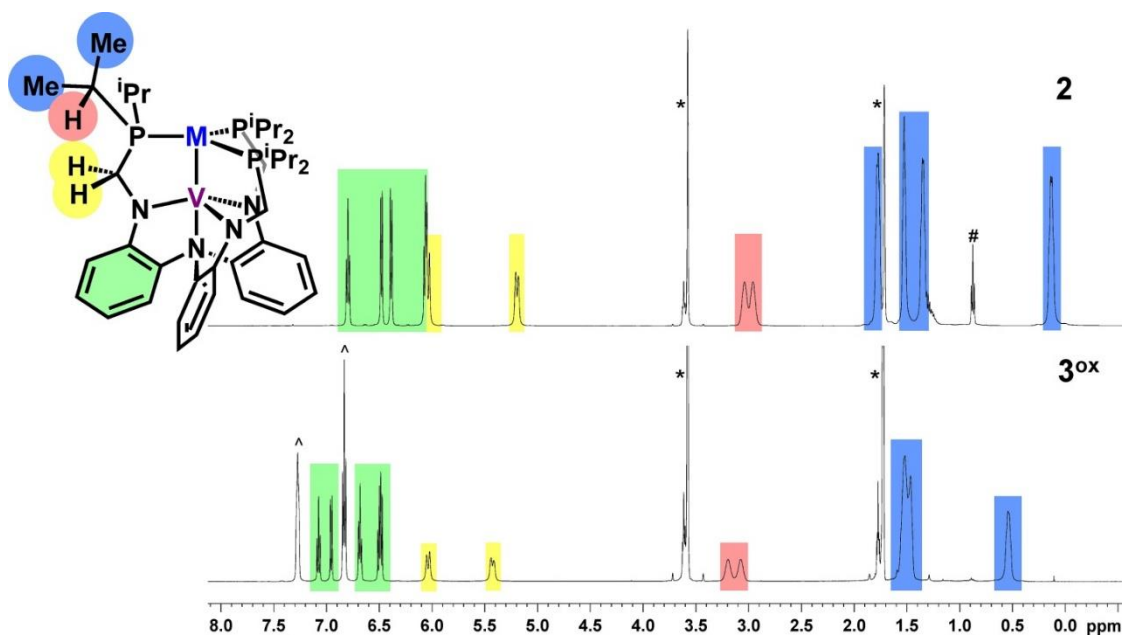


**Figure 2.5** Overlay of  $^1\text{H}$  NMR spectra of the  $(\text{d-d})^{10}$  complexes, **2** and **[3<sup>ox</sup>]BPh<sub>4</sub>**, in  $\text{THF-d}_8$  at rt. Marked peaks correspond to THF (\*), hexane (#), or  $[\text{BPh}_4]^-$  (^).

The  $^1\text{H}$  NMR spectra of **2** and **[3<sup>ox</sup>]BPh<sub>4</sub>** also display fluxional behavior at higher temperatures. The methylene protons of **2** and **3<sup>ox</sup>** coalesce at 88 and 68 °C, respectively (Figures A1.12–A1.15). The activation barriers ( $\Delta G^\ddagger$ ) for the fluxional process are 16.3 and 15.7 kcal/mol for **2** and **3<sup>ox</sup>**, respectively (Table A1.4). While the exact nature of the



fluxional process is not known, the two most likely possibilities are phosphine lability<sup>93</sup> and the twisting of the ligand arms without phosphine decoordination. The twisting mechanism may be more reasonable because the <sup>31</sup>P NMR resonance for **2** shifts by less than 0.5 ppm from 27 to 100 °C. The <sup>31</sup>P NMR signal for **3<sup>ox</sup>** shifts by 1.5 ppm over a similarly large temperature range, and although greater, the shift is sufficiently small to discount the phosphine lability. For both **2** and **3<sup>ox</sup>**, the aryl protons in the ligand backbone remain sharp, coupled, and unshifted over the wide range of temperatures examined. This is notable because it means that the *S* = 0 ground states of **2** and **3<sup>ox</sup>** are energetically well isolated and that an excited triplet state is not thermally accessible.

### 2.3.5 Magnetic Susceptibility and EPR Spectroscopy

The paramagnetic bimetallic complexes were further characterized by magnetic susceptibility measurements. The effective magnetic moment of NiVL (**4**) was determined by Evan's NMR solution method<sup>94</sup> at room temperature (rt) to be 2.39 μ<sub>B</sub>, which is significantly below the spin-only moment for *S* = 1 (2.83 μ<sub>B</sub>). A low Evan's magnetic moment of 2.41 μ<sub>B</sub> was also measured for monovanadium **1**, suggesting that the *g* value associated with the V<sup>III</sup> d<sup>2</sup> spin is significantly less than 2. Indeed, a low moment (2.23 μ<sub>B</sub>) was reported for a similar V<sup>III</sup> species, [HIPTN<sub>3</sub>N]V(NH<sub>3</sub>), where HIPTN<sub>3</sub>N is a bulky triamidoamine ligand.<sup>95</sup> Specifically, the susceptibilities of both **1** and **4** would be consistent with a low *g* value of 1.7. Of relevance, low *g* values of 1.7 have been corroborated by high-field EPR and/or variable-temperature magnetic susceptibility measurements for octahedral V<sup>III</sup> species, such as VBr<sub>3</sub>(THF)<sub>3</sub> and V(acac)<sub>3</sub>.<sup>96</sup>

Variable-temperature magnetic susceptibilities of [**2<sup>ox</sup>**]PF<sub>6</sub> and **3** were measured on powder samples from 4 to 290 K with an applied field of 1.0 T using a SQUID magnetometer. The (d-d)<sup>9</sup>**2<sup>ox</sup>** and (d-d)<sup>11</sup>**3** are anticipated to have *S* = 1/2 ground states. The effective magnetic moments of [**2<sup>ox</sup>**]PF<sub>6</sub> and **3** of 1.82 and 1.61 μ<sub>B</sub>, respectively, are both close to the spin-only value of 1.73 μ<sub>B</sub> for *S* = 1/2 (Figure 2.6). Of note, the solution magnetic moment of **3** is 1.80 μ<sub>B</sub>, which is slightly closer to the spin-only value. To fit the magnetic data for [**2<sup>ox</sup>**]PF<sub>6</sub>, a *g* value of 2.1 was used, which was determined from the EPR data (vide infra). For **3**, a *g* value of 1.9 was used to match the EPR data (vide infra), but a 5% diamagnetic impurity was also needed to fit the data. Finally, because the magnetic

moments of  $[2^{ox}]PF_6$  and **3** are essentially invariant from 15 to 290 K, their  $S = 1/2$  ground states are energetically well isolated.

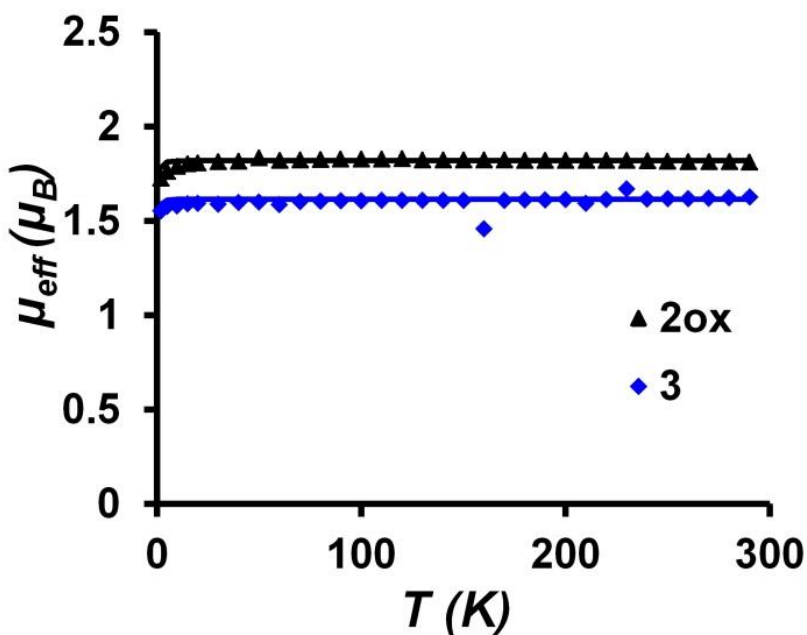


**Figure 2.6** Temperature dependence of the effective magnetic moment,  $\mu_{eff}$ , of  $[2^{ox}]PF_6$  ( $\blacktriangle$ ) and **3** ( $\blacklozenge$ ). The solid lines represent the spin-Hamiltonian simulations. See text and experimental section for fitting parameters.

The species  $[FeVL]^+$ ,  $[2^{ox}]PF_6$ , and  $CoVL$ , **3**, were further examined by X-band EPR spectroscopy to determine the metal site(s) of the unpaired spin. The EPR spectrum of  $[2^{ox}]PF_6$  in frozen THF at 20.0 K shows an almost axial signal (Figure 2.7). The fitted anisotropic  $g$  values,  $g_{\parallel} = 2.23$  and  $g_{\perp} = (2.08, 2.04)$ , give a  $g_{ave}$  of 2.12. The lack of a large hyperfine splitting and a  $g$  value greater than 2 are both strong indicators of an Fe-based spin rather than V.

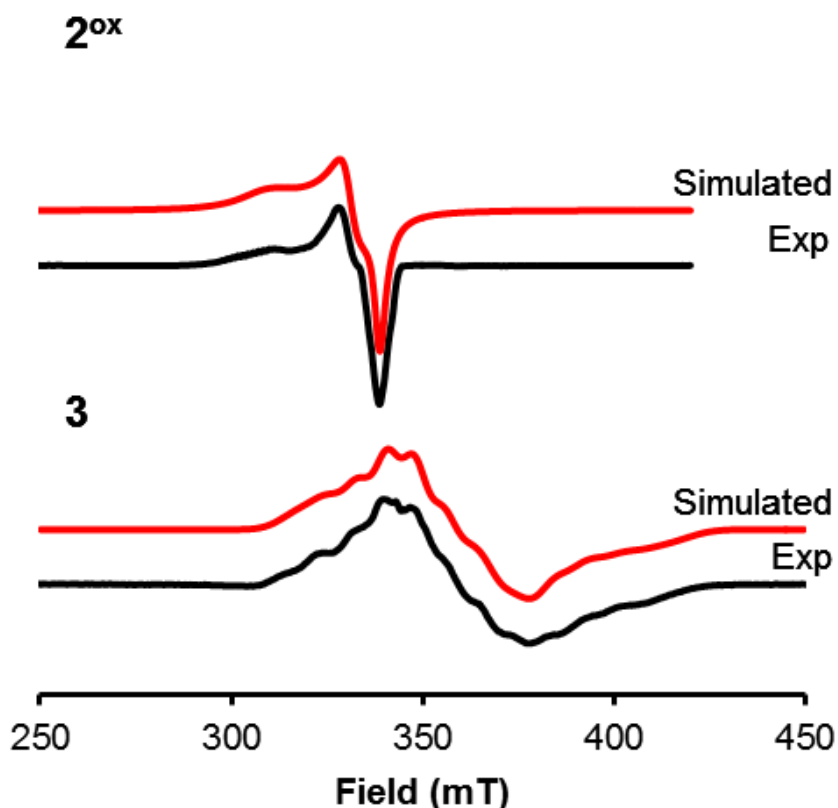


**Figure 2.7** X-band EPR spectra ( $dX''/dB$ ) of  $[2^{ox}]PF_6$  in frozen THF (20.0 K, frequency = 9.64 GHz, modulation to 10 G, power = 200  $\mu$ W) and **3** in frozen toluene (13.0 K). The simulation is shown in red above the experimental spectrum in black. Simulation parameters for  $2^{ox}$ ,  $g_{ave} = 2.12$ ,  $g = (2.04, 2.08, 2.23)$ ,  $W = (40, 75, 218)$  G; and for **3**,  $g_{ave} = 1.91$ ,  $g = (2.00, 1.92, 1.80)$ ,  $W = (0, 85, 50)$  G,  $A(I = 7/2) = (70.4, 22.8, 74.7) \times 10^{-4} \text{ cm}^{-1}$ .

The EPR spectrum of the CoVL complex **3** is rhombic with  $g = (2.00, 1.92, 1.80)$  and  $g_{ave}$  of 1.91. The EPR simulation of **3** indicates that the spin is essentially localized on one metal, either V or Co, because the powder distribution of hyperfine lines can be reproduced with a single nuclear spin  $I = 7/2$  with hyperfine coupling ( $A$ ) of  $(70.4, 22.8, 74.7) \times 10^{-4} \text{ cm}^{-1}$ . The corresponding coupling can be with either  $^{59}\text{Co}$  nuclei ( $I = 7/2$ ) or  $^{51}\text{V}$  ( $I = 7/2$ ), but a  $g$  value of less than 2 is distinctive for a V-based spin because of its less than half-filled d shell. A V-based spin is also corroborated by theory (vide infra).

### 2.3.6 Mössbauer Spectroscopy

To elucidate the Fe oxidation state in the FeV complexes, zero-field Mössbauer data were collected on powder samples of **2** and  $[2^{ox}]PF_6$  at 80 K, as shown in Figure 2.8. The isomer shifts ( $\delta$ ) for **2** and  $[2^{ox}]PF_6$  are identical at 0.25 mm/s, and their quadrupole splittings ( $\Delta E_Q$ ) are 5.97 and 4.04 mm/s, respectively. Large quadrupole splittings (from 5 to 6 mm/s) had been observed for the isostructural FeCr species, FeCrL and  $[FeCrL]^-$ , and were attributed to the presence of a strong axial electric field gradient that arises from the strongly covalent  $[FeCr]^{3+}$  core.<sup>10,28</sup> Hence, we propose that the same effect occurs in **2**. Consistent with this proposal,  $[2^{ox}]PF_6$ , which has a smaller quadrupole splitting of 4.04 mm/s, shows a substantial lengthening of the Fe–V bond by 0.1 Å in  $[2^{ox}]BPh_4$  relative to **2**.

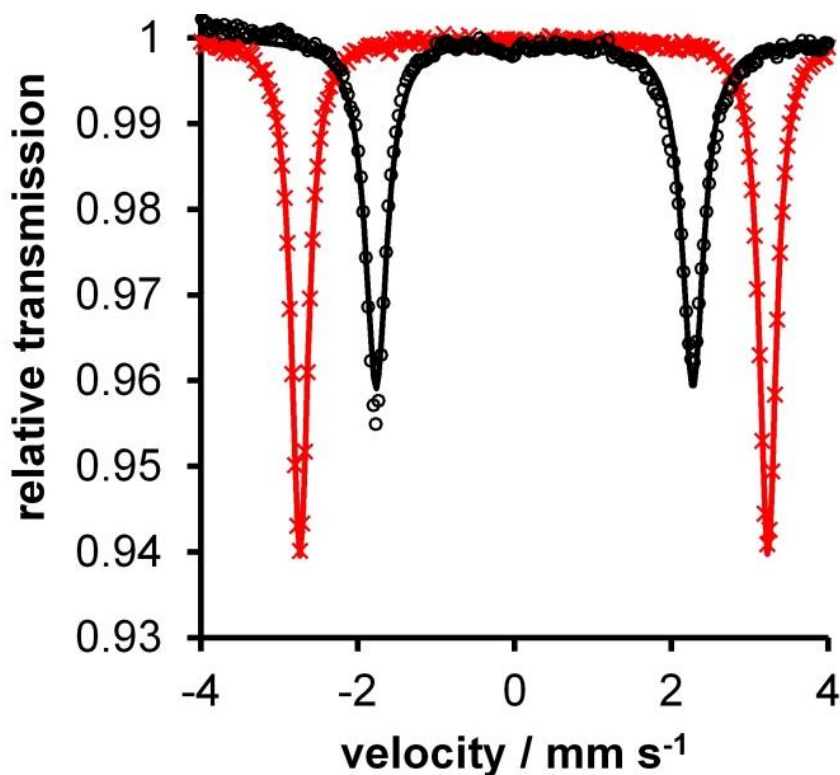


**Figure 2.8** Zero-field Mössbauer spectra overlay of **2** (red, ×) and  $[2^{ox}]PF_6$  (black, ○) at 80 K. The spectra were fitted with the following parameters (shown as solid lines): for **2**,  $\delta = 0.25$  and  $\Delta E_Q = 5.97$  mm s<sup>-1</sup>; and for  $[2^{ox}]PF_6$ ,  $\delta = 0.25$  and  $\Delta E_Q = 4.04$  mm s<sup>-1</sup>.

The isomer shifts of 0.25 mm/s for the FeV redox pair are between the shifts reported for the  $\text{Fe}^0\text{V}^{\text{III}}$  and  $\text{Fe}^{\text{I}}\text{V}^{\text{III}}$  complexes  $\text{Fe}(\text{PMe}_3)(\text{Ph}_2\text{PN}^i\text{Pr})_3\text{V}$  ( $\delta = 0.19$  mm/s) and  $\text{FeBr}(\text{Ph}_2\text{PN}^i\text{Pr})_3\text{V}$  ( $\delta = 0.33$  mm/s), respectively. The isomer shift value is identical with that reported for the isostructural  $\text{Fe}^0\text{Cr}^{\text{III}}$  complex  $\text{FeCrL}$ . One perplexing finding is that the isomer shift value is the same for **2** and  $[\mathbf{2}^{\text{ox}}]\text{PF}_6$  because it implies that the Fe oxidation states are the same, namely,  $\text{Fe}^0$ . We would interpret **2** as formally  $\text{Fe}^0\text{V}^{\text{III}}$ , but the EPR data and theoretical calculations of  $\mathbf{2}^{\text{ox}}$  (*vide infra*) strongly favor  $\text{Fe}^{\text{I}}\text{V}^{\text{III}}$  rather than  $\text{Fe}^0\text{V}^{\text{IV}}$ .

The linear relationship between the isomer shifts and oxidation states are known to deteriorate in low-valent Fe complexes because of M–ligand back-bonding. Shorter M–ligand bonds tend to lower isomer shifts (by increasing the 4s electron population), while higher Fe d counts typically raise isomer shifts (by shielding s electrons). Of note, the M–ligand bond distances around the Fe center (Fe–V and Fe–P) are shorter in **2** than in  $[\mathbf{2}^{\text{ox}}]\text{PF}_6$ . We speculate that the isomer shifts are coincidental for **2** and  $[\mathbf{2}^{\text{ox}}]\text{PF}_6$  because the M–ligand back-bonding in **2** is offset by its higher Fe d count.

### 2.3.7 Electronic Structure Calculations

Quantum chemical calculations were performed on the model complexes **2'**,  $\mathbf{2}^{\text{ox}'}$ , **3'**,  $\mathbf{3}^{\text{ox}'}$ , and **4'**, where the isopropyl groups were truncated to methyl groups ( $\text{L}^{\text{Me}}$ ). Geometry optimizations were conducted for several possible spin states using DFT (PBE<sup>97</sup>, Tables A1.6 and A1.7). Each ground-state structure was further investigated with complete active-space self-consistent field (CASSCF) calculations, followed by second-order perturbation theory (CASPT2). The model complexes each have a single, dominant electronic configuration, which accounts for 71–88% of the total ground-state wave function (Table 2.5). Hence, the ground states of **2'**,  $\mathbf{2}^{\text{ox}'}$ , **3'**,  $\mathbf{3}^{\text{ox}'}$ , and **4'** are reasonably close to being singly configurational.

**Table 2.5** Main electronic configuration of metal-vanadium complexes with formal and effective bond orders (FBO and EBO, respectively).<sup>a</sup>

[MVL <sup>Me</sup> ] <sup>0/+</sup>	d-count	main electronic configuration	% <sup>b</sup>	FSR <sub>c</sub>	FBO	EBO	Mayer BO
[FeVL <sup>Me</sup> ] <sup>+</sup> ( <b>2<sup>ox'</sup></b> )	9	$\pi^4\sigma^2(\text{Fe } d_{xy}, d_{x^2-y^2})^3$	71	0.83	3	2.42	1.99
FeVL <sup>Me</sup> ( <b>2'</b> )	10	$\pi^4\sigma^2(\text{Fe } d_{xy}, d_{x^2-y^2})^4$	75	0.79	3	2.51	2.26
[CoVL <sup>Me</sup> ] <sup>+</sup> ( <b>3<sup>ox'</sup></b> )	10	$\pi^4\sigma^2(\text{Co } d_{xy}, d_{x^2-y^2})^4$	75	0.84	3	2.49	1.73
CoVL <sup>Me</sup> ( <b>3'</b> )	11	$\pi^2(\text{Co } d_{xz})^2\sigma^2(\text{Co } d_{xy}, d_{x^2-y^2})^4(\text{V } d_{xz})^1$	72	0.89	2	1.55	1.36
NiVL <sup>Me</sup> ( <b>4'</b> )	12	$(\text{Ni } d_{xz}, d_{yz})^4(\text{Ni } d_z)^2(\text{Ni } d_{xy}, d_{x^2-y^2})^4(\text{V } d_{xz}, d_{yz})^2$	88	1.05	0	0	0.43

<sup>a</sup> For details, see Appendix 1 (Tables A1.10–A1.14 and Figures A1.18–A1.22).

<sup>b</sup> Percentage of the main electronic configuration in the total ground-state wavefunction.

<sup>c</sup> formal shortness ratio (experimentally determined from X-ray structures, see text for details).

The MO splitting across the series is shown in Figure 2.9, and the percent contributions of each M center to M–M bonding MOs are displayed in Table 2.6. For the systems where the d-electron count is 10 or fewer, as is the case for **2'**, **2<sup>ox'</sup>**, and **3<sup>ox'</sup>**, the MO diagrams predict a formal M–V triple bond ( $\sigma + 2 \pi$ ). The oxidation of **2'**{Fe–V}<sup>10</sup> to **2<sup>ox'</sup>**{Fe–V}<sup>9</sup> is predicted to occur primarily at Fe (Table A1.9). Moreover, the unpaired spin resides at the Fe center in **2<sup>ox'</sup>** (Figure A1.17), which is consistent with the EPR signal of **2**. Finally, the effective bond orders (EBOs) predicted for **2'**, **2<sup>ox'</sup>**, and **3<sup>ox'</sup>** are similar at  $\sim 2.5$ , which is lower than the formal bond order (FBO) of 3. This is characteristic of multiconfigurational wave functions because the partial occupation of high-lying, antibonding MOs will naturally result in lower bond orders. Overall, there is a good correlation between  $r$  and EBO ( $R^2 = 0.97$ ) but not with FBO ( $R^2 = 0.79$ ) (Figure A1.23).<sup>30</sup>

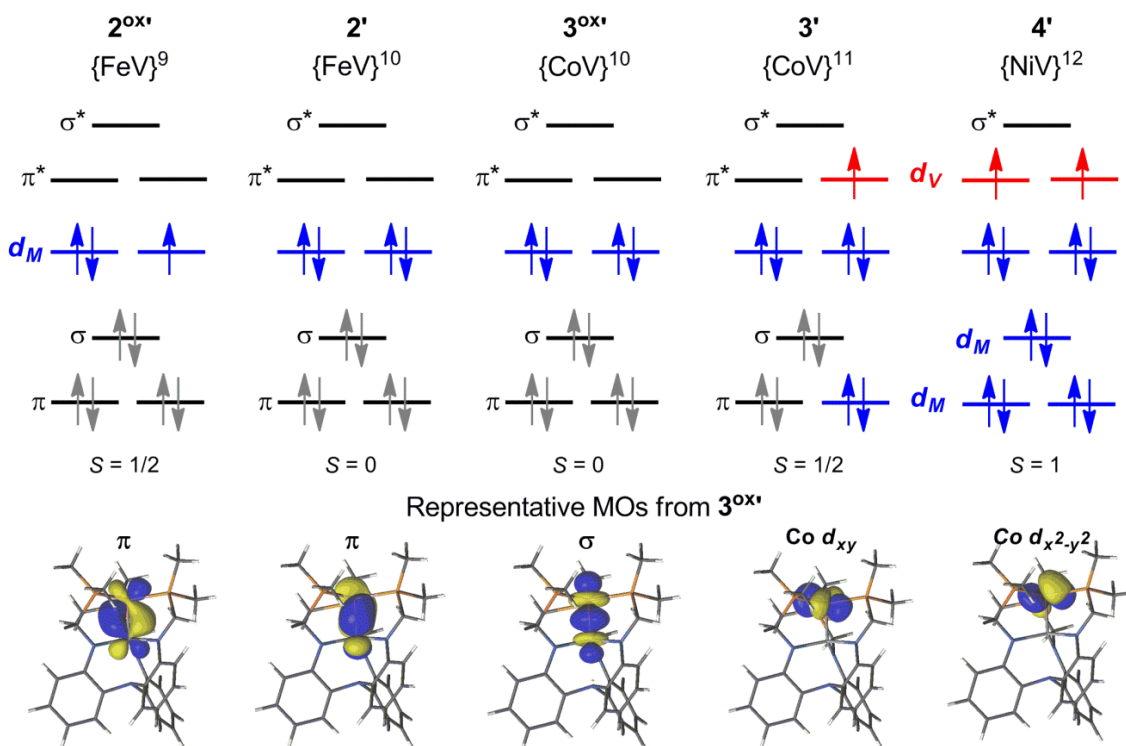


**Figure 2.9** Qualitative MO diagrams across the metal-vanadium series. Delocalized MOs are labeled according to their bond type (see representative examples at bottom) and shown in black. Localized metal and vanadium d-orbitals are shown in blue and red, respectively.

**Table 2.6** Percentage of Metal Character (%V, %M) in metal-vanadium bonding orbitals of  $\sigma$ - and  $\pi$ -symmetry from CASSCF calculations.<sup>a</sup>

[MVL] <sup>0/+</sup>	d-count	$\sigma$		$\pi$		$\pi^*$	
		%V	%M	%V	%M	%V	%M
[FeVL] <sup>+</sup> (2 <sup>ox+</sup> )	9	27	73	37 35	63 65	54 58	46 42
FeVL (2')	10	33	67	42 42	58 58	52 53	48 47
[CoVL] <sup>+</sup> (3 <sup>ox+</sup> )	10	22	78	35 35	65 65	57 58	43 42
CoVL (3')	11	22	78	42 (4)	58 (96)	55 (91)	45 (9)
NiVL (4')	12	(10)	(90)	(0) (0)	(100) (100)	(100) (100)	(0) (0)

<sup>a</sup> Parentheses are used to highlight polarized MOs, which are described as localized, e.g., M  $d_{xz}$ .

In the systems with more than 10 d electrons, such as CoV **3'** and NiV **4'**, the  $\sigma$ - and  $\pi$ -symmetric MOs become increasingly localized and, hence, nonbonding. Intriguingly, one of the  $\pi$ -symmetric MOs in **3'** is fully localized on Co, which complements a single  $\pi^*$ -symmetric MO becoming localized on V. Notably, the localization of  $\pi/\pi^*$ -symmetric MOs in **3'** was not observed for the isoelectronic FeCrL model species, which may suggest another difference between the V and Cr ancillary ions. The direct consequence of the increased localization is that the formal bond order decreases to 2 in **3'** ( $\sigma + \pi$ ). The EBO for **3'** is slightly lower at 1.55. In **3'** and **4'**, the unpaired spin is predicted to be centered at V (Figure A1.17). For the NiV species, only nonbonding, localized MOs are present, and hence the formal bond order is 0. An experimental FSR value near 1.0, however, suggests some bonding interaction in **4**, and so we investigated the possibility of dative bonding in **4'** using Mayer bond order indices. Indeed, the Mayer bond order for **4'** is nonzero at 0.46. A natural bond orbital (NBO) analysis reveals this interaction to be dative, Ni  $\rightarrow$  V. The interaction of lone pair of electrons in the Ni  $d_z^2$  orbital and an empty V  $d_z^2$  orbital provides an estimated electronic stabilization of  $\sim 20$  kcal/mol.<sup>98</sup>

Considering the difficulty in pinpointing oxidation states in M–M-bonded complexes, we performed a detailed analysis of the active-space orbitals to determine the d-electron counts at each metal (Experimental Section, Tables A1.10–A1.14). On the basis of the d counts for the multiconfigurational ground-state wave functions, the cationic species are well described by  $M^IV^{III}$  oxidation states, i.e.,  $Fe^IV^{III}$  and  $Co^IV^{III}$  in **2<sup>ox'</sup>** and **3<sup>ox'</sup>**, respectively. The calculated oxidation states of NiV **4'** is Ni(0.25)V(2.75), which is reasonably close to the formal description of  $Ni^0V^{III}$ . Finally, the neutral FeV and CoV species, **2'** and **3'**, respectively, are better described with partial oxidation states of M(0.5)V(2.5).

Last, TD-DFT calculations were performed on the  $(d-d)^{10}$  species **2'** and **3<sup>ox'</sup>** as well as  $(d-d)^{12}$ NiV **4'** to better understand the electronic excitations in the MV cores (M06-2X,<sup>99</sup> Experimental Section, Tables A1.15–A1.17). The lowest-energy transition in FeV **2'** and CoV **3<sup>ox'</sup>** corresponds to Fe  $\rightarrow$  V and Co  $\rightarrow$  V intermetal charge transfer, respectively. Moreover, the predicted excitation energies agree well with the corresponding experimental values (721 nm for **2'**, exptl 762 nm; 647 nm for **3<sup>ox'</sup>**, exptl 613 nm). A similar calculation for NiV **4'** predicted a NIR transition that closely matched to experiment when



the PBE functional was employed (916 for **4'**, exptl 905), and this excitation corresponded to a d–d transition at V. An investigation of the functional dependency of this transition in NiV **4'** showed that hybrid functionals tend to overpredict the excitation energy due to increased Ni–V mixing in the electronic ground state (Figure A1.24 and Table A1.17).

## 2.4 Conclusion of M-V complexes

The five [MVL]<sup>0,+</sup> complexes (M = Fe, Co, Ni) extend the FeV compounds reported by Thomas et al. and complement previous work on the isostructural MCrL series. To our knowledge, the MVL family showcases the first examples of coordination complexes with Co–V and Ni–V bonding interactions. Collectively, they add to the few examples of group 5 heterobimetallic complexes containing M–M multiple bonds. Across the period, the M–V bond order decreases from a maximal triple bond in FeVL to double in CoVL to a dative interaction in NiVL. A similar trend in bonding was observed for the MCrL series. The spin states of the neutral MVL also increase across the period, from  $S = 0$  for FeVL to  $S = 1/2$  for CoVL to  $S = 1$  for NiVL, whereby the unpaired spins are localized at V.

A key effect of changing the supporting M ion from Cr<sup>III</sup> to V<sup>III</sup> is to decrease the number of reversible electron-transfer processes in NiVL and CoVL, which have exactly two fewer than their MCrL analogues, although the redox profile of FeVL is similar to that of FeCrL. As revealed by theory, key differences between the V<sup>III</sup> and Cr<sup>III</sup> ancillary ions are the increasingly polarized nature of the MOs involved in M–M bonding in the MVL species. Despite the higher degree of polarization in M–V bonding orbitals, the formal shortness ratios in FeVL (FSR = 0.79) and CoVL (FSR = 0.89) are lower compared to those their MCrL congeners, FeCrL (FSR = 0.83) and CoCrL (FSR = 0.92), respectively. A future goal is to rationalize and predict the bonding and electronic structures of these highly polarized M–M species.

## 2.5 Experimental Section

### *General Considerations*

Unless otherwise stated, all manipulations were performed under an inert atmosphere in a glovebox or using standard Schlenk techniques. Standard solvents were deoxygenated by

sparging with inert gas and dried by passing through activated alumina columns of a SG Water solvent purification system. Deuterated solvents were purchased from Cambridge Isotope Laboratories, Inc., or Sigma-Aldrich, degassed via freeze–pump–thaw cycles, and stored over activated 4 Å molecular sieves. Elemental analyses were performed by Complete Analysis Laboratories, Inc. (Parsippany, NJ), or Robertson Microlit Laboratories, Inc. (Ledgewood, NJ). The ligand N(*o*-(NHCH<sub>2</sub>P<sup>i</sup>Pr<sub>2</sub>)C<sub>6</sub>H<sub>4</sub>)<sub>3</sub> (abbreviated as LH<sub>3</sub>) was synthesized according to literature procedures.<sup>12</sup>

### Synthesis of V(N(*o*-(NCH<sub>2</sub>P<sup>i</sup>Pr<sub>2</sub>)C<sub>6</sub>H<sub>4</sub>)<sub>3</sub>) (1)

A solution of neutral ligand (N(*o*-(NHCH<sub>2</sub>P<sup>i</sup>Pr<sub>2</sub>)C<sub>6</sub>H<sub>4</sub>)<sub>3</sub>) (0.512 g, 0.752 mmol) in Et<sub>2</sub>O (8 mL) was frozen in a LN<sub>2</sub> cold well and then layered with <sup>n</sup>BuLi (1.00 mL, 2.50 mmol). The mixture was stirred for 1 h at rt and then dried *in vacuo*. The resulting yellow oil was taken up in THF (6 mL) and frozen in a LN<sub>2</sub> cold well along with a solution of VCl<sub>3</sub>(THF)<sub>3</sub> (0.281 g, 0.752 mmol) in THF (8 mL). The thawing yellow solution of deprotonated ligand was layered on top of the frozen solution of VCl<sub>3</sub>(THF)<sub>3</sub> and allowed to warm to rt. The solution was stirred for 4 h to yield a brown solution. The reaction was dried *in vacuo* and then dissolved in benzene. The benzene solution was filtered through a Celite pad and dried *in vacuo*, giving a brown powder (0.472 g, 85% yield). Single crystals were grown by the slow evaporation of a concentrated diethyl ether solution. <sup>1</sup>H NMR (ppm, C<sub>6</sub>D<sub>6</sub>, 500 MHz): 30 (br), 12.2, 10.4, 9.3, 3.8, 1.0. Evans' method (C<sub>6</sub>D<sub>6</sub>): 2.41 μB. UV–vis–NIR [THF; λ<sub>max</sub>, nm (ε, M<sup>-1</sup> cm<sup>-1</sup>): 845 (300). Anal. Calcd for **1** (C<sub>39</sub>H<sub>60</sub>N<sub>4</sub>P<sub>3</sub>V): C, 64.27; H, 8.30; N, 7.69. Found: C, 64.18; H, 8.38; N, 7.53.

### Synthesis of FeV(N(*o*-(NCH<sub>2</sub>P<sup>i</sup>Pr<sub>2</sub>)C<sub>6</sub>H<sub>4</sub>)<sub>3</sub>) (2)

A solution of **1** (0.170 g, 0.233 mmol) in THF (2 mL) was added to a slurry of FeBr<sub>2</sub> (0.0508 g, 0.235 mmol) in THF (6 mL) with stirring. After 15 min, the homogeneous, dark-yellow-brown solution was added to KC<sub>8</sub> (0.0644 g, 0.477 mmol). The reaction was stirred for 4 h. After filtering through a Celite pad, the filtrate was dried *in vacuo*. The brown powder was dissolved in benzene, filtered through a Celite pad, and dried *in vacuo* to give a brown powder (0.166 g, 90% yield). Single crystals were grown by vapor diffusion of pentane into a concentrated toluene solution. <sup>1</sup>H NMR (ppm, THF-*d*<sub>8</sub>, 500 MHz): 6.78 (t, *J* = 7.7 Hz, 3H, aryl), 6.46 (d, *J* = 7.6 Hz, 3H, aryl), 6.37 (d, *J* = 8.1

Hz, 3H, aryl), 6.04 (m, 6H, overlapping aryl and methylene), 5.19 (d,  $J = 12.0$  Hz, 3H, methylene), 3.04 (br s, 3H, methine), 2.97 (br s, 3H, methine), 1.78 (br s, 9H, methyl), 1.54 (br s, 9H, methyl), 1.36 (d,  $J = 5.1$  Hz, 9H, methyl), 0.15 (d,  $J = 6.4$  Hz, 9H, methyl).  $^{31}\text{P}$  NMR (ppm, THF- $d_8$ , 200 MHz): 33.3.  $^{13}\text{C}$  NMR (ppm, THF- $d_8$ , 126 MHz): 155.7, 138.5, 128.0, 126.8, 114.9, 107.5, 72.9, 34.2, 28.6, 22.8, 20.4, 20.0, 18.4. UV-vis-NIR [THF;  $\lambda_{\text{max}}$ , nm ( $\epsilon$ ,  $\text{M}^{-1} \text{cm}^{-1}$ ): 464 (4100), 762 (1300). Anal. Calcd for **2**  $\text{C}_{39}\text{H}_{60}\text{N}_4\text{P}_3\text{VFe}$ : C, 59.70; H, 7.71; N, 7.14. Found: C, 59.65; H, 7.79; N, 7.09.

### Alternative Synthesis of **2**

A slurry of  $\text{KC}_8$  (0.0162 g, 0.120 mmol) in THF (4 mL) was added to a stirring solution of  $[\mathbf{2}^{\text{ox}}]\text{PF}_6$  (0.113 g, 0.116 mmol) in THF (3 mL). The reaction was allowed to stir at rt for 2 h and then was filtered through a Celite pad. The volatiles were removed *in vacuo*, and the brown powder was dissolved in benzene and filtered through a Celite pad. The volatiles were removed *in vacuo* to give a brown powder (0.065 g, 70% yield).

### Synthesis of $[\text{FeV}(\text{N}(\text{o}-(\text{NCH}_2\text{P}^i\text{Pr}_2)\text{C}_6\text{H}_4)_3)]\text{PF}_6$ ( $[\mathbf{2}^{\text{ox}}]\text{PF}_6$ )

A THF solution (6 mL) of  $\text{FeCl}_2$  (0.0515 g, 0.406 mmol) was added to a THF solution (4 mL) of **1** (0.303 g, 0.414 mmol), and the reaction was stirred for 30 min. A slurry of  $\text{KC}_8$  (0.0420 g, 0.311 mmol) in THF (3 mL) was added to the reaction solution, and the mixture was stirred for an additional 3 h. The reaction solution was then filtered through a Celite plug, and the volatiles were removed *in vacuo*. The brown powder was dissolved in THF (8 mL), and  $\text{TIPF}_6$  (0.0840 g, 0.240 mmol) in THF (4 mL) was added. The reaction was stirred for 3 h and filtered through Celite. After removal of all volatiles *in vacuo*, the resulting brown solid was washed with  $5 \times 5$  mL of toluene,  $3 \times 5$  mL of 1:1 THF/hexane, and  $3 \times 5$  mL of hexane. The resulting maroon powder was dried to afford  $[\mathbf{2}^{\text{ox}}]\text{PF}_6$  (0.113 g, 30% yield).  $^1\text{H}$  NMR (ppm, THF- $d_8$ , 500 MHz): 49.7, 29.9, 9.8, 9.5, 8.4, 6.0, 4.1, 0.5, -1.0. UV-vis-NIR [THF;  $\lambda_{\text{max}}$ , nm ( $\epsilon$ ,  $\text{M}^{-1} \text{cm}^{-1}$ ): 524 (3700), 785 (sh, 400). Anal. Calcd for  $[\mathbf{2}^{\text{ox}}]\text{PF}_6$  ( $\text{C}_{39}\text{H}_{60}\text{N}_4\text{F}_6\text{P}_4\text{VFe}$ ): C, 50.39; H, 6.51; N, 6.03. Found: C, 50.17; H, 6.66; N, 5.88.

### Synthesis of [FeV(N(*o*-(NCH<sub>2</sub>P<sup>i</sup>Pr<sub>2</sub>)C<sub>6</sub>H<sub>4</sub>)<sub>3</sub>)]BPh<sub>4</sub> ([2<sup>ox</sup>]BPh<sub>4</sub>)

A slurry of [FeCp<sub>2</sub>]BPh<sub>4</sub> (0.136 g, 0.269 mmol) in acetonitrile (5 mL) was added to a stirring slurry of **2** (0.209 g, 0.266 mmol) in acetonitrile (5 mL). The reaction mixture was stirred overnight, and the volatiles were removed *in vacuo*. The solid was washed with 5 × 5 mL of diethyl ether, 3 × 5 mL of toluene, 3 × 3 mL of hexane to obtain a dark-pink powder. Single crystals of [2<sup>ox</sup>]BPh<sub>4</sub> were grown by vapor diffusion of pentane into a concentrated THF solution (0.026 g, 9% crystalline yield). <sup>1</sup>H NMR (ppm, THF-*d*<sub>8</sub>, 400 MHz): 48.7, 31.1, 10.0, 9.7, 7.3, 6.8, 6.7, 6.3, 1.3, 0.0, -1.1. Anal. Calcd for [2<sup>ox</sup>]BPh<sub>4</sub> (C<sub>63</sub>H<sub>80</sub>N<sub>4</sub>BP<sub>3</sub>VFe): C, 68.55; H, 7.31; N, 5.08. Found: C, 67.28; H, 7.97; N, 4.56.

### Synthesis of CoV(N(*o*-(NCH<sub>2</sub>P<sup>i</sup>Pr<sub>2</sub>)C<sub>6</sub>H<sub>4</sub>)<sub>3</sub>) (**3**)

A solution of **1** (0.174 g, 0.238 mmol) in THF (4 mL) was added to a stirring slurry of CoBr<sub>2</sub>(0.0522 g, 0.237 mmol) in THF (2 mL). After 15 min, the homogeneous, dark-green-brown solution was added to KC<sub>8</sub> (0.0658 g, 0.487 mmol). The reaction was stirred for an additional 4 h and then filtered through a Celite pad. After the volatiles were removed *in vacuo*, the resulting brown powder was dissolved in benzene and filtered through a Celite pad. The filtrate was dried *in vacuo* to give a brown powder (0.175 g, 90% yield). Single crystals were grown by vapor diffusion of pentane into a concentrated toluene solution. <sup>1</sup>H NMR (ppm, C<sub>6</sub>D<sub>6</sub>, 500 MHz): 8.5, 8.4, 8.1, 5.8, 5.5, 4.4, 2.8, 2.6, 1.7, 1.1, 0.3, -8.7. Evans' method (C<sub>6</sub>D<sub>6</sub>): 1.80 μB. UV-vis-NIR [THF; λ<sub>max</sub>, nm (ε, M<sup>-1</sup> cm<sup>-1</sup>): 505 (sh, 3600), 1254 (600). Anal. Calcd for **3** C<sub>39</sub>H<sub>60</sub>N<sub>4</sub>P<sub>3</sub>VCo: C, 59.47; H, 7.68; N, 7.11. Found: C, 59.08; H, 7.63; N, 6.97.

### Synthesis of [CoV(N(*o*-(NCH<sub>2</sub>P<sup>i</sup>Pr<sub>2</sub>)C<sub>6</sub>H<sub>4</sub>)<sub>3</sub>)]BPh<sub>4</sub> ([3<sup>ox</sup>]BPh<sub>4</sub>)

A slurry of [FeCp<sub>2</sub>]BPh<sub>4</sub> (0.091 g, 0.180 mmol) in acetonitrile (5 mL) was added to a stirring slurry of **3** (0.156 g, 0.197 mmol) in acetonitrile (5 mL). The reaction mixture was stirred overnight, and the volatiles were removed *in vacuo*. The remaining solid was washed with 5 × 5 mL of diethyl ether, 3 × 5 mL of toluene, and 3 × 3 mL of hexane to obtain a green powder (0.093 g, 40% yield). Single crystals of **3<sup>ox</sup>** were grown by vapor diffusion of hexane into a concentrated THF solution. <sup>1</sup>H NMR (ppm, THF-*d*<sub>8</sub>, 500 MHz): 7.28 (br, 8 H, BPh<sub>4</sub>), 7.07 (t, *J* = 7.7 Hz, 3H, aryl), 6.95 (d, *J* = 7.3 Hz, 3H, aryl), 6.83

(t,  $J = 6.9$  Hz, 8H, BPh<sub>4</sub>), 6.68 (t,  $J = 6.9$  Hz, 4H, BPh<sub>4</sub>), 6.49 (m, 6H, overlapping aryl), 6.04 (d,  $J = 13.9$  Hz, 3H, methylene), 5.43 (d,  $J = 13.5$  Hz, 3H, methylene), 3.19 (br s, 3H, methine), 3.07 (br s, 3H, methine), 1.50 (br, 27H, methyl), 0.54 (br, 3H, methyl). <sup>31</sup>P NMR (ppm, THF-*d*<sub>8</sub>, 200 MHz): 15.7. <sup>13</sup>C NMR (ppm, THF-*d*<sub>8</sub>, 126 MHz): 165.5, 154.3, 139.3, 137.4, 129.8, 126.7, 125.8, 121.9, 120.4, 110.1, 72.9, 32.1, 27.5, 22.4, 20.3, 19.4, 17.9. UV–vis–NIR [THF;  $\lambda_{\text{max}}$ , nm ( $\epsilon$ , M<sup>-1</sup> cm<sup>-1</sup>): 441 (5200), 613 (2900). Anal. Calcd for [3<sup>ox</sup>]BPh<sub>4</sub>(C<sub>63</sub>H<sub>80</sub>N<sub>4</sub>BP<sub>3</sub>VCo): C, 68.36; H, 7.28; N, 5.06. Found: C, 68.07; H, 7.67; N, 4.45.

### Synthesis of NiV(N(*o*-(NCH<sub>2</sub>P<sup>i</sup>Pr<sub>2</sub>)C<sub>6</sub>H<sub>4</sub>)<sub>3</sub>) (4)

A solution of **1** (0.404 g, 0.555 mmol) in THF (12 mL) was added to solid bis(1,5-cyclooctadiene)nickel(0) (0.153 g, 0.555 mmol). The resulting solution retained the dark-brown color of **1** but quickly acquired a pink tint in place of its original orange tint. The reaction was stirred for 7 h, at which point the reaction mixture was dried *in vacuo*. Subsequent washing of the crude mixture with cold pentane followed by extraction into toluene using a Celite pad and drying *in vacuo* afforded a brown powder (0.316 g, 70% yield). Single crystals were grown by vapor diffusion of pentane into a concentrated benzene solution. <sup>1</sup>H NMR (ppm, C<sub>6</sub>D<sub>6</sub>, 400 MHz): 13.9, 6.9, 2.6, 1.2, 0.9, 0.5 (br sh). Evans' method (C<sub>6</sub>D<sub>6</sub>): 2.39  $\mu$ B. UV–vis–NIR [THF;  $\lambda_{\text{max}}$ , nm ( $\epsilon$ , M<sup>-1</sup> cm<sup>-1</sup>): 410 (5200), 905 (500). Anal. Calcd for **4** (C<sub>39</sub>H<sub>60</sub>N<sub>4</sub>P<sub>3</sub>VNi): C, 59.48; H, 7.68; N, 7.11. Found: C, 59.54; H, 7.37; N, 6.03.

### Physical Methods

<sup>1</sup>H NMR spectra were recorded on a Bruker 500 MHz or a Varian 300 MHz spectrometer at rt unless otherwise noted. All <sup>1</sup>H and <sup>13</sup>C NMR spectra were referenced to the residue solvent. Variable-temperature NMR experiments were conducted on a Bruker 500 MHz spectrometer, and the temperature of the NMR probe was calibrated against an external ethylene glycol standard. Diamagnetic anisotropy ( $\chi_{\parallel} - \chi_{\perp}$ ) is calculated from eqn 1<sup>91</sup>

$$(1) \quad \Delta\delta = \left(\frac{1}{3r^3}\right) \frac{(\chi_{\parallel} - \chi_{\perp})(1 - 3\cos^2(\theta))}{4\pi}$$

where  $\Delta\delta$  is the difference in the chemical shift (ppm) between the average methylene resonance in a bimetallic complex versus the reference complex, an isostructural Ni–Al

complex that has a Ni  $\rightarrow$  Al dative bond. The average distance of the methylene proton to the center of the M–M bond is  $r$ , the average acute angle between the proton and M–M axis is  $\theta$ , and the unit of  $\Delta\chi$  is  $10^{-36}\text{m}^3/\text{molecule}$ . The barrier to inversion,  $\Delta G^{\ddagger}$ , is calculated with eqn 2

$$(2) \quad \Delta G^{\ddagger} = R T_c (23.760 + \ln \left( \frac{T_c}{k_c} \right))$$

where the coalescence temperature  $T_c$  is in Kelvin,  $R$  is the ideal gas constant, and  $k_c = \pi\Delta\nu_0/\sqrt{2}$ , where  $\Delta\nu_0$  is the difference in frequency (Hz) between the exchanging protons.<sup>100</sup> Solution magnetic moments were determined using Evans' method.<sup>94,101</sup> UV–vis–NIR spectra were collected at rt on a Cary-14 spectrometer. Cyclic voltammetry was performed using a CH instruments 600 electrochemical analyzer. The one-cell setup used a glassy carbon working electrode, platinum wire counter electrode, and Ag/AgNO<sub>3</sub> reference electrode in CH<sub>3</sub>CN. Analyte solutions consisted of 0.4 M [<sup>n</sup>Bu<sub>4</sub>N][PF<sub>6</sub>], and the CVs were referenced internally to the Fc<sup>0/+</sup> redox couple. The starting potential of each cyclic voltammetry scan corresponds to zero current. Perpendicular-mode X-band EPR spectra were recorded at 20 and 13 K with a Bruker ESP 300 spectrometer equipped with an Oxford ESR 910 liquid-helium cryostat and an Oxford temperature controller. X-band EPR spectra were simulated using the program *ESIM* written by Eckhard Bill. Mössbauer data were recorded on an alternating-current constant-acceleration spectrometer. The minimum experimental line width was 0.24 mm/s (full width at half-height). The sample temperature was maintained constant at 80 K in an Oxford Instruments Variox or an Oxford Instruments Mössbauer-Spectromag 2000 cryostat, which is a split-pair superconducting magnet system for applied fields (up to 8 T). The field at the sample is oriented perpendicular to the  $\gamma$  beam. The <sup>57</sup>Co/Rh source (1.8 GBq) was positioned at rt inside the gap of the magnet system at a zero-field position. Isomer shifts are quoted relative to Fe metal at 300 K. Magnetic susceptibility data were measured from powder samples of solid material in the temperature range 2–300 K by using a SQUID susceptometer with a field of 1.0 T (MPMS-7, Quantum Design, calibrated with a standard palladium reference sample; error <2%). The experimental data were corrected for underlying diamagnetism by use of tabulated Pascal's constants ( $\chi_{\text{dia}} < 0$ ), as well as for temperature-independent paramagnetism ( $\chi_{\text{TIP}} > 0$ ).<sup>102,103</sup> The latter was

adjusted such that  $\chi T$  was obtained constant above 50 K after subtraction of  $\chi_{\text{TIP}}$ . The susceptibility and magnetization data were simulated with the program *julX* (version 141; E. Bill) using the following parameters:  $g = 2.1$ ,  $\chi_{\text{TIP}} = 0.573 \times 10^{-3}$  emu, and  $\chi_{\text{DIA}} = -0.487 \times 10^{-3}$  emu for  $[\mathbf{2}^{\text{ox}}]\text{PF}_6$  and  $g = 1.9$ ,  $\chi_{\text{TIP}} = 0.170 \times 10^{-3}$  emu,  $\chi_{\text{DIA}} = -0.422 \times 10^{-3}$  emu, and 5%  $S = 0$  impurity for **3**.

### **X-ray Crystallography**

Specimens of **1–4** were mounted on a Bruker Apex II CCD or a Bruker Photon 100 CMOS diffractometer for data collection at 173(2) or 123(2) K using either Mo  $K\alpha$  (graphite monochromator) or Cu  $K\alpha$  (normal parabolic mirrors) radiation. The Bruker Apex II software suite was used for data collection, integration, correction, and structure solution.<sup>104,105</sup> Complete refinement details and treatment of the data are provided in Appendix 1.

### **Computational Methods**

Quantum-chemical studies were performed on the five bimetallic species **2'**, **2<sup>ox'</sup>**, **3'**, **3<sup>ox'</sup>**, and **4'** in which the isopropyl groups are truncated to methyl groups. Gas-phase optimization of the all-spin states of the truncated systems was carried out with the PBE functional<sup>97</sup> implemented in the *Gaussian 09* program package.<sup>106</sup> For C and H atoms, the def2-SVP basis set was used, whereas the all-electron triple- $\zeta$ -quality basis set def2-TZVP was employed for N, P, Fe/Co/Ni, and V atoms.<sup>107</sup> Vibrational frequency analysis with the harmonic approximation was performed at optimized geometries to characterize the nature of the stationary points on the potential energy surface, and no imaginary frequencies were found for the optimized ground-state geometries.

These bimetallic species were further investigated with the complete active-space self-consistent-field (CASSCF) method, followed by second-order perturbation theory (CASPT2).<sup>108</sup> All CASSCF calculations were performed with the *MOLCAS-7.8* package<sup>109</sup> at the PBE-optimized structures, using the all-electron ANO-RCC basis sets.<sup>110,111</sup> In all of these calculations, the triple- $\zeta$ -quality ANO-RCC-VTZP basis set was used for Fe, Co, Ni, and V atoms, the double- $\zeta$ -quality ANO-RCC-VDZP basis set was used for P and N atoms, and the minimal basis ANO-RCC-MB was chosen for the C and H atoms. Scalar relativistic effects were included by using the Douglas–Kroll–Hess

Hamiltonian.<sup>112,113</sup> The two-electron integral evaluation was simplified by employing the Cholesky decomposition technique.<sup>114</sup> In the CASSCF/CASPT2 calculations, an active space of  $n$  electrons in 10 orbitals ( $n, 10$ ) was used for **2'**, **2<sup>ox'</sup>**, **3'**, and **3<sup>ox'</sup>**, where  $n$  is the number of 3d electrons of the two transition metals. Placement of all 10 3d orbitals did not give a stable active space, and two virtual V 3d orbitals were displaced by two Fe 4d orbitals. For **4'**, an active space of 12 electrons in 14 orbitals (8 3d + 5 Ni 4d + 1 Ni 5d) was used. NBO analysis was used, as implemented in *Gaussian 09*.<sup>115</sup> A detailed orbital analysis was performed to determine the d-electron count at the individual metals. In this analysis, the electron population of each active-space orbital is parsed between the two metals according to the metals' relative contribution in that orbital. The number of d electrons at each metal is then summed over all active orbitals to provide the total d-electron count.

TD-DFT calculations were also performed to investigate the nature of the electron excitations observed in the electronic absorption spectra. All calculations were performed by using the M06-2X functional<sup>99</sup>, as implemented in the *Gaussian 09* program package.<sup>106</sup> Solvent effects were considered by using the SMD model with THF as the solvent.<sup>116</sup> For **4'**, calculations with additional functionals were also investigated, including PBE<sup>117</sup>, B3LYP<sup>118</sup>, CAM-B3LYP<sup>119</sup>, M06, M06-2X<sup>99</sup>, M06-HF<sup>120</sup>, and M06-L<sup>121</sup>.



## **Chapter 3**

### **Dative vs. Covalent Bonding in Trigonal Ti-M Complexes**

### 3.1 Overview

A family of heterobimetallic complexes were synthesized by metalating the Ti(III) metalloligand,  $\text{Ti}(\text{o}-(\text{NCH}_2\text{P}^i\text{Pr}_2)\text{C}_6\text{H}_4)_3$ , with Fe, Co and Ni precursors. These heterobimetallic MTiL complexes were isolated, along with their one-electron oxidized analogues, and the one-electron reduced  $[\text{FeTiL}]^-$  complex (Figure 3.1). These complexes were characterized with X-ray crystallography, cyclic voltammetry, EPR and Mössbauer spectroscopy. The M–Ti interactions present a unique insight into M–M bonding where both dative and covalent interactions can occur between a Ti(III) or Ti(IV) center with a late metal.

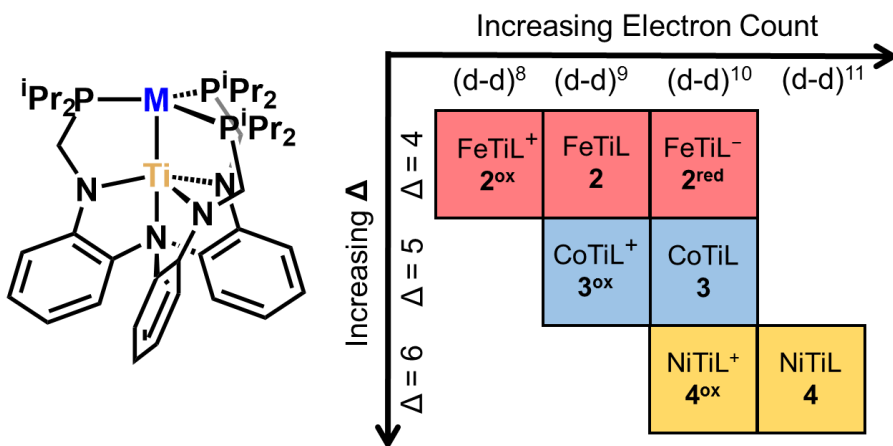


**Figure 3.1** Family of isolated MTiL combinations using ligand, L (left).

### 3.2 Introduction

Interactions between metals can span a huge range, from electrostatic and dative interactions to covalent multiple bonds.<sup>22,23,79,80,122</sup> Heterometallic complexes provide ample opportunity to study these different metal–metal interactions. Within the last three years, the field of metal–metal bonding between two first-row transition metals has rapidly expanded, largely providing complexes with covalent, and some with multiple, bonds. The Lu and Thomas groups are major contributors to the field of heterobimetallic chemistry, with a number of early-late transition metal combinations.<sup>10,11,16,19,20,85,86,123</sup>

In the Lu group, a study of the MCrL family revealed a periodic trend in the M–Cr bonding.<sup>20</sup> As the two metals were further separated on the periodic table, their bonding

orbitals become more localized, resulting in weaker bonds as the top metal moved further from Cr across the periodic table. A formal quintuple bond was found in the MnCrL complex, but moving just one metal over to Fe polarized the  $\delta$ -symmetry orbitals to non-bonding and dropped the bond order to three. At the other end of the spectrum, NiCrL shows what can be described as a polarized, single covalent bond at best. A similar MVL series revealed the same trend seen in the MCr series, while also showing how largely polarized these M–M bonds can become while still having very short M–M bond lengths.

19

Previous heterobimetallic complexes with an unsupported Ti–Co and Ti–Fe interaction were found to have polar metal-metal bonds, but these bonds were relatively long, and often underwent ionic dissociation of the metal-metal bond.<sup>122,124</sup> Recently, a short Ti–Ni bond was published using a phosphinopyrrolide ligand, and its short bond can be described as a result of polarized covalent bonds, with both  $\sigma$  and  $\pi$  interactions contributing to the Ti–Ni bonding.<sup>125</sup>

Extending these studies with a MTiL family will further allow for understanding of M–M interactions, specifically with highly polarized bonds. Using a Ti(III) ion in the tris-amide pocket of the double-decker ligand shown in Figure 4.3, the supporting metal is more susceptible to a change oxidation state upon installation of a second metal due to higher stability of Ti(IV) over Ti(III). The transfer of the one d-electron from the Ti(III) center can also generate formally more reduced active metals in the neutral state. The anticipated bonding in these MTiL complexes is expected to be very polarized, due to the energy mismatch between the d-orbitals of the two metals. The d-orbital energy mismatch is a result of the metals' separation on the periodic table resulting in a polarized covalent bond, which can only contribute a fraction of bonding compared to a fully delocalized covalent bond. The energy difference of the d-orbitals can be large enough such that the orbitals are localized on each metal and become non-bonding with respect to covalent interactions. However, these non-bonding d-orbitals can become involved in dative interactions between the metals, which is seen between the donation from  $d^n$  top metal to the  $d^0$  Ti(IV) center. The isolated complexes are summarized in Figure 3.1 and were characterized by X-ray crystallography, cyclic voltammetry, EPR and Mössbauer spectroscopies.

### 3.3 Results and Discussion

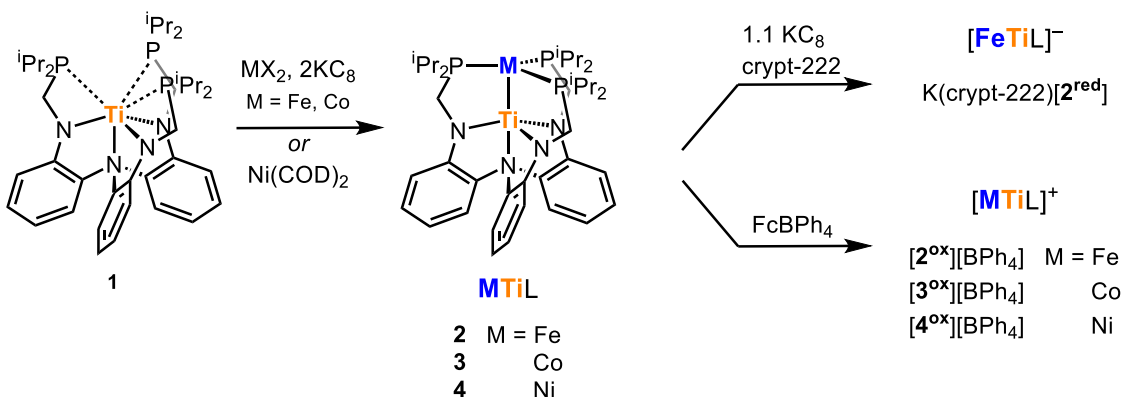
#### 3.3.1 Synthesis

The ligand  $N(o-(NHCH_2P^iPr_2)C_6H_4)_3$ , abbreviated as  $LH_3$ , was used to prepare a monometallic titanium(III) complex in good yield by deprotonation of  $LH_3$  with three equivalents of  $nBuLi$  followed by the addition of  $TiCl_3(THF)_3$  to afford **1**. The metalloligand **1** was subsequently metalated to install zerovalent iron, cobalt or nickel (Scheme 3.1). The  $FeTiL$  **2** and  $CoTiL$  **3** heterobimetallics were synthesized by adding one equivalent of  $MBr_2$  to **1** followed by the addition of 2.05 equivalents of  $KC_8$ . The  $NiTiL$  **4** complex was isolated from the reaction of **1** with  $Ni(COD)_2$  ( $COD = 1,5$ -cyclooctadiene).

Complexes **2** – **4** were each oxidized with 1 equiv. of ferrocenium tetraphenylborate ( $FcBPh_4$ ) to give the corresponding cationic species:  $[FeTiL]BPh_4$  ( $2^{ox}BPh_4$ ),  $[CoTiL]BPh_4$  ( $3^{ox}BPh_4$ ) and  $[NiTiL]BPh_4$  ( $4^{ox}BPh_4$ ). Tetraphenylborate was chosen as the counter anion due to its similar size to the bimetallic, which may aid packing of the two ions in the crystal. Due to the poor solubility of  $FcBPh_4$ , the reactions were run in acetonitrile overnight, and acetonitrile was found to bind irreversibly to Fe in  $2^{ox}$  (*vide infra*) and suspected to bind to Co in  $3^{ox}$ . The bound acetonitrile is suspected to disrupt the strong interaction of the two metals, so it is preferable to isolate the open analogue.<sup>126,127</sup> Of relevance, acetonitrile is presumed to be bound to Fe in  $FeCrL$  cation when the oxidation is run in acetonitrile, and a crystal structure of  $CoCrL$  cation shows an acetonitrile bound to the Co.<sup>28,53</sup> Conversely, no acetonitrile was found to bind Fe or Co in the cationic  $FeVL$  and  $CoVL$  species when the oxidation was conducted in acetonitrile.<sup>19</sup> No bound acetonitrile was found to be bound to Ni in  $4^{ox}$ . To isolate cationic  $FeTiL$  and  $CoTiL$  complexes without bound acetonitrile, an oxidant that is soluble in THF or a weakly coordinating solvent is needed such as  $Fc[B(Ar_F)_4]$  ( $B(Ar_F)_4 = B(3,5-(CF_3)_2C_6H_3)_4$ ).<sup>28</sup>

The one-electron reduced product of **2** was isolated by stirring **2** with one equivalent of  $KC_8$  in the presence of one equivalent of 222-cryptand to yield  $K(crypt-222)[FeTiL]$  ( $K(crypt-222)[2^{red}]$ ). The cyclic voltammogram of **3** shows a reversible reduction of **3** at  $-3.2$  V (*vide infra*) and multiple attempts to isolate a reduced  $CoTiL$  species were attempted. The most successful approach to isolate a reduced  $CoTiL$  involved running a solution of **3** in THF through a  $KC_8$  plug. However,  $^1H$  NMR spectroscopy indicated that

while new paramagnetic peaks that could correspond to a new reduced species were present, a significant fraction of the reaction was the neutral **3**. The harsh reduction potential along with the difficulty to isolate a pure material suggests that either a harsher reductant is needed to push the reaction forward, or the reduced species is unstable, and converts back to its more stable neutral state at room temperature. Although an irreversible reduction was present in the CV of **4**, no attempts to isolate a reduced NiTiL species were made due to a harsh  $E_{pa}$  of  $-3.1$  V (*vide infra*).



**Scheme 3.1** Synthetic route to isolated titanium heterobimetallic complexes.

### 3.3.2 X-ray Crystallography

Single-crystal X-ray structures were obtained for neutral species **2** – **4** and the cationic species **2<sup>ox</sup>** and **4<sup>ox</sup>**. Solid-state parameters are given in Table 3.1 and solid-state structures with average bond lengths are shown in Figure 3.2. All of the structurally characterized complexes have short relatively short M–Ti bonds, with FSR values less than 1. The formal shortness ratio (FSR), which is determined by dividing the observed M–Ti bond length by the sum of the metals’ metallic radii<sup>27</sup>, allows us to compare the heterometallic interactions across the series of metals.<sup>2</sup> A FSR significantly below one can imply the presence of multiple M–M bonds, and complexes **2**, **3**, and **4<sup>ox</sup>** all have FSR values less than 0.9. Complex **2** has the shortest M–M bond of the series, with an FSR of 0.83. The one electron oxidized complex **2<sup>ox</sup>** retains a short M–M interaction with a FSR of 0.94 despite the binding of acetonitrile to Fe, demonstrating a strong interaction remains between the Fe and Ti. The Fe moves 0.3 Å above the P<sub>3</sub> plane, which tracks with the 0.3

Å increase in the Fe–Ti bond and also the 0.8 Å increase in average Fe–P distances in **2<sup>ox</sup>**. However, the bound acetonitrile can contribute to these large changes about the Fe center, so it is difficult to attribute any changes in metal-ligand bond distances with a change in oxidation state in either of the metals.

Complex **3** also has a short M–M interaction with an FSR of 0.89, which is similar to its other neutral, doubly bonded CoML counterparts.<sup>87</sup> While the d<sup>10</sup> configuration of the Ti–Co bond suggests a triple bond, the FSR is more consistent with a double bond. Conversely, a similar trigonal Ti–Co complex from the Thomas lab has a much shorter Co–Ti, with an FSR of 0.81, which would be consistent with previous triply bonded complexes.<sup>59</sup> A possible explanation for this drastic difference in bonding between two d<sup>10</sup> CoTi complexes is the direct P–N linkage in the Thomas complex versus the P–C–N linkage in **L**. A short M–M interaction in **L** requires the compression of the P–C–N linkage into a twisted confirmation whereas the direct P–N linkage dictates a more rigid ligand framework. The Co–Ti bond in the Thomas complex does not have to compress the ligand, whereas the Co–Ti bond may lose some of its shortness as it compensates for the ligand compression.

Complex **4** has a FSR of 0.98, which is consistent with a dative interaction between the Ni(0) and Ti(III), and similar to previous neutral Ni–M complexes.<sup>19,20</sup> Removing an electron from Ti(III) to Ti(IV) in **4<sup>ox</sup>** dramatically decreases the Ni–Ti bond length (FSR = 0.88) by creating a stronger Ni–Ti dative interaction. Besides a 0.2 Å decrease in the Ni–Ti bond length upon oxidation, there are very few minor structural changes otherwise, again, making it difficult to attribute any metal-ligand bond length changes to an oxidation state change. A drastic change in Ni–Ti bond length was also seen using phosphinopyrrolide ligands, where the reduction of a d<sup>10</sup> to a d<sup>11</sup> NiTi complex resulted in a 0.4 Å increase in the Ni–Ti distance, and breaking the strong Ni–Ti bond.<sup>125</sup>

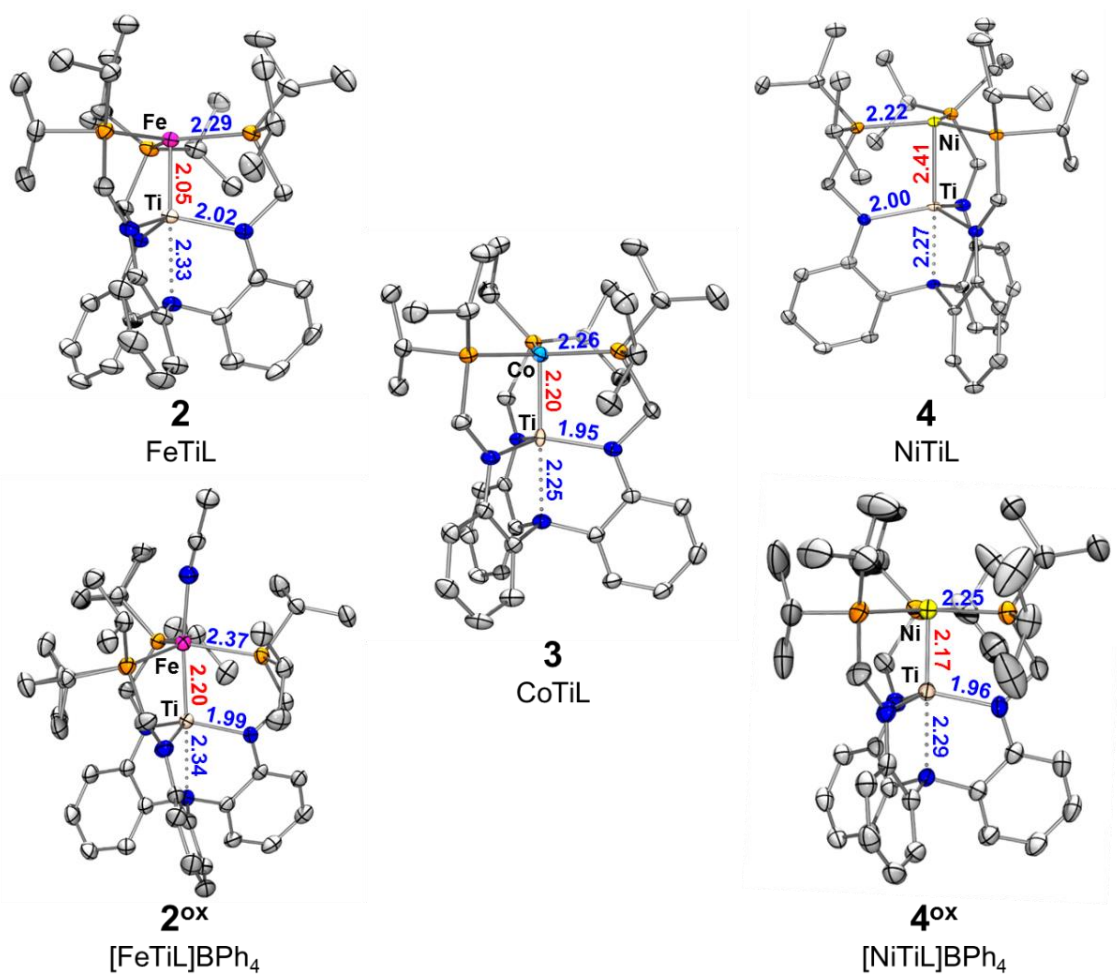


**Figure 3.2** Solid-state structures of 2 – 4, 2<sup>ox</sup> and 4<sup>ox</sup> shown at 50% thermal ellipsoid probability. H atoms, counterions, and non-coordinating solvent molecules have been omitted for clarity. The average bond lengths (Å) are shown.

**Table 3.1** Selected structural information for structurally characterized MTiL complexes.

	<b>2</b> FeTiL		<b>[2<sup>ox</sup>]BPh<sub>4</sub></b> [CH <sub>3</sub> CNFeTiL][BPh <sub>4</sub> ]	<b>3</b> CoTiL	<b>4</b> NiTiL		<b>[4<sup>ox</sup>]BPh<sub>4</sub></b> [NiTiL][BPh <sub>4</sub> ]
<b>charge</b>	0		+	0	0		+
<b>d electrons</b>	9		8	10	11		10
<b>M–Ti (Å)</b>	2.0635(6)	2.0458(8)	2.3455(4)	2.1979(8)	2.4096(7)	2.4139(7)	2.1715(8)
<b>FSR</b>	0.83	0.82	0.94	0.89	0.97	0.98	0.88
<b>M<sub>p</sub>–P (Å)</b>	2.2661(9)	2.2680(12)	2.3541(6)	2.2444(11)	2.2121(10)	2.2273(10)	2.2422(12)
	2.2889(9)	2.2747(10)	2.3643(5)	2.2553(11)	2.2184(10)	2.2101(10)	2.2455(13)
	2.3065(9)	2.3142(11)	2.3878(6)	2.2704(11)	2.2212(10)	2.2206(10)	2.2465(12)
<b>M<sub>p</sub>–P (ave) (Å)</b>	2.286		2.369	2.26	2.218		2.245
<b>M–N<sub>eq</sub> (Å)</b>	2.010(3)	2.014(3)	1.9879(16)	1.947(3)	1.996(3)	1.996(3)	1.952(3)
	2.015(3)	2.022(3)	1.9901(15)	1.954(3)	2.003(3)	1.999(3)	1.961(3)
	2.022(3)	2.022(3)	1.9905(16)	1.955(3)	2.004(3)	2.001(3)	1.963(3)
<b>Ti–N<sub>eq</sub> (ave) (Å)</b>	2.018		1.990	1.95	2.000		1.959
<b>Ti–N<sub>ap</sub> (Å)</b>	2.340(2)	2.328(3)	2.3395(15)	2.251(3)	2.265(3)	2.266(3)	2.288(3)
<b>M<sub>p</sub> to P3 plane (Å)</b>	0.037	0.021	0.333	-0.128	0.096	0.097	0.056
<b>M to N3 plane (Å)</b>	0.468	0.457	0.474	0.298	0.345	0.339	0.413
<b>P–M<sub>p</sub>–P angle (°)</b>	116.57(4)	113.79(4)	115.83(2)	119.63(4)	119.98(4)	120.67(4)	120.57(5)
	115.52(3)	128.98(4)	119.36(2)	118.16(4)	120.04(4)	118.66(4)	118.79(5)
	127.84(4)	117.21(4)	118.97(2)	121.25(4)	119.43(4)	120.11(4)	120.45(5)
<b>N<sub>eq</sub>–Ti–N<sub>eq</sub> (°)</b>	114.12(11)	112.73(12)	115.91(7)	117.50(13)	118.93(12)	117.31(12)	113.85(14)
	114.38(11)	114.40(12)	112.32(7)	116.68(13)	115.57(12)	118.80(12)	116.27(14)
	115.86(11)	117.99(12)	115.33(7)	118.93(13)	116.78(12)	115.40(11)	116.91(14)
<b>M–Ti–N<sub>ap</sub> (°)</b>	178.40(7)	179.45(7)	178.04(4)	178.90(8)	177.91(8)	179.29(8)	179.43(8)
<b>M–L (Å)</b>			2.0918(17)				



### 3.3.3 Cyclic Voltammetry

The cyclic voltammograms for **2** – **4** are shown in Figure 3.3 and their corresponding redox potentials are listed in Table 3.2. All three neutral complexes have multiple redox events, with at least one reductive and oxidative event for each. Complex **2** has two redox events, which is one less than previous Fe heterobimetallic complexes, FeCrL and FeVL. However, the potential of the reversible reduction for **2** at  $-2.09$  V is relatively mild in for bimetallic complexes with L. This reduction potential is the mildest of all the early-late heterobimetallic complexes by 100 mV, and at least 1 V more mild than either of the other Ti heterobimetallic complexes (Table 3.2). The CV of **3** shows three redox events, one reduction and two oxidations. The reduction of **3** is extremely harsh at  $-3.2$  V, which is significantly harsher than other CoM complexes. Complex **4** has a reversible oxidation event and an irreversible reduction event. The oxidation event for **4** is mild at  $-1.9$  V but the irreversible reduction event is harsh with the  $E_{pa}$  past  $-3$  V. Fortunately, the oxidation states in complex **4** can be predicted as Ni(0)/Ti(III), so it is feasible to assign the oxidation event for **4** as Ti based,  $Ti^{III/IV}$ . However, it is not straightforward to assign oxidation states for the metal pairs in **2** and **3**. A clean CV of the monometallic titanium may be able to help identify and confirm further redox assignments in these CVs but further information from EPR and Mössbauer spectroscopies can provide greater insight into the oxidation states at each metal in the isolated MTiL complexes.

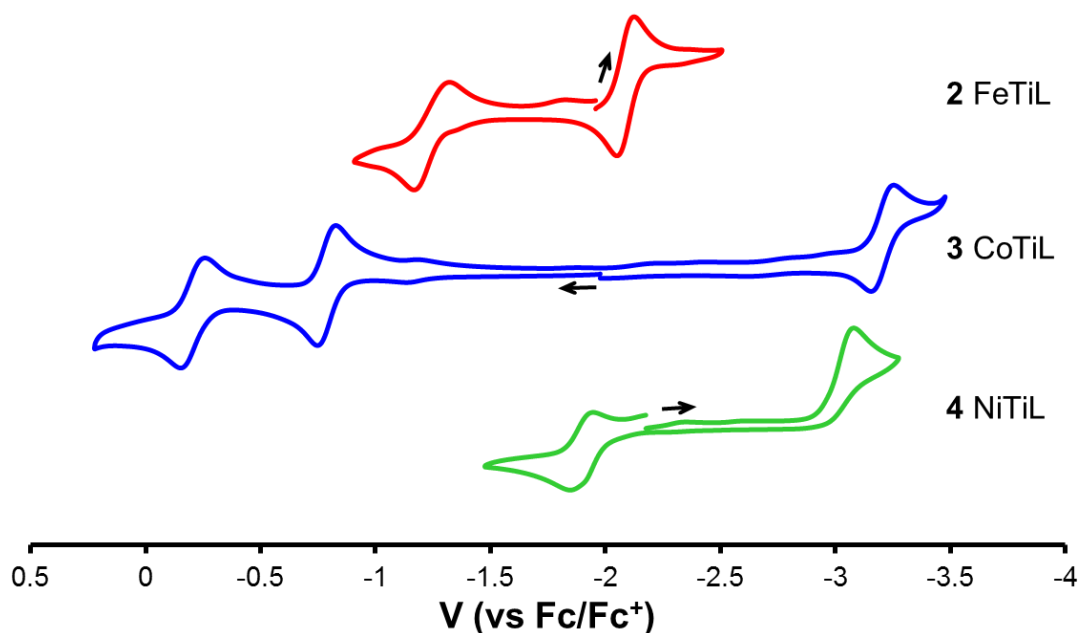


**Figure 3.3** Cyclic voltammograms of **2** – **4** in THF with 0.4 M [<sup>n</sup>Bu<sub>4</sub>N]PF<sub>6</sub> electrolyte starting at zero current with scan rate of 10 mV/s for **2**, 50 mV/s for **3** and 25 mV/s for **4**.

**Table 3.2** Redox potentials for **2** – **4**.

Complex	2 <sup>nd</sup> oxidation			1 <sup>st</sup> oxidation			1 <sup>st</sup> reduction		
	E <sub>1/2</sub> (V)	ΔE <sub>p</sub> (mV)	i <sub>pa</sub> /i <sub>pc</sub>	E <sub>1/2</sub> (V)	ΔE <sub>p</sub> (mV)	i <sub>pa</sub> /i <sub>pc</sub>	E <sub>1/2</sub> (V)	ΔE <sub>p</sub> (mV)	i <sub>pa</sub> /i <sub>pc</sub>
<b>2</b>	-			-1.25	154	0.94	-2.09	75	1.23
<b>3</b>	-0.21	105	1.19	-0.79	79	1.08	-3.21	98	0.89
<b>4</b>	-			-1.90	99	1.01	-3.08 <sup>a</sup>	-	-

<sup>a</sup> Irreversible, E<sub>pc</sub> reported

The preference for a M–M bond to have a d<sup>10</sup> core can also be seen in their CVs (Figure 3.4). The neutral CoTiL **3** has 10 d-electrons, and the stability of this d<sup>10</sup> core can be seen in the large separation of the oxidation and reduction peaks of over 2.4 V. In other d<sup>10</sup> neutral species such as FeVL<sup>19</sup> and MnCrL<sup>20</sup> a larger separation, albeit less pronounced

than **3**, exists between the first oxidation and reduction events as well (1.7 V and 1.1 V<sup>a</sup>, respectively). The separation between the oxidation and the reduction for these d<sup>10</sup> complexes tracks with the difference between the two metals' group number ( $\Delta N$ ), where the larger  $\Delta N$  has a greater separation. The MnCrL complex has the smallest separation between redox processes while also having a formal quintuple bond, suggesting that the more delocalized and covalent the interaction is between the metals, the easier for the complex to undergo redox events.

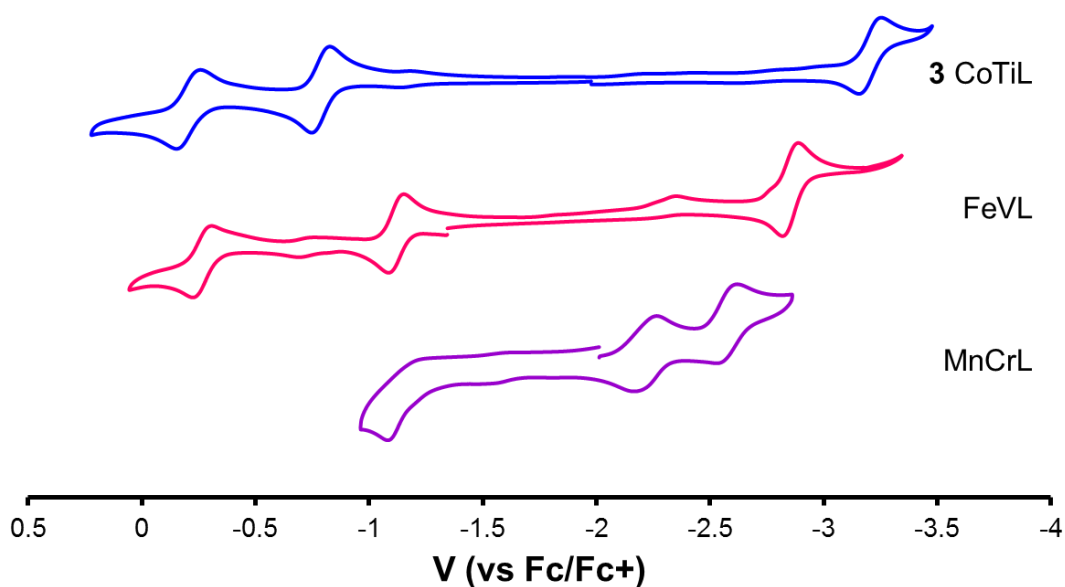


**Figure 3.4** Cyclic voltammograms of neutral d<sup>10</sup> complexes, CoTiL, FeVL and MnCrL in THF with 0.4 M or 0.1 M [<sup>n</sup>Bu<sub>4</sub>N]PF<sub>6</sub> electrolyte with a scan rate of 50 mV/s for CoTiL, 10 mV/s for FeVL and 250 mV/s for MnCrL.

The CVs of d<sup>9</sup> **2** and d<sup>11</sup> **4** also support the favorability of a 10 d-electron core shown by the mild reduction and oxidation potentials, respectively, which allow for the d<sup>10</sup> core to be attained by these complexes. The d<sup>9</sup> FeTiL **2** has the mildest reduction potential (-2.09 V) across the MCrL, MVL and MTiL heterobimetallic complexes with L. The

<sup>a</sup> Due to the irreversible nature of the MnCrL oxidation, the separation was determined from the E<sub>pa</sub> of the oxidation and the E<sub>1/2</sub> of the first reduction.

oxidation potential for **4** is also the mildest in the MCrL, MVL and MTiL series at  $-1.90$  V, suggesting that the closed shell Ni(0)/Ti(IV) core is a very stable complex.

### 3.3.4 EPR Spectroscopy

The heterobimetallic systems with half-integer spins were studied by X-band EPR spectroscopy, including **2**, **3<sup>ox</sup>**, and **4**. The EPR spectra provide insight into the location of the unpaired spin based on the observed hyperfine and superhyperfine interactions. Complex **2** is a doublet with 9 d-electrons and its EPR spectrum in toluene at 20.0 K shows an axial signal (Figure 3.5). The approximate g-values are  $g_x = g_y = 2.04$  and  $g_z = 2.25$ , which is consistent with the unpaired spin located at Fe. A previously reported  $S = 1/2$   $[\text{N}_2\text{FeAIL}]^-$  complex has similar g-values ( $g_{\text{ave}} = 2.09$ ) and is consistent with the unpaired spin located at Fe.<sup>52</sup> The observed superhyperfine coupling in **2** has a six-line pattern that is consistent with coupling to three  $I = 1/2$   $^{31}\text{P}$  nuclei. Superhyperfine interactions from the three phosphines on  $g_x$  and  $g_y$  suggest that the unpaired electron lies in an Fe based  $d(x^2 - y^2)$  or  $d(xy)$  orbitals.

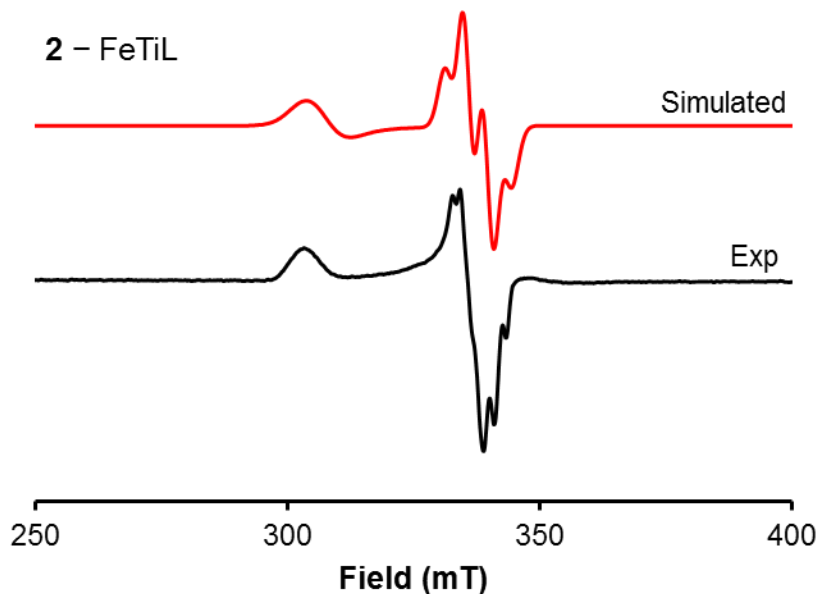


**Figure 3.5** X-band EPR spectrum ( $dX''/dB$ ) of **2** (black) in frozen toluene (20.0 K, frequency = 9.64 GHz, modulation to 10G and power = 200  $\mu\text{W}$ ). The simulation shown in red with simulation parameters:  $g_{\text{ave}} = 2.11$ ,  $g = (2.25, 2.04, 2.04)$ ,  $W = (45, 18, 20)$  G,  $A(3 I = 1/2) = (0, 90, 85) \times 10^{-4} \text{ cm}^{-1}$ .

Complex **3<sup>ox</sup>** is an isoelectronic  $d^9$  complex with **2**, and also has a doublet ground state. The EPR spectrum exhibits a rhombic signal at 25 K in THF (Figure 3.6) with approximate  $g$ -values of  $g_x = 2.06$ ,  $g_y = 2.11$ , and  $g_z = 2.31$ . The hyperfine coupling present in the spectrum exhibits an approximate eight-line pattern that would be consistent with splitting with a  $^{59}\text{Co}$   $I = 7/2$  nucleus. The unpaired spin located on the cobalt suggests that the complex is in a formal Co(0)/Ti(IV) oxidation state.

The EPR spectrum of **4** shows a doublet ground spin state for the  $d^{11}$  species at 24 K (Figure 3.7). While the major isotopes of both Ni ( $^{58}\text{Ni}$  68.1 %,  $^{60}\text{Ni}$  26.2 %) and Ti ( $^{48}\text{Ti}$  73.7 %) have a nuclear spin  $I = 0$ , the complicated superhyperfine splitting observed in **4** can be attributed to the N donors around Ti. If the three equivalent amide donors were the only interactions contributing to the superhyperfine coupling, a seven-line pattern is expected. However, more than seven lines are observed in the EPR spectrum of **4**, suggesting that the apical amine donor contributes to the superhyperfine interactions as well. These superhyperfine interactions are consistent with the unpaired spin located on Ti, and a formal Ti(III) oxidation state.

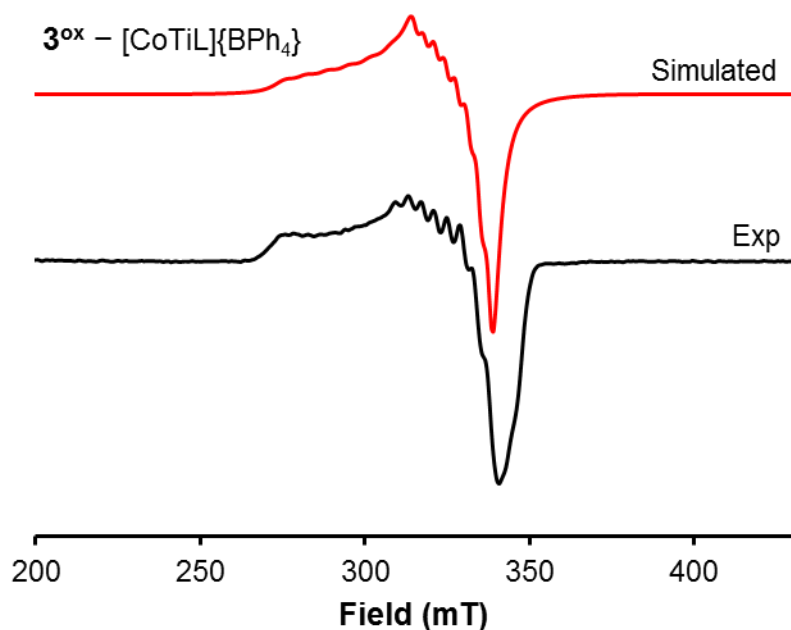
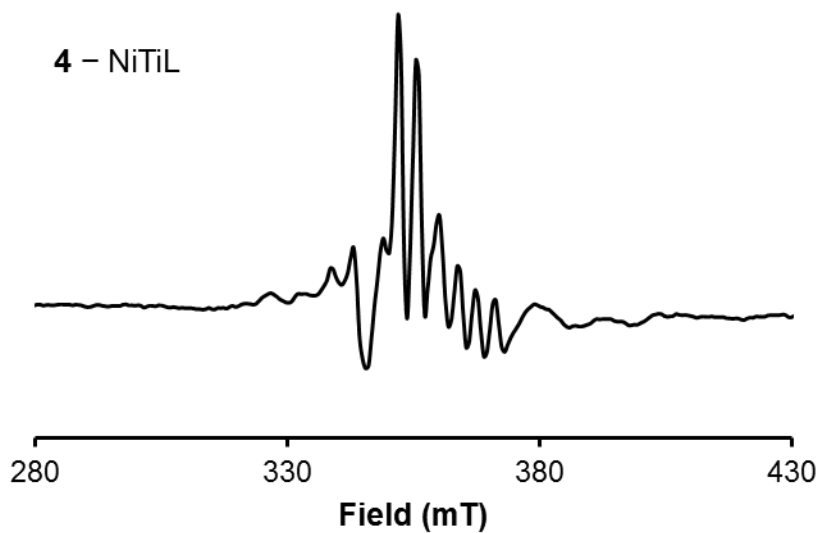


**Figure 3.6** X-band EPR spectrum ( $dX''/dB$ ) of **3<sup>ox</sup>** (black) in frozen THF (25.0 K, frequency = 9.64 GHz, modulation to 10G and power = 200  $\mu$ W). The simulation shown in red with simulation parameters:  $g_{ave} = 2.16$ ,  $g = (2.06, 2.11, 2.31)$ ,  $W = (110, 60, 120)$  G and  $A(I = 7/2) = (0, 32, 70) \times 10^{-4} \text{ cm}^{-1}$ .



e

**Figure 3.7** X-band EPR spectrum ( $dX''/dB$ ) of **4** (black) in frozen toluene (24.0 K, frequency = 9.64 GHz, modulation to 10G and power = 200  $\mu$ W).

### 3.3.5 Mössbauer Spectroscopy

To gain insights into the Fe oxidation states in the TiFeL complexes, zero-field  $^{57}\text{Fe}$  Mössbauer data was collected on powder samples of **2** and **2<sup>red</sup>** at 80 K as shown in Figures 3.8 and 3.9. Both spectra were fit with two contributing components, the bimetallic and an impurity. The impurities are suspected to be similar to those seen in attempts to obtain Mössbauer spectra on FeVL complexes, suggesting that a similar alternative synthesis for FeTiL complexes can be used to obtain pure material.<sup>19</sup> The isomer shifts for both complexes are similar at  $\delta = 0.35$  and  $0.31$  mm/s for **2** and **2<sup>red</sup>** respectively, suggesting that the oxidation state of the iron is similar in both complexes. Previous neutral Fe heterobimetallics FeVL<sup>19</sup> and FeCrL<sup>10</sup> both have a lower isomer shift of  $0.25$  mm/s, which suggests that the Fe center in **2** is more similar to the Fe in  $[\text{N}_2\text{FeAlL}]^-$  which has an Fe(-1) center with an isomer shift of  $0.38$  mm/s.<sup>52</sup> This supports the assignment of Fe(-1)/Ti(IV) formal oxidation states for **2**, and a strong dative interaction between the  $d^9$  Fe and  $d^0$  Ti. The isomer shift of the one electron reduced complex, **2<sup>red</sup>**, is relatively unchanged, indicating that the reduction occurs at titanium to generate an Fe(-1)/Ti(III) complex. The addition of the electron to titanium creates the possibility of a covalent interaction between the Fe and Ti centers.

The large difference in the quadrupole splitting of these two FeTi complexes offer a unique contrast not previously observed in isostructural iron bimetallics. Complex **2** has a relatively low quadrupole splitting of  $2.64$  mm/s when compared with other neutral FeML complexes (Table 3.3) that have multiple bonding and a quadrupole splitting above  $4$  mm/s. This low quadrupole splitting can be attributed to the lack of a covalent interaction between the Fe and Ti, where only a dative interaction is present. However, when **2** is reduced to **2<sup>red</sup>**, the quadrupole splitting increases to  $4.35$  mm/s, which is consistent with the larger quadrupole splitting seen in other multiply bonded Fe heterobimetallics. The contrast in these quadrupole splitting values in complexes with FSR values  $\ll 1$  suggest that Mössbauer spectroscopy can be a useful tool in describing the type of strong, covalent bonding between two metals, where  $\Delta E_Q$  values greater than  $4$  mm/s indicate the presence of a strong, covalent interaction with multiple bonding and those less than  $4$  mm/s indicate dative bonding Fe-M interactions. The Mössbauer parameters for **2<sup>ox</sup>** would be useful to

support the theory that Mössbauer can help describe bonding interactions if the Fe(0)/Ti(IV) are predicted correctly. Complex  $2^{ox}$  should have a  $\Delta E_Q$  less than 4 mm/s, similar to **2**, with an isomer shift close to 0.25 mm/s, similar to other Fe(0) heterobimetallics in this ligand system. However, an apical ligand on Fe, such as the acetonitrile in  $2^{ox}$  may also contribute to a lower quadrupole splitting even with covalent bonding, as is seen in Thomas' triply bonded Fe–V complexes that have an apical halide or phosphine donor.<sup>11</sup>

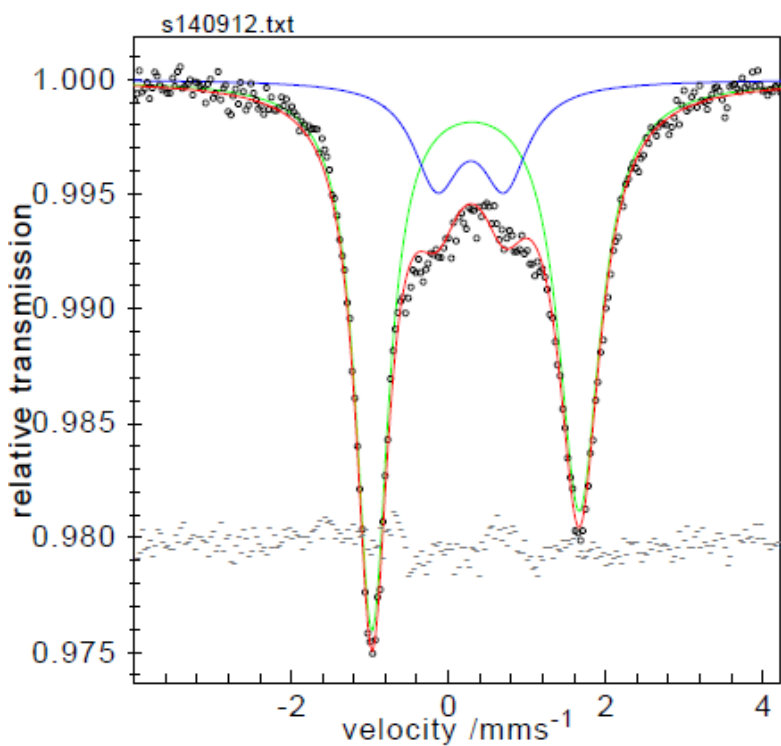


**Figure 3.8** Zero-field Mössbauer spectrum of **2** at 80 K. The spectrum was fit with the following parameters: for **2** (green, 79.5%),  $\delta = 0.35$  and  $\Delta E_Q = 2.64$  mm/s and for an impurity (blue, 20.5%),  $\delta = 0.28$  and  $\Delta E_Q = 0.86$  mm/s.



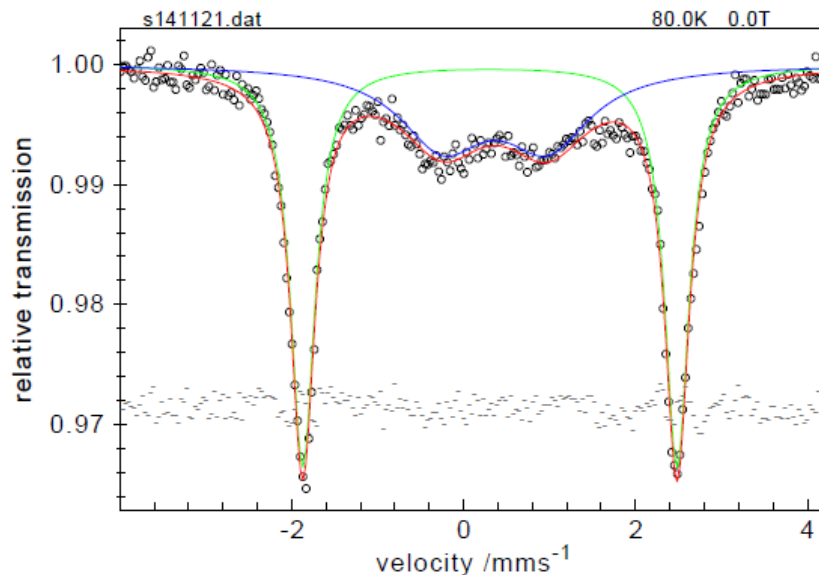


**Figure 3.9** Zero-field Mössbauer spectrum of  $2^{\text{red}}$  at 80 K. The spectrum was fit with the following parameters: for  $2^{\text{red}}$  (green, 61%),  $\delta = 0.31$  and  $\Delta E_Q = 4.35$  mm/s and for an impurity (blue, 39%),  $\delta = 0.37$  and  $\Delta E_Q = 1.22$  mm/s.

**Table 3.3** Mössbauer parameters for Fe heterobimetallics in L, as well as other multiply bonded Fe heterobimetallics.

Complex	$\delta$ (mm s <sup>-1</sup> )	$\Delta E_Q$ (mm s <sup>-1</sup> )	r	d count	Ref
[FeTiL] <sup>-</sup>	0.31	4.35		10	This work
FeTiL	0.35	2.64	0.83	9	This work
FeVL	0.25	5.97	0.79	10	19
[FeVL] <sup>+</sup>	0.25	4.04	0.84	9	19
[FeCrL] <sup>+</sup>	0.18	5.86	0.84	10	28
FeCrL	0.25	5.92	0.83	11	10
[FeCrL] <sup>-</sup>	0.29	5.2	0.84	12	10
N <sub>2</sub> FeAIL	0.54	0.91	1.11	8	52
[N <sub>2</sub> FeAIL] <sup>-</sup>	0.38	1.24	1.02	9	52
V( <sup>i</sup> PrNPPH <sub>2</sub> ) <sub>3</sub> FeBr	0.33	2.01	0.86	9	11
V( <sup>i</sup> PrNPPH <sub>2</sub> ) <sub>3</sub> Fe(PMe <sub>3</sub> )	0.19	1.85	0.86	10	11

### 3.3.6 Discussion

The early/late transition metal pairings in the MTiL family present two challenges that are exaggerated due to the location of the metals on the periodic table. The use of the less stable Ti(III) redox state in metalloligand TiL over Ti(IV) makes the assignment of oxidation states ambiguous for the bimetallics based on their synthesis. The uncertainty of the oxidation states in addition to the large d-orbital energy mismatch in these heterobimetallics complicates the bonding pictures between these metals, as the distinction between polarized covalent bonds and strong dative interactions becomes blurred. The oxidation state of Ti becomes crucial in the bonding description because a covalent bond must have d-electron contributions from both metals, and  $d^0$  Ti(IV) does not satisfy this requirement. Therefore, it is crucial to assign oxidation states in these bimetallics in order to have an accurate understanding of the bonding interactions that occur between the metals. Changes in oxidation state can be observed in changes in metal-ligand bond lengths, but either minor structural changes or the addition of a coordinating solvent molecule has left structural differences unhelpful in oxidation state assignment, leaving EPR and Mössbauer spectroscopies to provide the most insight into oxidation states.

Complex **4** has a  $[\text{NiTi}]^{3+}$  core, which provides an intuitive oxidation state assignment of Ni(0)Ti(III). This assignment is confirmed in the EPR spectrum of **4** in which the N superfine interactions indicate an unpaired electron on Ti. The FSR close to 1 for **4** suggests that the large energy mismatch between Ni and Ti results in only a single dative interaction similar to previously reported NiML complexes.<sup>19,20</sup> The CV of **4** has a mild oxidation event at  $-1.9$  V, which is assigned as a  $\text{Ti}^{\text{III/IV}}$  couple. The closed shell Ni(0)Ti(IV) complex **4<sup>ox</sup>** (FSR = 0.88) demonstrates how multiple dative interactions can result in similarly short M–M bonds as their covalent counterparts.

Complexes **2** and **3** present a greater challenge to assign oxidations for each metal due to the relatively more common reduced oxidation states for Fe and Co, Fe(–I) and Co(–I). Complex **2** can be either Fe(0)Ti(III) or Fe(–I)Ti(IV). The  $d^9$  core of **2** allows EPR spectroscopy to identify the location of the unpaired electron, thus providing an oxidation state assignment. The EPR spectrum of **2** attributes the unpaired spin to Fe, thus indicating a  $d^9$ , Fe(–I) center. The assignment of Fe(–I) for **2** suggests that the Ti transfers an electron

to the Fe upon the second metalation, providing a strong, multiple dative bond between Ti and Fe. The dative interaction is thought to be the influence on the more normal quadrupole splitting ( $\Delta E_Q = 2.64$  mm/s) in the Mössbauer spectrum for **2** as opposed to the larger quadrupole splitting ( $\Delta E_Q = 4.35$  mm/s) observed for **2<sup>red</sup>**. The oxidation states for **2<sup>red</sup>** can be thought of as Fe(-I)Ti(III), with the d-electron from Ti(III) contributing to a covalent interaction in the Fe-Ti bond, reflected in the larger quadrupole splitting. The oxidation states of **2<sup>ox</sup>** are assigned as Fe(0)Ti(IV), and a change in isomer shift in the Mössbauer spectrum would confirm this assignment.

EPR spectroscopy has also been helpful to assign the oxidation states for **3<sup>ox</sup>** as Co(0)Ti(IV). The hyperfine coupling in the EPR spectrum suggests a Co based spin for **3<sup>ox</sup>**, resulting in the assignment of Co(0). However, a lack of spectroscopic information on the diamagnetic complex **3** maintains its ambiguous oxidation state assignments of either Co(0)Ti(III) or Co(-I)Ti(IV). In order to definitively assign the oxidation states, X-ray absorption spectroscopy (XAS) would be needed, and XAS spectroscopy would also provide an excellent complement for the other complexes in the MTiL family.

### 3.4 Conclusion

The seven isolated [MTiL]<sup>-/0/+</sup> complexes expand the library of early-late heterobimetallic complexes in the double-decker ligand L. The neutral complexes share an ambiguous oxidation state assignment for the metals, which EPR and Mössbauer spectroscopies have been able to shed some light. Preliminary oxidation state assignment for the FeTiL complexes are Fe(-I)Ti(IV) for **2**, Fe(0)Ti(IV) for **2<sup>ox</sup>** and Fe(-I)Ti(III) for **2<sup>red</sup>**. However, in order to definitively assign the oxidation states and understand the bonding interactions, X-ray absorption spectroscopy would be needed. The NiTiL neutral complex **4** lends insight into how the oxidation of Ti(III) to Ti(IV) can drastically shorten the Ni-Ti bond by creating a very strong dative interaction, which can be seen throughout the various MTiL complexes in this series.

The lesson learned from the MTiL family of complexes is the flexibility of the M-Ti interaction, which can have polarized covalent interactions in addition to strong dative interactions. Unlike the unreactive, multiply bonded heterobimetallics in the MVL

and MCrL, this flexible M–Ti interaction can prove to be a more reactive complex that can be used for reactivity studies in the future.

### 3.5 Experimental Section

#### 3.5.1 General Considerations

Unless otherwise stated, all manipulations were performed under an inert atmosphere in a glovebox or using standard Schlenk techniques. Standard solvents were deoxygenated by sparging with inert gas and dried by passing through activated alumina columns of a SG Water solvent purification system. Deuterated solvents were purchased from Cambridge Isotope Laboratories, Inc. or Sigma Aldrich, degassed via freeze-pump-thaw cycles, and stored over activated 4 Å molecular sieves. Elemental analyses were performed by Robertson Microlit Laboratories, Inc. (Ledgewood, NJ). The ligand N(*o*-(NHCH<sub>2</sub>P<sup>I</sup>Pr<sub>2</sub>)C<sub>6</sub>H<sub>4</sub>)<sub>3</sub> (abbreviated as H<sub>3</sub>L) was synthesized according to literature procedures.<sup>12</sup> Monometallic TiL and complex **3** were previously published.<sup>87</sup>

#### 3.5.2 Physical Methods

<sup>1</sup>H NMR spectra were recorded on a Bruker 400 or 500 MHz spectrometer at rt unless otherwise noted. All <sup>1</sup>H and <sup>13</sup>C NMR spectra are referenced to the internal solvent residual. Solution magnetic moments were determined using Evans' method.<sup>94,101</sup> Cyclic voltammetry was performed using a CH instruments 600 electrochemical analyzer. The one-cell setup used a glassy carbon working electrode, Pt wire counter electrode, and Ag/AgNO<sub>3</sub> reference electrode in CH<sub>3</sub>CN. Analyte solutions consisted of 0.4 M [<sup>n</sup>Bu<sub>4</sub>N][PF<sub>6</sub>] and the voltammograms were referenced internally to the Fc<sup>0/+</sup> redox couple. Perpendicular mode X-band EPR spectra were recorded at 20 – 25 K with a Bruker ESP 300 spectrometer equipped with an Oxford ESR 910 liquid helium cryostat and an Oxford temperature controller. X-band EPR spectra were simulated using the program ESIM written by Eckhard Bill. Mössbauer data were recorded on an alternating constant acceleration spectrometer. The minimum experimental line width was 0.24 mm s<sup>-1</sup> (full width at half-height). The sample temperature was maintained constant at 80 K in an Oxford Instruments Variox or an Oxford Instruments Mössbauer-Spectromag 2000

cryostat, which is a split-pair superconducting magnet system for applied fields (up to 8 T). The field at the sample is oriented perpendicular to the  $\gamma$ -beam. The  $^{57}\text{Co}/\text{Rh}$  source (1.8 GBq) was positioned at rt inside the gap of the magnet system at a zero-field position. Isomer shifts are quoted relative to iron metal at 300 K.

### 3.5.3 Synthetic Procedures

#### *Synthesis of **2**, $\text{FeTi}(\text{N}(\text{o}-(\text{NCH}_2\text{P}^i\text{Pr}_2)\text{C}_6\text{H}_4)_3)$ .*

A solution of TiL (0.221 g, 0.305 mmol) in THF (2 mL) was added to a stirring slurry of  $\text{FeBr}_2$  (0.0648 g, 0.300 mmol) in THF (6 mL). After 15 min,  $\text{KC}_8$  (0.0825 g, 0.611 mmol) was added to the dark yellow-brown solution. The reaction was stirred for an additional 4 h, prior to filtering through Celite. The volatiles were removed *in vacuo*, and the resulting brown powder was reconstituted in benzene and filtered through a Celite pad before being dried *in vacuo* to give a brown powder (0.221 g, 94 % yield). Single crystals were grown by vapor diffusion of pentane into a concentrated toluene solution.  $^1\text{H}$  NMR (ppm,  $\text{C}_6\text{D}_6$ , 400 MHz): 31.4, 16.2, 8.9, 5.5, 4.6, 4.1, 2.4, 1.2, 0.9, -2.8, -3.6, -6.8. Anal. Calcd. for **2**  $\text{C}_{39}\text{H}_{60}\text{N}_4\text{P}_3\text{TiFe}$ : 59.93 C, 7.74 H, 7.17 N. Found: 59.51 C, 7.29 H, 6.74 N.

#### *Synthesis of **2**<sup>ox</sup> $[\text{FeTiL}]\{\text{BPh}_4\}, [\text{FeTi}(\text{N}(\text{o}-(\text{NCH}_2\text{P}^i\text{Pr}_2)\text{C}_6\text{H}_4)_3)]\{\text{BPh}_4\}$ .*

A slurry of  $\text{FcBPh}_4$  (0.0718 g, 0.142 mmol) in acetonitrile (4 mL) was added to a stirring slurry of **2** (0.111 g, 0.142 mmol) in acetonitrile (4 mL). The reaction mixture was stirred overnight, and the volatiles were removed *in vacuo*. The remaining solid was washed with 5 x 5 mL diethyl ether, 3 x 5 mL toluene, 3 x 3 mL hexane to obtain a green powder (0.0682 g, 44 % yield). Single crystals of  $[\text{FeTiL}]\{\text{BPh}_4\}$  were grown by vapor diffusion of pentane into a concentrated THF solution.  $^1\text{H}$  NMR (ppm,  $\text{THF-}d_8$ , 500 MHz): 38.4, 35.0, 25.8, 21.9, 15.6, 7.2, 6.7, 0.9, -5.2, -8.9, -20.4, -51.1.

*Synthesis of 2<sup>red</sup> K(crypt-222)[FeTiL], K(C<sub>18</sub>H<sub>36</sub>N<sub>2</sub>O<sub>6</sub>)[FeTi(N(o-(NCH<sub>2</sub>P<sup>i</sup>Pr<sub>2</sub>)C<sub>6</sub>H<sub>4</sub>)<sub>3</sub>)]*

A solution of **2** (0.0727 g, 0.093 mmol) in THF (8 mL) was added to a vial containing K<sub>2</sub>C<sub>8</sub> (0.0127 g, 0.094 mmol). A solution of crypt-222 (0.0330 g, 0.088 mmol) in THF (4 mL) was added to the stirring reaction mixture, and was allowed to stir for 16 h. The resulting brown solution was filtered through a celite plug to remove graphite and the volatiles were removed *in vacuo*. The resulting brown powder was washed with 5 x 5 mL portions of benzene and then dried to obtain a brown powder (0.0694, 62 % yield). <sup>1</sup>H NMR (ppm, THF-d<sub>8</sub>, 500 MHz): 6.54 (*t*, *J* = 7.2 Hz, 3H), 6.34 (*d*, *J* = 7.2 Hz, 3H), 6.06 (*d*, *J* = 7.6 Hz, 3H), 5.67 (*t*, *J* = 7.1 Hz, 3H), 5.46 (*d*, *J* = 10.0 Hz, 3H), 4.72 (*d*, *J* = 9.3, 3H), 3.43 (*br*, crypt), 2.86 (*s*, 3H), 2.64 (*s*, 3H), 2.44 (*br*, crypt), 1.46 (*s*, 9H), 1.13 (*s*, 9H), 1.03 (*s*, 9H), 0.27 (*s*, 9H). <sup>31</sup>P NMR (ppm, THF-d<sub>8</sub>, 200 MHz): 41.5.

*Synthesis of 4, NiTi(N(o-(NCH<sub>2</sub>P<sup>i</sup>Pr<sub>2</sub>)C<sub>6</sub>H<sub>4</sub>)<sub>3</sub>).*

A solution of TiL (0.248 g, 0.343 mmol) in THF (8 mL) was added to solid bis(1,5-cyclooctadiene)nickel(0) (0.0947 g, 0.344 mmol). The reaction was stirred for 5 h, and then dried *in vacuo*. The crude residue was washed with cold pentane, then extracted into toluene, and filtered through a Celite pad. The resulting filtrate was dried *in vacuo* to afford a brown powder (0.203 g, 76% yield). Single crystals were grown through the slow diffusion of pentane into a concentrated benzene solution. <sup>1</sup>H NMR (ppm, C<sub>6</sub>D<sub>6</sub>, 400 MHz): 18.1, 9.1, 8.3, 7.4, 4.9, 3.2, 1.6, 1.2, 1.0, 0.9, -0.3, -1.4. Anal. Calcd. for **4** C<sub>39</sub>H<sub>60</sub>N<sub>4</sub>P<sub>3</sub>TiNi: 59.72 C, 7.71 H, 7.14 N. Found: 60.03 C, 7.61 H, 6.07 N.

*Synthesis of 4<sup>ox</sup>, [NiTi(N(o-(NCH<sub>2</sub>P<sup>i</sup>Pr<sub>2</sub>)C<sub>6</sub>H<sub>4</sub>)<sub>3</sub>)] [BPh<sub>4</sub>].*

A slurry of FcBPh<sub>4</sub> (0.0305 g, 0.0603 mmol) in acetonitrile (3 mL) was added to a stirring slurry of **4** (0.0478 g, 0.0610 mmol) in acetonitrile (3 mL). The reaction mixture was stirred overnight, and the volatiles were removed *in vacuo*. The remaining solid was washed with 5 x 5 mL diethyl ether, 3 x 5 mL toluene, 3 x 3 mL hexane to obtain a red powder (0.0216 g, 32 % yield). Single crystals of [NiTiL]{BPh<sub>4</sub>} were grown by the slow diffusion of pentane into a concentrated THF solution. <sup>1</sup>H NMR (ppm, THF-d<sub>8</sub>, 400 MHz): 7.27 (*s*,

BPh<sub>4</sub>), 7.12 (*d*, *J* = 7.4 Hz, 3H), 7.07 (*t*, *J* = 7.4 Hz, 3H), 6.84 (*t*, *J* = 7.1 Hz, BPh<sub>4</sub>), 6.69 (*t*, *J* = 7.0 Hz, BPh<sub>4</sub>), 6.58 (*t*, *J* = 7.5 Hz, 3H), 6.32 (*d*, *J* = 7.7 Hz, 3H), 4.88 (*s*, 3H), 4.35 (*s*, 3H), 2.83 (*s*, 6H), 1.39 (*br s*, 24H), 1.06 (*br s*, 12H). <sup>31</sup>P NMR (ppm, THF-*d*<sub>8</sub>, 162 MHz): -5.1.

#### 3.5.4 X-ray Crystallography

A red plate of **2**, an orange plate of **4**, a green block of **2<sup>ox</sup>**, and a red needle **4<sup>ox</sup>** were placed on the tip of a 0.1 mm diameter glass capillary and mounted on a Bruker APEX II CCD diffractometer or a Bruker Photon 100 CMOS diffractometer for data collection at 173(2) K or 123(2) K. The data collection was carried out using Mo K $\alpha$  radiation (graphite monochromator) or Cu K $\alpha$  radiation (normal parabolic mirrors).<sup>104</sup> The data intensity was corrected for absorption and decay (SADABS). Final cell constants were obtained from least-squares fits of all measured reflections and the structure was solved using SHELXS-08 and refined using SHELXL-08.<sup>105</sup> A direct-methods solution was calculated which provided most non-hydrogen atoms from the E-map. Full-matrix least-squares/difference Fourier cycles were performed to locate the remaining non-hydrogen atoms and all non-hydrogen atoms were refined with anisotropic displacement parameters with the exception of a disordered THF molecule in **2** and **4<sup>ox</sup>** which were refined isotropically. Hydrogen atoms were placed in ideal positions and refined as riding atoms with relative isotropic displacement parameters. Two disordered isopropyl groups were modeled over two positions using SAME restraints in **2<sup>ox</sup>**. Crystallographic details are summarized in Table 3.4.

**Table 3.4** Crystallographic details for **2**, **2<sup>ox</sup>**, **4** and **4<sup>ox</sup>**.

	<b>2</b> FeTiL	<b>2<sup>ox</sup></b> [CH <sub>3</sub> CNFeTiL]BPh <sub>4</sub>	<b>4</b> NiTiL	<b>4<sup>ox</sup></b> [NiTiL]BPh <sub>4</sub>
chemical formula	C <sub>39</sub> H <sub>60</sub> N <sub>4</sub> P <sub>3</sub> FeTi, 0.5(C <sub>4</sub> H <sub>8</sub> O)	C <sub>41</sub> H <sub>63</sub> N <sub>5</sub> P <sub>3</sub> FeTi, C <sub>4</sub> H <sub>8</sub> O	2(C <sub>39</sub> H <sub>60</sub> N <sub>4</sub> P <sub>3</sub> NiTi), 2(C <sub>4</sub> H <sub>8</sub> O)	C <sub>39</sub> H <sub>60</sub> N <sub>4</sub> P <sub>3</sub> NiTi, 2(C <sub>4</sub> H <sub>8</sub> O)
fw	817.62	1213.93	1713.06	1247.84
crystal system	triclinic	monoclinic	triclinic	monoclinic
space group	P-1	P2 <sub>1</sub> /n	P-1	P2 <sub>1</sub> /n
a (Å)	12.3500(4)	19.0003(10)	12.5471(3)	17.4548(15)
b (Å)	19.4587(6)	13.5808(7)	14.0969(4)	14.3797(12)
c (Å)	19.7453(6)	25.8558(14)	24.6228(7)	26.547(2)
α (deg)	113.0340(14)	90	91.7870(10)	90
β (deg)	95.5470(14)	105.0700(10)	98.7420(10)	101.0620(10)
γ (deg)	101.1830(15)	90	94.6870(10)	90
V (Å <sup>3</sup> )	4204.9(2)	6442.4(6)	4286.0(2)	6539.3(10)
Z	4	4	2	4
D <sub>calcd</sub> (g cm <sup>-3</sup> )	1.292	1.252	1.327	1.267
λ (Å), μ (mm <sup>-1</sup> )	1.54178, 5.718	0.71073, 0.47	1.54178, 3.472	0.71073, 0.531
T (K)	123(2)	173(2)	123(2)	173(2)
θ range (deg)	2.48 to 74.82	1.194 to 27.484	3.148 to 75.137	1.563 to 27.493
reflns collected	63960	72935	35958	62709
unique reflns	13163	11477	12704	9169
data/restraint/params	17020/0/909	14700/6/803	17030/0/979	14912/0/710
R1, wR2 (I > 2σ(I))	0.0523, 0.1355	0.0381, 0.0550	0.0566, 0.1324	0.0703, 0.1199



## Chapter 4

### Bimetallic cobalt-dinitrogen complexes: impact of the supporting metal on N<sub>2</sub> activation

Reproduced with permission from: Clouston, L. J.; Bernales, V.; Carlson, R. K.; Gagliardi, L.; Lu, C. C., Bimetallic Cobalt–Dinitrogen Complexes: Impact of the Supporting Metal on N<sub>2</sub> Activation. *Inorg. Chem.* **2015**, *54* (19), 9263-9270. Copyright 2015 American Chemical Society.

## 4.1 Overview

Expanding a family of cobalt bimetallic complexes, we report the synthesis of the Ti(III) metalloligand,  $\text{Ti}[\text{N}(o\text{-}(\text{NCH}_2\text{P}(\text{iPr})_2)\text{C}_6\text{H}_4)_3]$  (abbreviated as TiL), and three heterobimetallics that pair cobalt with an early transition metal ion:  $\text{CoTiL}$  (**1**),  $\text{K}(\text{crypt-222})[(\text{N}_2)\text{CoVL}]$  (**2**), and  $\text{K}(\text{crypt-222})[(\text{N}_2)\text{CoCrL}]$  (**3**). The latter two complexes, along with previously reported  $\text{K}(\text{crypt-222})[(\text{N}_2)\text{CoAlL}]$  and  $\text{K}(\text{crypt-222})[(\text{N}_2)\text{Co}_2\text{L}]$ , constitute an isostructural series of cobalt-dinitrogen bimetallics that bind dinitrogen in an end-on fashion, i.e.  $[(\text{N}_2)\text{CoML}]^-$ . The characterization of **1–3** includes cyclic voltammetry, X-ray crystallography, and infrared spectroscopy. The  $[\text{CoTiL}]^{0/-}$  reduction potential is extremely negative at  $-3.20$  V versus  $\text{Fc}^+/\text{Fc}$ . In the  $\text{CoML}$  series where M is a transition metal, the reduction potentials shift anodically as M is varied across the first-row period. Among the  $[(\text{N}_2)\text{CoML}]^-$  compounds, the dinitrogen ligand is weakly activated, as evidenced by N–N bond lengths between 1.110(8) and 1.135(4) Å, and by N–N stretching frequencies between 1971 and 1995  $\text{cm}^{-1}$ . Though changes in  $\nu_{\text{N}_2}$  are subtle, the extent of  $\text{N}_2$  activation decreases across the first-row period. A correlation is found between the  $[\text{CoML}]^{0/-}$  reduction potentials and  $\text{N}_2$  activation, where the more cathodic potentials correspond to lower N–N frequencies. Theoretical calculations of the  $[(\text{N}_2)\text{CoML}]^-$  complexes reveal important variations in the electronic structure and Co–M interactions, which depend on the exact nature of the supporting metal ion, M.

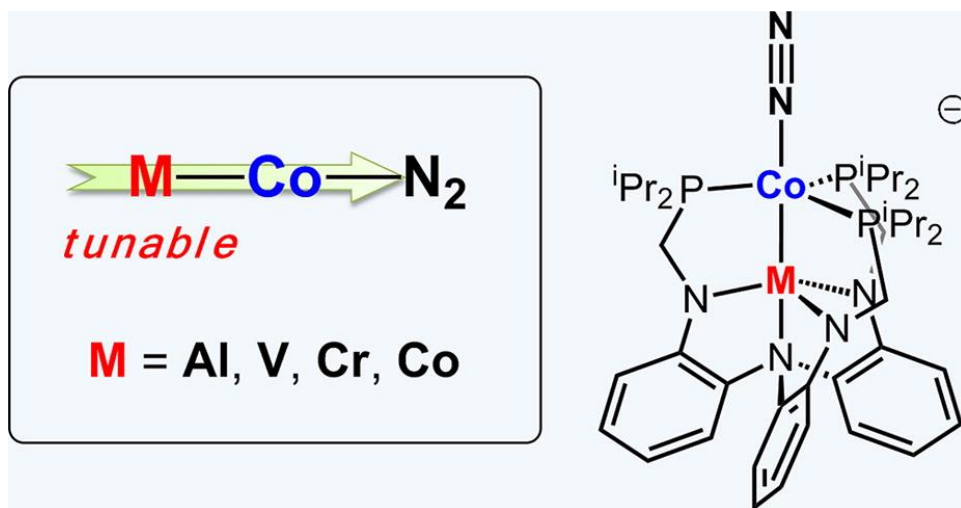


**Figure 4.1** Series of  $[(\text{N}_2)\text{CoML}]^-$  complexes isolated using ligand L (right).

## 4.2 Introduction

Cobalt is generally surpassed by iron as the choice first-row metal for N<sub>2</sub> activation. In synthetic systems where both cobalt-dinitrogen and iron-dinitrogen adducts are known, the cobalt counterparts typically activate N<sub>2</sub> more weakly.<sup>12,37,52,62,64,66,69,128-136</sup> This has been attributed to the energetically lower Co d orbitals being worse at  $\pi$ -back-bonding to the N<sub>2</sub> substrate.<sup>50</sup> Nonetheless, the N<sub>2</sub>-coordination chemistry at cobalt is substantial, as shown in Figure 4.2.<sup>16,58,62,64,73,76,128,130,132</sup> Included in these examples are the few exceptional cases where cobalt site(s) reduce N<sub>2</sub> by two or more electrons. The cobalt tri(phosphino)borate complex (Figure 4.2B) mediates an overall two-electron transformation of N<sub>2</sub> to the diazenido species, Co–N=NR.<sup>62</sup> Cobalt diketiminate complexes, when subjected to alkali metals, capture N<sub>2</sub> within a Co–N=N–Co linkage, representing a formal two-electron reduction of N<sub>2</sub> (Figure 4.2A).<sup>132</sup>

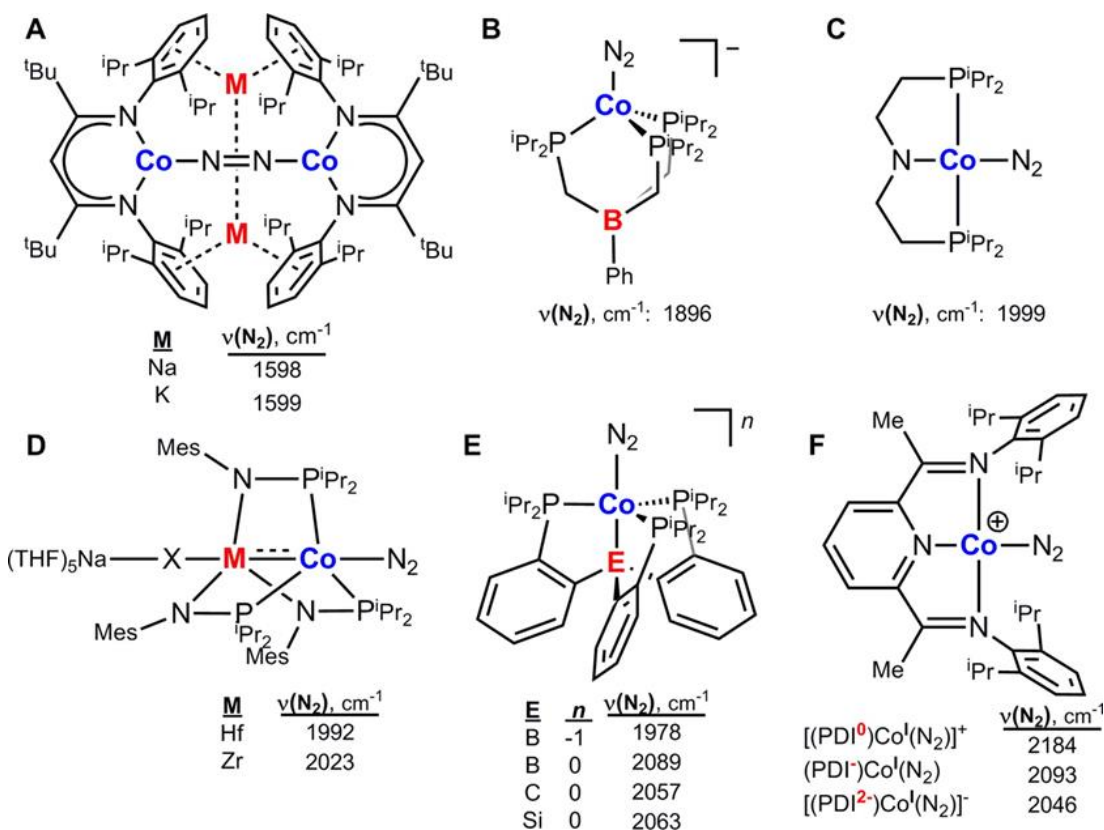


**Figure 4.2** Selected examples of cobalt-dinitrogen complexes from the literature that showcase N<sub>2</sub> activation and tuning of the metal countercation, ligand oxidation state, and ancillary element.

Of relevance, monocobalt and dicobalt complexes have been discovered to catalyze the silylation of  $N_2$  to two  $N(\text{SiMe}_3)_3$  molecules in a six-electron redox reaction.<sup>29,137</sup> The dicobalt system features a metal–metal interaction in the precatalyst. Using hemilabile interactions between a catalytic metal center and an ancillary main group ion is a powerful strategy in small-molecule activation.<sup>135,136</sup> An enlightening example is the iron-boratrane system that mediates the reduction of  $N_2$  to  $NH_3$  with seven turnovers at ambient temperature and pressure.<sup>66,69</sup> Recently, the cobalt-boratrane congener (Figure 4.2E) was shown to be competent in fixing  $N_2$  to  $NH_3$  with 2.4 turnovers.<sup>73</sup> The flexibility of the Co–B interaction was further reinforced as an important factor, as the cobalt complexes of the analogous C and Si ligands were essentially incompetent in the catalysis.

Also of relevance, the ZrCo heterobimetallic system (Figure 4.2D) harnesses early-late transition metal cooperativity to completely rupture strong C=O bonds in  $CO_2$  and benzophenone in a stoichiometric manner.<sup>138,139</sup> Cleavage of C=O bonds is inherent in the reactivity of a related TiCo complex, which reductively couples aryl ketones to alkenes.<sup>86</sup> Metal cooperativity also operates in triiron platforms that mediate the multielectron reduction and N=N cleavage of azobenzene.<sup>57</sup>

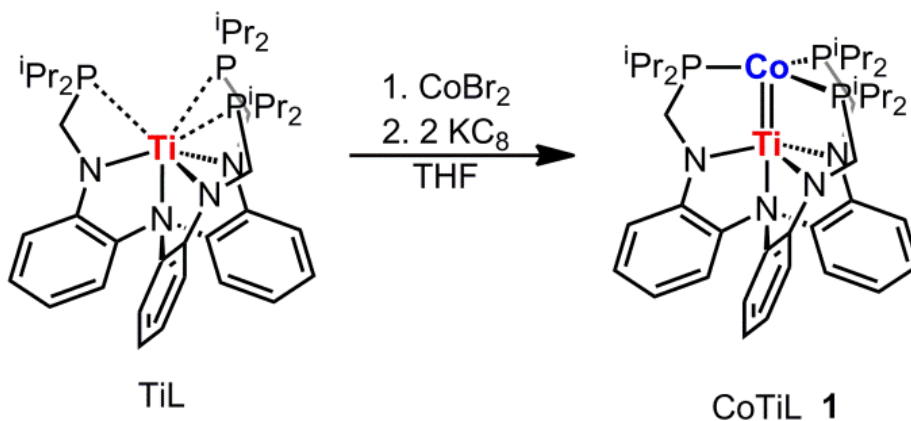
We have been targeting a family of CoM bimetallics to understand how an ancillary metal tunes the Co–M interaction and the overall properties of the bimetallic complex.<sup>12,19,20,52</sup> Reduction of the CoM bimetallics provided access to four cobalt-dinitrogen complexes, which are isostructural and showcase tunability of the supporting metal ion. Through synthesis, physical/spectroscopic characterization, and theoretical calculations, we unravel the impact of the ancillary metal on  $N_2$  activation in these cobalt bimetallics.

## 4.3 Results and Discussion

### 4.3.1 Synthesis and characterization of CoTiL (1)

The cobalt–titanium complex, CoTiL (**1**), is the latest addition to a growing family of isostructural cobalt bimetallics, where  $L = [N(o\text{-(NCH}_2\text{P}(i\text{Pr})_2)\text{C}_6\text{H}_4)_3]^{3-}$ . Previously, we reported CoVL,<sup>19</sup>(28) CoCrL,<sup>20</sup>(27) Co<sub>2</sub>L,<sup>29</sup>(22) and (N<sub>2</sub>)CoAIL,<sup>12</sup>(15) where the latter is

the only (CoM)<sup>3+</sup> example in this ligand scaffold, thus far, to bind N<sub>2</sub> in the apical pocket. Complex **1** was synthesized by mixing CoBr<sub>2</sub> and the metalloligand TiL, followed by reduction with 2 equiv of KC<sub>8</sub> (Scheme 4.1). As complex **1** is (d-d)<sup>10</sup> and diamagnetic, it was characterized by multinuclear NMR spectroscopy. A single <sup>31</sup>P signal is observed at 17.1 ppm, suggesting 3-fold symmetry. The <sup>1</sup>H NMR spectrum is consistent with a locked C<sub>3</sub> conformation, where the methylene protons in the ligand arms are diastereotopic, and the diisopropyl phosphine groups are split into two methine and four methyl peaks.



**Scheme 4.1** Synthesis of compound **1**.

The molecular structure of CoTiL contains a short Co–Ti bond distance of 2.1979(8) Å, which is significantly smaller than the sum of two metals’ single-bond radii at 2.48 Å (Figure 4.3, Table 4.1).<sup>27</sup> The formal shortness ratio (FSR), the quotient of the metal–metal bond length and the sum of the metals’ single-bond radii, is 0.89 for **1**. Of note, it is strikingly longer than the Co–Ti bond length of 2.02 Å in (PMe<sub>3</sub>)Co(*i*Pr<sub>2</sub>PNAr)<sub>2</sub>Ti(Cl),<sup>86</sup> where the FSR is 0.81 and was interpreted as a Co–Ti triple bond. It is, however, similar to the Co–M bond lengths in the isostructural CoCrL and CoVL compounds (2.14 and 2.12 Å, with FSR values of 0.92 and 0.89, respectively), which were interpreted as Co–M double bonds. By analogy, **1** likely has a Co–Ti double bond.

**Table 4.1** Geometrical parameters, including bond lengths (Å), formal shortness ratio (FSR), and angles (deg), for **1** – **3**, [(N<sub>2</sub>)Co<sub>2</sub>L]<sup>−</sup> and [(N<sub>2</sub>)CoAIL]<sup>−</sup>. N–N bond stretching frequencies (cm<sup>−1</sup>) and reduction potentials (V vs Fc<sup>+</sup>/Fc) are also listed.

	<b>1</b> CoTiL	<b>2<sup>b</sup></b> K(crypt-222) [(N <sub>2</sub> )CoVL]	<b>3<sup>b</sup></b> K(crypt-222) [(N <sub>2</sub> )CoCrL]	K(crypt-222) [(N <sub>2</sub> )Co <sub>2</sub> L]	K(crypt-222) [(N <sub>2</sub> )CoAIL]		
<b>Co–M (Å)</b>	2.1979(8)	2.6466(7)	2.6661(7)	2.5822(11)	2.5377(12)	2.6771(7)	2.507(2)
<b>FSR<sup>a</sup></b>	0.89	1.11	1.12	1.11	1.09	1.16	1.02
<b>Co–N (Å)</b>		1.796(3)	1.788(3)	1.792(5)	1.813(5)	1.770(4)	1.789(3)
<b>N–N (Å)</b>		1.130(4)	1.135(4)	1.135(6)	1.120(7)	1.114(4)	1.110(8)
	2.2444(11)	2.2024(9)	2.1859(10)	2.1907(15)	2.1988(14)	2.2505(10)	
<b>Co–P (Å)</b>	2.2553(11)	2.2049(A)	2.1968(10)	2.1918(14)	2.2057(14)	2.2515(10)	2.177(1)
	2.2704(11)	2.2121(10)	2.2094(10)	2.1965(14)	2.2188(15)	2.2651(11)	
	1.947(3)	1.952(3)	1.946(3)	1.953(4)	1.975(4)	1.929(3)	
<b>M–Neq (Å)</b>	1.954(3)	1.954(3)	1.949(3)	1.974(4)	1.975(5)	1.931(3)	1.898(3)
	1.955(3)	1.958(3)	1.957(3)	1.980(4)	1.979(4)	1.933(3)	
<b>M–Nap (Å)</b>	2.251(3)	2.212(2)	2.222(3)	2.202(4)	2.183(4)	2.135(3)	2.324(6)
<b>Co to P3-plane</b>	-0.128	0.407	0.428	0.312	0.357	0.383	0.375
<b>M to N3-plane</b>	0.298	0.356	0.343	0.34	0.328	0.249	0.426
	119.63(4)	109.29(4)	107.59(4)	116.36(6)	122.21(6)	124.02(4)	
<b>P–Co–P angle (°)</b>	118.16(4)	124.97(4)	121.18(4)	117.64(6)	113.74(6)	112.75(4)	117.10(2)
	121.25(4)	115.63(4)	120.04(4)	120.01(6)	116.31(6)	114.70(4)	
	117.50(13)	117.35(11)	116.39(12)	115.07(18)	118.3(2)	119.01(11)	
<b>Neq–M–Neq (°)</b>	116.68(13)	117.03(11)	118.89(12)	107.07(18)	128.26(19)	118.38(12)	115.11(8)
	118.93(13)	115.89(11)	115.65(12)	128.88(19)	105.13(19)	117.71(12)	
<b>Co–M–Nap (°)</b>	178.90(8)	179.03(7)	178.37(8)	179.06(11)	178.91(12)	178.97(8)	180
<b>v(N<sub>2</sub>) (cm<sup>−1</sup>)</b>		1971		1990		1994	1995
<b>[CoM]<sup>0/-</sup> redox potential (V)</b>	-3.20	-2.48		-2.32		-2.12	-0.95

<sup>a</sup> FSR = (M–V bond distance) / (sum of M and V single-bond radii).<sup>27</sup> See text.

<sup>b</sup> Two unique molecules per asymmetric unit.

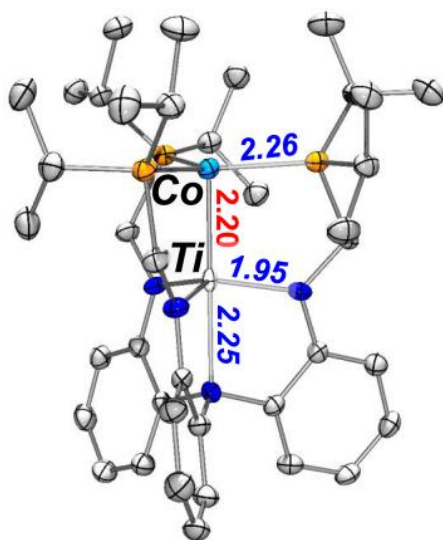


**Figure 4.3** Molecular structure of **1** shown at 50% thermal ellipsoid probability. Hydrogen atoms were omitted for clarity. Average bond lengths (Å) are shown.

Of note, the Co–P bond lengths in CoTiL are similar to those in CoVL, CoCrL, Co<sub>2</sub>L, and (N<sub>2</sub>)CoAIL, which all fall between 2.21 and 2.30 Å (Appendix Table A3.1). For the cobalt-transition metal complexes, the P–Co–P bond angles also adhere to a narrow range of 118–121°. Variation of the supporting metal from Ti to Cr in the amide-binding pocket, hence, has little impact on the ligation of the cobalt in the phosphine pocket. Only (N<sub>2</sub>)CoAIL shows a significant distortion from 3-fold symmetry with P–Co–P bond angles of 105, 112, and 132°. The distortion could arise from a Jahn–Teller distortion of a d<sup>9</sup> Co(0) center in 3-fold symmetry.

#### 4.3.2 Electrochemistry of CoML series

Multiple redox processes have been observed in the cyclic voltammograms (CVs) of the cobalt-transition metal complexes (Figure 4.4, Appendix Table A3.3). The CV of CoTiL (**1**) shows two reversible oxidations at –0.79 and –0.21 V versus Fc<sup>+</sup>/Fc. Under argon, a quasi-reversible reduction occurs at –3.20 V, which becomes fully irreversible under N<sub>2</sub>. Similar electrochemical behavior was observed for CoVL, CoCrL, and Co<sub>2</sub>L, in which the first reductive process is irreversible under N<sub>2</sub> but becomes more reversible under argon.<sup>19,20,29</sup> The behavior is consistent with a rapid chemical reaction, such as N<sub>2</sub> binding, following electron transfer. The (N<sub>2</sub>)CoAIL complex has a reversible oxidation

event at  $-1.18$  V, and a reversible reduction event under argon at  $-2.11$  V versus  $\text{Fc}^+/\text{Fc}$ , which has the same reduction potential as  $\text{Co}_2\text{L}$ . The reduction of  $(\text{N}_2)\text{CoAIL}$  under  $\text{N}_2$  is irreversible, and scan speed dependent, suggesting that a  $\text{N}_2$  binding equilibrium exists in the neutral state. For the ancillary transition metals, the  $[\text{CoML}]^{0/-}$  redox potentials become increasingly mild as the supporting metal is varied across the period, i.e. from early to late:  $\text{CoTiL} < \text{CoVL} < \text{CoCrL} < \text{Co}_2\text{L}$ .

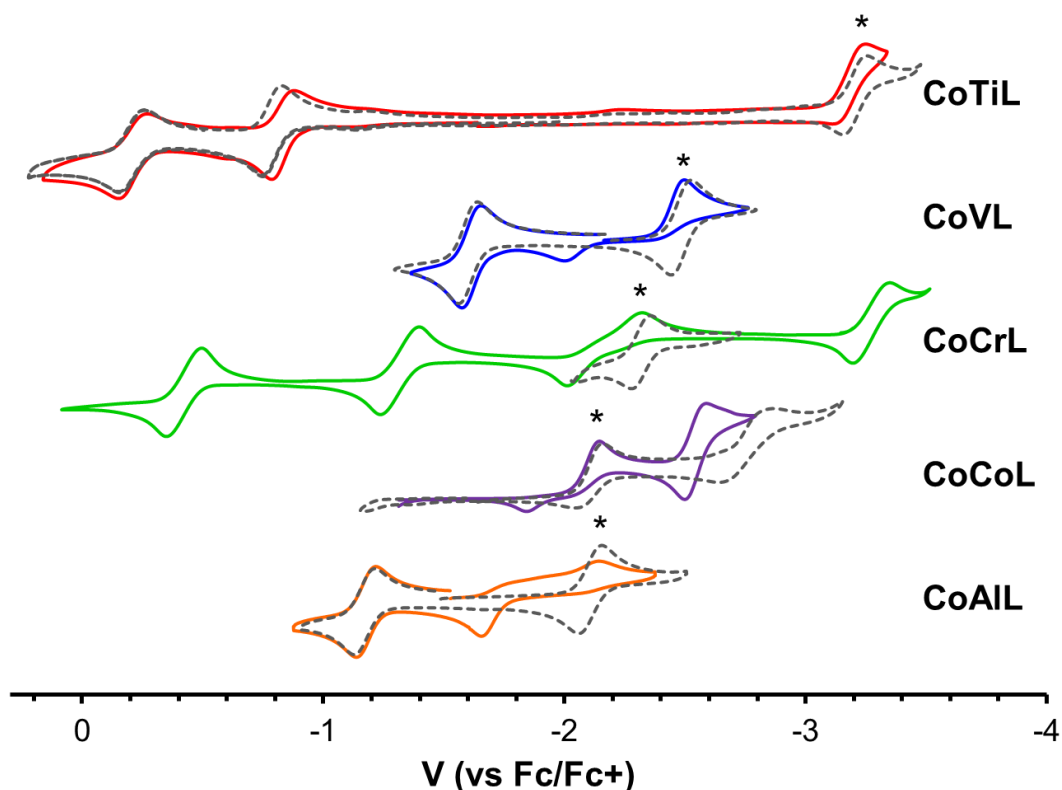


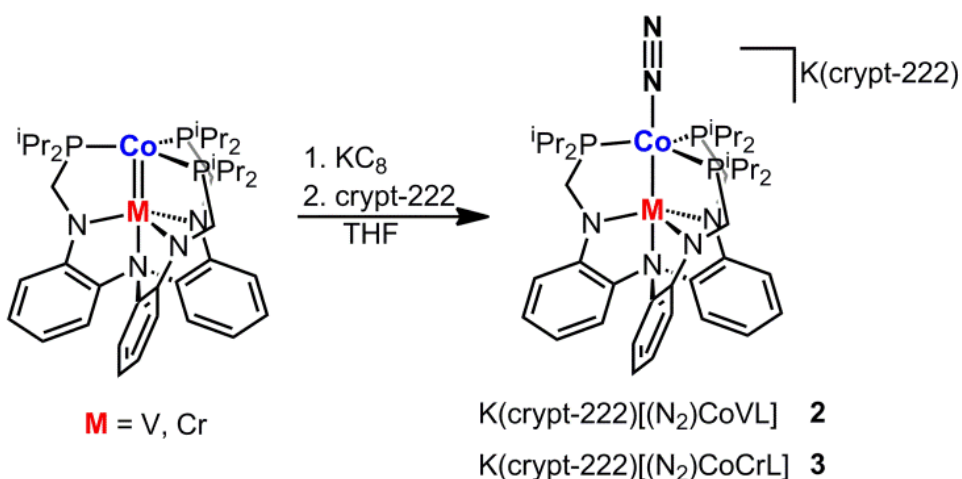
**Figure 4.4** Cyclic voltammograms of  $\text{CoML}$  complexes collected under an atmosphere of  $\text{N}_2$  (colored lines) or argon (---) in  $0.4$  M  $[\text{nBu}_4\text{N}]\text{PF}_6$  in THF at a scan speed of  $50$  mV/s. Exceptions:  $250$  mV/s for  $\text{CoAIL}$ , and  $10$  mV/s for  $\text{CoCrL}$  and  $\text{Co}_2\text{L}$ , which was dissolved in  $0.1$  M  $[\text{nBu}_4\text{N}]\text{PF}_6$  in DME. Asterik (\*) indicates  $[\text{CoML}]^{0/-}$  redox couple.

#### 4.3.3 Synthesis and characterization of dinitrogen adducts 2 and 3

To probe  $\text{N}_2$  activation, chemical reduction of the  $\text{CoML}$  species with  $\text{KC}_8$  followed by addition of crypt-222 provided the end-on  $\text{N}_2$  complexes,  $[(\text{N}_2)\text{CoML}]^-$  (Scheme 4.2).



Both  $\text{K}(\text{crypt-222})[(\text{N}_2)\text{CoVL}]$  (**2**) and  $\text{K}(\text{crypt-222})[(\text{N}_2)\text{CoCrL}]$  (**3**) were successfully generated, but we were unable to isolate any reduced CoTi species. The solution-state magnetic moments of **2** and **3** were measured to be 2.68 and 3.58  $\mu\text{B}$ , respectively. Hence, the ground states of **2** and **3** are assigned as  $S = 1$  and  $S = 3/2$ , respectively, as they are close to the spin-only moments of 2.83 and 3.87  $\mu\text{B}$ , respectively. The remaining anionic members,  $[(\text{N}_2)\text{Co}_2\text{L}]^-$  and  $[(\text{N}_2)\text{CoAlL}]^-$ , were reported previously, and are  $S = 1$  and  $S = 0$ , respectively.<sup>29,52,137</sup>(16, 22)



**Scheme 4.2** Synthesis of compounds **2** and **3**.

Figure 4.5 shows the molecular structures of **2** and **3**. The unit cell for **2** and **3** each contains two unique molecules. The N–N bond elongates upon binding, from 1.098 Å in free  $\text{N}_2$  to 1.130(4)/1.135(4) Å and 1.120(7)/1.135(6) Å in **2** and **3**, respectively (Table 4.1).<sup>140</sup>(52) By this metric,  $\text{N}_2$  is slightly less activated in  $[(\text{N}_2)\text{Co}_2\text{L}]^-$  and  $[(\text{N}_2)\text{CoAlL}]^-$ , which have N–N bond lengths of 1.114(4) and 1.110(8) Å, respectively. Although M– $\text{N}_2$  bond length can be useful to assess metal– $\text{N}_2$  back-bonding, the Co–N bond distances in the  $[(\text{N}_2)\text{CoML}]^-$  complexes are roughly similar, from 1.77 to 1.81 Å (with esd's up to 0.005 Å). Moreover, the Co–N bond in **3** differs by 0.02 Å in the two independent molecules, which also makes it difficult to judge or attribute any subtle differences in Co–N bonds to the supporting metals. Overall, cobalt centers are typically poor at  $\pi$ -back-bonding to  $\text{N}_2$ , and the N–N and Co–N metrics of these cobalt bimetallics are consistent with weak  $\text{N}_2$  activation.

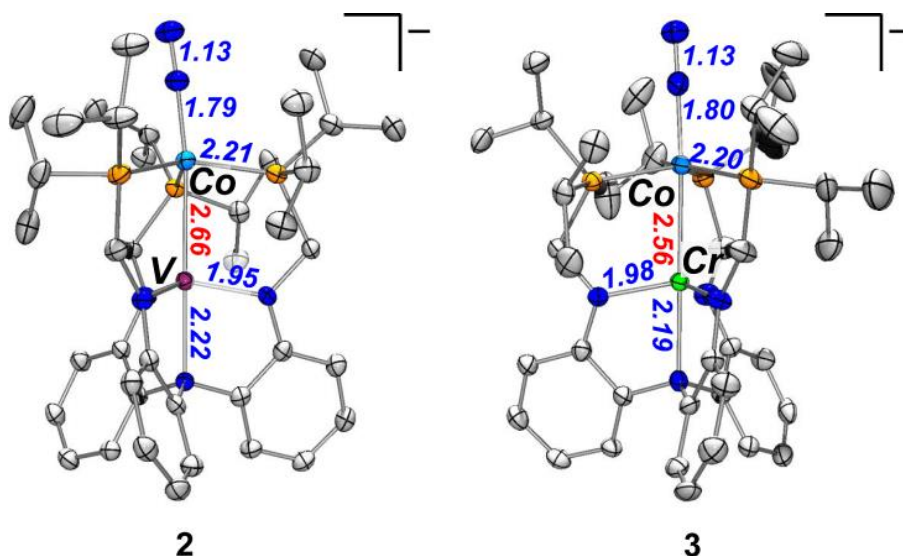


**Figure 4.5** Molecular structures of **2** and **3** shown at 50% thermal ellipsoid probability. Hydrogen atoms, K(crypt-222) counterion, and non-coordinating solvent molecules were omitted for clarity. Average bond lengths (Å) are shown.

Upon reduction, the FSR values of the Co–M bonds in the cobalt-transition metal pairs all increase above unity (1.1 to 1.2). Presumably, elongation of the Co–M bond is a direct consequence of N<sub>2</sub> binding trans to the supporting metal and, thereby, weakening the Co–M interaction. Only [(N<sub>2</sub>)CoAIL]<sup>−</sup> shows a decrease in FSR (1.06 to 1.02) relative to its neutral analogue (Appendix Table A3.1). Again, N<sub>2</sub> already occupies the apical pocket in the neutral complex, and so, the increase in cobalt electron density (by one electron) is interpreted to increase cobalt back-bonding to the Lewis acidic Al(III) center. Finally, systematic changes in the Co–P bond lengths can be discerned among the K(crypt-222)[(N<sub>2</sub>)CoML] compounds. Specifically, the Co–P bond distances increase according to the order 2.18 Å in [(N<sub>2</sub>)CoAIL]<sup>−</sup> < 2.19–2.21 in **2** and **3** < 2.26 Å in [(N<sub>2</sub>)Co<sub>2</sub>L]<sup>−</sup>, where the latter has substantially longer Co–P bonds than the others.

The N–N bond stretching frequency should be a more precise measure of N<sub>2</sub> activation. The N–N frequencies were measured on solid KBr samples of the K(crypt-222)[(N<sub>2</sub>)CoML] complexes. In order of increasing N<sub>2</sub> activation, the frequencies are: 1995 cm<sup>−1</sup>, [(N<sub>2</sub>)CoAIL]<sup>−</sup> ≈ 1994 cm<sup>−1</sup>, [(N<sub>2</sub>)Co<sub>2</sub>L]<sup>−</sup> > 1990 cm<sup>−1</sup>, [(N<sub>2</sub>)CoCrL]<sup>−</sup> > 1971 cm<sup>−1</sup>, [(N<sub>2</sub>)CoVL]<sup>−</sup>.<sup>29,52</sup> The N–N frequencies, which span 24 cm<sup>−1</sup>, are all consistent with a weakly activated N<sub>2</sub> ligand. A general correlation can be made about the relationship of

the N–N stretching frequency and the redox potentials. The more cathodic the reduction potential, the more activated the N–N stretching frequency (Table 4.1). The Co<sub>2</sub>L and (N<sub>2</sub>)CoAIL both have very similar N–N stretching frequencies and reduction potentials, suggesting a similar Co environment in each complex. The similarities between the Co<sub>2</sub>L and (N<sub>2</sub>)CoAIL complexes is interesting because their formal Co oxidation states Co<sup>0</sup> and Co<sup>-1</sup>, respectively (*vide infra*), but the supporting metal choice results in a similar N<sub>2</sub> activation.

#### 4.3.4 Theory

The [(N<sub>2</sub>)CoML]<sup>-</sup> series and CoTiL (**1**) were investigated using density functional theory (DFT) and complete active space self-consistent field (CASSCF) calculations. Optimizations were performed at the DFT level of the [(N<sub>2</sub>)CoML]<sup>-</sup> anions without truncation for M = Al, Ti, V, Cr, and Co. To model **1**, CoTiL<sup>Me</sup> (**1'**) was used where PiPr<sub>2</sub> groups were truncated to PMe<sub>2</sub> (see Experimental Section). The DFT optimized structures were then used as inputs for multiconfigurational CASSCF calculations with second-order perturbation (CASPT2).

The qualitative molecular orbital (MO) diagram of CoTiL<sup>Me</sup> (**1'**) was identical by DFT and CASSCF methods, and the latter is shown in Figure 4.6. The main electronic configuration,  $\pi^4\sigma^2(\text{Co } 3d_{xy}, d_{x^2-y^2})^4$ , accounts for 83% of the total wave function. To consider the entire ground-state wave function, the occupation numbers were summed over all configurations to give the “total” electronic configuration,  $\pi^{3.82}\sigma^{1.89}(\text{Co } 3d_{xy}, d_{x^2-y^2})^{3.88}\sigma^{*0.11}\pi^{*0.18}(\text{Co } 4d_{xy}, d_{x^2-y^2})^{0.12}$ . Although the calculations reveal three Co–Ti bonding MOs ( $\sigma + 2\pi$ ), these MOs are quite polarized and cannot be considered as three full bonds. The steep polarization of the  $\sigma$  (Co/Ti: 71/29%) and  $\pi$  MOs (Co/Ti: 86/14% for both) means weakened  $\sigma$  and  $\pi$  bonds, which may be consistent with an experimental FSR that suggests a double Co–Ti bond, rather than triple.

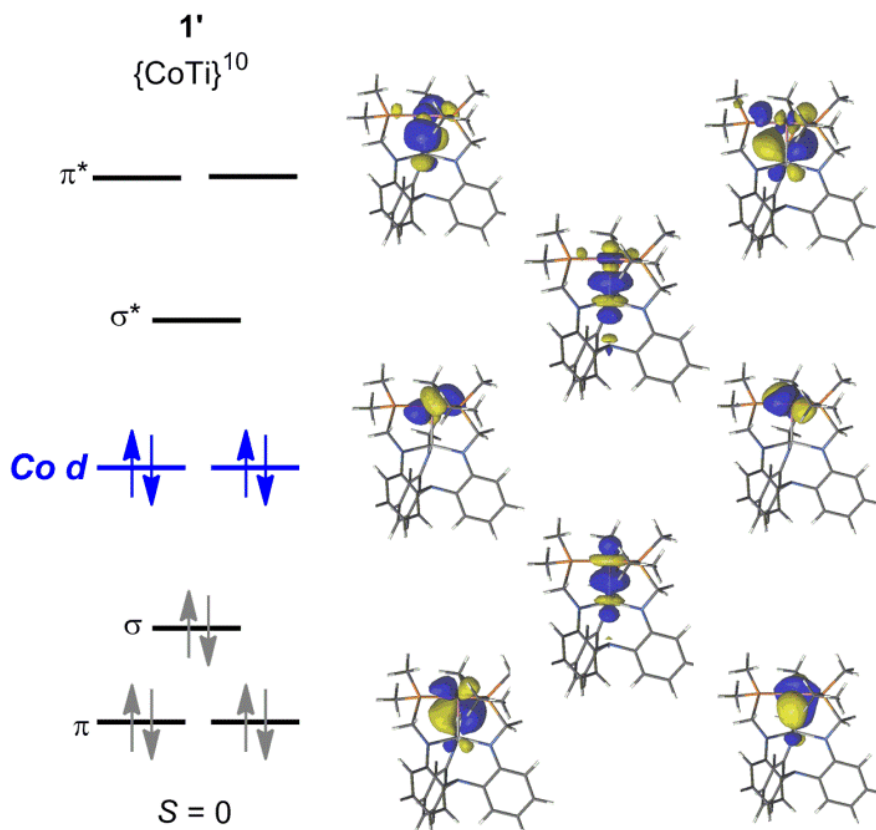


**Figure 4.6** Qualitative MO diagram showing the natural orbitals for  $\text{CoTiL}^{\text{Me}}$  ( $1'$ ) that arise from CASSCF calculations (energy ordering from DFT). The dominating electronic configuration (83%) is shown. The  $\sigma/\sigma^*$  and  $\pi/\pi^*$  labels refer to Co–Ti natural bonding orbitals.

The qualitative splitting diagram for the  $[(\text{N}_2)\text{CoML}]^-$  series is shown in Figure 4.7. The  $[(\text{N}_2)\text{CoTiL}]^-$  species is purely hypothetical since its experimental congener has not yet been isolated. The energy ordering of the orbitals was based on the DFT calculations. Similar natural orbitals resulted from the CASSCF calculations (Appendix Figures A3.8–A3.12), and the polarization of the  $\sigma$ -symmetry MO was obtained from the latter. Across the  $[(\text{N}_2)\text{CoML}]^-$  series, the  $\text{N}_2$   $\pi^*$  molecular orbitals are energetically inaccessible, lying well above the HOMO/SOMO for each species. This is consistent with weak  $\text{N}_2$  activation and preservation of the N–N triple bond. Of interest, the energy gap between the  $\text{N}_2$   $\pi^*$  MOs and the Co  $d_{xy}/d_{x^2-y^2}$  orbitals remains constant across the different supporting metals, and so, these orbitals were used as a benchmark for comparing Co d-orbital energies.

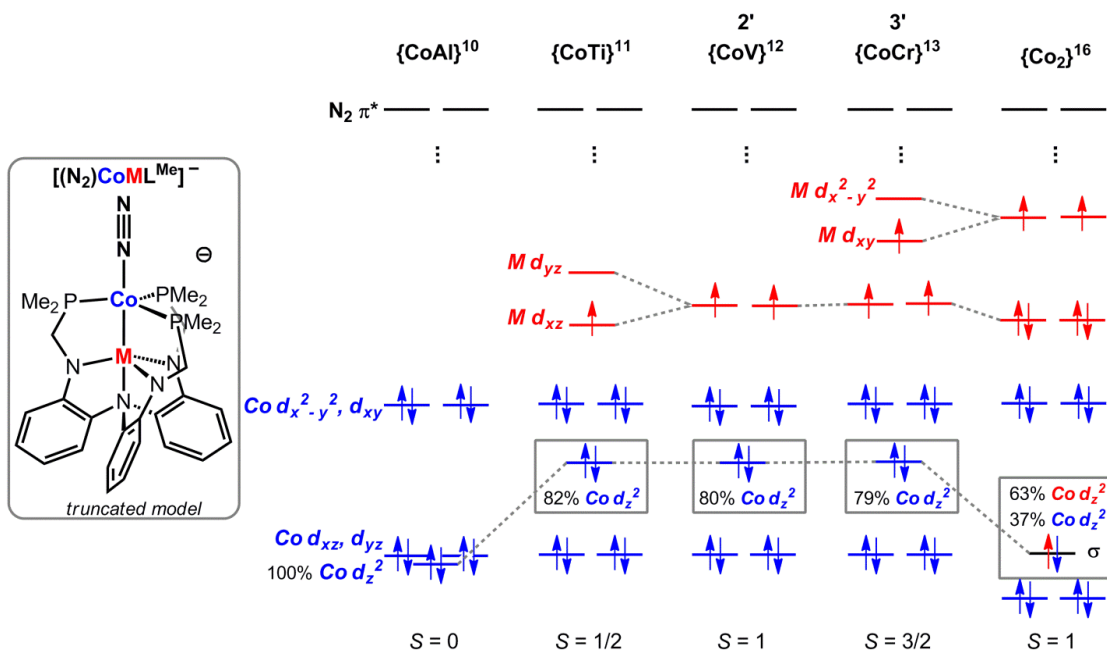


**Figure 4.7** Qualitative MO diagrams of the d-orbital manifold for the  $[(N_2)CoML]^-$  series, where  $M = Al, Ti, V, Cr,$  and  $Co$ . In the  $\{CoM\}^n$  descriptor,  $n$  is the number of valence d electrons. Polarization of the  $\sigma$ -symmetry MO is given as a percentage.

For the transition metal pairings, one notable difference between the  $[(N_2)CoML]^-$  anions and their neutral  $CoML$  analogues is the greater localization of electrons at the individual metal centers in the anions. Indeed, the only MO with any degree of delocalization is the  $\sigma$  ( $Co-M$ ). For  $M = Ti, V,$  and  $Cr$ , the  $\sigma$  ( $Co-M$ ) is heavily polarized toward cobalt, such that the probability percentages at the two metals,  $Co$  and  $M$ , are approximately 80 and 20%, respectively. Hence, by DFT, the  $CoTi, CoV,$  and  $CoCr$  analogues have electronic structures that are approximate to the  $CoAl$  species, where the cobalt center is formally subvalent,  $d^{10} Co(-I)$ , and the supporting metals are trivalent,  $d^0 Al(III), d^1 Ti(III), d^2 V(III),$  and  $d^3 Cr(III)$ . (Note: A detailed CASSCF analysis suggests that the oxidation state of the bimetallic core may be closer to  $Co(0.5)M(2.5)$  in the  $CoTi, CoV,$  and  $CoCr$  species. See Appendix Table A.17.) For  $M = Ti, V,$  and  $Cr$ , the ligand-field splitting of the cobalt-based d orbitals remains fairly constant for  $M = Ti, V,$  and  $Cr$ , where the  $Co d_{z^2}$  electrons are intermediate in energy between the nonbonding  $d_{xz}/d_{yz}$  and metal–ligand antibonding  $d_{xy}/d_{x^2-y^2}$  orbitals. In contrast, the  $Co d_{z^2}$  electrons are greatly stabilized by the Lewis acidic  $Al(III)$  supporting ion in  $[(N_2)CoAl]^-$ .

The dicobalt analogue,  $[(\text{N}_2)\text{Co}_2\text{L}]^-$ , is the stand-out in this series. Unsurprisingly, its electronic structure is different, since it is the only late-late metal pairing. Opposed to the  $\text{Co}(-\text{I})\text{M}(\text{III})$  redox states of the other anions, the oxidation state of the dicobalt core is  $\text{Co}(0)\text{Co}(\text{II})$ . The key difference is the presence of a more delocalized  $\text{Co-Co}$   $\sigma$ -bonding MO (63/37%). Hence, a formal single bond is predicted between the two metal centers. The better overlap and mixing between the two metals' d orbitals is likely responsible for the greater ligand-field splitting for the phosphine-ligated cobalt compared to the other anions. Of note, the different oxidation state of  $\text{Co}(0)$  in the dicobalt anion versus  $\text{Co}(-\text{I})$  in other  $[(\text{N}_2)\text{CoML}]^-$  anions may have observable ramifications. Recall that the  $\text{Co-P}$  bonds are significantly longer in  $[(\text{N}_2)\text{Co}_2\text{L}]^-$  (2.26 Å) compared to the Al, V, and Cr counterparts (2.19–2.21 Å). The shorter  $\text{Co-P}$  bond lengths in the latter complexes are consistent with a more reduced cobalt site, which can better back-bond to the phosphine ligands.

#### 4.4 Conclusion

The neutral  $\text{CoTiL}$  complex is the fifth member of a  $(\text{CoM})^{3+}$  family supported by the triphosphino(triamido)amine scaffold. The  $\text{Co-Ti}$  bond is short at 2.20 Å. Theory predicts three metal-metal bonding MOs ( $\sigma + 2\pi$ ), but the extent of polarization should be taken into account when assigning bond order. Based on a formal shortness ratio of 0.89, we approximate a  $\text{Co-Ti}$  double bond. Three one-electron transfers are observed in the CV of  $\text{CoTiL}$ . The  $[\text{CoTiL}]^{0/-}$  reduction potential is extremely negative at -3.20 V. Including  $(\text{N}_2)\text{CoAlL}$ , the  $(\text{CoM})^{+3/+2}$  redox couples in this family span a wide range of 1.1 V. Clearly, the supporting metal ion has a large impact on the  $[\text{CoML}]^{0/-}$  reduction potentials. Moreover, the  $[\text{CoML}]^{0/-}$  reduction potentials shift anodically as M is varied across the first-row period.

Of interest to  $\text{N}_2$  activation, four isostructural  $[(\text{N}_2)\text{CoML}]^-$  complexes were isolated and characterized for  $\text{M} = \text{Al}, \text{V}, \text{Cr},$  and  $\text{Co}$ .<sup>29,52,137</sup> The range of  $\text{N-N}$  bond lengths in the  $\text{N}_2$  adducts,  $[(\text{N}_2)\text{CoML}]^-$ , is extremely narrow from 1.110(8) to 1.135(4) Å. Likewise, the stretching frequencies of the  $\text{N}_2$  adducts span only 24  $\text{cm}^{-1}$ . Thus, varying the supporting metal ion has a limited impact on the extent of  $\text{N}_2$  activation, perhaps

because N<sub>2</sub> binding at the trans position tends to weaken the Co–M interaction. Though the changes in  $\nu_{N_2}$  are subtle, N<sub>2</sub> activation in the [(N<sub>2</sub>)CoML]<sup>−</sup> series does decrease across the first-row period. As might be expected, there is a general correspondence between the [CoML]<sup>0/−</sup> reduction potentials ( $E_{1/2}^\circ$ ) and N<sub>2</sub> activation:

$$E_{1/2}^\circ \text{ ([CoML]}^{0/-} \text{ or } [(N_2)\text{CoAIL}]^{0/-}): \quad \text{Al} \sim \text{Co} < \text{Cr} < \text{V} \ll \text{Ti}$$

$$\nu_{N_2} \text{ (} [(N_2)\text{CoAIL}]^- \text{):} \quad \text{Al} \sim \text{Co} > \text{Cr} > \text{V}$$

Varying the supporting metal ion also changes the electronic structure of the [(N<sub>2</sub>)CoML]<sup>−</sup> species. As elucidated through theory, the oxidation state of the bimetallic (CoM)<sup>2+</sup> core is Co(−I)M(III) for M = Al, Ti, V, and Cr. The dicobalt anion is unique in that the oxidation states are Co(0)Co(II). The Co–M interactions, which appear similarly weak for M = Ti, V, and Cr, are potentially significant for Al and Co, albeit in different manifestations. In [(N<sub>2</sub>)CoAIL]<sup>−</sup>, an inverse dative bond (Co → Al) greatly stabilizes the Co d<sub>z2</sub> electrons, a consequence of pairing cobalt with the Lewis acidic ancillary ion, Al(III). In [(N<sub>2</sub>)Co<sub>2</sub>L]<sup>−</sup>, the late–late pairing enables better d-orbital overlap such that a Co–Co  $\sigma$  bond is formed.

## 4.5 Experimental Section

### 4.5.1 General Considerations

Unless otherwise stated, all manipulations were performed under an inert atmosphere in a glovebox or using standard Schlenk techniques. Standard solvents were deoxygenated by sparging with inert gas and dried by passing through activated alumina columns of a SG Water solvent purification system. Deuterated solvents were purchased from Cambridge Isotope Laboratories, Inc. or Sigma Aldrich, degassed via freeze-pump-thaw cycles, and stored over activated 4 Å molecular sieves. Elemental analyses were performed by Complete Analysis Laboratories, Inc. (Parsippany, NJ) or Robertson Microlit Laboratories, Inc. (Ledgewood, NJ). <sup>1</sup>H NMR spectra were recorded on Varian 300 MHz or a Bruker 500 MHz spectrometer at ambient temperature unless otherwise stated. Solution magnetic moments were determined using Evans' method.<sup>94,101</sup> Cyclic voltammetry was performed

using a CH instruments 600 electrochemical analyzer. The one-cell setup used a glassy carbon working electrode, Pt wire counter electrode, and Ag/AgNO<sub>3</sub> reference electrode in CH<sub>3</sub>CN. Analyte solutions consisted of 0.4 M [<sup>n</sup>Bu<sub>4</sub>N]PF<sub>6</sub> and the voltammograms were referenced internally to the FeCp<sub>2</sub><sup>0/+</sup> (abbreviated as Fc<sup>+</sup>/Fc) redox couple. The ligand N(*o*-(NHCH<sub>2</sub>P<sup>i</sup>Pr<sub>2</sub>)C<sub>6</sub>H<sub>4</sub>)<sub>3</sub> (abbreviated as H<sub>3</sub>L), CoVL, and CoCrL were synthesized according to literature procedures.<sup>12,20,87</sup>

#### 4.5.2 Synthetic Procedures

##### *Synthesis of Ti(N(*o*-(NCH<sub>2</sub>P<sup>i</sup>Pr<sub>2</sub>)C<sub>6</sub>H<sub>4</sub>)<sub>3</sub>)*

A solution of neutral ligand (N(*o*-(NHCH<sub>2</sub>P<sup>i</sup>Pr<sub>2</sub>)C<sub>6</sub>H<sub>4</sub>)<sub>3</sub>) (0.308 g, 0.453 mmol) in Et<sub>2</sub>O (5 mL) was frozen in a LN<sub>2</sub> coldwell. The solid was layered with <sup>n</sup>BuLi (0.560 mL, 1.40 mmol), and the mixture was allowed to thaw overnight. The volatiles of the resulting yellow solution were removed *in vacuo*. The resulting yellow oil was taken up in THF (5 mL) and frozen in a LN<sub>2</sub> cold well along with a solution of TiCl<sub>3</sub>(THF)<sub>3</sub> (0.168 g, 0.454 mmol) in THF (5 mL). The thawing yellow solution of deprotonated ligand was layered on top of the frozen solution of TiCl<sub>3</sub>(THF)<sub>3</sub>, and allowed to warm to rt. The solution was allowed to stir for 3 h to yield a brown solution. The reaction was dried *in vacuo*, and reconstituted in benzene. The benzene solution was filtered through a Celite pad and dried *in vacuo*, resulting in a brown powder (0.320 g, 97% yield). <sup>1</sup>H NMR (ppm, C<sub>6</sub>D<sub>6</sub>, 500 MHz): 8.5, 6.2, 5.0, 1.9, 1.0, -2.7. Anal. Calcd. for TiL, C<sub>39</sub>H<sub>60</sub>N<sub>4</sub>P<sub>3</sub>Ti: 64.55 C, 8.33 H, 7.72 N. Found: 64.09 C, 8.12 H, 7.44 N.

##### *Synthesis of 1 CoTi(N(*o*-(NCH<sub>2</sub>P<sup>i</sup>Pr<sub>2</sub>)C<sub>6</sub>H<sub>4</sub>)<sub>3</sub>)*

A solution of TiL (0.174 g, 0.238 mmol) in THF (4 mL) was added to a slurry of CoBr<sub>2</sub> (0.0522 g, 0.237 mmol) in THF (2 mL) while stirring. After 15 min, a homogeneous, dark green brown solution formed, and the solution was added to KC<sub>8</sub> (0.0658 g, 0.487 mmol). The green color disappeared within minutes, and the reaction was stirred for an additional 4 h. The reaction solution was filtered through a Celite pad, and the volatiles were removed *in vacuo*. The brown powder was reconstituted in benzene and filtered through a Celite pad to remove salts. The resulting brown solution was dried *in vacuo* to give a brown powder (0.175 g, 93% yield). Single crystals were grown through the slow dissipation of pentane



into a concentrated toluene solution.  $^1\text{H}$  NMR (ppm, THF- $d_8$ , 500 MHz): 6.80 (*t*,  $J = 7.7$  Hz, 3H), 6.71 (*d*,  $J = 7.7$  Hz, 3H), 6.16 (*d*,  $J = 7.7$  Hz, 3H), 6.12 (*t*,  $J = 7.2$  Hz, 3H), 5.28 (*d*,  $J = 11.5$  Hz, 3H), 4.53 (*d*,  $J = 11.4$ , 3H), 2.96 (*s*, 3H), 2.77 (*s*, 3H), 1.60 (*s*, 9H), 1.46 (*s*, 9H), 1.34 (*s*, 9H), 0.53 (*s*, 9H).  $^{31}\text{P}$  NMR (ppm, THF- $d_8$ , 200 MHz): 17.1.  $^{13}\text{C}$  NMR (ppm, THF- $d_8$ , 126 MHz): 156.2, 138.2, 128.4, 126.9, 114.4, 108.0, 68.9, 33.35, 28.53, 23.16, 20.26, 19.53, 17.84. Anal. Calcd. for **1**  $\text{C}_{39}\text{H}_{60}\text{N}_4\text{P}_3\text{TiCo}$ : 59.70 C, 7.71 H, 7.14 N. Found: 59.82 C, 8.04 H, 6.74 N.

*Synthesis of 2*  $K(\text{crypt-222})[(\text{N}_2)\text{CoVL}]$ ,

$K(\text{C}_{18}\text{H}_{36}\text{N}_2\text{O}_6)[(\text{N}_2)\text{CoV}(\text{N}(\text{o}-(\text{NCH}_2\text{P}^i\text{Pr}_2)\text{C}_6\text{H}_4)_3)]$

A solution of CoVL (0.0817 g, 0.104 mmol) in THF (8 mL) was added to a vial containing  $\text{KC}_8$  (0.0293 g, 0.217 mmol). A solution of crypt-222 (0.402 g, 0.107 mmol) in THF (4 mL) was added to the stirring reaction mixture, and was allowed to stir for 16 h. The resulting brown solution was filtered through a Celite plug to remove graphite, and the volatiles were removed *in vacuo*. The resulting brown powder was washed with 5 x 5 mL portions of benzene and then dried to obtain a brown powder (0.113 g, 89 % yield). Single crystals were grown through the layering of a THF solution with hexane.  $^1\text{H}$  NMR (ppm, THF- $d_8$ , 500 MHz): 27.1, 12.3, 8.7, 5.5, 3.4, 2.4, 1.3, 0.9, -27.5. Evans' Method (THF- $d_8$ ):  $\mu_{\text{eff}} = 2.68$  B.M. IR ( $\nu_{\text{N-N}}$ ,  $\text{cm}^{-1}$ , KBr pellet): 1971. Anal. Calcd. for **2**  $\text{C}_{57}\text{H}_{96}\text{CoVKN}_8\text{O}_6\text{P}_3$ : 55.60 C, 7.86 H, 9.1 N. Found: 55.99 C, 8.51 H, 7.41 N and 55.67 C, 7.88 H, 7.64 N for two independent samples. Note: Partial  $\text{N}_2$  loss during the combustion procedure may account for the low N%.

*Synthesis of 3*  $K(\text{crypt-222})[(\text{N}_2)\text{CoCrL}]$ ,

$K(\text{C}_{18}\text{H}_{36}\text{N}_2\text{O}_6)[(\text{N}_2)\text{CoCr}(\text{N}(\text{o}-(\text{NCH}_2\text{P}^i\text{Pr}_2)\text{C}_6\text{H}_4)_3)]$

THF (6 mL) was added to CoCrL (0.104 g, 0.132 mmol), and the solution was transferred to a slurry of  $\text{KC}_8$  (0.019 g, 0.138 mmol). The mixture was allowed to stir for 4 h, and the remaining graphite was filtered off through a Celite plug. The remaining red-brown solution was dried *in vacuo*. The solid was taken up in THF (2 mL) and added to a stirring solution of crypt-222 in THF (6 mL) and allowed to stir for 1 h. The solution was dried *in vacuo* to give a dark powder (0.140 g, 88 % yield). Single crystals were grown via the

slow diffusion of pentane into a concentrated THF solution.  $^1\text{H}$  NMR (ppm, THF- $d_8$ , 300 MHz): 15.8, 8.3, 6.5, -21.3. Evans' Method (THF- $d_8$ ):  $\mu_{\text{eff}} = 3.58$  B.M. IR ( $\nu_{\text{N-N}}$ ,  $\text{cm}^{-1}$ , KBr pellet): 1991. Anal. Calcd. for **3**  $\text{C}_{57}\text{H}_{96}\text{CoCrKN}_8\text{O}_6\text{P}_3$ : 55.55 C, 7.85 H, 9.09 N. Found: 56.86 C, 8.11 H, 6.89 N, which is consistent with  $\text{K}(\text{crypt-222})[\text{CoCrL}]$ ,  $\text{C}_{57}\text{H}_{96}\text{CoCrKN}_6\text{O}_6\text{P}_3$ : 56.84 C, 8.03 H, 6.98 N.

#### 4.5.3 X-ray crystallography

A brown block of **1**, a brown needle of **2**, and a brown needle of **3** were placed on the tip of a 0.1 mm diameter glass capillary and mounted on a Bruker APEX II CCD diffractometer or a Bruker Photon 100 CMOS diffractometer for data collection at 173(2) K or 123(2) K. The data collection was carried out using Mo  $\text{K}\alpha$  radiation (graphite monochromator) or Cu  $\text{K}\alpha$  radiation (normal parabolic mirrors).<sup>104</sup> The data intensity was corrected for absorption and decay (SADABS). Final cell constants were obtained from least-squares fits of all measured reflections and the structure was solved using SHELXS-08 and refined using SHELXL-08.<sup>105</sup> A direct-methods solution was calculated which provided most non-hydrogen atoms from the E-map. Full-matrix least-squares/difference Fourier cycles were performed to locate the remaining non-hydrogen atoms and all non-hydrogen atoms were refined with anisotropic displacement parameters with the exception of a disordered THF molecule in **2** is refined isotropically. Hydrogen atoms were placed in ideal positions and refined as riding atoms with relative isotropic displacement parameters. Complex **3** was refined as an inversion twin with the main component contributing 54 %. A disordered isopropyl group in **3** was modeled using SHELXTL EADP constraints, and the geometrical restraints SAME and SADI. Electron density attributed to two disordered molecules of pentane in the asymmetric unit was removed using Platon SQUEEZE.<sup>141</sup> Crystallographic details are summarized in Table 4.2.

**Table 4.2** Crystallographic Details for compounds **1–3**.

	<b>1</b>	<b>2</b>	<b>3</b>
chemical formula	C <sub>39</sub> H <sub>60</sub> N <sub>4</sub> P <sub>3</sub> TiCo	C <sub>39</sub> H <sub>60</sub> N <sub>6</sub> P <sub>3</sub> VCo · KC <sub>18</sub> H <sub>36</sub> N <sub>2</sub> O <sub>6</sub> · C <sub>4</sub> H <sub>8</sub> O	2(C <sub>39</sub> H <sub>60</sub> N <sub>6</sub> P <sub>3</sub> CrCo) · 2(KC <sub>18</sub> H <sub>36</sub> N <sub>2</sub> O <sub>6</sub> )
fw	784.65	1303.4	2464.7
cryst syst	monoclinic	orthorhombic	monoclinic
space group	<i>P2<sub>1</sub>/n</i>	<i>Pna2<sub>1</sub></i>	<i>P2<sub>1</sub></i>
<i>a</i> (Å)	13.5781(18)	63.552(2)	11.2453(3)
<i>b</i> (Å)	13.9450(18)	11.0817(4)	31.9918(7)
<i>c</i> (Å)	20.821(3)	18.9917(7)	18.9780(4)
<i>α</i> (deg)	90	90	90
<i>β</i> (deg)	94.250(2)	90	95.0420(10)
<i>γ</i> (deg)	90	90	90
<i>V</i> (Å <sup>3</sup> )	3931.5(9)	13375.2(8)	6801.1(3)
<i>Z</i>	4	8	2
<i>D</i> <sub>calcd</sub> (g cm <sup>-3</sup> )	1.326	1.295	1.204
<i>λ</i> (Å), <i>μ</i> (mm <sup>-1</sup> )	0.71073, 0.780	1.54178, 4.785	1.54178, 4.831
<i>T</i> (K)	173(2)	123(2)	173(2)
<i>θ</i> range (deg)	1.73–27.50	2.71–74.71	2.337–74.662
reflns collected	9018	25425	27151
unique reflns	5711	22340	23744
data/restraint/params	9018/0/445	25425/1/1476	27151/8/1428
R1, wR2 ( <i>I</i> > 2σ( <i>I</i> ))	0.0527, 0.1170	0.0440, 0.1054	0.0470, 0.1130

## 4.6 Computational Methods

### 4.6.1 DFT Calculations

DFT calculations were performed on the full molecules, CoTiL and [(N<sub>2</sub>)CoML]<sup>-</sup> (where M = Al, Ti, V, Cr, Co). Gas-phase optimizations of all possible spin states were carried out using the M06-L<sup>121</sup> functional and def2-TZVP<sup>107</sup> (for N, P, Al, Ti, V, Cr, and Co atoms)/def2-SVP (for C, H atoms) basis sets. The experimental structures were used as initial geometries. In one case, CoTiL, the optimized Co–Ti distance did not match well to

experimental data (both M06-L and PBE underestimated by  $\sim 0.14$  Å), so the Co–Ti bond distance was kept fixed, while the rest of the molecule was allowed to relax. Vibrational frequency analysis with the harmonic approximation was performed at the optimized geometries to characterize the nature of the stationary points on the potential energy surface. Gibbs free energies at 298.15 K were computed by adding zero-point vibrational energies, and thermal vibrational–rotational entropy in the quasi-harmonic approximation calculated at the M06-L/def2-TZVP (for N, P, Al, Ti, V, Cr and Co)/def2-SVP(for C, H) level. Solvation effects were also considered by performing single-point calculations for all intermediates using the SMD solvation model<sup>116</sup> with the diffuse basis set, def2-TZVPD<sup>142</sup> (for N, P, Al, Ti, V, Cr, and Co; def2-SVP for C and H) and THF as the solvent. In summary, the energies of all calculated structures were determined at the M06-L/def2-TZVP and M06-L/def2-TZVPD/SMD levels of theory, where the former is used for geometry optimizations and the latter for single-point energy calculations. The *Gaussian 09* suite of programs<sup>106</sup> was used for all DFT calculations. Additionally, CM5 charges<sup>143,144</sup> was performed for all species (Appendix Table A3.10).

#### 4.6.2 Multi-reference calculations

Four species,  $\text{CoTiL}^{\text{Me}}$  and  $[(\text{N}_2)\text{CoML}]^-$  (where M = Ti, V, Cr), were further investigated by multi-reference calculations using the DFT-optimized geometries in the MOLCAS-7.8 program.<sup>109</sup> (Note: In the single case of  $\text{CoTiL}^{\text{Me}}$ , the ligand's  $\text{P}^i\text{Pr}_2$  groups were truncated to  $\text{PMe}_2$  because previous calculations on neutral  $\text{CoML}^{\text{Me}}$  species also used the truncated ligand.) The complete active space self-consistent field (CASSCF)<sup>108</sup> method was used, followed by multiconfigurational second order perturbation theory, CASPT2.<sup>145</sup> The following relativistic all-electron basis sets were used: ANO-RCC-VTZP for Co, Cr, V, and Ti; ANO-RCC-VDZP for P and N; and ANO-RCC-MB for C and H atoms.<sup>110,111</sup> Scalar relativistic effects were included by using the Douglas–Kroll–Hess Hamiltonian.<sup>112,113</sup> The two-electron integral evaluation was simplified by using the resolution-of-identity (RI)<sup>146</sup> and the Cholesky decomposition technique.<sup>114</sup> To avoid intruder states, an imaginary level shift of 0.2 au was used in the CASPT2 calculations.<sup>147</sup>

## **Chapter 5**

### **Understanding the Cooperation of Co–M Interactions and Ligand Hemi-lability in the Catalytic Reductive Silylation of N<sub>2</sub>**

Theory contributions from Varinia Bernales

## 5.1 Introduction

The conversion of molecular dinitrogen into ammonia, often referred to as nitrogen fixation, is a fundamental transformation in both biology and chemistry. The Haber-Bosch process is responsible for the industrial fixation of nitrogen, contributing the primary source of ammonia for nitrogen based fertilizers.<sup>148,149</sup> On the biological side, nitrogenase enzymes fix N<sub>2</sub> at ambient conditions, making it an intriguing target for mechanistic studies and synthetic model complexes.<sup>38,40,41,150-152</sup> Homogeneous molecular catalysts have been studied extensively for the reduction of N<sub>2</sub> to provide insight into the mechanism of nitrogenases as well as to develop a less energy-intensive alternative to the Haber-Bosch process.

Successful molecular catalysts for N<sub>2</sub> fixation use the transition metals: Mo<sup>74,153-156</sup>, Fe<sup>69-72</sup>, and Co<sup>73</sup>. A Mo catalyst developed by Schrock has been studied extensively, allowing for the isolation of Chatt-type intermediates which support the Chatt and Schrock catalytic mechanisms for the reduction of N<sub>2</sub> (Figure 5.1).<sup>95,153,157,158</sup> In the Chatt/Schrock cycle, three H atoms first add to the distal nitrogen and break the N–N bond, to give a M≡N moiety, which is further reduced by the addition of three H atoms to release a second equivalent of NH<sub>3</sub>. Recent *in-situ* spectroscopic studies of an Fe catalyst provide further details on the active species during the reduction of N<sub>2</sub>.<sup>72</sup> A hemi-labile interaction between iron and the apical ligand *trans* to N<sub>2</sub> is proposed to be critical to facilitating catalytic activity.<sup>70,72</sup> Additionally, an alternative, combined pathway was proposed based on the observed fixation of nitrogen by a model Fe catalyst, where two distal additions of protons and electrons were followed by two proximal additions prior to the release of two equivalent of ammonia.<sup>75</sup>

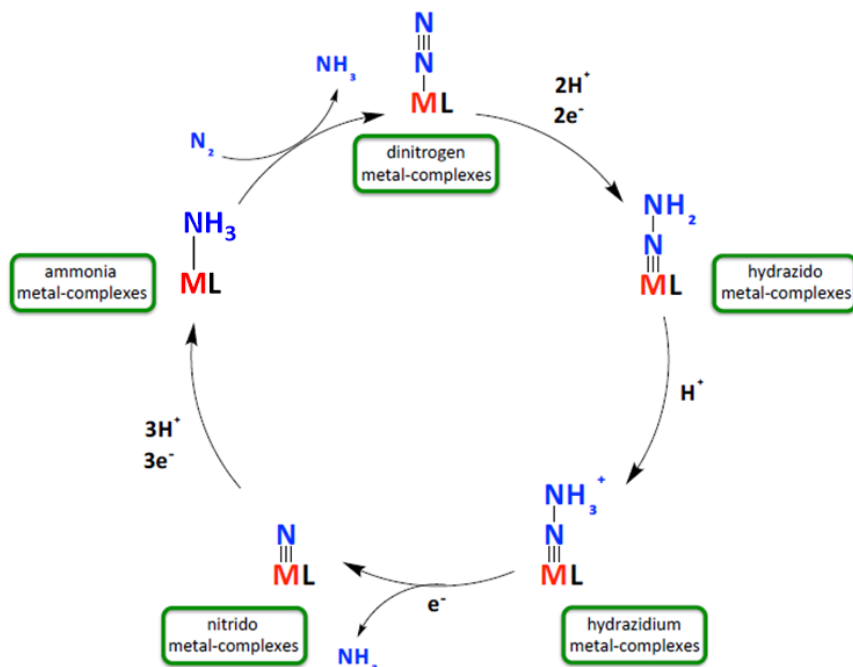


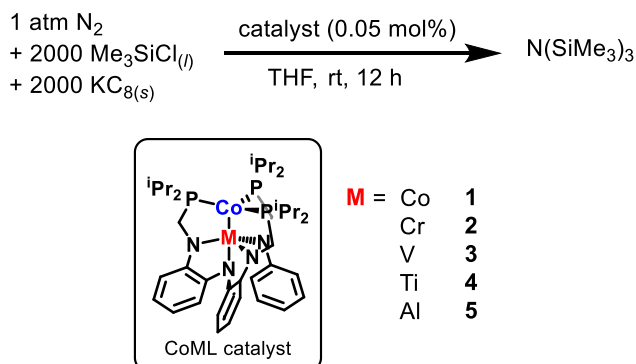
**Figure 5.1** Chatt/Schrock cycle for the mechanism of  $N_2$  reduction to ammonia

The silylation of  $N_2$  is an alternative process to reductively cleave the strong  $N_2$  triple bond. The use of a silyl reagent, such as  $SiMe_3Cl$ , acts as a substitute for the proton reagents and forms a tertiary amine,  $N(SiMe_3)_3$ , instead of ammonia. Silylation catalysts that are effective for reducing  $N_2$  also primarily contain Mo, Fe or Co.<sup>29,71,137,159-164</sup> To date, a Mo catalyst developed by Nishibayashi holds the highest TON of 226<sup>2</sup> to generate  $N(SiMe_3)_3$ .<sup>162</sup> However, recently a dicobalt catalyst was found to attain a comparatively high turnover with a better yield of 30%.<sup>29</sup> Mechanistic studies are crucial in the reductive silylation of  $N_2$ , as the bulky  $SiMe_3$  groups can provide additional steric strain in the cycle, which could alter the mechanistic cycle from that previously proposed for  $N_2$  reduction to ammonia. Control studies with the dicobalt catalyst implicate a bimetallic active species, and mechanistic studies suggest the Co–Co interaction aids in catalysis. These initial catalytic studies have led to an experimental and theoretical study of a series of CoM bimetallic to identify the ability of an active Co center to be tuned by the supporting metal choice.

<sup>2</sup>Catalytic conditions: 8000 equiv  $Me_3SiCl$ , 8000 equiv Na over 2 additions of reagents, in THF for 200 h at rt

## 5.2 Catalytic reductive silylation of N<sub>2</sub> with Co heterobimetallics

Following the successful catalytic reduction of N<sub>2</sub> to N(SiMe<sub>3</sub>)<sub>3</sub> with dicobalt complex **1**, Co<sub>2</sub>L, four additional cobalt heterobimetallics were tested (Scheme 5.1). In a previously reported study, an isostructural series of [N<sub>2</sub>CoML]<sup>-</sup> complexes, including **1<sup>red</sup>**, was evaluated for the ability of the supporting metal to influence the activation of N<sub>2</sub> (Figure 5.2).<sup>87</sup> Heterobimetallic complexes [N<sub>2</sub>CoCrL]<sup>-</sup> (**2<sup>red</sup>**) and [N<sub>2</sub>CoVL]<sup>-</sup> (**3<sup>red</sup>**), were found to activate N<sub>2</sub> more strongly than [N<sub>2</sub>Co<sub>2</sub>L]<sup>-</sup> (**1<sup>red</sup>**). The neutral heterobimetallics, **2** – **5**, were subjected to the same catalytic conditions as **1** and the results are listed in Table 5.1. The catalytic reactions were conducted over a period of 12 h with a 0.13 mM catalyst concentration with 2000 equivalents each of KC<sub>8</sub> and Me<sub>3</sub>SiCl. The homobimetallic **1** remained the most active catalyst with the highest equivalents of amine obtained per equivalent of catalyst, referred to as turnover number (TON), at 160(17). The early-late heterobimetallic complexes **2** – **4** had similar activities, but overall achieved a higher TON than the Lewis acid supported **5**, CoAlL. The results of catalysis allow these five bimetallics to be classified into three distinct groups based on catalytic activity: homobimetallic (**1**), early-late heterobimetallics (**2** – **4**) and Lewis acid supported bimetallic (**5**). The distinct catalytic performance of these three groups represent a periodic trend based on supporting metal type, demonstrating ability to tune the reactivity of an active metal via interaction with a varied supporting metal. Furthermore, in order to understand how the supporting metal can hinder or promote catalysis, a detailed kinetic and mechanistic study was conducted.



**Scheme 5.1** Catalytic conditions for reductive silylation of N<sub>2</sub> with CoML bimetallic catalysts.



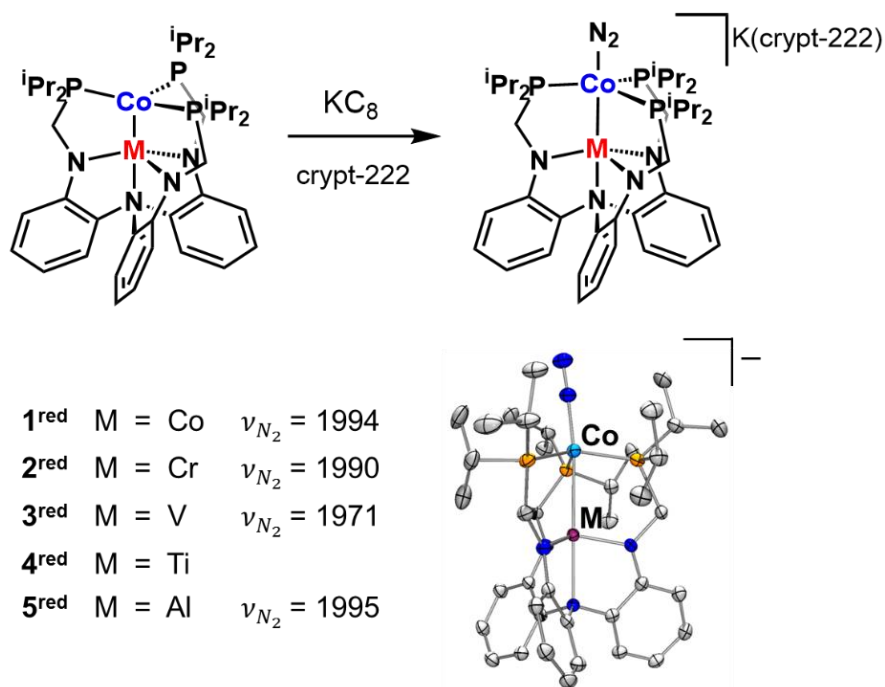


**Figure 5.2** Isolation of a series of  $[\text{N}_2\text{CoML}]^-$  complexes and their corresponding  $\text{N}_2$  stretching frequencies

**Table 5.1** Catalytic results for the formation of  $\text{N}(\text{SiMe}_3)_3$ , quantified via GC-MS.

	catalyst	% yield	TON
<b>1</b>	Co <sub>2</sub> L	24	160 ± 17
<b>2</b>	CoCrL	16	107 ± 11
<b>3</b>	CoVL	13	86 ± 8
<b>4</b>	CoTiL	13	85 ± 20
<b>5</b>	CoAlL	4	30 ± 9

### 5.3 Kinetic studies

Previous kinetic studies of **1** revealed a pseudo-first-order dependence on catalyst concentration.<sup>29</sup> The comparison of initial rates for the CoML series can provide further insight into the role of the supporting metal identity. The kinetics of the reductive silylation of  $\text{N}_2$  with CoML bimetallic catalysts were investigated with two methods. Method 1 focused on the identification of the initial rates of the reaction by analyzing aliquots of a

catalytic reaction taken at various time points for up to an hour. Method 2 involved setting up individual catalytic reactions that were quenched at various time points for up to six hours, which shows the entire progress of the reaction over time. For both methods, the quantification of  $\text{N}(\text{SiMe}_3)_3$  was determined by hydrolyzing the amine to  $\text{NH}_4\text{Cl}$  and analyzing the concentration of  $\text{NH}_4\text{Cl}$  by the indophenol method.<sup>165,166</sup>

Qualitatively, both methods show similar trends for the different CoML complexes (Appendix Figure A4.4), however, method 2 is more reliable due to its ability maintain consistent catalytic conditions. The initial rates seen from method 1 correlates to the overall TON of the catalyst, where the fastest catalyst ( $\text{Co}_2\text{L}$ ) also obtains the highest TON and the slowest catalyst ( $\text{CoAlL}$ ) generates the fewest TON (see appendix Figures A4.1–A4.2). Method 2 qualitatively reveals the trend seen from method 1 and also shows the time it takes for the catalysis to be complete for each catalyst. The catalysis appears to be complete after only 1 h for  $\text{CoAlL}$ , while it takes at least 3 h for the other CoML catalyzed reactions to be complete (Figure 5.3, right). A possible explanation for the earlier completion of the  $\text{CoAlL}$  catalysis is catalyst decomposition.

While these kinetic studies are helpful to confirm the groupings of the CoML catalysts first identified by the overall TON, some desired kinetic data remains to be collected. Two competing reactions take place with the formation of the amine, the THF ring-opening by  $\text{SiMe}_3$  radical and the coupling of  $\text{SiMe}_3$  radical to form hexamethyldisilane. The THF ring-opening by  $\text{SiMe}_3$  was found to not affect the reaction for **1** by achieving a similarly high TON when the catalysis was run in DME instead of THF.<sup>29</sup> The formation of hexamethyldisilane has yet to be thoroughly investigated. The selection of a reductant will influence the catalysis as well, as the vast excess of  $\text{KC}_8$  as a potent reductant in the catalysis creates a heterogeneous reaction mixture. Moving to either a soluble reductant such as pentamethyl cobaltocene or an alkali metal will change the kinetics of the reaction, and may lead to more optimal catalytic conditions. The use of an alkali metal such as  $\text{Na}(\text{s})$  or  $\text{K}(\text{s})$  will slow the reaction, but the formation of  $\text{SiMe}_3$  radicals should be limited by the surface area of the metal and may result in fewer side reactions involving the  $\text{SiMe}_3$  radical, thereby potentially resulting in a higher yield of amine product.

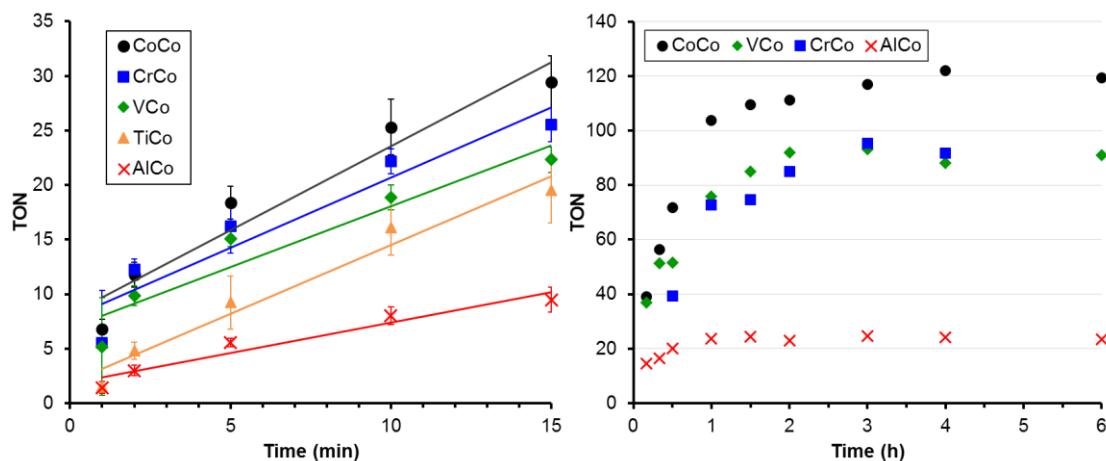


**Figure 5.3** Kinetic studies for CoML complexes with method 1 shown on the left and method 2 shown on the right.<sup>3</sup>

## 5.4 Catalytic mechanism

### 5.4.1 Theoretical mechanistic studies

Previously, a theoretical study was performed to investigate a catalytic mechanism for the reductive silylation of  $N_2$  by **1**.<sup>29</sup> Three mechanistic pathways were calculated with the assumptions that 1) the reducing conditions present for catalysis results in  $SiMe_3$  radical as the active silyl reagent<sup>162</sup> and 2) the bimetallic species is primarily anionic throughout the mechanism.<sup>29</sup> All three proposed mechanistic pathways (Figure 5.4) begin with two consecutive additions of  $SiMe_3$  radical to the distal nitrogen of the  $Co-N_2$  unit to form the disilylhydrazido species,  $[LCo_2N_2(SiMe_3)_2]^-$ . The first path (I) involves a third addition of  $SiMe_3$  radical to the distal nitrogen, followed by  $N-N$  bond cleavage to give a cobalt nitrido ( $Co\equiv N$ ) intermediate. However, the third  $SiMe_3$  radical is unable to add to the distal nitrogen due to the high barrier caused by the steric bulk of the  $SiMe_3$  group in combination with the isopropyl groups on the ligand. The other pathways (II and III) involve the third addition of the  $SiMe_3$  radical to the proximal nitrogen. Pathway II follows a fourth  $SiMe_3$  radical addition to the distal nitrogen, followed by  $N-N$  bond cleavage to give a metal imido ( $Co=NSiMe_3$ ) intermediate. Similar to path I, path II is ruled out by the high barrier

<sup>3</sup> Multiple runs show a lower overall TON ( $122 \pm 7$ ) of the  $Co_2L$  complex when quantified via the indophenol method vs. the GC quantification method provided in Table 5.1

for a third distal SiMe<sub>3</sub> attack on the distal N. The steric hindrance created by the isopropyl phosphines leaves path III as a viable route, involving the expulsion and spontaneous conversion of [N<sub>2</sub>(SiMe<sub>3</sub>)<sub>3</sub>]<sup>-</sup> into 2 equivalents of N(SiMe<sub>3</sub>)<sub>3</sub>.<sup>162</sup>

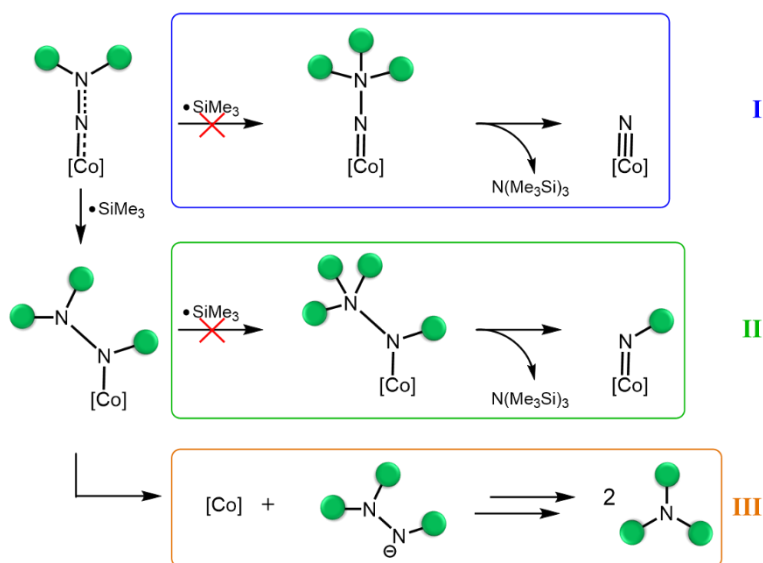


**Figure 5.4** Investigated mechanistic routes to the reductive silylation of N<sub>2</sub>. Green circles represent SiMe<sub>3</sub> groups and [Co] represents the active Co center of the bimetallic catalyst.

All five CoML catalysts were found to follow Pathway III as the general mechanistic route. As the steric bulk played a major factor in the general mechanistic pathway, ligand hemi-lability has also been found to play a key role during the catalysis. In order to have a large enough pocket for the third addition of SiMe<sub>3</sub> radical to the proximal N, one of the phosphine ligand arms must decoordinate from the top cobalt, to form an “open” intermediate. One obvious difference in the mechanistic pathways between CoAIL and the other CoML bimetallics is the hemi-lability of a phosphine arm to create space for the reactivity to occur. Figure 5.5 shows the calculated mechanism for four of the five CoML (M = Co, Cr, V, Ti) complexes. In this route, two additions of SiMe<sub>3</sub> radical form intermediate D, which then creates sufficient steric strain to decoordinate a phosphine arm, forming open intermediate D\* and creating sufficient room to add a third SiMe<sub>3</sub>. The ligand remains with two phosphine arms bound and one phosphine arm unbound until

$[\text{N}_2(\text{SiMe}_3)_3]^-$  is ejected, reforming the neutral CoML species. In the case of  $M = \text{Ti}, \text{V}, \text{Cr}$  and  $\text{Ti}$ , the decooordination of the phosphine comes after the rate determining step, C to D. The activation barrier of the rate determining step for all four of these complexes are within error of each other, from 16 – 18 kcal/mol.

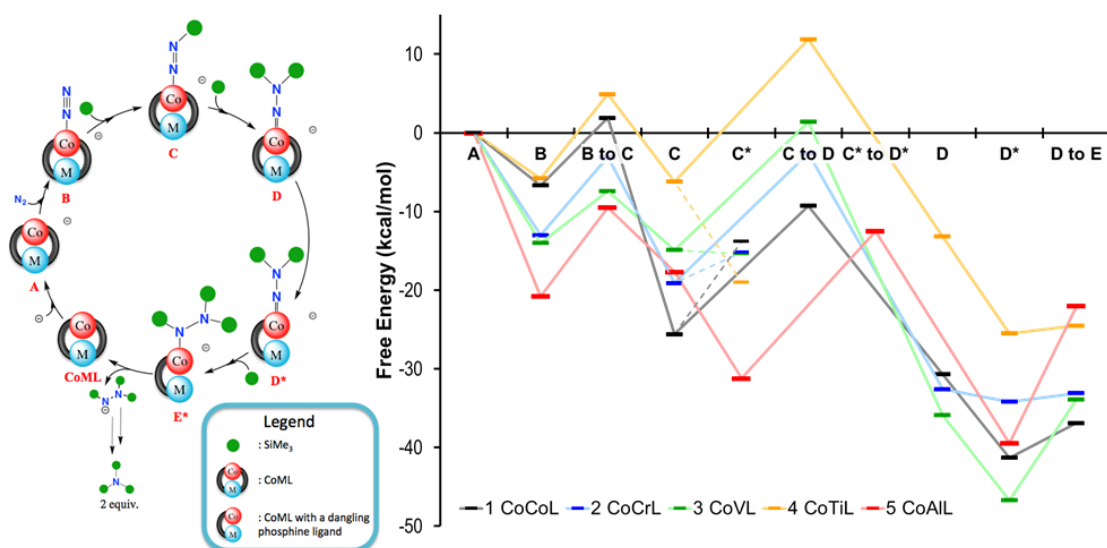


**Figure 5.5** Calculated mechanism for the bimetallic mediated silylation of  $\text{N}_2$ . The mechanistic cycle is present on the left, with intermediates containing a dangling phosphine arm are labeled with an asterisk, e.g.,  $\text{D}^*$ . The energetics of the intermediates for each CoML catalyst are shown on the right. Solid lines represent the most energetically favorable mechanistic pathway, while dashed lines represent the free energies of the decooordination of a phosphine at intermediate C, prior to the rate determining step.

However, CoAIL appears to have the most labile phosphine ligands as a phosphine arm decoordinates after only one addition of  $\text{SiMe}_3$ , causing closed intermediate C to form open intermediate  $\text{C}^*$ . This phosphine decooordination step occurs prior to the rate determining step for CoAIL, altering the transition state to have an open structure making the rate determining step  $\text{C}^*$  to  $\text{D}^*$ . The activation barrier of  $\text{C}^*$  to  $\text{D}^*$  is higher in CoAIL at 20.3 kcal/mol, suggesting that this higher activation barrier leads at least in part to the lower experimental TON seen for CoAIL.

### 5.4.2 Electronic structure during catalysis

A spin density analysis was done for the CoML intermediates throughout the catalytic cycle. Plots of the spin density throughout catalysis are shown in Figure 5.6. CoTiL is omitted from these plots due to poor structural agreement between the DFT optimized and experimental structures of CoTiL, with the Co–Ti calculated to be over 1 Å longer than the experimental bond length.<sup>4</sup> The spin density plots reveal information about the oxidation states of the metals during the catalysis as well as the covalency of binding of the N<sub>2</sub> unit to the Co center. The spin density on the supporting metal tends to remain constant throughout the catalytic cycle with the exception of CoCrL, which undergoes a change of approximately one electron prior to the rate determining step (Figure 5.6, top). This change in spin density in Cr causes the electronic structure of the CoCrL complex to have a Cr(II) supporting metal, which resembles the Co<sub>2</sub>L structure rather than the M(III) supporting metal in the rest of the group (Appendix, Figure A4.6). A decrease in Co spin density is seen at intermediate C, where the N<sub>2</sub> unit begins to become functionalized with SiMe<sub>3</sub> groups. A correlation in increase spin density at intermediate C is seen in CoAlL and CoVL, suggesting that N<sub>2</sub> unit has more radical nature, but becomes more covalent after the isomerization to the open intermediate.

The Co<sub>2</sub>L electronic structure is unique out of the three complexes because the supporting cobalt stays, generally, Co(II) throughout the catalytic cycle, while the other supporting metals are M(III). This forces the Co<sub>p</sub> in Co<sub>2</sub>L to be roughly at least a half oxidation state higher during the catalytic cycle (Co oxidation state plot). The more electropositive nature of this cobalt may indicate slightly higher affinity for the anionic N<sub>2</sub>-based ligand. The Co<sub>2</sub>L complex also undergoes a spin state change upon decoordination of the phosphine arm, where it becomes low spin in the open complex, likely due to a stronger interaction between the two cobalt metals.

---

<sup>4</sup> Plots including CoTiL can be found in the appendix, Figure A4.7.

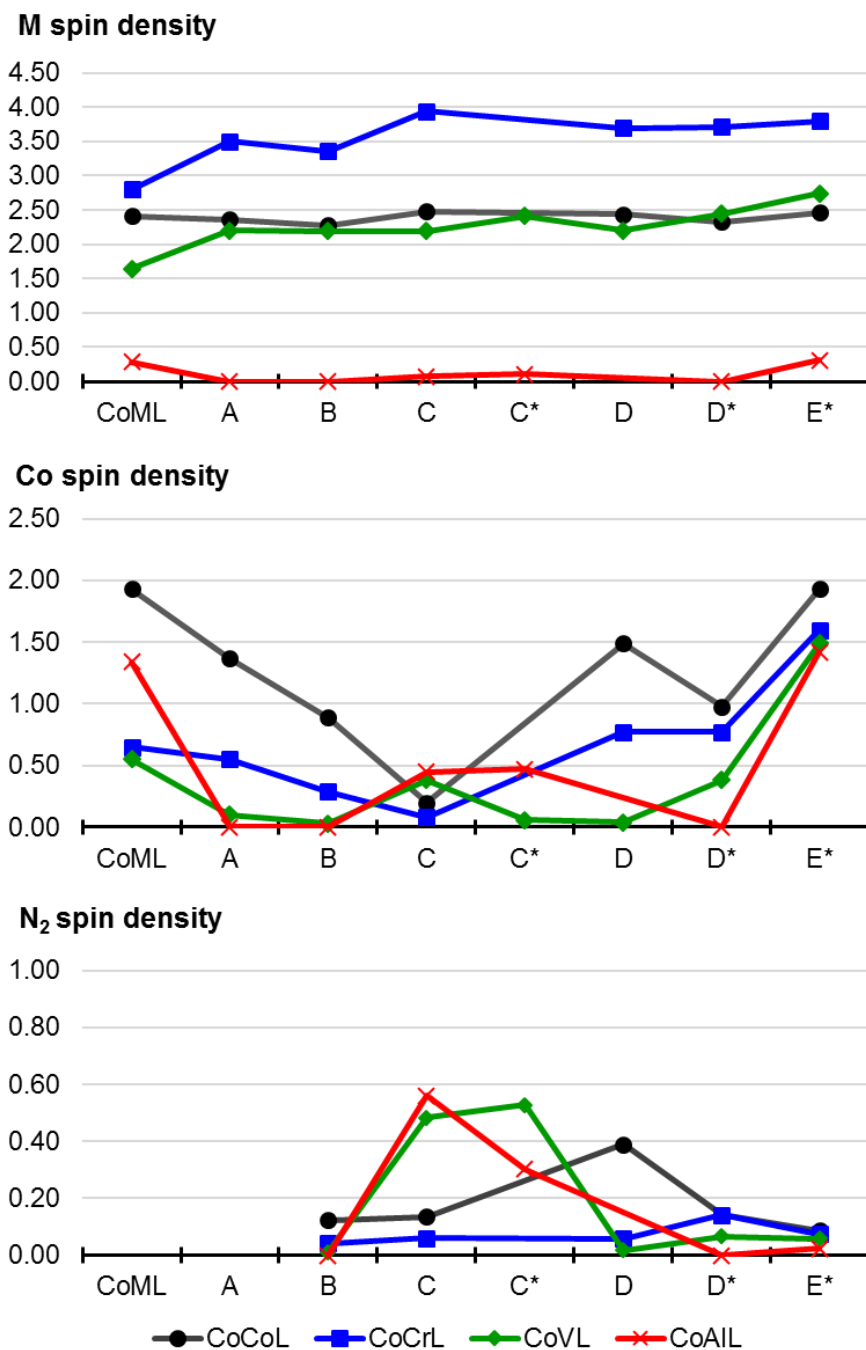


**Figure 5.6** Plot of the spin density values (number of unpaired electrons) located at supporting metal M (top), Co (middle) and N<sub>2</sub> (bottom) throughout the catalytic cycle. The absolute value of the spin density is displayed.

### 5.4.3 Ligand hemi-lability and Co–M interactions

The energy of the barriers ( $\Delta G^\ddagger$ ) of the rate determining step, C to D, are similar for catalysts **1** – **4**, so an alternate explanation for the differences in catalytic activity for these complexes was sought. The phosphine ligand decooordination plays a crucial role in the catalytic mechanism for the reduction of  $N_2$  to tris(trimethylsilyl)amine (Figure 5.8). The steric bulk of the ligand requires the dissociation of a phosphine ligand from the active Co in order for the necessary equivalents of  $SiMe_3$  radical to attack and reduce  $N_2$ . The timing of the dissociation of the phosphine appears to be important to the catalytic activity. The metal combinations in which the phosphine dissociates after a single addition of  $SiMe_3$  at intermediate C (Figure 5.7) are interpreted to be less robust catalysts, perhaps because this dissociation occurs prior to the rate determining second  $SiMe_3$ –addition. The build-up of an “open” intermediate prior to the rate determining step leaves  $C^*$  more vulnerable to decomposition, which could be seen in CoAIL and CoTiL. When the phosphine dissociates at intermediate D to form  $D^*$  after the rate determining step, the formation and dissociation of the hydrazido fragment is essentially barrierless, and higher turnovers are achieved.

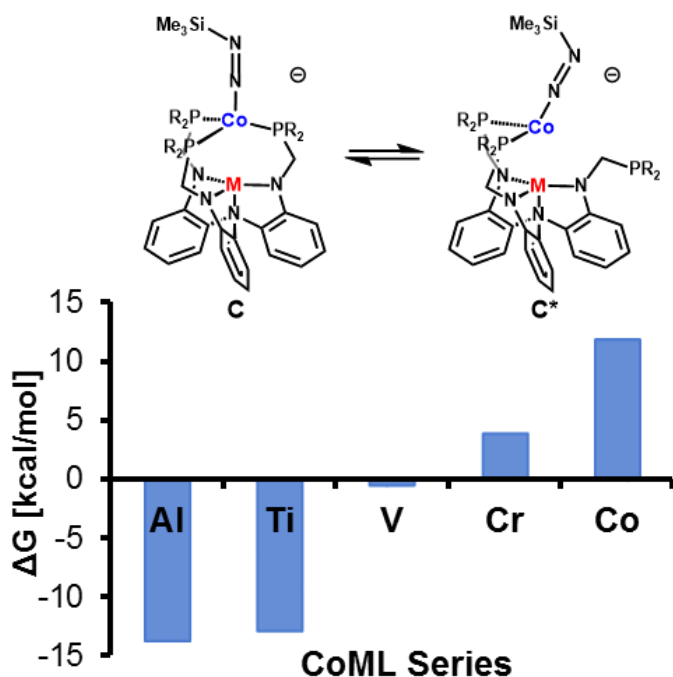


**Figure 5.7** Decoordination of one phosphine ligand on intermediate C to  $C^*$  (top) and the energy difference ( $\Delta G$ , kcal/mol) between  $C^*$  and C (bottom).



On the surface, the role of the Co–M interaction appears to be negligible, due largely in part to the lack of a strong interaction during the majority of the catalytic mechanism. However, the hemi-lability of the phosphine arm relies on the interaction between Co and the supporting metal. Figure 5.9 shows the change in the Co–M interaction throughout the catalytic cycle when compared to intermediate B. Positive values in the plot indicate that the Co–M distance is elongated. The variability of the Co–M interaction is different amongst the three catalytic groups, where the CoAIL interaction is constant while the Co<sub>2</sub>L undergoes a wide array of changes throughout the mechanism. The remaining mid-range catalysts do see some change in Co–M interactions, albeit very minor. The distance between Al and Co changes less than 0.1 Å throughout the catalytic cycle, implying the Co–Al remains intact throughout the catalytic cycle. This remaining interaction in the Co–Al pairing may be what stabilizes Co in the top pocket, allowing a phosphine arm to decoordinate more easily and at an earlier state in the catalytic cycle. CoML catalysts where M = Ti and V were also seen to be in equilibrium between C and C\* (Figure 5.7) and exhibit a very small change (< 0.07 Å) in their Co–M distance, suggesting that a stronger Co–M interaction stabilizes the Co center to lose a phosphine ligand.<sup>93,167</sup> Further support for a Co–M interaction stabilizing the open intermediates can be seen in the drastic decrease of the Co–Co distance upon the decoordination of the phosphine ligand in D to D\* (Figure 5.9).

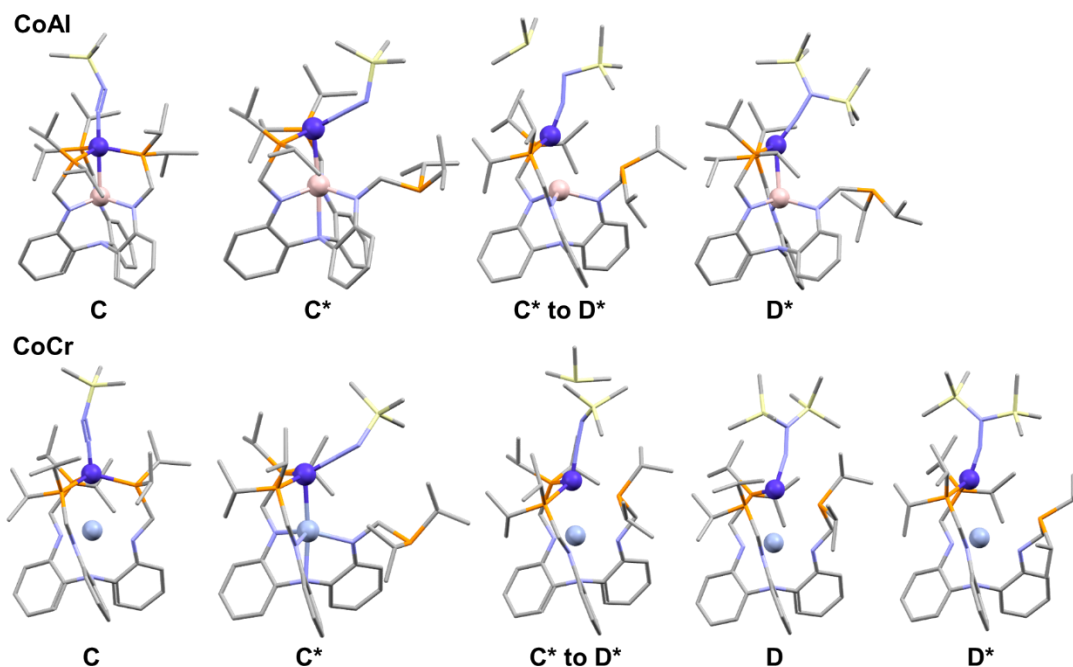


**Figure 5.8** DFT optimized structures of intermediates C through D\* for CoAl and CoCr

Tracking the Co–P bond distances throughout the catalytic cycle can also provide insight into the hemi-lability of a phosphine donor. Figure 5.10 follows the progress of the longest Co–P distance plotted with the average Co–P distance of the remaining two phosphine ligands. Unsurprisingly, the hemi-labile phosphine to cobalt distance changes dramatically, over 2 Å, in an open intermediate. Upon closer inspection (Figure 5.10, bottom), it is noted that the Co–P distances tend to be longer in closed intermediates and shorten when the third phosphine is no longer bound to Co. These trends in Co–P distances between the closed and open isomers hold true for both intermediates C and D. Another trend seen over the CoML complexes is the elongated Co–P distance in C\* is approximately 1 Å longer than the Co–P distance in D\*. The optimized structures show that the phosphine electron lone pair is pointing away from the Co center in C\* but appears to point towards the Co D\* (Figure 5.8). Although it appears that the dangling P ligand could have a weak interaction with the Co in D\*, the Co–P distance is not within the sum of their van der Waals radii. A possible explanation for this difference is that the main contributor to the hemi-lability of the phosphine ligand in C\* is due to the electronic environment of the Co, where more electron-poor Co holds onto the phosphine ligand more

strongly. However, in intermediate D\*, the hemi-lability of the phosphine is now due to the steric strain caused by the second addition of a SiMe<sub>3</sub> radical, which is found to be energetically favorable for all CoM complexes.

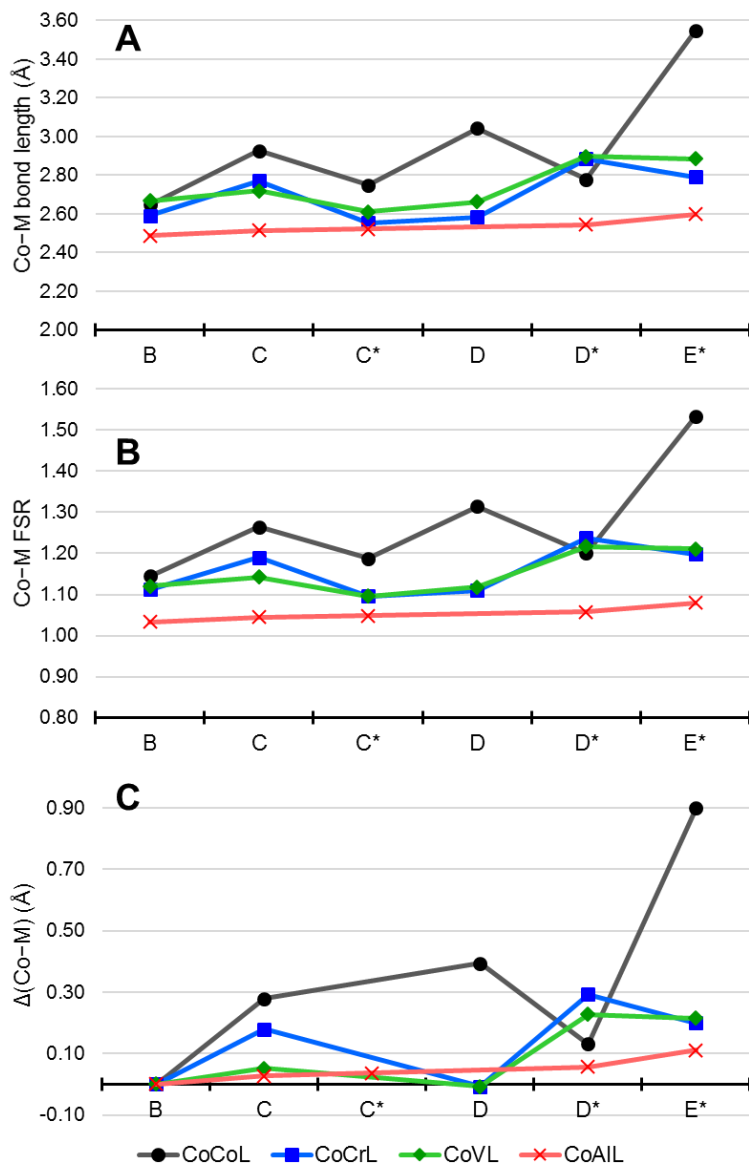


**Figure 5.9** (A) Plot of the Co–M bond distance (Å) in intermediates B through E\* taken from the DFT geometry optimized structures (B) FSR plot for the Co–M distance; (C) Plot of the change in Co–M distance (Å) throughout the catalytic cycle, the difference is calculated as Co–M distance in intermediate B subtracted from the distance in each intermediate. Positive values indicate a longer Co–M distance.<sup>5</sup>

<sup>5</sup> Plots for CoTiL omitted due to inconsistent DFT results (*vide supra*), figures showing CoTiL in plots can be seen in Appendix Figures A4.8 and A4.9.

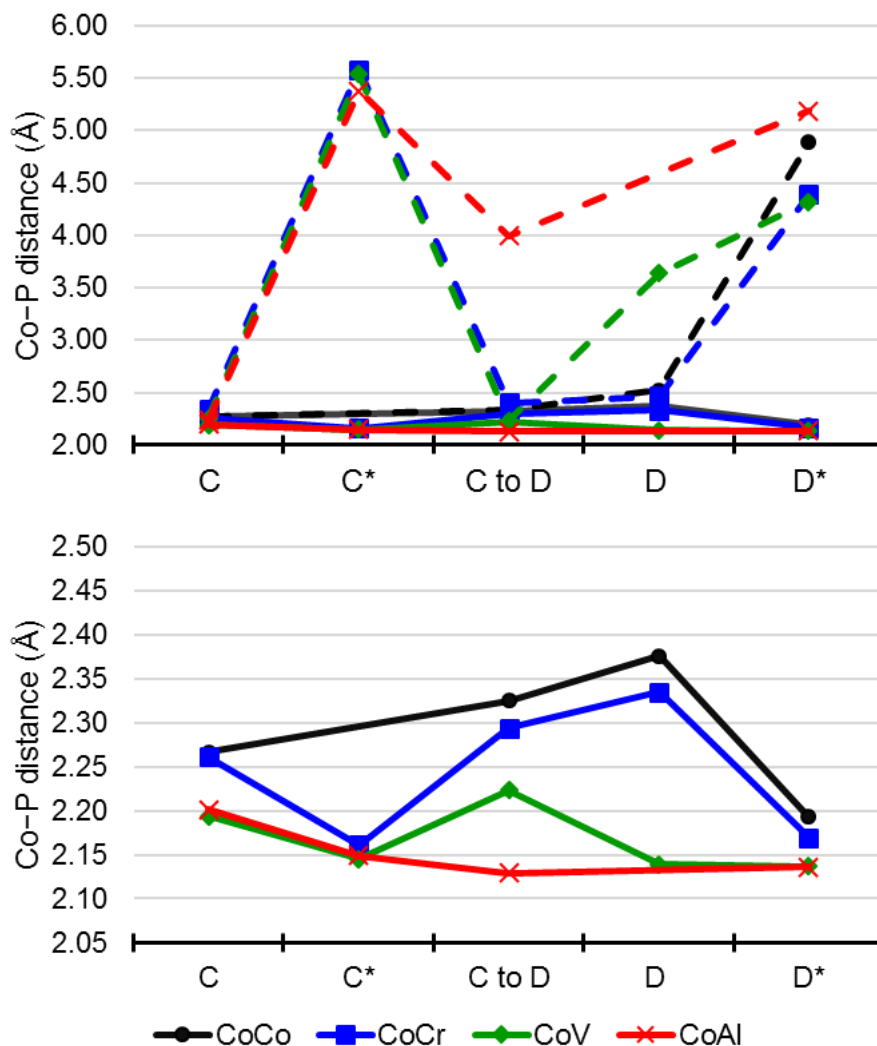


**Figure 5.10** Plot of the Co–P distances (Å) from the DFT optimized intermediates (top) with an enlargement of the shorter distances shown below. Solid lines represent the average distance of the two closest phosphines and dashed lines represent the longest Co–P distance.

Catalyst stability is a viable explanation for the differences in catalytic activity. During stoichiometric attempts to isolate a silylated intermediate, a decomposition product with a resonance in the  $^{31}\text{P}$  NMR spectrum at  $-43.9$  ppm was detected. This decomposition product was identified as  $^i\text{Pr}_2\text{PSiMe}_3$  through an independent synthesis of the compound.<sup>168</sup> The  $^i\text{Pr}_2\text{PSiMe}_3$  resonance was detected during *in-operando* studies with all five CoML catalysts when 10 equivalents of  $\text{KC}_8$  and  $\text{TMSCl}$  were allowed to react for 30 min. The  $^i\text{Pr}_2\text{PSiMe}_3$  was quantified in these *in-operando* studies to determine if the amount of

catalyst decomposition corresponded to the turnover numbers for the CoML catalysts. The  $^1\text{Pr}_2\text{PSiMe}_3$  is presumed to be formed when a phosphine arm is decoordinated from the cobalt center, as it was found to be in the open intermediates C\* and D\* along the mechanistic pathway. If the phosphine arm must be free in order to be susceptible to decomposition, CoML catalysts that are more likely to form open intermediates would sustain more decomposition during catalysis, resulting in lower turnovers. This statement holds true for catalysts **2** – **4** during the *in-operando* studies, with the most  $^1\text{Pr}_2\text{PSiMe}_3$  detected for **4**, followed by **3** and with **2** having the least amount of  $^1\text{Pr}_2\text{PSiMe}_3$  detected (appendix, Figure A4.5). Surprisingly, complex **5** showed the least amount of  $^1\text{Pr}_2\text{PSiMe}_3$ , but the appearance of a free ligand resonance could imply that demetallation of the ligand has occurred, perhaps with the assistance of  $^1\text{Pr}_2\text{PSiMe}_3$  ligands. These studies are at best qualitative due to the complicated nature of the possible decomposition products. Typical catalytic conditions can lead to further decomposition of  $^1\text{Pr}_2\text{PSiMe}_3$  via reduction or metal ligation, which can be more difficult to track with  $^{31}\text{P}$  NMR spectroscopy.

Because previous studies demonstrate that  $\text{CoCl}_2$  with three alkyl phosphine ligands can provide high turnovers when subjected to the same catalytic conditions, three equivalents of  $^1\text{Pr}_2\text{PSiMe}_3$  with an equivalent of  $\text{CoCl}_2$  was used as a control to identify the effect this possible *in-situ* generated complex could have after CoML decomposition. The results of the  $^1\text{Pr}_2\text{PSiMe}_3$  control along with other relevant controls are listed in table 5.2. The modest TON of 64 from  $^1\text{Pr}_2\text{PSiMe}_3$  with  $\text{CoCl}_2$  suggests that while decomposed CoML catalyst could contribute to the overall TON, the significantly higher TON in the cases of CoML catalysts where M = Ti, V, Cr, and Co, suggest that the decomposition cannot account for the observed activity.

**Table 5.2** Catalytic results for the formation of N(SiMe<sub>3</sub>)<sub>3</sub> with alternative Co based catalysts

Precatalyst	% yield	TON
CoCl <sub>2</sub>	1	6 ± 2
CoCl <sub>2</sub> + 3 PMe( <i>i</i> -Pr) <sub>2</sub>	14	94 ± 19
2 CoCl <sub>2</sub> + LH <sub>3</sub>	25	172 ± 16
CoCl <sub>2</sub> + LH <sub>3</sub>	16	103 ± 20
CoCl <sub>2</sub> + 3 ( <i>i</i> -Pr) <sub>2</sub> PSiMe <sub>3</sub>	10	64 ± 3

## 5.5 Conclusion

A series of five Co bimetallic complexes were found to be competent catalysts for the reduction of N<sub>2</sub> to N(SiMe<sub>3</sub>)<sub>3</sub>. The homobimetallic Co<sub>2</sub>L maintained the highest catalytic activity, followed by the early/late heterobimetallic complexes: CoCrL, CoVL, and CoTiL. Theoretical calculations revealed all CoML complexes follow the same general catalytic mechanism, with the CoAIL having the highest barrier, potentially due to the stabilization of an open C isomer immediately preceding the transition state. The remaining four CoML bimetallics cannot be distinguished by the barrier's energy of the rate determining step, but the differences in the hemi-lability of a phosphine ligand provides some suggestions as to the different catalytic abilities of the bimetallics. The Co<sub>2</sub>L catalyst strikes the best compromise between the strength of the Co–M interaction and the Co–P binding to decoordinate a phosphine arm after the rate determining step to achieve a straightforward route to catalysis in addition to a more robust catalyst. The supporting metal was found to play a crucial role on the hemi-lability of the phosphine ligand, which was found to be essential for catalysis.

## 5.6 Experimental Section

*General procedure for the catalytic reduction of  $N_2$  into  $N(\text{SiMe}_3)_3$  and analysis by GC-MS.*

A concentrated stock solution of precatalyst in THF was prepared, and an aliquot of the stock solution containing 5.2  $\mu\text{mol}$  of precatalyst was transferred to a 100 mL sealable, cylindrical, thick walled reaction flask. The aliquot was diluted with THF to have a final volume of 40 mL, achieving a final concentration of precatalyst to be 0.13 mM.  $\text{Me}_3\text{SiCl}$  (1.3 mL, 10.5 mmol) was added to the flask followed by the addition of  $\text{KC}_8$  (1.4 g, 10.4 mmol) and the flask was sealed and stirred at RT for 15 h. A Büchner funnel was used to filter off the graphite of the reaction solution and the solids were washed with portions of THF (3 x 10mL). The filtrate was condensed to approx. 5 mL by rotary evaporation and then the volatiles were subsequently vacuum transferred with heating to collect the organic products. The collected solution was diluted in THF to 25.0 mL and a 1.0 mL aliquot was mixed with a 1:1 volumetric ratio of a 30.0 mM fluorenone standard solution in THF. The sample was then analyzed by GC-MS to quantify the concentration of  $N(\text{SiMe}_3)_3$ .

*General procedure for the catalytic reduction of  $N_2$  into  $N(\text{SiMe}_3)_3$  and analysis by UV-vis*

A concentrated stock solution of precatalyst (1.56 mM) in THF was prepared and a 1.0 mL aliquot of the stock solution was transferred to a 20 mL scintillation vial containing  $\text{KC}_8$  (0.421 g, 3.12 mmol) and 11 mL of THF to total 12 mL overall.  $\text{Me}_3\text{SiCl}$  (0.4 mL, 3.15 mmol) was added to the vial and the vial was sealed and allowed to stir overnight. An aliquot (~5 mL) of the reaction solution was filtered to remove graphite, and a 3.0 mL portion of the filtered reaction solution was quenched overnight with 3 mL of 20% aqueous HCl solution to convert  $N(\text{SiMe}_3)_3$  into  $\text{NH}_4\text{Cl}$ . The quenched reaction solution was diluted with  $\text{H}_2\text{O}$  to 10.0 mL and an 80  $\mu\text{L}$  aliquot was subjected to the indophenol method to quantify ammonia.<sup>165,166</sup> The indophenol method was carried out by mixing the 80  $\mu\text{L}$  aliquot with aqueous solutions of nitroprusside/phenol (10 mL) and NaOH/NaOCl (10 mL) and after 30 min, the mixture was analyzed by UV-vis spectroscopy to determine the concentration of indophenol ( $\lambda = 625 \text{ nm}$ ).

*In-operando studies to identify catalyst decomposition*

Precatalyst, CoML, (0.010 mmol) is dissolved in 5 mL THF and added to a vial containing KC<sub>8</sub> (13.5 mg, 0.10 mmol). Me<sub>3</sub>SiCl (13.0  $\mu$ L, 0.10 mmol) was added, and the reaction was allowed to stir for 30 minutes. The reaction solution was filtered, and the volatiles were removed *in vacuo*. The remaining residue was taken up in 0.5 mL of THF with a PPh<sub>3</sub> standard (0.02 mmol) and a <sup>31</sup>P NMR spectrum was taken. The PPh<sub>3</sub> standard peak (−5.4 ppm) was integrated and calibrated to 1.0, and the peak at −43.9 ppm (<sup>1</sup>Pr<sub>2</sub>PSiMe<sub>3</sub>) was integrated to determine the amount of decomposed phosphine present.

*General procedure for the kinetic studies of the catalytic reduction of N<sub>2</sub> to N(SiMe<sub>3</sub>)<sub>3</sub> (method 1)*

Precatalyst (0.014 mmol) was dissolved in 110 mL THF (0.13 mM) in a 240 mL glass jar with a Teflon cap. Me<sub>3</sub>SiCl (3.6 mL, 28.4 mmol) was added to the jar, followed by the addition of KC<sub>8</sub> (3.87 g, 28.7 mmol). Reaction time began at the addition of KC<sub>8</sub> and ~4 mL aliquots were removed from the reaction solution at varying time points (t = 1, 2, 5, 10, 15, 20, 30, 40, 50, 60 min). The aliquots were filtered immediately to remove solids, and 3.0 mL of each aliquot was transferred to a vial. To convert N(SiMe<sub>3</sub>)<sub>3</sub> into NH<sub>4</sub>Cl, 3 mL of a 20% HCl solution was added to each aliquot and stirred overnight. The reaction mixtures were then diluted with H<sub>2</sub>O to 10.0 mL and an 80.0  $\mu$ L aliquot was subjected to the quantification of ammonia via the indophenol method.<sup>165,166</sup> The reaction aliquot was mixed with fresh aqueous solutions of nitroprusside/phenol (10 mL) and NaOH/NaOCl (10 mL). After 30 min, the reaction was analyzed by UV-vis spectroscopy to determine the concentration of indophenol ( $\lambda_{\text{max}} = 625$  nm).



*General procedure for the kinetic studies of the catalytic reduction of N<sub>2</sub> to N(SiMe<sub>3</sub>)<sub>3</sub> (method 2)*

A concentrated stock solution of precatalyst (1.56 mM) in THF was prepared and a 1.0 mL aliquot of the stock solution was transferred to a 20 mL scintillation vial containing KC<sub>8</sub> (0.421 g, 3.12 mmol) and 11 mL of THF to total 12 mL overall. Me<sub>3</sub>SiCl (0.4 mL, 3.15 mmol) was added to the vial and the vial was sealed and allowed to stir for its allotted time (t = 10, 20, 30, 60, 90, 120, 180, 240, 360 min). All nine reactions were set up subsequently. An aliquot (~5 mL) of the reaction solution was filtered to remove graphite, and a 3.0 mL portion of the filtered reaction solution was quenched overnight with 3 mL of 20% aqueous HCl solution to convert N(SiMe<sub>3</sub>)<sub>3</sub> into NH<sub>4</sub>Cl. The quenched reaction solution was diluted with H<sub>2</sub>O to 10.0 mL and an 80 μL aliquot was subjected to the indophenol method to quantify ammonia.<sup>165,166</sup> The indophenol method was carried out by mixing the 80 μL aliquot with aqueous solutions of nitroprusside/phenol (10 mL) and NaOH/NaOCl (10 mL) and after 30 min, the mixture was analyzed by UV-vis spectroscopy to determine the concentration of indophenol ( $\lambda = 625$  nm).

## **5.7 Computational Details**

Full geometry optimizations were performed on all structures by using density functional theory (DFT) level of theory with the M06-L<sup>121</sup> functional and the def2-TZVP (for K, N, P, Al, Ti, V, Cr and Co atoms) / def2-SVP (for C, H atoms) basis sets<sup>107</sup>. The experimental crystal structures of the dinitrogen adducts of CoAlL, CoVL and CoCrL anionic species were used as initial geometries for their corresponding calculated structures. Geometries for the Co<sub>2</sub>L species were taken from Ref. <sup>29</sup>. All optimized intermediate structures were found to have all real frequencies. All optimized transition states were found to have a single imaginary frequency along the reaction coordinate. Gibbs free energies ( $\Delta G$ ) at 298.15 K were computed by adding zero-point vibrational energies, and thermal vibrational-rotational entropy in the quasi-harmonic approximation calculated at the M06-L/def2-TZVP (for K, N, P, Al, Ti, V, Cr and Co)/def2-SVP (for C, H) level. Solvation effects were also included by performing single-point calculations for all intermediates using the SMD solvation model<sup>116</sup> with the diffuse basis functions, def2-TZVPD<sup>142</sup> (for K,

N, P, Al, Ti, V, Cr and Co)(def2-SVP for C and H) and THF as the solvent. In summary, the energies of all calculated structures geometry optimizations were performed at the M06-L/def2-TZVP level, followed by single-point energy calculations at the M06-L/def2-TZVPD/SMD level of theory. The Gaussian09 suite of programs<sup>106</sup> was employed. Additionally, Natural Bond Orbital (NBO)<sup>115</sup> and CM5 charges<sup>143,144</sup> analysis were performed for all species and reported in Appendix, Table A4.7.

## Bibliography

- (1) Cotton, F. A.; Curtis, N. F.; Harris, C. B.; Johnson, B. F. G.; Lippard, S. J.; Mague, J. T.; Robinson, W. R.; Wood, J. S. *Science* **1964**, *145*, 1305.
- (2) *Multiple Bonds Between Metal Atoms*; 3rd Ed ed.; Springer: New York, NY, 2005.
- (3) Falvello, L. R.; Foxman, B. M.; Murillo, C. A. *Inorg. Chem.* **2014**, *53*, 9441.
- (4) Nguyen, T.; Sutton, A. D.; Brynda, M.; Fettinger, J. C.; Long, G. J.; Power, P. P. *Science* **2005**, *310*, 844.
- (5) In *Molecular Metal-Metal Bonds*; Wiley-VCH: Weinheim, Germany, 2015.
- (6) Stephan, D. W. *Coordination Chemistry Reviews* **1989**, *95*, 41.
- (7) Cooper, B. G.; Napoline, J. W.; Thomas, C. M. *Catalysis Reviews* **2012**, *54*, 1.
- (8) Morse, M. D. *Chem. Rev.* **1986**, *86*, 1049.
- (9) Spain, E. M.; Morse, M. D. *J. Phys. Chem.* **1992**, *96*, 2479.
- (10) Rudd, P. A.; Liu, S.; Planas, N.; Bill, E.; Gagliardi, L.; Lu, C. C. *Angew. Chem. Int. Ed.* **2013**, *52*, 4449.
- (11) Kuppuswamy, S.; Powers, T. M.; Krogman, J. P.; Bezpalko, M. W.; Foxman, B. M.; Thomas, C. M. *Chem. Sci.* **2013**, *4*, 3557.
- (12) Rudd, P. A.; Liu, S.; Gagliardi, L.; Young, V. G.; Lu, C. C. *J. Am. Chem. Soc.* **2011**, *133*, 20724.
- (13) Tereniak, S. J.; Carlson, R. K.; Clouston, L. J.; Young, V. G.; Bill, E.; Maurice, R.; Chen, Y.-S.; Kim, H. J.; Gagliardi, L.; Lu, C. C. *J. Am. Chem. Soc.* **2014**, *136*, 1842.
- (14) Zall, C. M.; Clouston, L. J.; Young, V. G.; Ding, K.; Kim, H. J.; Zhrebetskyy, D.; Chen, Y.-S.; Bill, E.; Gagliardi, L.; Lu, C. C. *Inorg. Chem.* **2013**, *52*, 9216.
- (15) Nagashima, H.; Sue, T.; Oda, T.; Kanemitsu, A.; Matsumoto, T.; Motoyama, Y.; Sunada, Y. *Organometallics* **2006**, *25*, 1987.

- (16) Greenwood, B. P.; Forman, S. I.; Rowe, G. T.; Chen, C.-H.; Foxman, B. M.; Thomas, C. M. *Inorg. Chem.* **2009**, *48*, 6251.
- (17) Kuppaswamy, S.; Bezpalko, M. W.; Powers, T. M.; Turnbull, M. M.; Foxman, B. M.; Thomas, C. M. *Inorg. Chem.* **2012**, *51*, 8225.
- (18) Krogman, J. P.; Foxman, B. M.; Thomas, C. M. *J. Am. Chem. Soc.* **2011**, *133*, 14582.
- (19) Clouston, L. J.; Bernales, V.; Cammarota, R. C.; Carlson, R. K.; Bill, E.; Gagliardi, L.; Lu, C. C. *Inorg. Chem.* **2015**, *54*, 11669.
- (20) Clouston, L. J.; Siedschlag, R. B.; Rudd, P. A.; Planas, N.; Hu, S.; Miller, A. D.; Gagliardi, L.; Lu, C. C. *J. Am. Chem. Soc.* **2013**, *135*, 13142.
- (21) Eisenhart, R. J.; Carlson, R. K.; Clouston, L. J.; Young, V. G.; Chen, Y.-S.; Bill, E.; Gagliardi, L.; Lu, C. C. *Inorg. Chem.* **2015**, *54*, 11330.
- (22) Wagner, F. R.; Noor, A.; Kempe, R. *Nat. Chem.* **2009**, *1*, 529.
- (23) Nair, A. K.; Harisomayajula, N. V. S.; Tsai, Y.-C. *Dalton Trans.* **2014**, *43*, 5618.
- (24) Miller, D. L., University of Minnesota, 2013.
- (25) Eames, E. V.; Hernández Sánchez, R.; Betley, T. A. *Inorg. Chem.* **2013**, *52*, 5006.
- (26) Zall, C. M., University of Minnesota, 2013.
- (27) Pauling, L. *J. Am. Chem. Soc.* **1947**, *69*, 542.
- (28) Eisenhart, R. J.; Rudd, P. A.; Planas, N.; Boyce, D. W.; Carlson, R. K.; Tolman, W. B.; Bill, E.; Gagliardi, L.; Lu, C. C. *Inorg. Chem.* **2015**, *54*, 7579.
- (29) Siedschlag, R. B.; Bernales, V.; Vogiatzis, K. D.; Planas, N.; Clouston, L. J.; Bill, E.; Gagliardi, L.; Lu, C. C. *J. Am. Chem. Soc.* **2015**, *137*, 4638.
- (30) La Macchia, G.; Li Manni, G.; Todorova, T. K.; Brynda, M.; Aquilante, F.; Roos, B. O.; Gagliardi, L. *Inorg. Chem.* **2010**, *49*, 5216.
- (31) Cotton, F. A.; Daniels, L. M.; Falvello, L. R.; Matonic, J. H.; Murillo, C. A. *Inorg. Chim. Acta* **1997**, *256*, 269.

- (32) Jones, C.; Schulten, C.; Rose, R. P.; Stasch, A.; Aldridge, S.; Woodul, W. D.; Murray, K. S.; Moubaraki, B.; Brynda, M.; La Macchia, G.; Gagliardi, L. *Angew. Chem. Int. Ed.* **2009**, *48*, 7406.
- (33) Zall, C. M.; Zhrebetsky, D.; Dzubak, A. L.; Bill, E.; Gagliardi, L.; Lu, C. C. *Inorg. Chem.* **2012**, *51*, 728.
- (34) Hopkins, M. D.; Gray, H. B.; Miskowski, V. M. *Polyhedron* **1987**, *6*, 705.
- (35) San Filippo, J. *Inorg. Chem.* **1972**, *11*, 3140.
- (36) Smith, J. M.; Subedi, D. *Dalton Trans.* **2012**, *41*, 1423.
- (37) Yu, R. P.; Darmon, J. M.; Milsmann, C.; Margulieux, G. W.; Stieber, S. C. E.; DeBeer, S.; Chirik, P. J. *J. Am. Chem. Soc.* **2013**, *135*, 13168.
- (38) Spatzal, T.; Aksoyoglu, M.; Zhang, L.; Andrade, S. L. A.; Schleicher, E.; Weber, S.; Rees, D. C.; Einsle, O. *Science* **2011**, *334*, 940.
- (39) Lancaster, K. M.; Roemelt, M.; Ettenhuber, P.; Hu, Y.; Ribbe, M. W.; Neese, F.; Bergmann, U.; DeBeer, S. *Science* **2011**, *334*, 974.
- (40) Einsle, O.; Tezcan, F. A.; Andrade, S. L. A.; Schmid, B.; Yoshida, M.; Howard, J. B.; Rees, D. C. *Science* **2002**, *297*, 1696.
- (41) Hoffman, B. M.; Lukoyanov, D.; Yang, Z.-Y.; Dean, D. R.; Seefeldt, L. C. *Chem. Rev.* **2014**, *114*, 4041.
- (42) Thomas, C. M. *Comments on Inorganic Chemistry* **2011**, *32*, 14.
- (43) Bullock, R. M.; Casey, C. P. *Acc. Chem. Res.* **1987**, *20*, 167.
- (44) Casey, C. P. *J. Organomet. Chem.* **1990**, *400*, 205.
- (45) Buchwalter, P.; Rosé, J.; Braunstein, P. *Chem. Rev.* **2015**, *115*, 28.
- (46) Wheatley, N.; Kalck, P. *Chem. Rev.* **1999**, *99*, 3379.
- (47) Mankad, N. P. *Chem. Eur. J.* **2016**, *22*, 5822.
- (48) Mazzacano, T. J.; Mankad, N. P. *J. Am. Chem. Soc.* **2013**, *135*, 17258.

- (49) Zhang, X.-X.; Wayland, B. B. *J. Am. Chem. Soc.* **1994**, *116*, 7897.
- (50) Holland, P. L. *Dalton Trans.* **2010**, *39*, 5415.
- (51) MacKay, B. A.; Fryzuk, M. D. *Chem. Rev.* **2004**, *104*, 385.
- (52) Rudd, P. A.; Planas, N.; Bill, E.; Gagliardi, L.; Lu, C. C. *Eur. J. Inorg. Chem.* **2013**, *2013*, 3898.
- (53) Eisenhart, R. J.; Clouston, L. J.; Lu, C. C. *Acc. Chem. Res.* **2015**, *48*, 2885.
- (54) Zhao, Q.; Betley, T. A. *Angew. Chem. Int. Ed.* **2011**, *50*, 709.
- (55) Powers, T. M.; Fout, A. R.; Zheng, S.-L.; Betley, T. A. *J. Am. Chem. Soc.* **2011**, *133*, 3336.
- (56) Eames, E. V.; Harris, T. D.; Betley, T. A. *Chem. Sci.* **2012**, *3*, 407.
- (57) Powers, T. M.; Betley, T. A. *J. Am. Chem. Soc.* **2013**, *135*, 12289.
- (58) Setty, V. N.; Zhou, W.; Foxman, B. M.; Thomas, C. M. *Inorg. Chem.* **2011**, *50*, 4647.
- (59) Wu, B.; Gramigna, K. M.; Bezpalko, M. W.; Foxman, B. M.; Thomas, C. M. *Inorg. Chem.* **2015**, *54*, 10909.
- (60) Zhou, W.; Saper, N. I.; Krogman, J. P.; Foxman, B. M.; Thomas, C. M. *Dalton Trans.* **2014**, *43*, 1984.
- (61) Napoline, J. W.; Bezpalko, M. W.; Foxman, B. M.; Thomas, C. M. *Chem. Commun.* **2013**, *49*, 4388.
- (62) Betley, T. A.; Peters, J. C. *J. Am. Chem. Soc.* **2003**, *125*, 10782.
- (63) Mankad, N. P.; Whited, M. T.; Peters, J. C. *Angew. Chem. Int. Ed.* **2007**, *46*, 5768.
- (64) Whited, M. T.; Mankad, N. P.; Lee, Y.; Oblad, P. F.; Peters, J. C. *Inorg. Chem.* **2009**, *48*, 2507.
- (65) Lee, Y.; Mankad, N. P.; Peters, J. C. *Nat. Chem.* **2010**, *2*, 558.

- (66) Moret, M.-E.; Peters, J. C. *Angew. Chem. Int. Ed.* **2011**, *50*, 2063.
- (67) Moret, M.-E.; Peters, J. C. *J. Am. Chem. Soc.* **2011**, *133*, 18118.
- (68) Suess, D. L. M.; Peters, J. C. *J. Am. Chem. Soc.* **2013**, *135*, 4938.
- (69) Anderson, J. S.; Rittle, J.; Peters, J. C. *Nature* **2013**, *501*, 84.
- (70) Creutz, S. E.; Peters, J. C. *J. Am. Chem. Soc.* **2014**, *136*, 1105.
- (71) Ung, G.; Peters, J. C. *Angew. Chem. Int. Ed.* **2015**, *54*, 532.
- (72) Del Castillo, T. J.; Thompson, N. B.; Peters, J. C. *J. Am. Chem. Soc.* **2016**, *138*, 5341.
- (73) Del Castillo, T. J.; Thompson, N. B.; Suess, D. L. M.; Ung, G.; Peters, J. C. *Inorg. Chem.* **2015**.
- (74) Arashiba, K.; Kinoshita, E.; Kuriyama, S.; Eizawa, A.; Nakajima, K.; Tanaka, H.; Yoshizawa, K.; Nishibayashi, Y. *J. Am. Chem. Soc.* **2015**, *137*, 5666.
- (75) Rittle, J.; Peters, J. C. *J. Am. Chem. Soc.* **2016**, *138*, 4243.
- (76) Suess, D. L. M.; Tsay, C.; Peters, J. C. *J. Am. Chem. Soc.* **2012**, *134*, 14158.
- (77) Nair, A. K.; Harisomayajula, N. V. S.; Tsai, Y.-C. *Inorg. Chim. Acta* **2015**, *424*, 51.
- (78) Kornecki, K. P.; Berry, J. F.; Powers, D. C.; Ritter, T. In *Progress in Inorganic Chemistry*; John Wiley & Sons, Inc.: 2014; Vol. 58.
- (79) Krogman, J. P.; Thomas, C. M. *Chem. Commun.* **2014**, *50*, 5115.
- (80) Collman, J. P.; Boulatov, R. *Angew. Chem. Int. Ed.* **2002**, *41*, 3948.
- (81) Murillo, C. A. In *Multiple Bonds Between Metal Atoms*; Cotton, F. A., Murillo, C. A., Walton, R. A., Eds.; Springer Science: New York, 2005, p 23.
- (82) Oishi, M.; Kino, M.; Saso, M.; Oshima, M.; Suzuki, H. *Organometallics* **2012**, *31*, 4658.

- (83) Langenberg, J. D.; Morse, M. D. *Chem. Phys. Lett.* **1995**, 239, 25.
- (84) Cotton, F. A. In *Multiple Bonds Between Metal Atoms*; Cotton, F. A., Murillo, C. A., Walton, R. A., Eds.; Springer Science: New York, 2005, p 35.
- (85) Greenwood, B. P.; Rowe, G. T.; Chen, C.-H.; Foxman, B. M.; Thomas, C. M. *J. Am. Chem. Soc.* **2010**, 132, 44.
- (86) Wu, B.; Bezpalko, M. W.; Foxman, B. M.; Thomas, C. M. *Chem. Sci.* **2015**, 6, 2044.
- (87) Clouston, L. J.; Bernales, V.; Carlson, R. K.; Gagliardi, L.; Lu, C. C. *Inorg. Chem.* **2015**, 54, 9263.
- (88) Pyykkö, P.; Riedel, S.; Patzschke, M. *Chem. Eur. J.* **2005**, 11, 3511.
- (89) Pyykkö, P.; Atsumi, M. *Chem. Eur. J.* **2009**, 15, 12770.
- (90) Bertini, I.; Luchinat, C.; Parigi, G. In *Solution NMR of Paramagnetic Molecules*; Elsevier: Amsterdam, Netherlands, 2001, p 189.
- (91) McConnell, H. M.; Holm, C. H. *J. Chem. Phys.* **1957**, 27, 314.
- (92) Harris, R. K. *Nuclear Magnetic Resonance Spectroscopy*; Longman: London, 1986.
- (93) Sircoglou, M.; Bontemps, S.; Bouhadir, G.; Saffon, N.; Miqueu, K.; Gu, W.; Mercy, M.; Chen, C.-H.; Foxman, B. M.; Maron, L.; Ozerov, O. V.; Bourissou, D. *J. Am. Chem. Soc.* **2008**, 130, 16729.
- (94) Evans, D. F. *J. Chem. Soc.* **1959**, 2003.
- (95) Smythe, N. C.; Schrock, R. R.; Müller, P.; Weare, W. W. *Inorg. Chem.* **2006**, 45, 9197.
- (96) Krzystek, J.; Fiedler, A. T.; Sokol, J. J.; Ozarowski, A.; Zvyagin, S. A.; Brunold, T. C.; Long, J. R.; Brunel, L.-C.; Telser, J. *Inorg. Chem.* **2004**, 43, 5645.
- (97) Perdew, J. P.; Ernzerhof, M.; Burke, K. *J. Chem. Phys.* **1996**, 105, 9982.
- (98) Chocholousova, J.; Spirko, V.; Hobza, P. *Phys. Chem. Chem. Phys.* **2004**, 6, 37.



- (99) Zhao, Y.; Truhlar, D. G. *Theor. Chem. Acc.* **2008**, *120*, 215.
- (100) Pregosin, P. S. *NMR in Organometallic Chemistry*; Wiley-VCH: Somerset, NJ, USA, 2012.
- (101) Sur, S. K. *J. Magn. Reson.* **1989**, *82*, 169.
- (102) O'Connor, C. J. *Progress in Inorganic Chemistry*; 29th ed.; John Wiley & Sons, Inc: New York, NY, 1982.
- (103) Weast, R. C. A., M. J. *CRC Handbook of Chemistry and Physics*; CRC Press Inc.: Boca Raton, FL, 1979.
- (104) Bruker; Bruker AXS Inc: Madison, WI USA, 2007.
- (105) Sheldrick, G. *Acta Crystallogr., Sect. A: Found. Crystallogr.* **2008**, *64*, 112.
- (106) Frisch, M. J.; Trucks, G. W.; Schlegel, H. B.; Scuseria, G. E.; Robb, M. A.; Cheeseman, J. R.; Scalmani, G.; Barone, V.; Mennucci, B.; Petersson, G. A.; Nakatsuji, H.; Caricato, M.; Li, X.; Hratchian, H. P.; Izmaylov, A. F.; Bloino, J.; Zheng, G.; Sonnenberg, J. L.; Hada, M.; Ehara, M.; Toyota, K.; Fukuda, R.; Hasegawa, J.; Ishida, M.; Nakajima, T.; Honda, Y.; Kitao, O.; Nakai, H.; Vreven, T.; Montgomery Jr., J. A.; Peralta, J. E.; Ogliaro, F.; Bearpark, M. J.; Heyd, J.; Brothers, E. N.; Kudin, K. N.; Staroverov, V. N.; Kobayashi, R.; Normand, J.; Raghavachari, K.; Rendell, A. P.; Burant, J. C.; Iyengar, S. S.; Tomasi, J.; Cossi, M.; Rega, N.; Millam, N. J.; Klene, M.; Knox, J. E.; Cross, J. B.; Bakken, V.; Adamo, C.; Jaramillo, J.; Gomperts, R.; Stratmann, R. E.; Yazyev, O.; Austin, A. J.; Cammi, R.; Pomelli, C.; Ochterski, J. W.; Martin, R. L.; Morokuma, K.; Zakrzewski, V. G.; Voth, G. A.; Salvador, P.; Dannenberg, J. J.; Dapprich, S.; Daniels, A. D.; Farkas, Ö.; Foresman, J. B.; Ortiz, J. V.; Cioslowski, J.; Fox, D. J.; Gaussian, Inc.: Wallingford, CT, USA, 2009.
- (107) Weigend, F.; Ahlrichs, R. *Phys. Chem. Chem. Phys.* **2005**, *7*, 3297.
- (108) Roos, B. O.; Taylor, P. R.; Siegbahn, E. M. *Chem. Phys.* **1980**, *48*, 157.
- (109) Aquilante, F.; De Vico, L.; Ferre, N.; Ghigo, G.; Malmqvist, P.-a.; Neogrady, P.; Pedersen, T. B.; Pitonak, M.; Reiher, M.; Roos, B. O.; Serrano-Andres, L.; Urban, M.; Veryazov, V.; Lindh, R. *J. Comput. Chem.* **2010**, *31*, 224.
- (110) Roos, B. O.; Lindh, R.; Malmqvist, P.-A.; Veryazov, V.; Widmark, P.-O. *J. Phys. Chem. A* **2004**, *108*, 2851.

- (111) Roos, B. O.; Lindh, R.; Malmqvist, P.-A.; Veryazov, V.; Widmark, P.-O. *J. Phys. Chem. A* **2005**, *109*, 6575.
- (112) Douglas, M.; Kroll, N. M. *Ann. Phys.* **1974**, *82*, 89.
- (113) Hess, B. A. *Phys. Rev. A: Gen. Phys.* **1986**, *33*, 3742.
- (114) Aquilante, F.; Lindh, R.; Bondo Pedersen, T. *J. Chem. Phys.* **2007**, *127*, 114107/1.
- (115) Glendening, E. D.; Reed, A. E.; Carpenter, J. E.; Weinhold, F.; 3.1 ed. 2013.
- (116) Marenich, A. V.; Cramer, C. J.; Truhlar, D. G. *J. Phys. Chem. B* **2009**, *113*, 6378.
- (117) Perdew, J. P.; Burke, K.; Ernzerhof, M. *Phys. Rev. Lett.* **1997**, *78*, 1396.
- (118) Becke, A. D. *J. Chem. Phys.* **1993**, *98*, 5648.
- (119) Yanai, T.; Tew, D. P.; Handy, N. C. *Chem. Phys. Lett.* **2004**, *393*, 51.
- (120) Zhao, Y.; Truhlar, D. G. *J. Phys. Chem. A* **2006**, *110*, 13126.
- (121) Zhao, Y.; Truhlar, D. G. *J. Chem. Phys.* **2006**, *125*, 194101/1.
- (122) Gade, L. H. *Angew. Chem. Int. Ed.* **2000**, *39*, 2658.
- (123) Kuppuswamy, S.; Bezpalko, M. W.; Powers, T. M.; Wilding, M. J. T.; Brozek, C. K.; Foxman, B. M.; Thomas, C. M. *Chem. Sci.* **2014**, *5*, 1617.
- (124) Friedrich, S.; Memmler, H.; Gade, L. H.; Li, W.-S.; McPartlin, M. *Angew. Chem. Int. Ed.* **1994**, *33*, 676.
- (125) Dunn, P. L.; Carlson, R. K.; Gagliardi, L.; Tonks, I. A. *Dalton Trans.* **2016**, Advance article.
- (126) Cotton, F. A.; Daniels, L. M.; Murillo, C. A.; Pascual, I.; Zhou, H.-C. *J. Am. Chem. Soc.* **1999**, *121*, 6856.
- (127) Cotton, F. A.; Ilsley, W. H.; Kaim, W. *J. Am. Chem. Soc.* **1980**, *102*, 3464.
- (128) Rozenel, S. S.; Padilla, R.; Arnold, J. *Inorg. Chem.* **2013**, *52*, 11544.

- (129) Chomitz, W. A.; Arnold, J. *Chem. Commun.* **2007**, 4797.
- (130) Bowman, A. C.; Milsmann, C.; Atienza, C. C. H.; Lobkovsky, E.; Wieghardt, K.; Chirik, P. J. *J. Am. Chem. Soc.* **2010**, *132*, 1676.
- (131) Archer, A. M.; Bouwkamp, M. W.; Cortez, M.-P.; Lobkovsky, E.; Chirik, P. J. *Organometallics* **2006**, *25*, 4269.
- (132) Ding, K.; Pierpont, A. W.; Brennessel, W. W.; Lukat-Rodgers, G.; Rodgers, K. R.; Cundari, T. R.; Bill, E.; Holland, P. L. *J. Am. Chem. Soc.* **2009**, *131*, 9471.
- (133) Smith, J. M.; Lachicotte, R. J.; Pittard, K. A.; Cundari, T. R.; Lukat-Rodgers, G.; Rodgers, K. R.; Holland, P. L. *J. Am. Chem. Soc.* **2001**, *123*, 9222.
- (134) Yu, R. P.; Darmon, J. M.; Hoyt, J. M.; Margulieux, G. W.; Turner, Z. R.; Chirik, P. J. *ACS Catal.* **2012**, *2*, 1760.
- (135) Lin, T.-P.; Peters, J. C. *J. Am. Chem. Soc.* **2013**, *135*, 15310.
- (136) Lin, T.-P.; Peters, J. C. *J. Am. Chem. Soc.* **2014**, *136*, 13672.
- (137) Imayoshi, R.; Tanaka, H.; Matsuo, Y.; Yuki, M.; Nakajima, K.; Yoshizawa, K.; Nishibayashi, Y. *Chem. Eur. J.* **2015**, *21*, 8905.
- (138) Marquard, S. L.; Bezpalko, M. W.; Foxman, B. M.; Thomas, C. M. *J. Am. Chem. Soc.* **2013**, *135*, 6018.
- (139) Krogman, J. P.; Bezpalko, M. W.; Foxman, B. M.; Thomas, C. M. *Inorg. Chem.* **2013**, *52*, 3022.
- (140) Huber, K. P.; Herzberg, G. *Molecular Spectra and Molecular Structure, 4: Constants of Diatomic Molecules*; Van Nostrand Reinhold, 1979.
- (141) Spek, A. L. *Acta Crystallogr., Sect. D: Biol. Crystallogr.* **2009**, *65*, 148.
- (142) Rappoport, D.; Furche, F. *J. Chem. Phys.* **2010**, *133*, 134105/1.
- (143) Marenich, A. V.; Cramer, C. J.; Truhlar, D. G.; University of Minnesota: Minneapolis, MN, 2011.
- (144) Marenich, A. V.; Jerome, S. V.; Cramer, C. J.; Truhlar, D. G. *J. Chem. Theory Comput.* **2012**, *8*, 527.

- (145) Andersson, K.; Malmqvist, P. A.; Roos, B. O. *J. Chem. Phys.* **1992**, *96*, 1218.
- (146) Vahtras, O.; Almloef, J.; Feyereisen, M. W. *Chem. Phys. Lett.* **1993**, *213*, 514.
- (147) Forsberg, N.; Malmqvist, P.-A. *Chem. Phys. Lett.* **1997**, *274*, 196.
- (148) Ertl, G. *Journal of Vacuum Science & Technology A* **1983**, *1*, 1247.
- (149) Ertl, G. *Angew. Chem. Int. Ed.* **2008**, *47*, 3524.
- (150) Burgess, B. K.; Lowe, D. J. *Chem. Rev.* **1996**, *96*, 2983.
- (151) Howard, J. B.; Rees, D. C. *Chem. Rev.* **1996**, *96*, 2965.
- (152) Kowalska, J.; DeBeer, S. *Biochimica et Biophysica Acta (BBA) - Molecular Cell Research* **2015**, *1853*, 1406.
- (153) Yandulov, D. V.; Schrock, R. R. *Science* **2003**, *301*, 76.
- (154) Arashiba, K.; Miyake, Y.; Nishibayashi, Y. *Nat. Chem.* **2011**, *3*, 120.
- (155) Kuriyama, S.; Arashiba, K.; Nakajima, K.; Tanaka, H.; Kamaru, N.; Yoshizawa, K.; Nishibayashi, Y. *J. Am. Chem. Soc.* **2014**, *136*, 9719.
- (156) Tanaka, H.; Arashiba, K.; Kuriyama, S.; Sasada, A.; Nakajima, K.; Yoshizawa, K.; Nishibayashi, Y. *Nat. Commun.* **2014**, *5*.
- (157) Chatt, J.; Dilworth, J. R.; Richards, R. L. *Chem. Rev.* **1978**, *78*, 589.
- (158) Chatt, J.; Leigh, G. J. *Chemical Society Reviews* **1972**, *1*, 121.
- (159) Shiina, K. *J. Am. Chem. Soc.* **1972**, *94*, 9266.
- (160) Komori, K.; Oshita, H.; Mizobe, Y.; Hidai, M. *J. Am. Chem. Soc.* **1989**, *111*, 1939.
- (161) Mori, M. *J. Organomet. Chem.* **2004**, *689*, 4210.
- (162) Tanaka, H.; Sasada, A.; Kouno, T.; Yuki, M.; Miyake, Y.; Nakanishi, H.; Nishibayashi, Y.; Yoshizawa, K. *J. Am. Chem. Soc.* **2011**, *133*, 3498.

- (163) Yuki, M.; Tanaka, H.; Sasaki, K.; Miyake, Y.; Yoshizawa, K.; Nishibayashi, Y. *Nat. Commun.* **2012**, *3*, 1254.
- (164) Liao, Q.; Saffon-Merceron, N.; Mézailles, N. *Angew. Chem. Int. Ed.* **2014**, *53*, 14206.
- (165) Bolleter, W. T.; Bushman, C. J.; Tidwell, P. W. *Anal. Chem.* **1961**, *33*, 592.
- (166) Weatherburn, M. W. *Anal. Chem.* **1967**, *39*, 971.
- (167) Bouhadir, G.; Bourissou, D. *Chemical Society Reviews* **2016**, *45*, 1065.
- (168) Bailey, J. A.; Haddow, M. F.; Pringle, P. G. *Chem. Commun.* **2014**, *50*, 1432.

## Appendix 1

Supporting information figures for Chapter 2

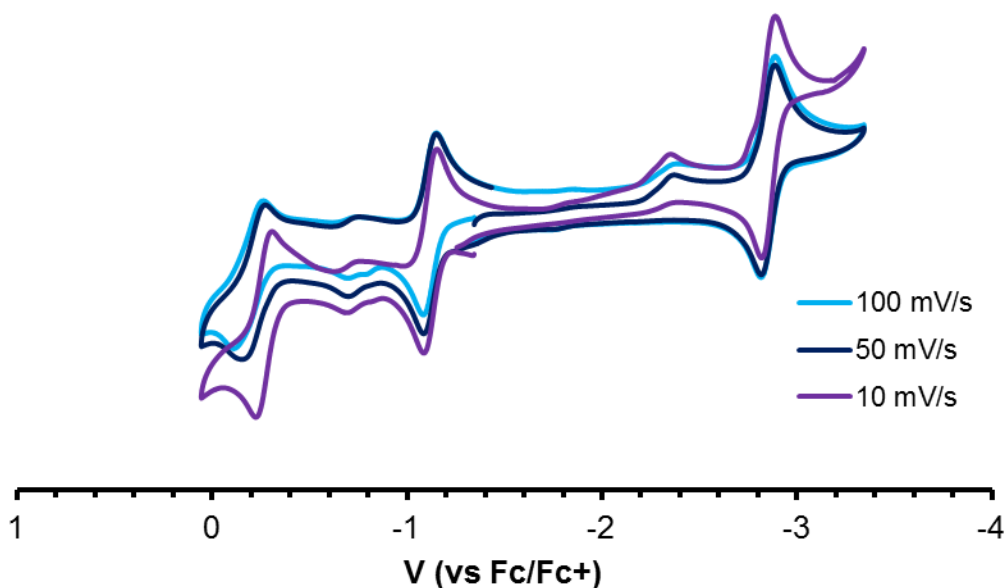


**Figure A1.1** Cyclic voltammetry study of **2** – FeV showing there is no scan speed dependence between 10 – 100 mV/s (0.4 M [<sup>n</sup>Bu<sub>4</sub>N][PF<sub>6</sub>] in THF). The current values were normalized by dividing the measured current by the square root of the scan speed.

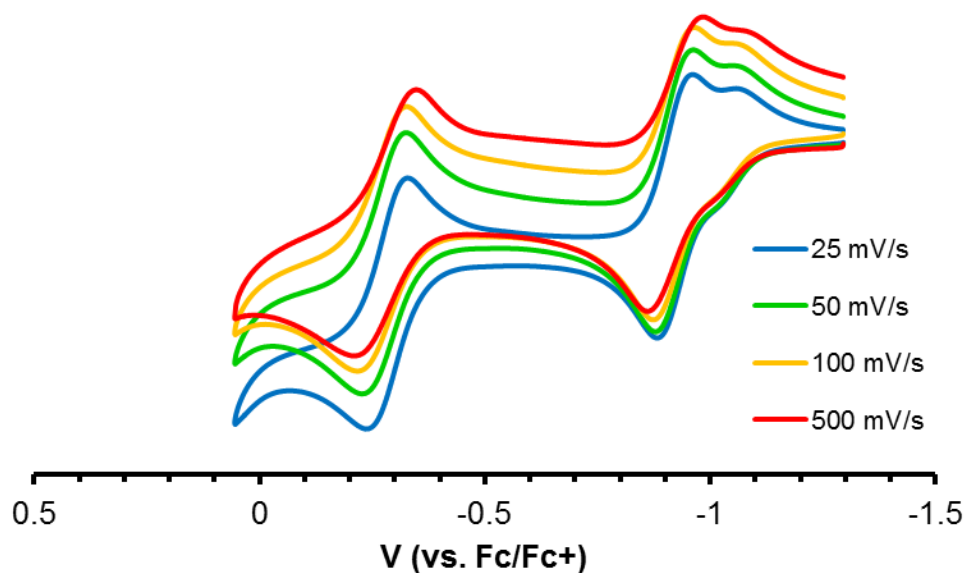


**Figure A1.2** Cyclic voltammetry study of **4** – NiV showing there is no scan speed dependence between 25 – 100 mV/s (0.4 M [<sup>n</sup>Bu<sub>4</sub>N][PF<sub>6</sub>] in THF). The current values were normalized by dividing the measured current by the square root of the scan speed.

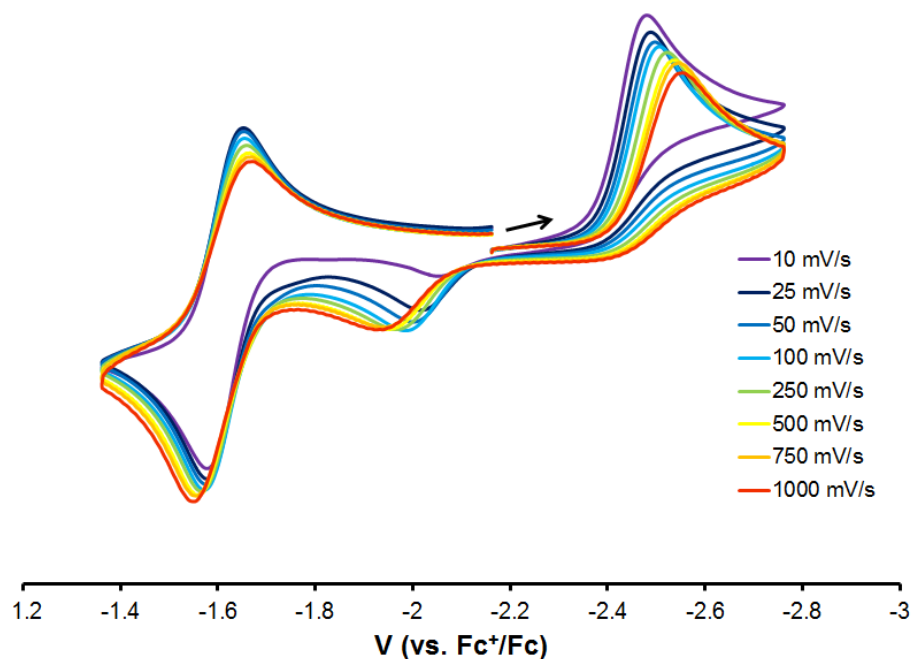


**Figure A1.3** Cyclic voltammetry study of **3** – CoV demonstrating a scan speed dependence between 10 – 1000 mV/s (0.4 M [ $n$ Bu<sub>4</sub>N][PF<sub>6</sub>] in THF). The current values were normalized by dividing the measured current by the square root of the scan speed.

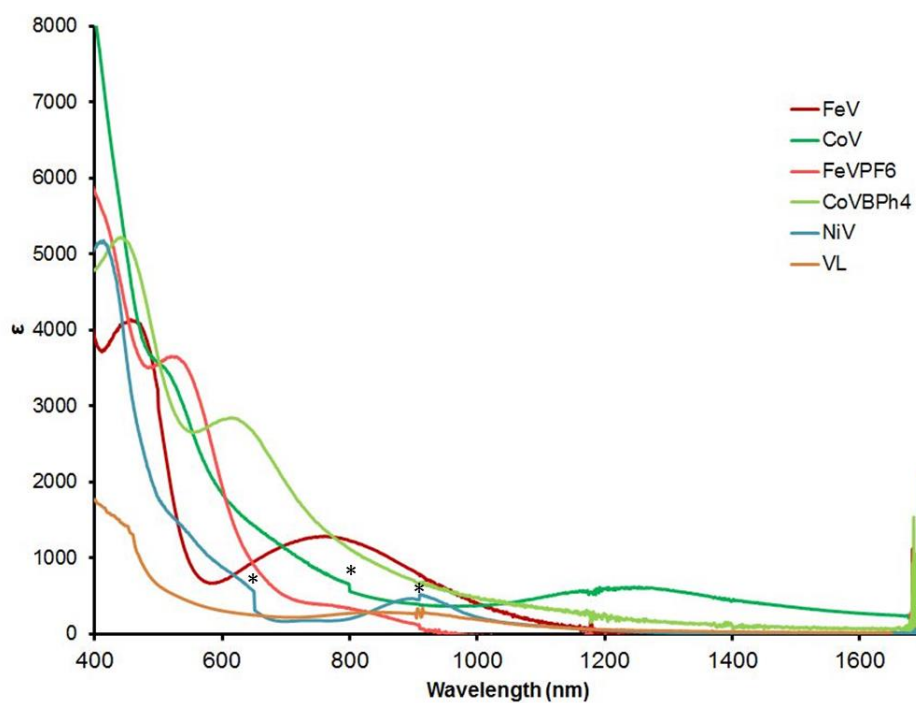


**Figure A1.4** Vis-NIR spectra of complexes **1–4** in THF. Asterisks note spectral discontinuities due to a lamp change.

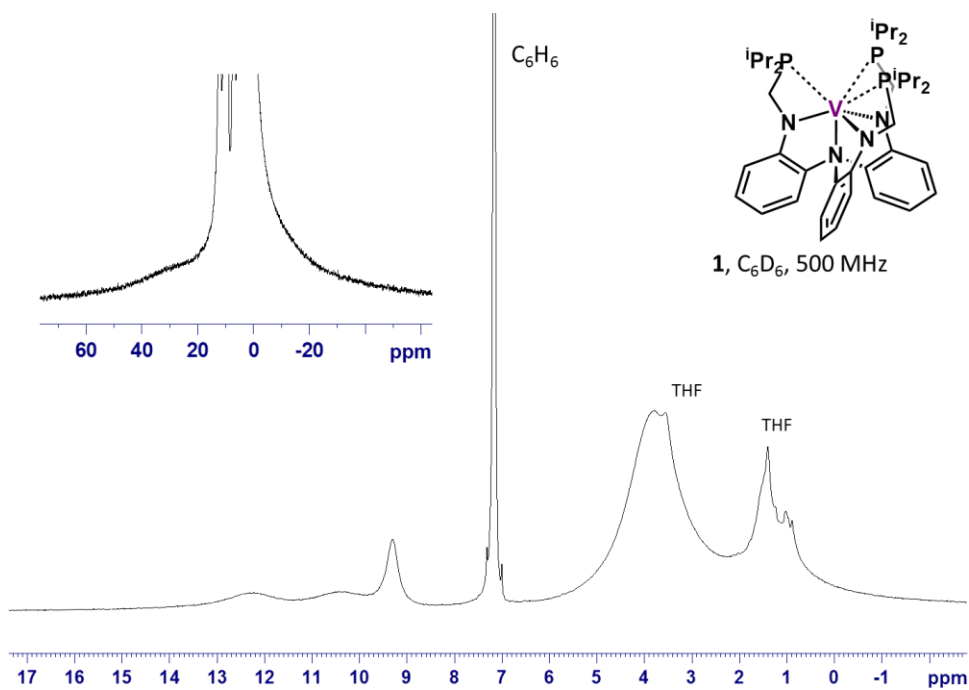


**Figure A1.5**  $^1\text{H}$  NMR spectrum of **1** in  $\text{C}_6\text{D}_6$  (500 MHz). Inset shows a zoom of the broad peak at 30 ppm.

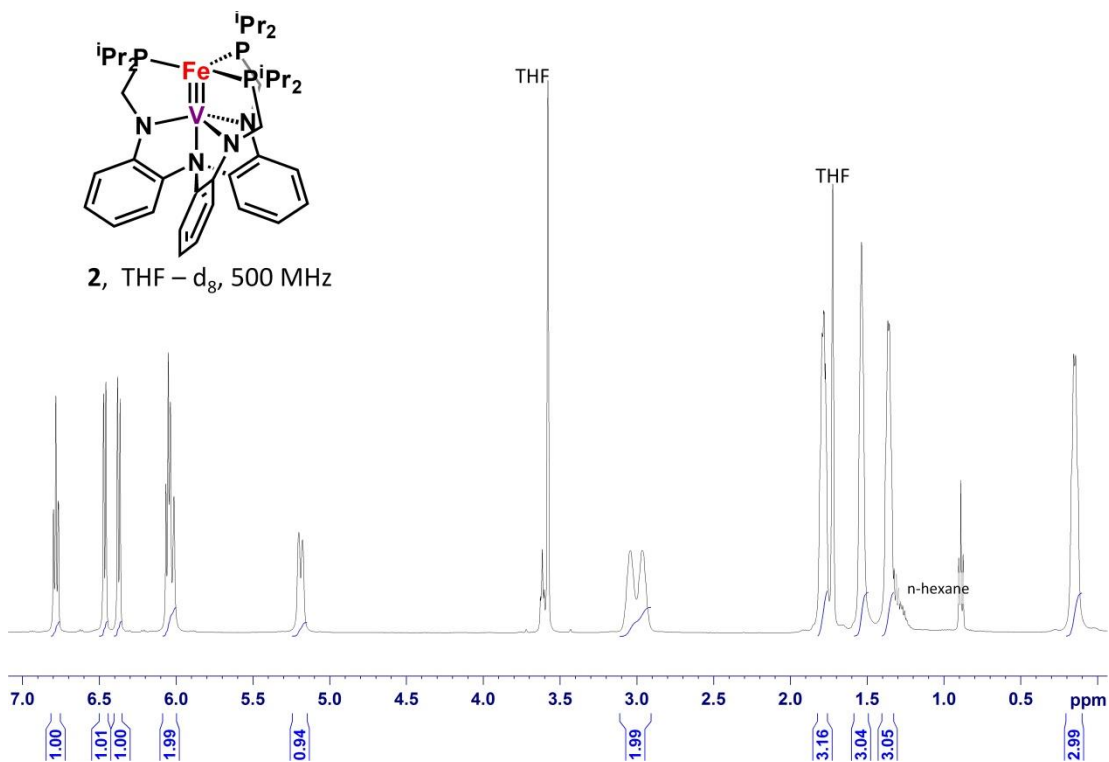


**Figure A1.6**  $^1\text{H}$  NMR spectrum of **2** in  $\text{THF-d}_8$  (500 MHz).



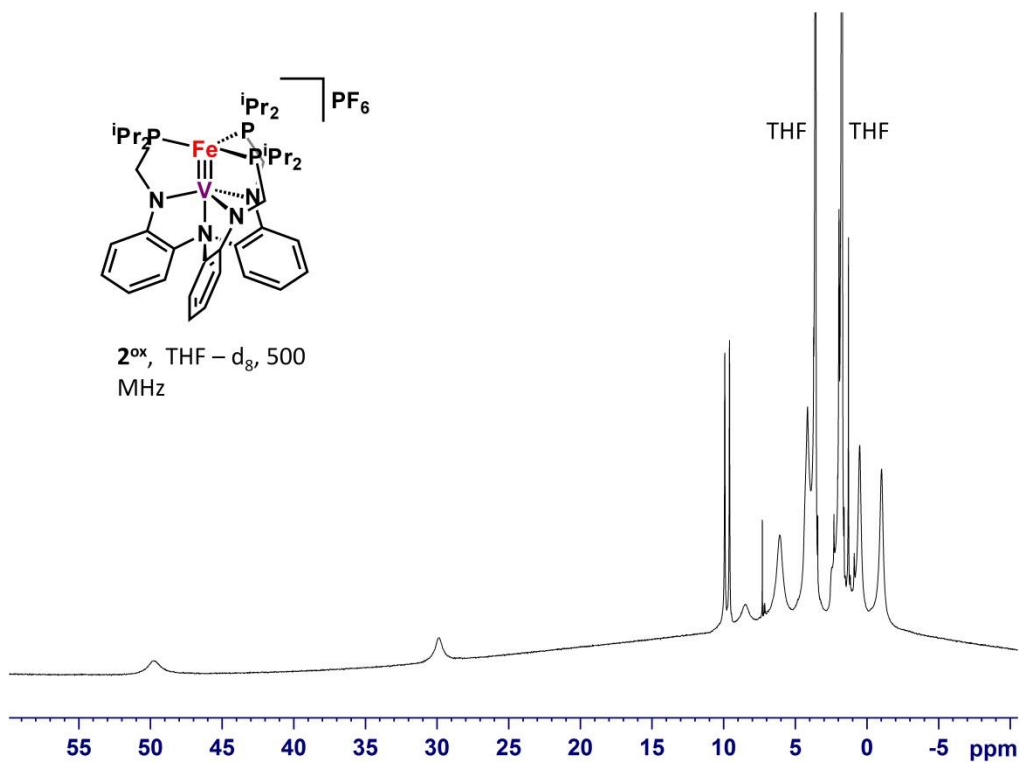


**Figure A1.7**  $^1\text{H}$  NMR spectrum of  $2^{ox}[\text{PF}_6]$  in THF- $d_8$  (500 MHz).

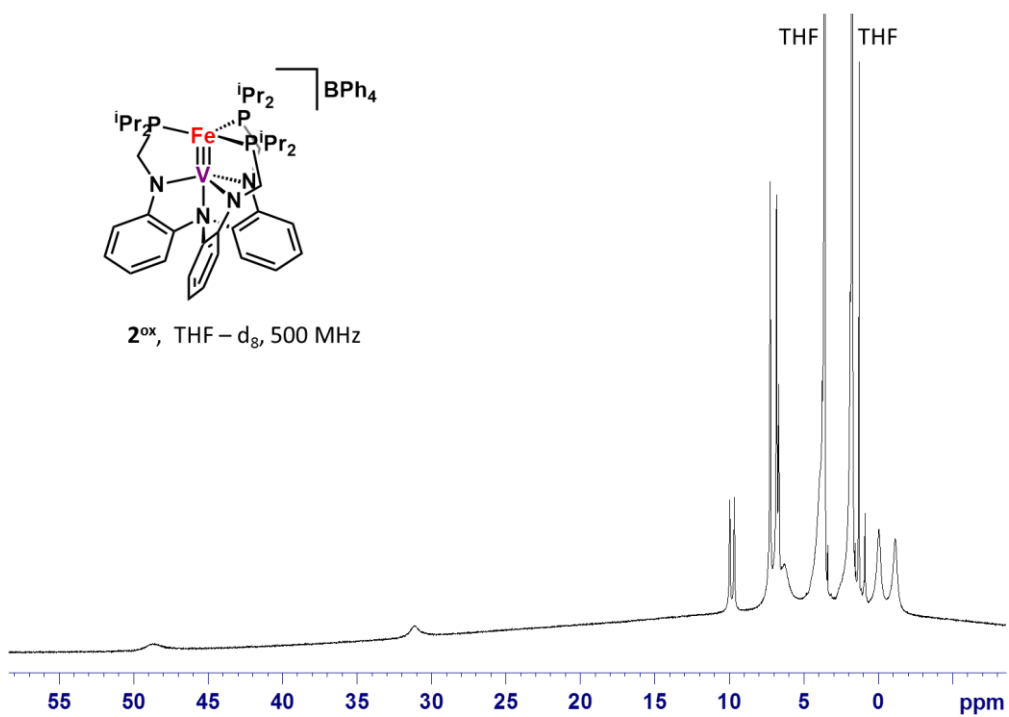


**Figure A1.8**  $^1\text{H}$  NMR spectrum of  $2^{ox}[\text{BPh}_4]$  in THF- $d_8$  (400 MHz).

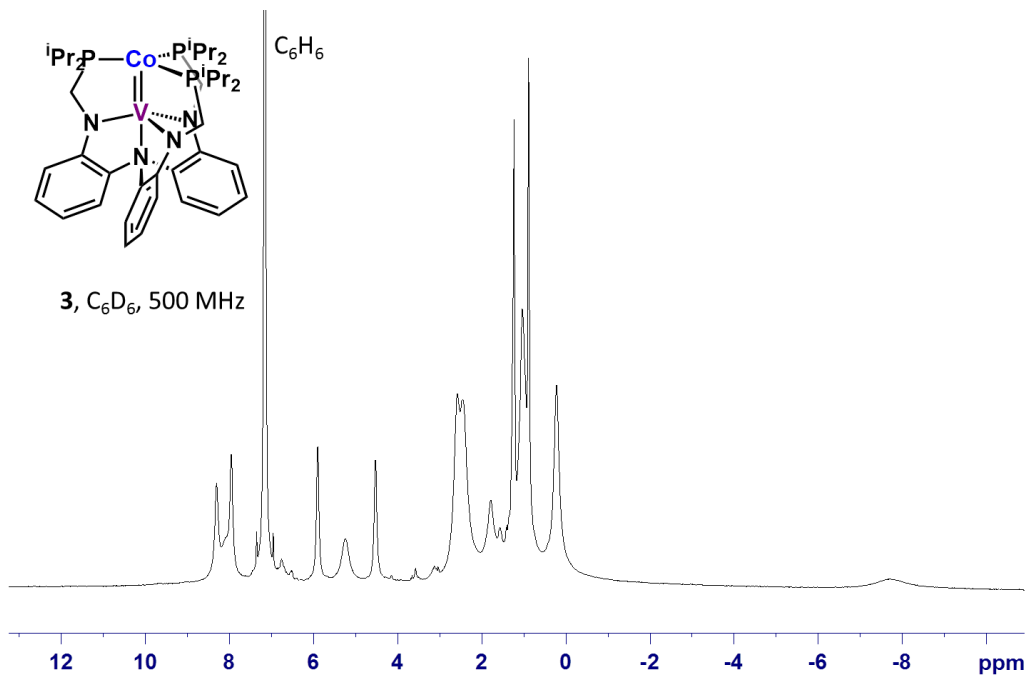


**Figure A1.9**  $^1\text{H}$  NMR spectrum of **3** in  $\text{C}_6\text{D}_6$  (500 MHz).

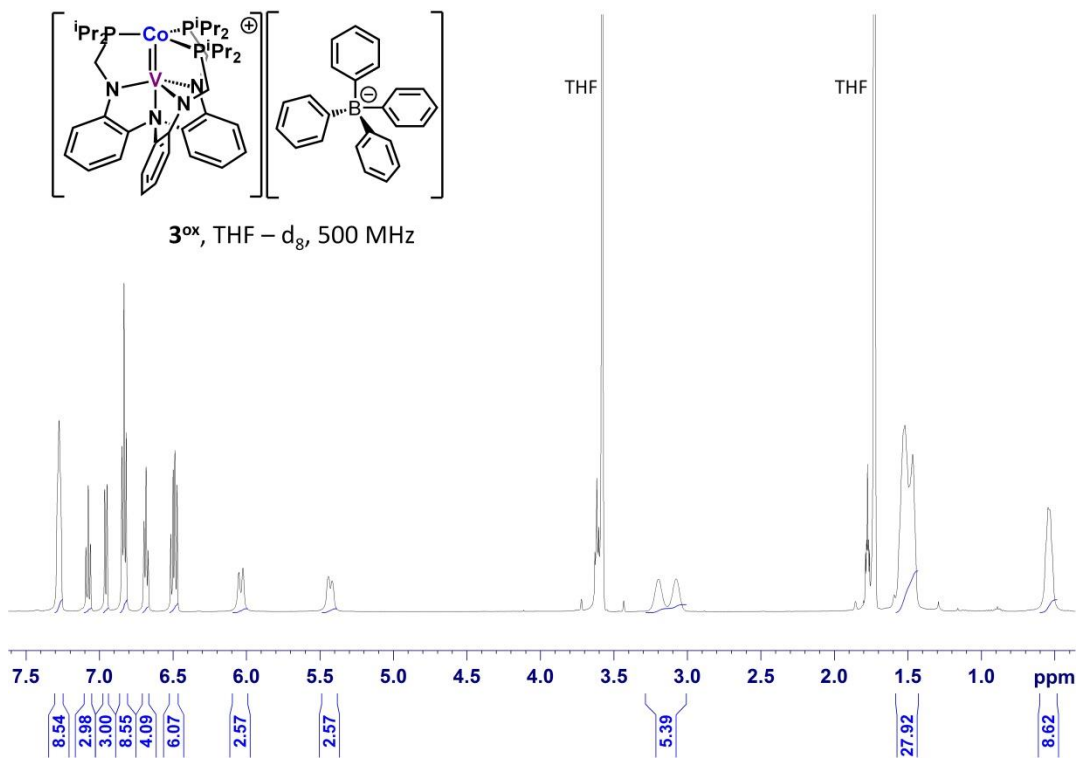


**Figure A1.10**  $^1\text{H}$  NMR spectrum of **3<sup>ox</sup>** in  $\text{THF}-d_8$  (500 MHz).

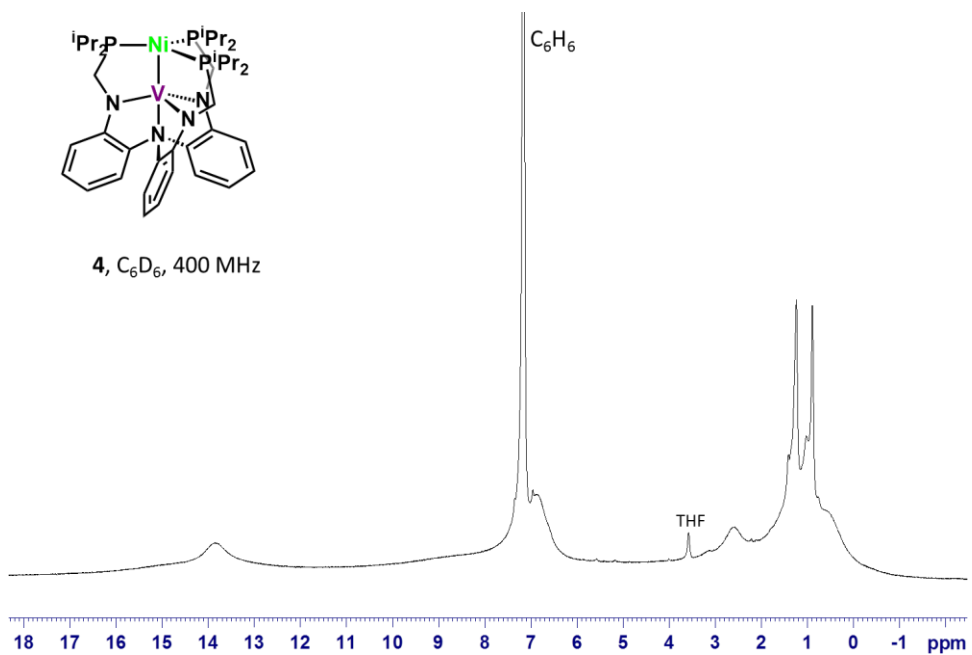


**Figure A1.11** <sup>1</sup>H NMR spectrum of **4** in C<sub>6</sub>D<sub>6</sub> (400 MHz).

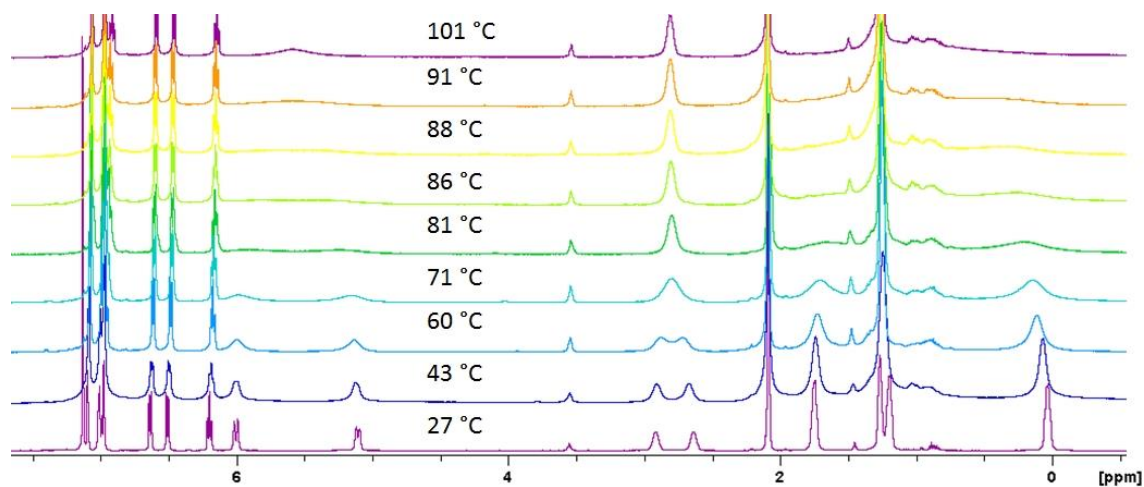


**Figure A1.12** Variable temperature <sup>1</sup>H NMR spectra of **2** in toluene-d<sub>8</sub> (500 MHz). Coalescence of the methylene resonances occurs at 88 °C.

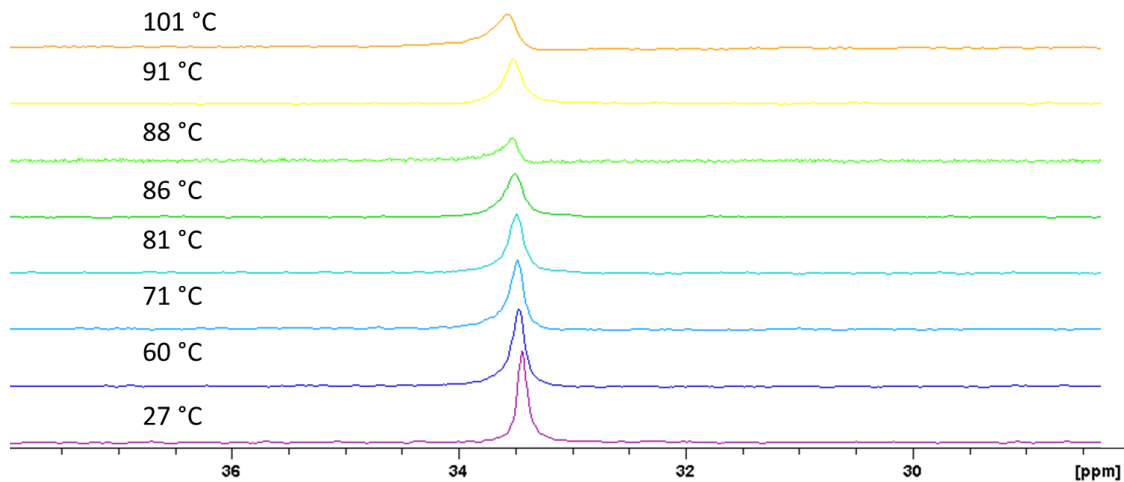


**Figure A1.13** Variable temperature  $^{31}\text{P}$  NMR spectra of **2** in toluene- $d_8$  (200 MHz).

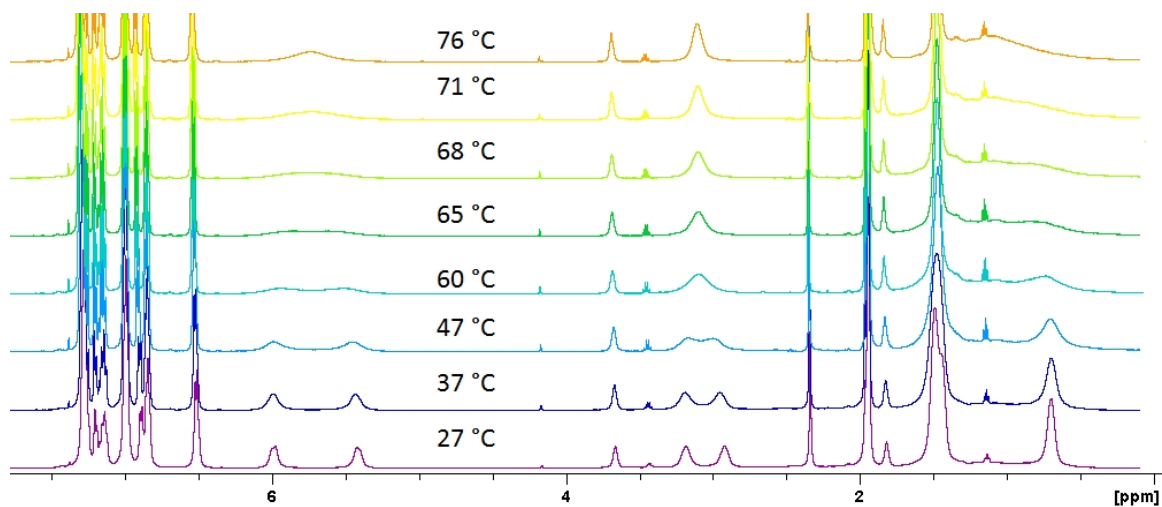


**Figure A1.14** Variable temperature  $^1\text{H}$  NMR spectra of **3<sup>ox</sup>** in  $\text{CD}_3\text{CN}$  (500 MHz). Coalescence of the methylene resonances occurs at 68 °C.

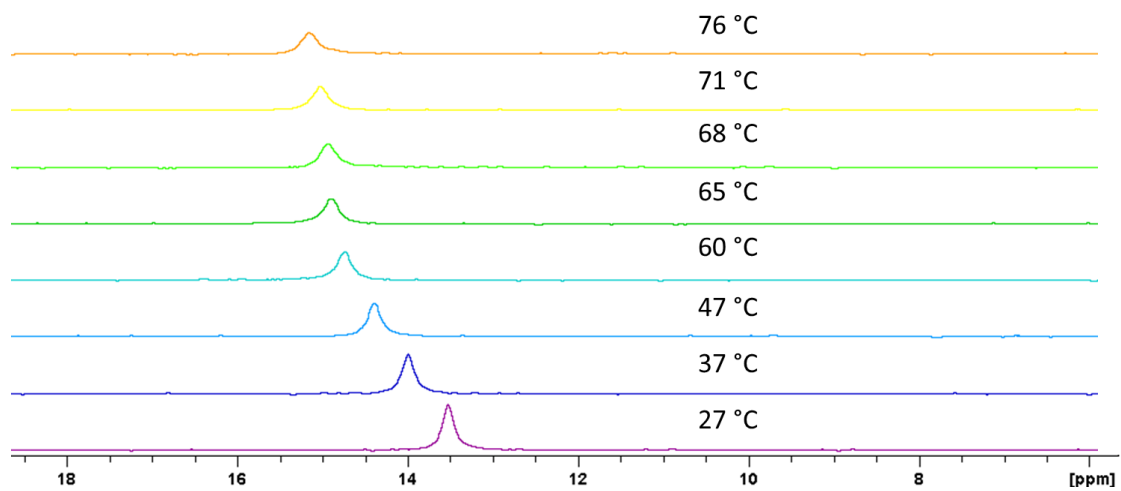


**Figure A1.15** Variable temperature  $^{31}\text{P}$  NMR spectra of  $3^{\text{ox}}$  in  $\text{CD}_3\text{CN}$  (200 MHz).

### Diamagnetic anisotropy determination

The diamagnetic anisotropy,  $(\chi_{\parallel} - \chi_{\perp})$ , of our molecules is calculated from the following equation:

$$\Delta\delta = \left(\frac{1}{3r^3}\right) \frac{(\chi_{\parallel} - \chi_{\perp})(1 - 3\cos^2(\theta))}{4\pi}$$

where  $\Delta\delta$  is the difference in chemical shift (ppm) between the average methylene resonance in a bimetallic complex versus the reference complex, the isostructural Ni-Al complex which has a Ni→Al dative bond. The distance of the methylene proton to the center of the metal-metal bond is  $r$ , the acute angle between the proton and the metal-metal axis is  $\theta$  and the unit of  $\Delta\chi$  is  $10^{-36} \text{ m}^3 \text{ molecule}^{-1}$ . The ambiguity of the assignment of methylene protons in the bimetallic complexes relative to the reference molecules allows for two different options in calculating the diamagnetic anisotropy, demonstrated in the figure and tables below for both **2** and **3<sup>ox</sup>**.

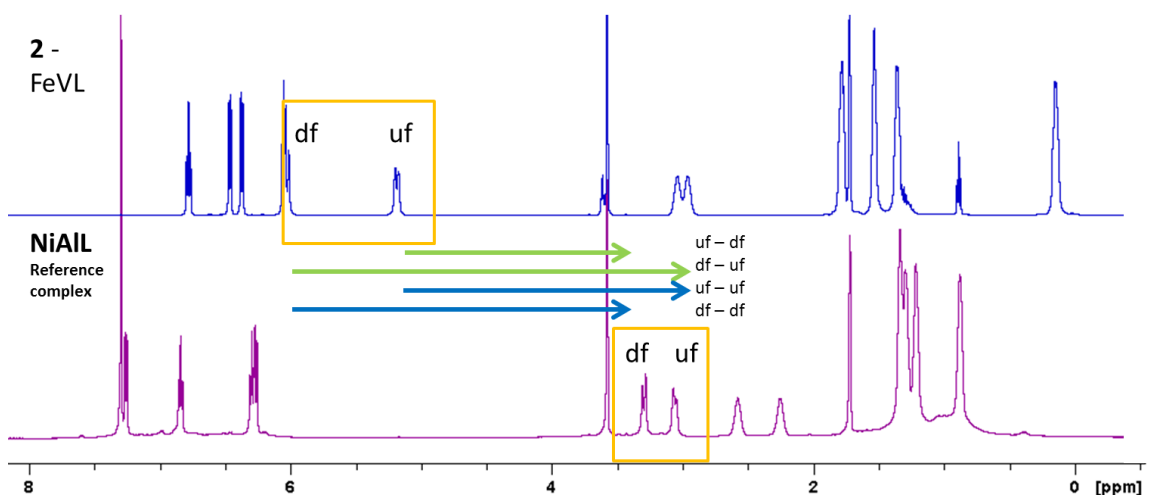


**Figure A1.16** Overlay of  $^1\text{H}$  NMR spectra of **2** and reference complex NiAl in THF- $d_8$ . The methylene protons used to calculate diamagnetic anisotropy are boxed in yellow and the two methods of calculating the diamagnetic anisotropy are shown. Blue arrows demonstrate both downfield (df) resonances and both upfield (uf) resonances correlating to each other, whereas the green arrows indicate that resonances are inverted, with the uf proton of **2** relating to the df proton of the reference and the df proton of **2** corresponding to the uf proton of the reference.

**Table A1.1** Calculation spreadsheet for the diamagnetic anisotropy of **2** in THF-d<sub>8</sub>.

	2-FeV			2-FeV		AlNi		
	r (Å)	θ (°)	θ (radians)	ppm	ppm	Δδ	Δχ	
Ha1	3.794	79.62	1.390	5.19	3.06	-2.13	-4858.504	uf-uf
				5.19	3.3	-1.89	-4311.067	uf-df
Ha2	3.777	79.39	1.386	5.19	3.06	-2.13	-4816.506	uf-uf
				5.19	3.3	-1.89	-4273.801	uf-df
Ha3	3.797	78.87	1.377	5.19	3.06	-2.13	-4948.984	uf-uf
				5.19	3.3	-1.89	-4391.352	uf-df
Hb1	3.475	86.66	1.513	6.03	3.3	-2.73	-4363.182	df-df
				6.03	3.06	-2.97	-4746.758	df-uf
Hb2	3.507	85.87	1.499	6.03	3.3	-2.73	-4509.33	df-df
				6.03	3.06	-2.97	-4905.755	df-uf
Hb3	3.501	85.89	1.499	6.03	3.3	-2.73	-4485.541	df-df
				6.03	3.06	-2.97	-4879.875	df-uf

**Table A1.2** Calculation spreadsheet for the diamagnetic anisotropy of **3<sup>ox</sup>** in THF-d<sub>8</sub>.

	3ox-CoVBPh4			3ox-CoVBPh4		AlNi		
	r (Å)	θ (°)	θ (radians)	ppm	ppm	Δδ	Δχ	
Ha1	3.769	79.99	1.396	5.46	3.06	-2.4	-5327.029	uf-uf
				5.46	3.3	-2.16	-4794.326	uf-df
Ha2	3.757	79.95	1.395	5.46	3.06	-2.4	-5280.48	uf-uf
				5.46	3.3	-2.16	-4752.432	uf-df
Ha3	3.775	80.64	1.407	5.46	3.06	-2.4	-5286.885	uf-uf
				5.46	3.3	-2.16	-4758.197	uf-df
Hb1	3.431	87.03	1.519	6.07	3.3	-2.77	-4251.918	df-df
				6.07	3.06	-3.01	-4620.316	df-uf
Hb2	3.442	87.06	1.519	6.07	3.3	-2.77	-4292.245	df-df
				6.07	3.06	-3.01	-4664.137	df-uf
Hb3	3.399	88.66	1.547	6.07	3.3	-2.77	-4107.499	df-df
				6.07	3.06	-3.01	-4463.383	df-uf

**Table A1.3** Average  $\Delta\chi$  and standard deviations for the two different calculation methods (uf-uf vs. uf-df) for **2** and **3ox**. Both methods of calculating the diamagnetic anisotropy result in the same value to two significant figures, providing confidence in the evaluating trends within the complexes.

	<b>2 - FeV</b>		<b>3ox - CoVBPh4</b>	
	$\Delta\chi$	STDEV	$\Delta\chi$	STDEV
<b>uf-uf</b>	4664	240	4758	595
<b>uf-df</b>	4585	292	4675	123

**Table A1.4** Calculation of the energy barrier ( $\Delta G^\ddagger$  in kcal/mol) for the fluxional process equilibrating the diastereotopic methylene protons in the ligand backbone.

	<b>2</b>	<b>3ox</b>
solvent	toluene- d <sub>8</sub>	CD <sub>3</sub> CN
T <sub>c</sub> (K)	361	341
$\Delta$ (ppm)	0.88	0.57
$\Delta$ (Hz)	440.7	285.8
k <sub>c</sub>	978.99	634.89
R	0.001987	0.00199
$\Delta G^\ddagger$ (kcal/mol)	<b>16.3</b>	<b>15.7</b>



### *X-Ray Crystallography and Structure Refinement Details*

A brown block of **1**, a dark orange block of **2**, a red-brown needle of **2<sup>ox</sup>**, a brown block of **3**, a green plate of **3<sup>ox</sup>**, and a brown hexagonal plate of **4** were placed on the tip of a 0.1 mm diameter glass capillary and mounted on a Bruker APEX II CCD diffractometer or a Bruker Photon 100 CMOS diffractometer for data collection at 173(2) K or 123(2) K. The data collection was carried out using Mo K $\alpha$  radiation (graphite monochromator) or Cu K $\alpha$  radiation (normal parabolic mirrors). The data intensity was corrected for absorption and decay (SADABS).<sup>10</sup> Final cell constants were obtained from least-squares fits of all measured reflections and the structure was solved using SHELXS-08 and refined using SHELXL-08.<sup>11</sup> A direct-methods solution was calculated which provided most non-hydrogen atoms from the E-map. Full-matrix least-squares/difference Fourier cycles were performed to locate the remaining non-hydrogen atoms and all non-hydrogen atoms were refined with anisotropic displacement parameters with the exception of a disordered toluene molecule in **3** is refined isotropically. Hydrogen atoms were placed in ideal positions and refined as riding atoms with relative isotropic displacement parameters. A disordered toluene molecule in **2** and **3** resides on an inversion center and was modeled using SHELXTL SAME, SADI and FLAT geometrical restraints. Disordered THF solvent molecules were removed from the unit cell of **2<sup>ox</sup>** using Platon SQUEEZE<sup>12</sup>, and a disordered isopropyl group in **2<sup>ox</sup>** was modeled using SHELXTL EADP constraints, and the geometrical restraints SAME and SADI.

**Table A1.5** Crystallographic details of complexes **1** – **4**.

	<b>1</b> VL	<b>2</b> FeVL	<b>2<sup>ox</sup> [BPh<sub>4</sub>]</b> FeVL[BPh <sub>4</sub> ]
chemical formula	C <sub>39</sub> H <sub>60</sub> N <sub>4</sub> P <sub>3</sub> V	C <sub>39</sub> H <sub>60</sub> FeN <sub>4</sub> P <sub>3</sub> V 0.5(C <sub>7</sub> H <sub>8</sub> )	C <sub>39</sub> H <sub>60</sub> FeN <sub>4</sub> P <sub>3</sub> V B(C <sub>24</sub> H <sub>20</sub> ), 2(C <sub>4</sub> H <sub>8</sub> O)
fw	728.76	830.68	1248.03
cryst syst	monoclinic	triclinic	monoclinic
space group	P2 <sub>1</sub> /n	P-1	P2 <sub>1</sub> /c
a (Å)	11.4420(2)	11.2034(4)	17.3253(4)
b (Å)	19.7730(4)	14.1739(6)	14.3670(4)
c (Å)	17.4838(4)	14.3424(6)	26.5458(6)
$\alpha$ (deg)	90	71	90
$\beta$ (deg)	94.476(1)	81	101.115(1)
$\gamma$ (deg)	90	83	90
V (Å <sup>3</sup> )	3943.5(1)	2117.1(2)	6483.6(3)
Z	4	2	4
D <sub>calcd</sub> (g cm <sup>-3</sup> )	1.227	1.303	1.279
$\lambda$ (Å), $\mu$ (mm <sup>-1</sup> )	1.54178, 3.487	0.71073, 0.711	1.54178, 4.067
T (K)	173(2)	173(2)	123(2)

$\theta$ range (deg)	3.38 to 66.72	1.52 to 27.45	2.60 to 68.33
reflns collected	78965	24610	50661
unique reflns	6979	9574	11778
data/restraint/params	6979/0/436	9574/10/509	11778/8/758
R1, wR2 (I > 2 $\sigma$ (I) )	0.0297, 0.0742	0.0359, 0.0791	0.0475, 0.1135

	<b>3</b>	<b>3<sup>ox</sup></b>	<b>4</b>
	<b>CoVL</b>	<b>[BPh<sub>4</sub>]CoVL</b>	<b>NiVL</b>
chemical formula	C <sub>39</sub> H <sub>60</sub> CoN <sub>4</sub> P <sub>3</sub> V, 0.5(C <sub>7</sub> H <sub>8</sub> )	C <sub>39</sub> H <sub>60</sub> CoN <sub>4</sub> P <sub>3</sub> V B(C <sub>24</sub> H <sub>20</sub> ),2(C <sub>4</sub> H <sub>8</sub> O)	C <sub>39</sub> H <sub>60</sub> N <sub>4</sub> NiP <sub>3</sub> V, C <sub>6</sub> H <sub>6</sub>
fw	833.76	1251.11	865.61
cryst syst	triclinic	monoclinic	trigonal
space group	P-1	P2 <sub>1</sub> /c	P-3
a (Å)	11.1828(6)	17.3813(5)	10.875(3)
b (Å)	14.1917(7)	14.3313(4)	10.875(3)
c (Å)	14.3156(7)	26.5204(7)	21.431(6)
$\alpha$ (deg)	70.779(1)	90	90
$\beta$ (deg)	80.653(1)	100.631(2)	90
$\gamma$ (deg)	82.740(1)	90	120
V (Å <sup>3</sup> )	2110.3(2)	6492.7(3)	2195(1)
Z	2	4	2
D <sub>calcd</sub> (g cm <sup>-3</sup> )	1.312	1.28	1.31
$\lambda$ (Å), $\mu$ (mm <sup>-1</sup> )	0.71073, 0.763	1.54178, 4.271	0.71073, 0.787
T (K)	173(2)	123(2)	173(2)
$\theta$ range (deg)	1.52 to 27.40	2.59 to 66.79	1.90 to 27.30
reflns collected	22893	48756	10182
unique reflns	9844	11373	3270
data/restraint/params	9488/0/474	11373/0/760	3270/0/167
R1, wR2 (I > 2 $\sigma$ (I) )	0.0377, 0.0818	0.0748, 0.1790	0.0546, 0.1319

## Computational Details

**Table A1.6** Selected bond lengths and angles for comparison of DFT optimized structures using the PBE functional with experimental X-ray structures.

	<b>2 - FeVL</b>		<b>2<sup>ox</sup> - FeV+</b>		<b>3 - CoVL</b>		<b>3<sup>ox</sup> - CoV+</b>		<b>4 - NiVL</b>	
	<b>Exp</b>	<b>DFT</b>	<b>Exp</b>	<b>DFT</b>	<b>Exp</b>	<b>DFT</b>	<b>Exp</b>	<b>DFT</b>	<b>Exp</b>	<b>DFT</b>
M-V (Å)	1.8940(4)	1.870	1.9791(6)	1.950	2.1234(4)	2.141	1.9930(11)	1.974	2.4873(14)	2.537
M-P	2.2585(6)	2.200	2.2829(8)	2.234	2.2315(7)	2.182	2.2356(16)	2.203	2.2051(11)	2.186
	2.2599(6)	2.201	2.2992(9)	2.258	2.2317(6)	2.166	2.2448(15)	2.203	2.2051(11)	2.186
	2.2705(6)	2.201	2.3042(9)	2.267	2.2434(6)	2.178	2.2470(16)	2.203	2.2051(11)	2.186
V-Neq	1.9584(17)	1.971	1.933(2)	1.939	1.9442(18)	1.957	1.925(4)	1.936	1.957(3)	1.950
	1.9645(17)	1.970	1.933(2)	1.948	1.9543(18)	1.987	1.926(4)	1.935	1.957(3)	1.950
	1.9682(17)	1.971	1.937(2)	1.945	1.9694(17)	1.941	1.926(4)	1.936	1.957(3)	1.950
V-Nap	2.3082(16)	2.352	2.293(2)	2.307	2.2266(17)	2.274	2.272(4)	2.288	2.149(5)	2.155
P-M-P angle	119.53(2)	119.0	120.46(4)	110.2	120.61(3)	120.9	118.20(6)	119.9	119.658(6)	118.8
	119.54(2)	118.5	112.79(3)	109.6	120.01(2)	121.9	119.92(7)	119.7	119.657(6)	118.9
	118.80(2)	119.1	125.66(4)	139.3	119.33(3)	117.2	120.29(6)	119.4	119.656(6)	119.0
Neq - V-Neq	113.70(7)	115.6	117.22(9)	114.6	114.20(8)	118.3	117.92(17)	116.1	118.00(4)	118.5
	116.33(7)	115.5	115.39(9)	113.7	117.03(8)	116.1	114.69(18)	116.1	118.00(4)	118.3
	115.09(7)	115.3	117.34(9)	119.5	116.84(8)	114.3	116.90(17)	115.7	118.00(4)	118.4
M-V- Nap	179.29(5)	179.88	177.90(6)	176.6	177.67(5)	177.0	179.60(11)	179.9	180	180.0

**Table A1.7** Calculated relative energies of various possible spin states at DFT and CASSCF levels of theory.

FeV <sup>+</sup> (d <sup>9</sup> )	Spin state	$\langle S^2 \rangle_{\text{pure}}$	$\langle S^2 \rangle_{\text{calc}}$	DFT (PBE) (kcal/mol)	CASSCF (kcal/mol)	CASPT2 (kcal/mol)	Percent of main configuration
	<b>doublet</b>	<b>0.75</b>	<b>0.75</b>	<b>0.0</b>	<b>0.0</b>	<b>0.0</b>	<b>71%</b>
	quartet	3.75	3.75	26.6	35.0	49.6	78%
	sextet	8.75	8.75	39.9	60.9	106.6	95%
FeV (d <sup>10</sup> )	Spin state	$\langle S^2 \rangle_{\text{pure}}$	$\langle S^2 \rangle_{\text{calc}}$	DFT (PBE) (kcal/mol)	CASSCF (kcal/mol)	CASPT2 (kcal/mol)	Percent of main configuration
	<b>singlet</b>	<b>0.00</b>	<b>0.00</b>	<b>0.0</b>	<b>0.0</b>	<b>0.0</b>	<b>75%</b>
	triplet	2.00	2.00	23.3	43.5	41.4	79%
	quintet	6.00	6.00	39.8	92.6	88.8	89%
	septet	12.00	12.00	55.6	139.8	144.5	94%
CoV <sup>+</sup> (d <sup>10</sup> )	Spin state	$\langle S^2 \rangle_{\text{pure}}$	$\langle S^2 \rangle_{\text{calc}}$	DFT (PBE) (kcal/mol)	CASSCF (kcal/mol)	CASPT2 (kcal/mol)	Percent of main configuration
	<b>singlet</b>	<b>0.00</b>	<b>0.00</b>	<b>0.0</b>	<b>0.0</b>	<b>0.0</b>	<b>75%</b>
	triplet	2.00	2.00	20.1	26.7	46.6	84%
	quintet	6.00	6.00	36.5	49.8	111.3	96%
	septet	12.00	12.00	67.6	126.2	168.7	97%
CoV (d <sup>11</sup> )	Spin state	$\langle S^2 \rangle_{\text{pure}}$	$\langle S^2 \rangle_{\text{calc}}$	DFT (PBE) (kcal/mol)	CASSCF (kcal/mol)	CASPT2 (kcal/mol)	Percent of main configuration
	<b>doublet</b>	<b>0.75</b>	<b>0.75</b>	<b>0.0</b>	<b>0.0</b>	<b>0.0</b>	<b>72%</b>
	quartet	3.75	3.75	13.5	13.7	37.3	90%
	sextet	8.75	8.75	35.1	51.9	56.0	96%
NiV (d <sup>12</sup> )	Spin state	$\langle S^2 \rangle_{\text{pure}}$	$\langle S^2 \rangle_{\text{calc}}$	DFT (PBE) (kcal/mol)	CASSCF (kcal/mol)	CASPT2 (kcal/mol)	Percent of main configuration
	singlet	0.00	0.02	9.9	36.2	26.4	44.3/44.1%
	<b>triplet</b>	<b>2.00</b>	<b>2.00</b>	<b>0.0</b>	<b>0.0</b>	<b>0.0</b>	<b>88.4%</b>
	quintet	6.00	6.00	35.7	47.3	47.3	94.2%
	septet	12.00	12.00	86.7	140.0	184.5	97.3%

**Table A1.8** Calculated charges at the metal centers of the ground spin state.

<b>FeV<sup>+</sup> (d<sup>9</sup>)</b>	<b>Fe</b>		<b>V</b>	
	<b>Mulliken</b>	<b>LoProp</b>	<b>Mulliken</b>	<b>LoProp</b>
<b>CASSCF</b>	-0.4806	0.6485	2.8015	1.1903
<b>DFT</b>	-0.2600	N/A	0.9151	N/A

<b>FeV (d<sup>10</sup>)</b>	<b>Fe</b>		<b>V</b>	
	<b>Mulliken</b>	<b>LoProp</b>	<b>Mulliken</b>	<b>LoProp</b>
<b>CASSCF</b>	-0.8636	0.3889	2.7628	1.1082
<b>DFT</b>	-0.2877	N/A	0.9628	N/A

<b>CoV<sup>+</sup> (d<sup>10</sup>)</b>	<b>Co</b>		<b>V</b>	
	<b>Mulliken</b>	<b>LoProp</b>	<b>Mulliken</b>	<b>LoProp</b>
<b>CASSCF</b>	-0.1704	0.5558	2.6309	1.2143
<b>DFT</b>	-0.2971	N/A	0.8967	N/A

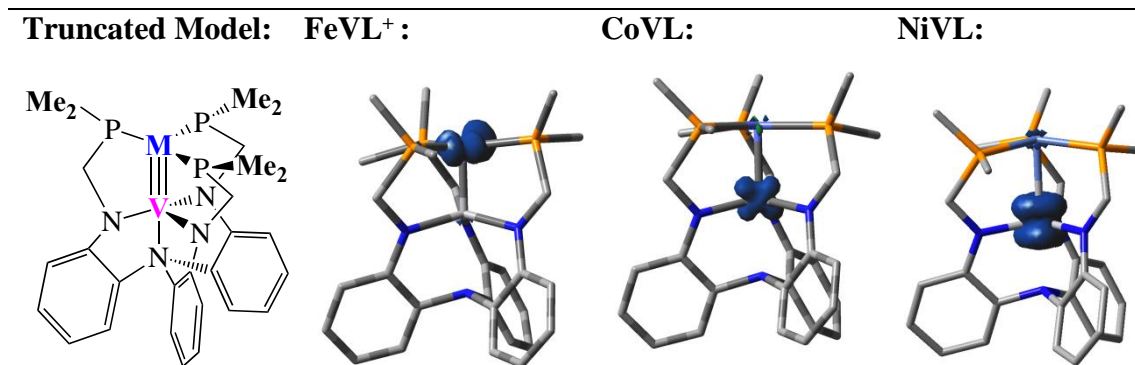
<b>CoV (d<sup>11</sup>)</b>	<b>Co</b>		<b>V</b>	
	<b>Mulliken</b>	<b>LoProp</b>	<b>Mulliken</b>	<b>LoProp</b>
<b>CASSCF</b>	-0.1881	0.3517	2.4121	1.1930
<b>DFT</b>	-0.2313	N/A	0.8431	N/A

<b>NiV (d<sup>12</sup>)</b>	<b>Ni</b>		<b>V</b>	
	<b>Mulliken</b>	<b>LoProp</b>	<b>Mulliken</b>	<b>LoProp</b>
<b>CASSCF</b>	-0.4944	0.1997	2.4535	1.3482
<b>DFT</b>	-0.1449	N/A	0.7895	N/A

**Table A1.9** CASSCF Mulliken spin densities at the metal centers of the ground spin state.

	Spin density from CASSCF		Spin density from DFT	
	M	V	M	V
FeV <sup>+</sup> (d <sup>9</sup> )	1.27	-0.31	1.07	-0.25
FeV (d <sup>10</sup> )	0.00	0.00	0.00	0.00
CoV <sup>+</sup> (d <sup>10</sup> )	0.00	0.00	0.00	0.00
CoV (d <sup>11</sup> )	-0.09	1.06	-0.06	1.16
NiV (d <sup>12</sup> )	-0.01	1.98	0.00	2.22



M = Fe Co, or Ni

**Figure A1.17** Spin density of FeV cation (left,  $\langle S^2 \rangle_{\text{calc}} = 0.75$ ), CoV neutral (middle,  $\langle S^2 \rangle_{\text{calc}} = 0.75$ ), and NiV neutral (middle,  $\langle S^2 \rangle_{\text{calc}} = 2.00$ ). Blue density corresponds to alpha electron excess, using isosurfaces = 0.02 a.u. Carbon atoms are in gray, nitrogen is in blue, phosphorus in orange and hydrogen are not show for clarity of the structure. The spin-density of the FeVL<sup>+</sup> is located on the Fe atom, while in the CoVL and NiVL is located in the V atom.

**Table A1.10** Detailed CASSCF orbital analysis of **2'** - FeV neutral species.

	orbital type	%Fe	%V	total electrons	Electron Fe	Electron V
orbital 156	$\pi$	58.03	41.97	1.83	1.06	0.77
orbital 157	4d <sub>Fe</sub>	97.37	2.63	0.06	0.06	0.00
orbital 158	$\pi^*$	47.33	52.67	0.17	0.08	0.09
orbital 159	d <sub>Fe</sub>	100.00	0.00	1.93	1.93	0.00
orbital 160	d <sub>Fe</sub>	100.00	0.00	1.93	1.93	0.00
orbital 161	$\sigma^*$	42.61	57.39	0.15	0.06	0.09
orbital 162	$\pi$	58.10	41.90	1.83	1.07	0.77
orbital 163	4d <sub>Fe</sub>	97.95	2.05	0.06	0.06	0.00
orbital 164	$\pi^*$	47.60	52.40	0.17	0.08	0.09
orbital 165	$\sigma$	66.52	33.48	1.85	1.23	0.62
total electrons=				10.00	7.58	2.42

**Table A1.11** Detailed CASSCF orbital analysis of **2<sup>ox'</sup>** - FeV cationic species.

orbital type	%Fe	%V	total electrons	Electron Fe	Electron V
$\pi$	62.5	37.5	1.78	1.12	0.67
d*	98.3	1.7	0.04	0.04	0.00
$\pi^*$	45.5	54.5	0.22	0.10	0.12
d	100.0	0.0	1.96	1.96	0.00
d	98.9	1.1	0.99	0.98	0.01
$\sigma^*$	35.4	64.6	0.15	0.05	0.10
$\pi$	65.4	34.6	1.79	1.17	0.62
d*	86.5	13.5	0.01	0.01	0.00
$\pi^*$	41.9	58.1	0.21	0.09	0.12
$\sigma$	73.3	26.7	1.85	1.36	0.49
total electrons=			9.00	6.87	2.13

**Table A1.12** Detailed CASSCF orbital analysis of **3'** - CoV neutral species.

	orbital type	%Co	%V	total electrons	Electron Co	Electron V
orbital 156	d	100.00	0.00	1.94	1.94	0.00
orbital 157	$\pi$	57.71	42.29	1.67	0.96	0.70
orbital 158	$\sigma$	78.00	22.00	1.89	1.47	0.41
orbital 159	$d_v$	8.86	91.14	1.04	0.09	0.94
orbital 160	$d_{Co}$	96.22	3.78	1.96	1.89	0.07
orbital 161	$\sigma^*$	32.42	67.58	0.12	0.04	0.08
orbital 162	d	97.13	2.87	1.93	1.88	0.06
orbital 163	$\pi^*$	44.98	55.02	0.34	0.15	0.19
orbital 164	4d	95.83	4.17	0.06	0.05	0.00
orbital 165	4d	98.87	1.13	0.06	0.06	0.00
total electrons=				11.00	8.54	2.46

**Table A1.13** Detailed CASSCF orbital analysis of **3<sup>ox'</sup>** - CoV cationic species.

	orbital type	%Co	%V	total electrons	Electron Co	Electron V
orbital 156	$\pi$	65.19	34.81	1.81	1.18	0.63
orbital 157	$d_{Co}$	100.00	0.00	1.96	1.96	0.00
orbital 158	$\sigma^*$	31.13	68.87	0.12	0.04	0.08
orbital 159	$d_{Co}$	100.00	0.00	1.96	1.96	0.00
orbital 160	$\sigma$	77.52	22.48	1.88	1.46	0.42
orbital 161	$\pi^*$	42.38	57.62	0.20	0.08	0.11
orbital 162	$\pi^*$	43.22	56.78	0.20	0.08	0.11
orbital 163	$\pi$	65.04	34.96	1.81	1.17	0.63
orbital 164	$4d_{Co}$	98.27	1.73	0.03	0.03	0.00
orbital 165	$4d_{Co}$	98.29	1.71	0.03	0.03	0.00
total electrons=				10.00	8.01	1.99



**Table A1.14** Detailed CASSCF orbital analysis of **4'** - NiV neutral species.

orbital type	%Ni	%V	total electrons	Electron Ni	Electron V
Ni d $\pi$	100%	0%	1.95	1.95	0
Ni d $\pi$	100%	0%	1.96	1.96	0
Ni d $\sigma$	90.1%	9.9%	1.91	1.72	0.19
Ni d $\delta$	100%	0%	1.97	1.97	0
Ni d $\delta$	100%	0%	1.97	1.97	0
V d $\pi$	0%	100%	1.00	0	1.00
V d $\pi$	0%	100%	1.00	0	1.00
$\sigma^*$	60.9%	39.1%	0.005	0.003	0.002
Ni'(4d/5d/4p/f)	90.0%	10.0%	0.002	0.002	0
4d	100%	0%	0.05	0.05	0
4d	40.9%	59.1%	0.09	0.04	0.05
4d	100%	0%	0.03	0.03	0
4d	100%	0%	0.03	0.03	0
4d	100%	0%	0.03	0.03	0
total electrons=			12.00	9.76	2.24

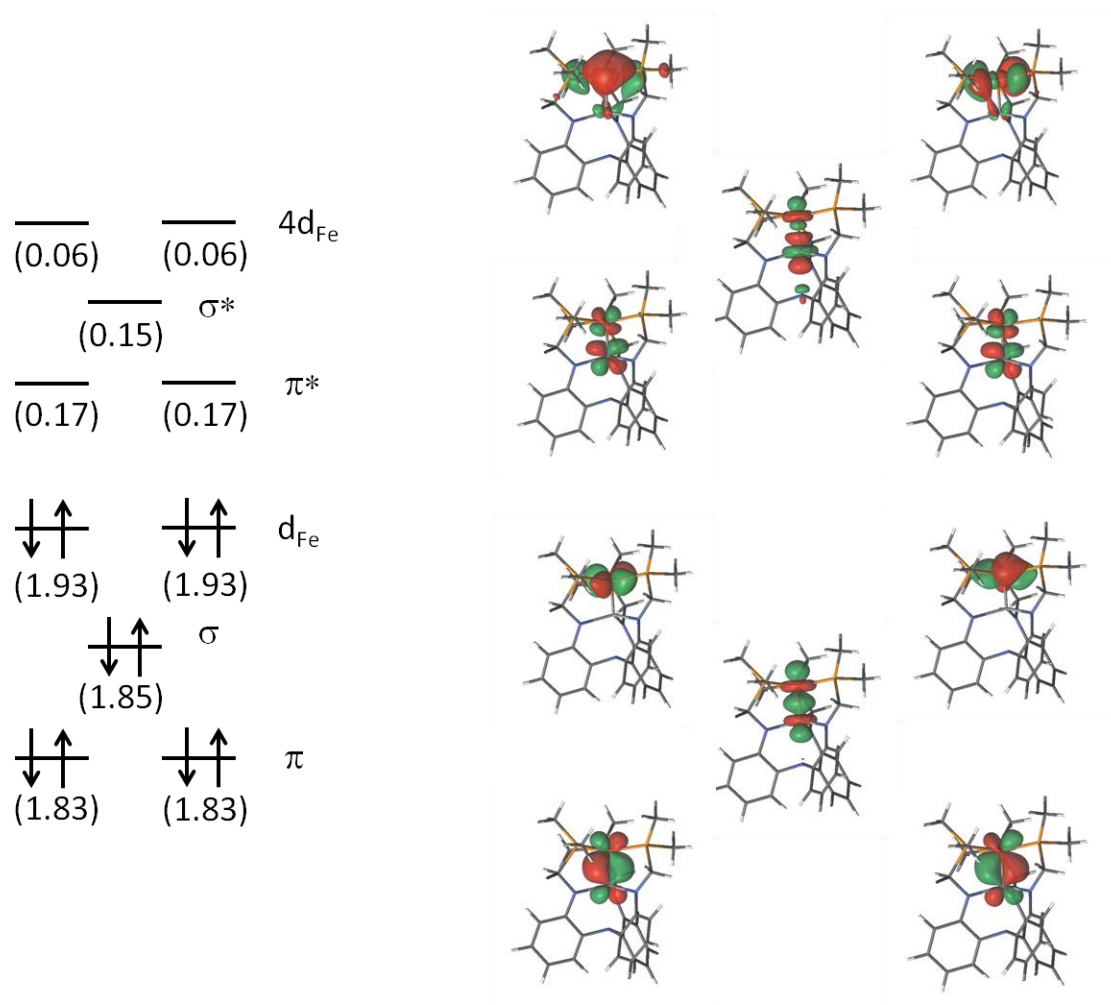


**Figure A1.18** Qualitative MO diagram showing the natural orbitals for **2'** – FeVL resulting from CASSCF calculations. The complete active space of 10 d-electrons in 10 orbitals is shown, with the occupancies per MO. Only the dominating electronic configuration (75 %) is shown. Effective bond order (computed by (bonding occupancies – antibonding occupancies)/2) is 2.51.

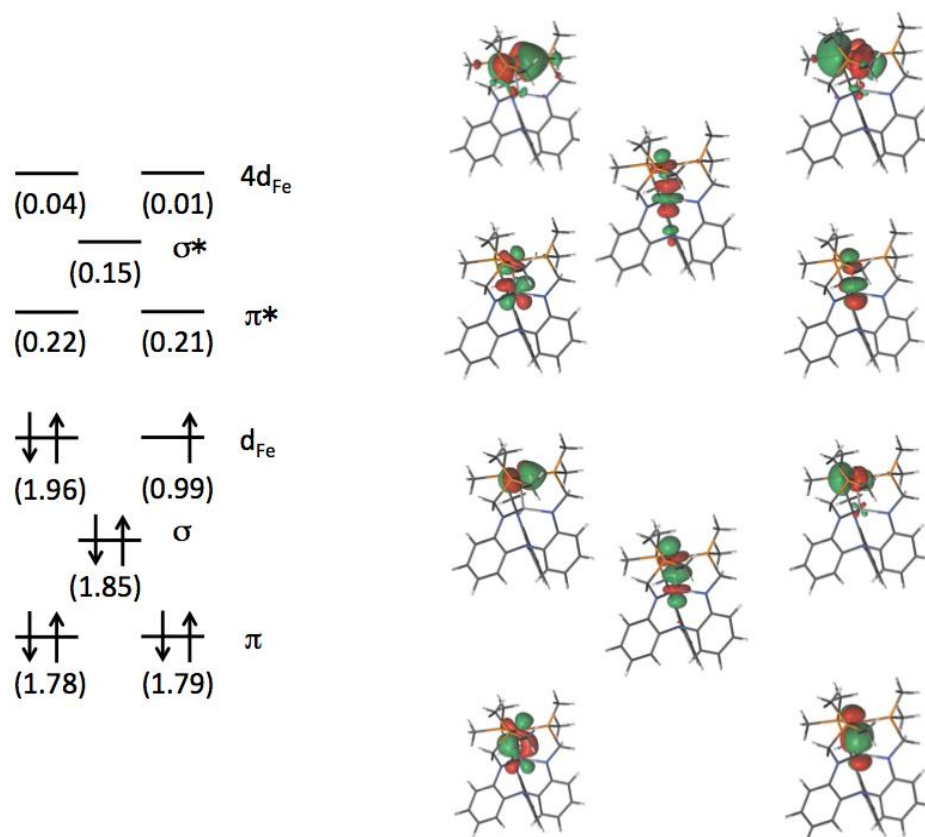


**Figure A1.19** Qualitative MO diagram showing the natural orbitals for  $2^{ox1}$  resulting from CASSCF calculations. The complete active space of 9 d-electrons in 10 orbitals is shown, with the occupancies per MO. Only the dominating electronic configuration (71 %) is shown. Effective bond order (computed by (bonding occupancies – antibonding occupancies)/2) is 2.42.

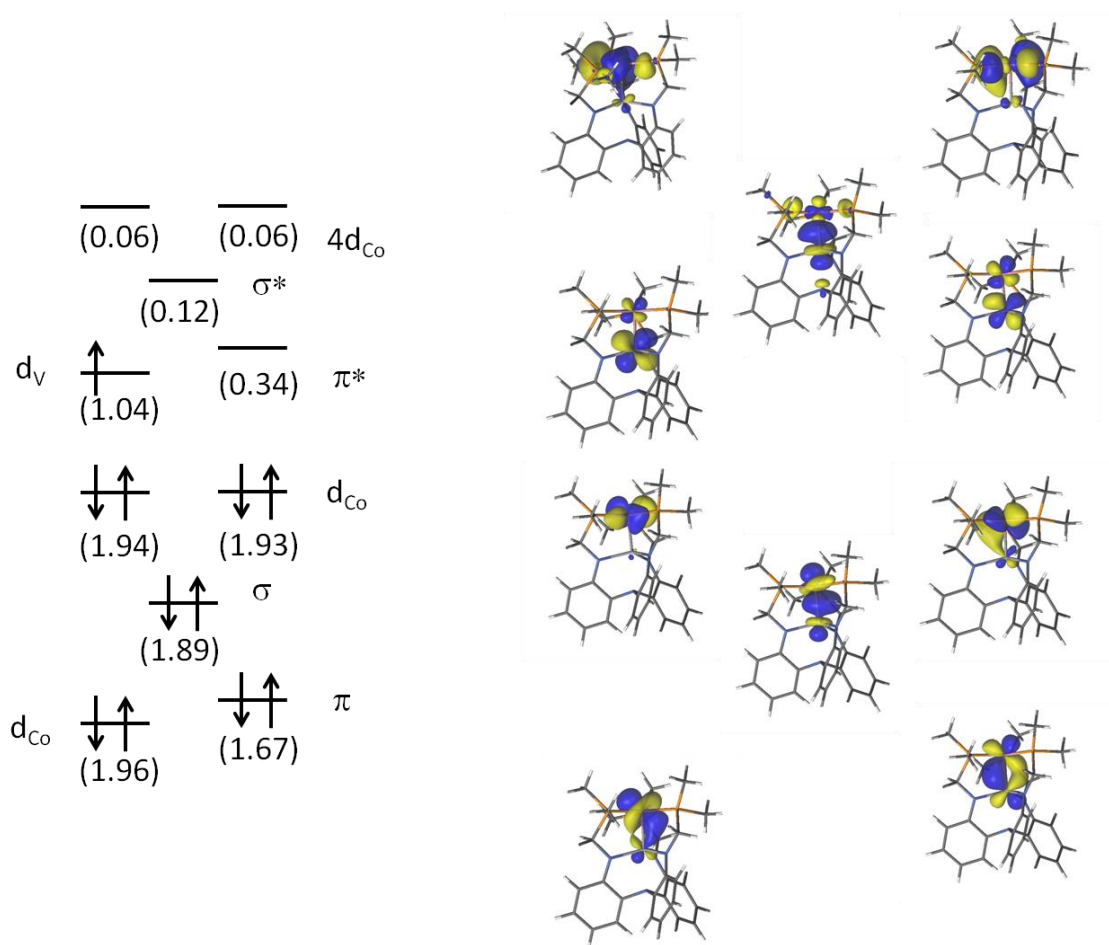


**Figure A1.20** Qualitative MO diagram showing the natural orbitals for **3'** resulting from CASSCF calculations. The complete active space of 11 d-electrons in 10 orbitals is shown, with the occupancies per MO. Only the dominating electronic configuration (72 %) is shown. Effective bond order (computed by (bonding occupancies – antibonding occupancies)/2) is 1.55.

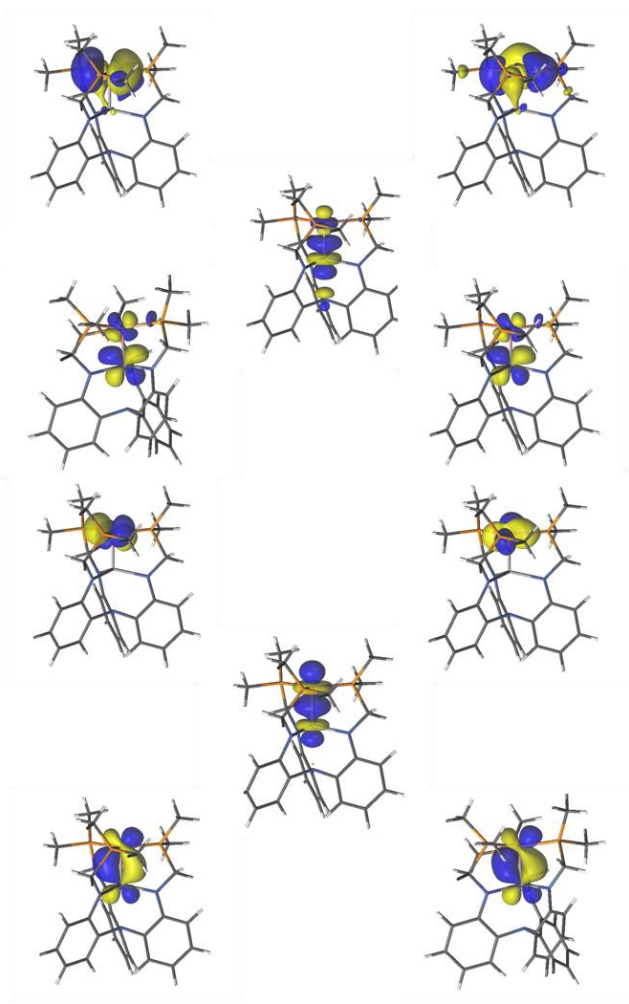
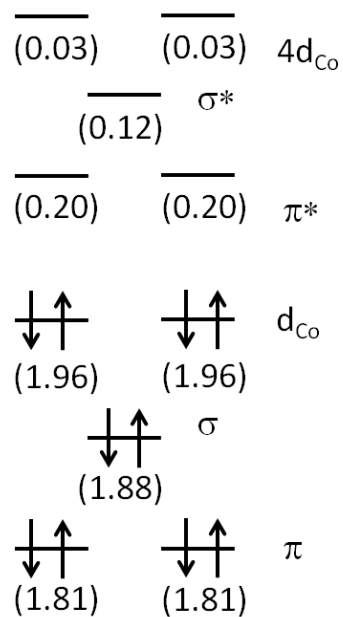


**Figure A1.21** Qualitative MO diagram showing the natural orbitals for  $3^{ox9}$  resulting from CASSCF calculations. The complete active space of 10 d-electrons in 10 orbitals is shown, with the occupancies per MO. Only the dominating electronic configuration (75 %) is shown. Effective bond order (computed by (bonding occupancies – antibonding occupancies)/2) is 2.49.

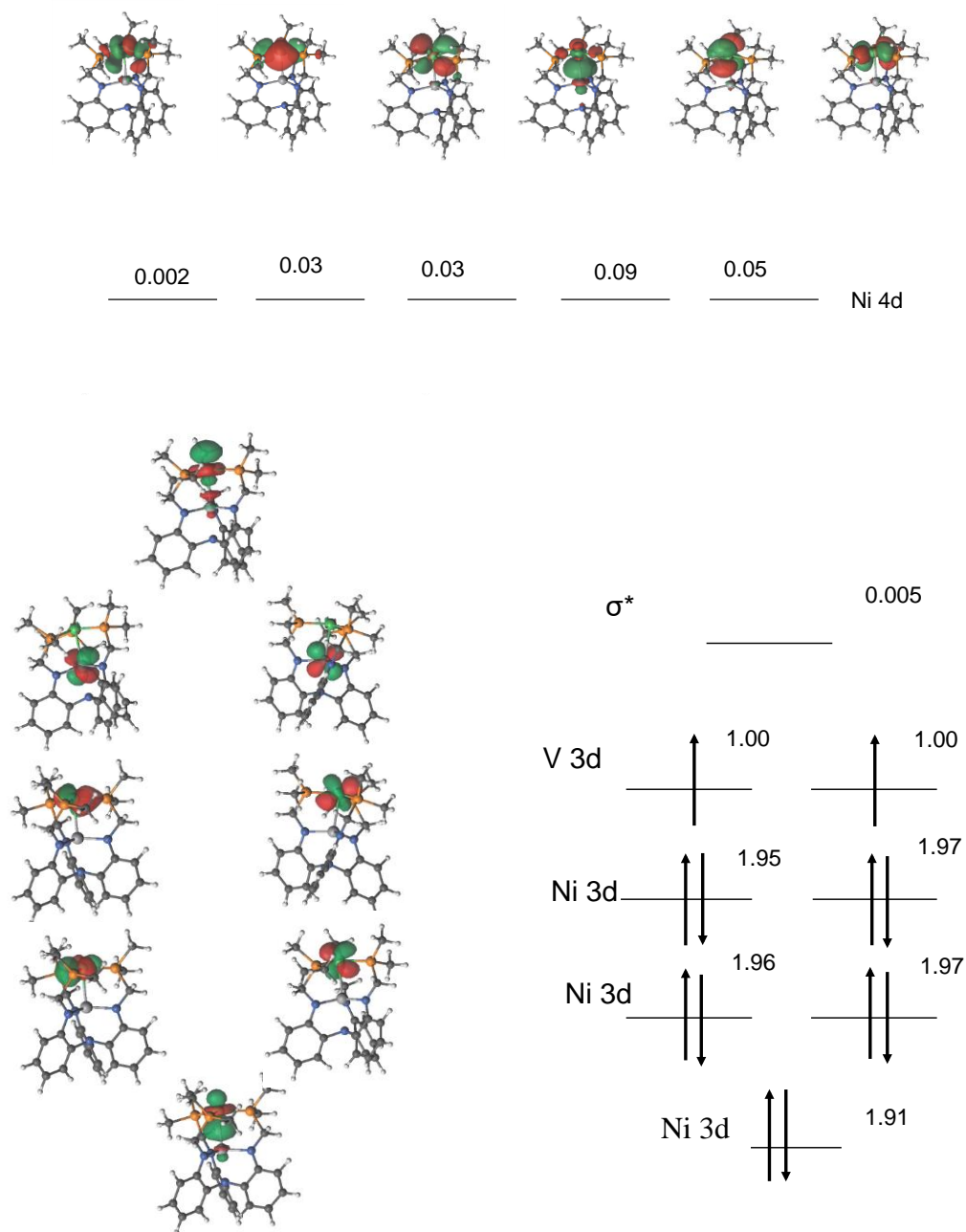


**Figure A1.22** Qualitative MO diagram showing the natural orbitals for **4'** resulting from CASSCF calculations. The complete active space of 12 *d*-electrons in 14 orbitals is shown, with the occupancies per MO. Only the dominating electronic configuration (88.4%) is shown. Effective and formal bond orders are both 0.

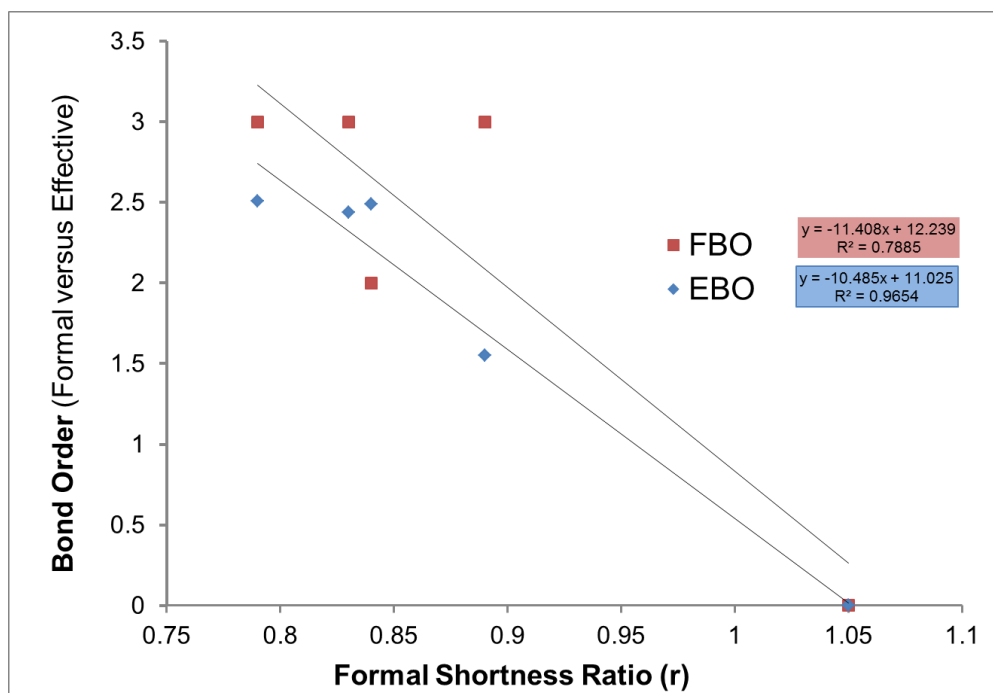


**Figure A1.23** Plot of bond order (formal versus effective, or FBO vs. EBO) against the experimentally determined formal shortness ratio ( $r$ ).

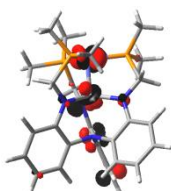
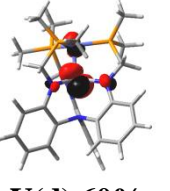
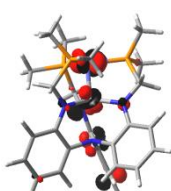
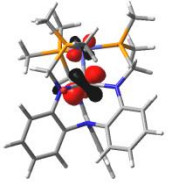
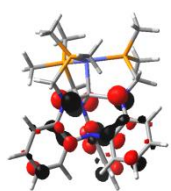
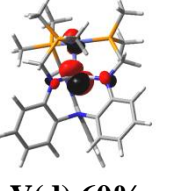
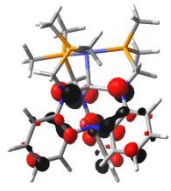
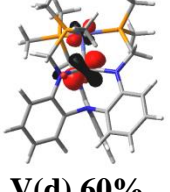
**Table A1.15** TD-DFT Excitation Energies and their MO Interpretations for **2**, FeVL neutral complex ( $d^{10}$ ) using the M06-2X functional.

Wavelength (nm) (Energy in eV)	Oscillator strength	Orb. Transition (Percent) <sup>a</sup>	Transition <sup>b</sup>	
			From:	To:
720.95 (1.720 eV)	0.0026	159 → 162 (24%)	 <b>Fe(d) 55%</b>	 <b>V(d) 55%</b>
		160 → 161 (28%)	 <b>Fe(d) 54%</b>	 <b>V(d) 55%</b>

<sup>a</sup> Some of the excited energies correspond to a single transition. Many of the excited energies correspond to multiple transitions, and the major contributing transitions are shown with their percent contributions

<sup>b</sup> Atomic orbital contributions (up to 10%) to the FeVL neutral complex are included.

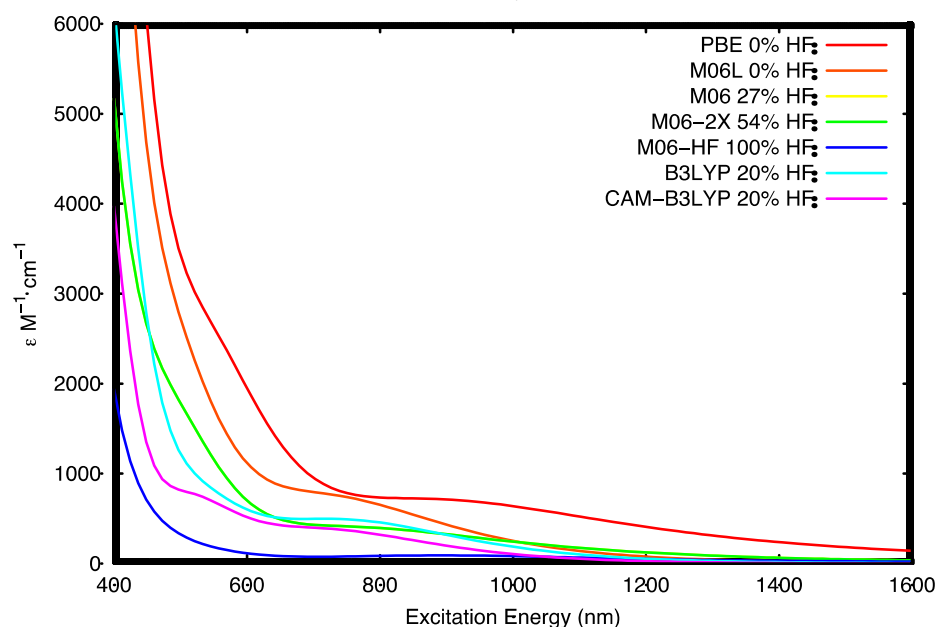
**Table A1.16** TD-DFT Excitation Energies and their MO Interpretations for **3ox**, CoVL cation complex ( $d^{10}$ ) using the M06-2X functional.

Wavelength (nm)	Oscillator strength	Orb. Transition (Percent) <sup>a</sup>	Transition <sup>b</sup>	
			From:	To:
646.66 (1.917 eV)	0.0288	158 → 161 (33%)	 <b>Co(d) 42%</b>	 <b>V(d) 60%</b> <b>Co(d) 17%</b>
		158 → 162 (33%)	 <b>Co(d) 42%</b>	 <b>V(d) 60%</b> <b>Co(d) 17%</b>
573.91 (2.160 eV)	0.0214	160 → 161 (90%)	 <b>N(p) 36%</b>	 <b>V(d) 60%</b> <b>Co(d) 17%</b>
573.85 (2.161 eV)	0.0215	160 → 162 (90%)	 <b>N(p) 36%</b>	 <b>V(d) 60%</b> <b>Co(d) 17%</b>

<sup>a</sup> Some of the excited energies correspond to a single transition. Many of the excited energies correspond to multiple transitions, and the major contributing transitions are shown with their percent contributions.

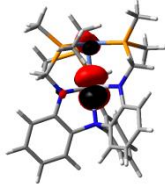
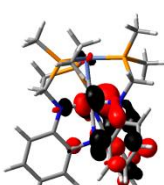
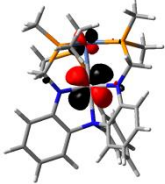
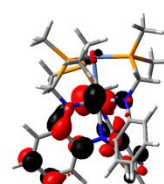
<sup>b</sup> Atomic orbital contributions (up to 10%) to the CoVL cation complex are included.

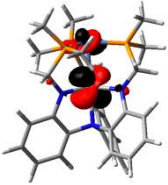
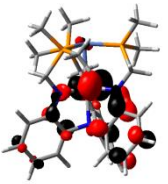
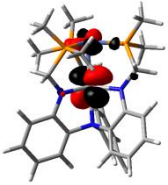
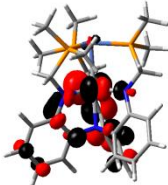
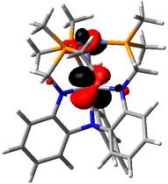
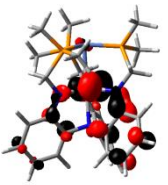
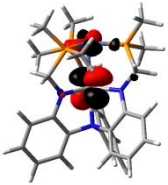
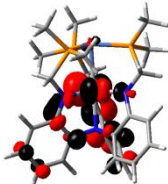
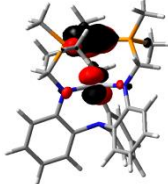
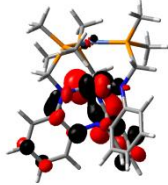


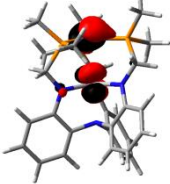
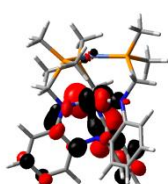
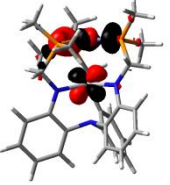
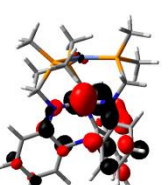
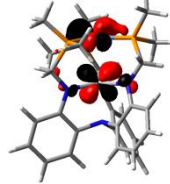
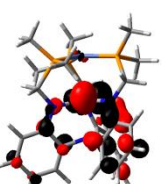
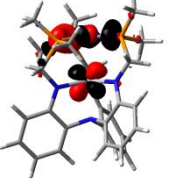
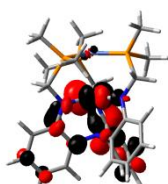


**Figure A1.24** Predicted vis-NIR spectra for NiVL(4) by using different DFT functionals. The percent of Hartree-Fock on the functional is shown in the legend.

**Table A1.17** TD-DFT Excitation Energies and their MO Interpretations for 4, NiVL neutral complex ( $d^{12}$ ).

Functionals	Wavelength (nm)	Oscillat or strength	Orb. Transition (Percent)	Transition Atom (type of orbital) percentage <sup>b</sup>	
				From:	To:
PBE	916 (1.4 eV)	0.0111	162A → 165A (39%)	 <b>V(d) 76%</b> <b>Ni(d) 11%</b>	 <b>V(d) 38%</b>
			161A → 164A (38%)	 <b>V(d) 76%</b> <b>Ni(d) 11%</b>	 <b>V(d) 38%</b>

	737 (1.7 eV)	0.0107	162A → 164A (50%)	 <b>V(d) 68%</b> <b>Ni(d) 17%</b>	 <b>V(d) 45%</b>
			161A → 165A (49%)	 <b>V(d) 68%</b> <b>Ni(d) 17%</b>	 <b>V(d) 45%</b>
M06-L	737 (1.7 eV)	0.0107	162A → 164A (50%)	 <b>V(d) 68%</b> <b>Ni(d) 17%</b>	 <b>V(d) 45%</b>
			161A → 165A (49%)	 <b>V(d) 68%</b> <b>Ni(d) 17%</b>	 <b>V(d) 45%</b>
M06	820 (1.5 eV)	0.0053	162A → 165A (16%)	<b>Ni (d) 32%</b> <b>V (d) 29%</b>	<b>V (d) 41%</b>
			159A → 165A (14%)	<b>Ni (d) 39%</b> <b>V (d) 35%</b>	<b>V (d) 41%</b>
			161A → 164A (14%)	<b>Ni (d) 32%</b> <b>V (d) 29%</b>	<b>V (d) 41%</b>
			158A → 164A (12%)	<b>Ni (d) 39%</b> <b>V (d) 35%</b>	<b>V (d) 41%</b>
			161A → 165A (11%)	<b>Ni (d) 32%</b> <b>V (d) 29%</b>	<b>V (d) 41%</b>
M06-2X	820 (1.5 eV)	0.0053	162A → 165A (16%)	 <b>Ni (d) 32%</b> <b>V (d) 29%</b>	 <b>V (d) 41%</b>

M06-HF	942 (1.3 eV)	0.0019	159A → 165A (14%)	 <b>Ni (d) 39%</b> <b>V (d) 35%</b>	 <b>V (d) 41%</b>
			161A → 164A (14%)	 <b>Ni (d) 32%</b> <b>V (d) 29%</b>	 <b>V (d) 41%</b>
			158A → 164A (12%)	 <b>Ni (d) 39%</b> <b>V (d) 35%</b>	 <b>V (d) 41%</b>
			161A → 165A (11%)	 <b>Ni (d) 32%</b> <b>V (d) 29%</b>	 <b>V (d) 41%</b>
B3LYP	789 (1.6 eV)	0.0028	162A → 164A (10%)	<b>Ni (d) 32%</b> <b>V (d) 29%</b>	<b>V (d) 41%</b>
			162A → 165A (18%)	<b>Ni (d) 36%</b> <b>V (d) 24%</b>	<b>V (d) 33%</b>
			158A → 164A (14%)	<b>Ni (d) 39%</b> <b>V (d) 32%</b>	<b>V (d) 33%</b>
			159A → 164A (13%)	<b>Ni (d) 39%</b> <b>V (d) 32%</b>	<b>V (d) 33%</b>
CAM-B3LYP	770 (1.6 eV)	0.0021	156A → 164A (8%)	<b>Ni (d) 43%</b> <b>V (d) 26%</b>	<b>V (d) 29%</b>
			157A → 165A (8%)	<b>Ni (d) 43%</b> <b>V (d) 26%</b> <b>C (p) 10%</b>	<b>V (d) 29%</b>
			154A → 164A (8%)	<b>Ni (d) 44%</b> <b>V (d) 42%</b>	<b>V (d) 29%</b>
			160A → 164A (8%)	<b>Ni (d) 41%</b>	<b>V (d) 29%</b>

<sup>a</sup> Some of the excited energies correspond to a single transition. Many of the excited energies correspond to multiple transitions, and the major contributing transitions are shown with their percent contributions.

<sup>b</sup> Atomic orbital contributions (up to 10%) of the NiVL neutral complex are included.

## Appendix 2

Supporting information files for Chapter 3

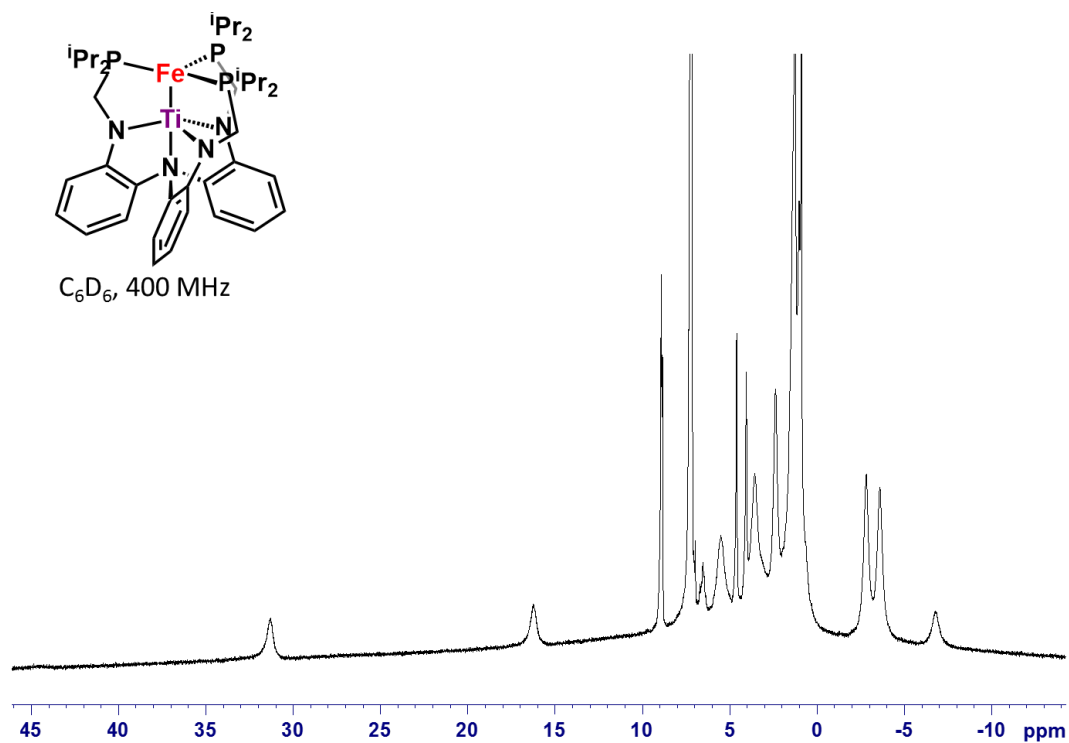


**Figure A2.1** <sup>1</sup>H NMR spectrum of **2** in C<sub>6</sub>D<sub>6</sub> (500 MHz).

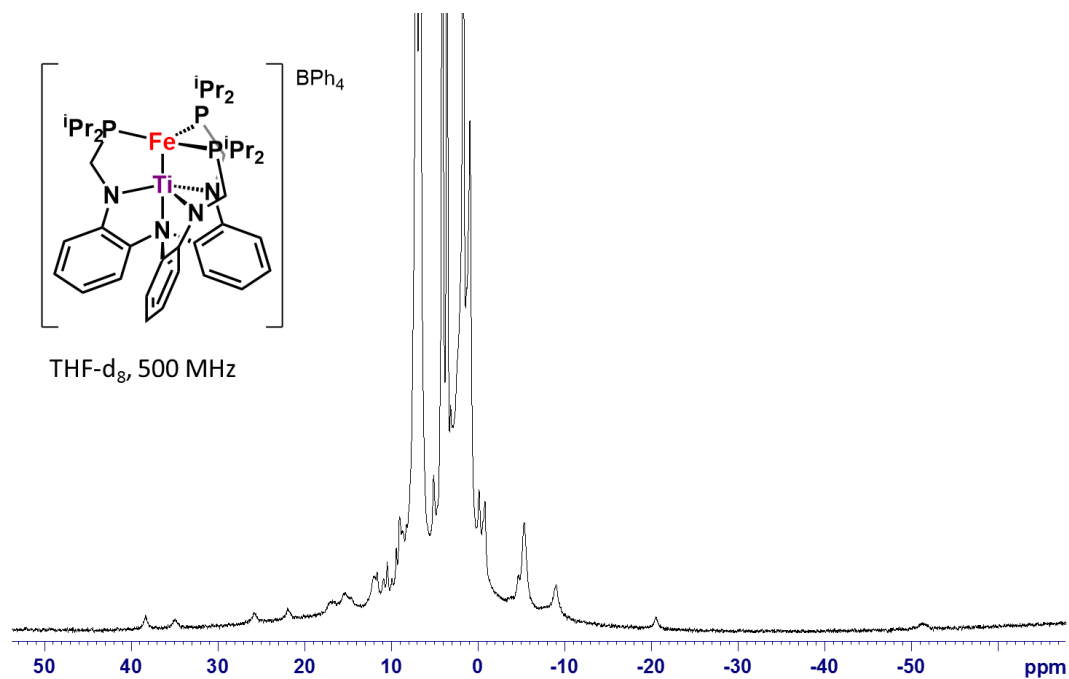


**Figure A2.2** <sup>1</sup>H NMR spectrum of **2<sup>ox</sup>** in THF-d<sub>8</sub> (500 MHz).

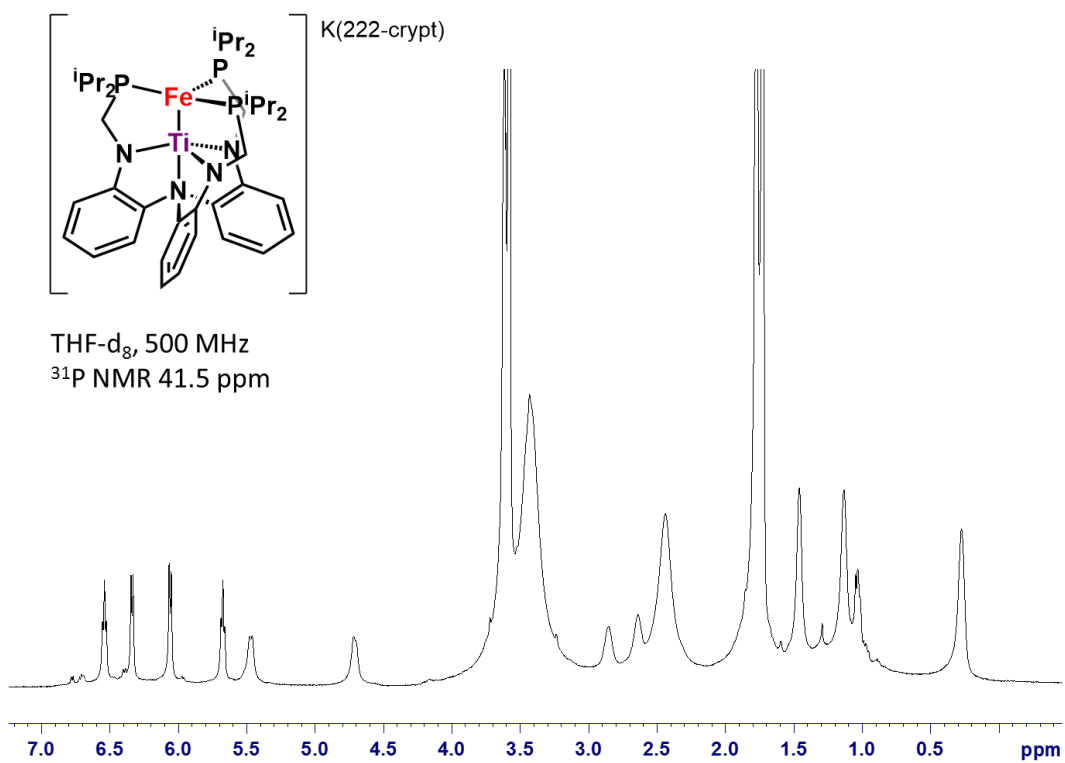


**Figure A2.3** <sup>1</sup>H NMR spectrum of **2<sup>red</sup>** in THF-d<sub>8</sub> (500 MHz).

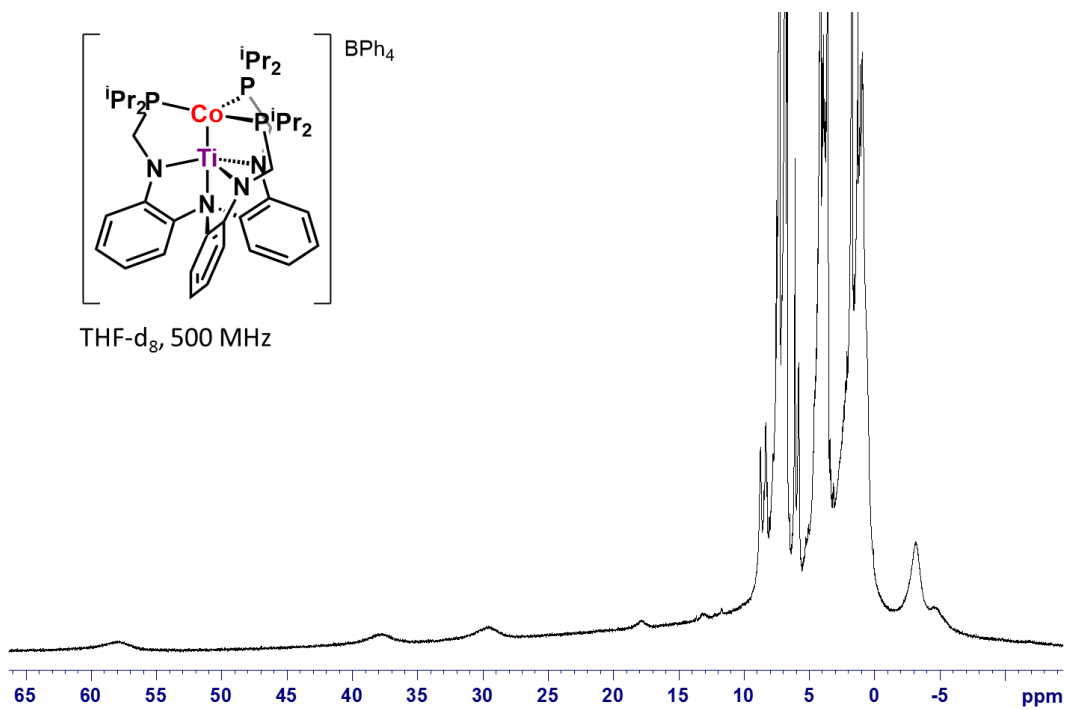


**Figure A2.4** <sup>1</sup>H NMR spectrum of **3<sup>ox</sup>** in THF-d<sub>8</sub> (500 MHz).

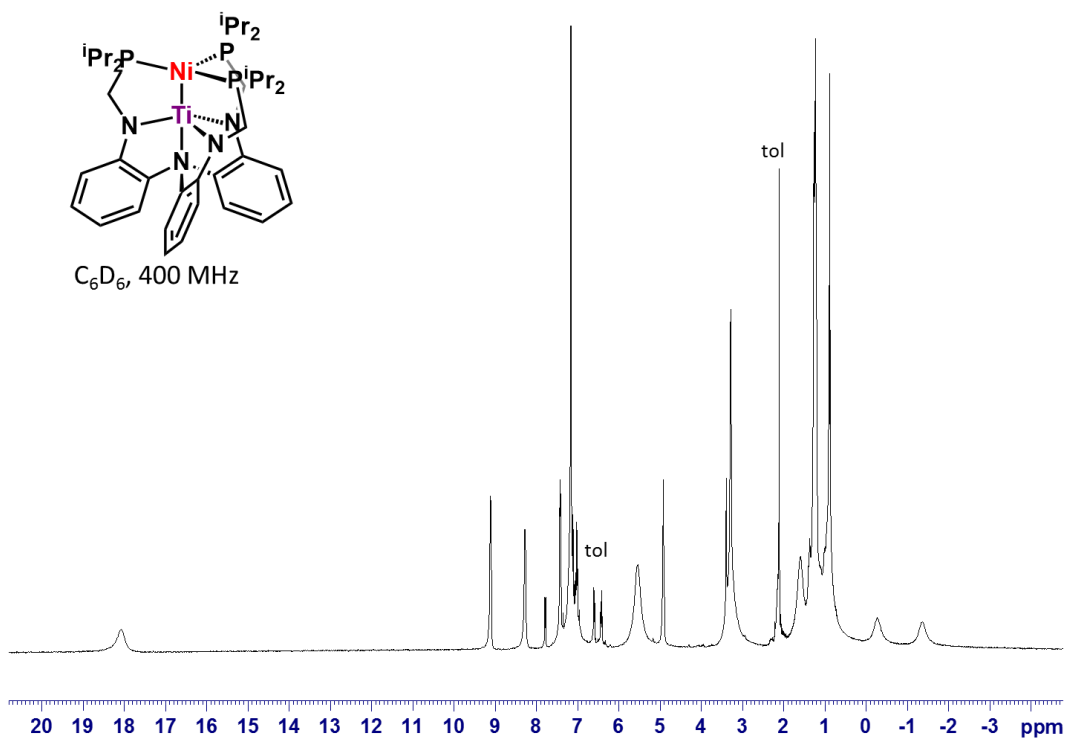


**Figure A2.5**  $^1\text{H}$  NMR spectrum of **4** in  $\text{C}_6\text{D}_6$  (400 MHz).

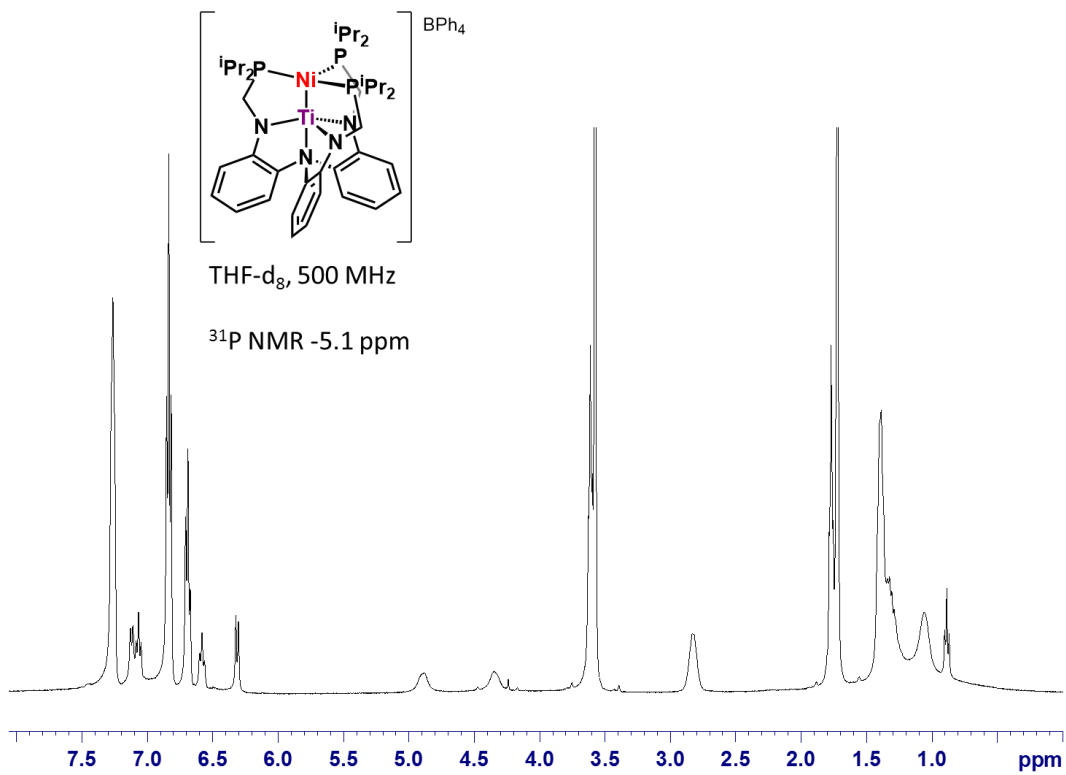


**Figure A2.6**  $^1\text{H}$  NMR spectrum of **4<sup>ox</sup>** in THF-d<sub>8</sub> (500 MHz).

## Appendix 3

Supporting information figures for Chapter 4

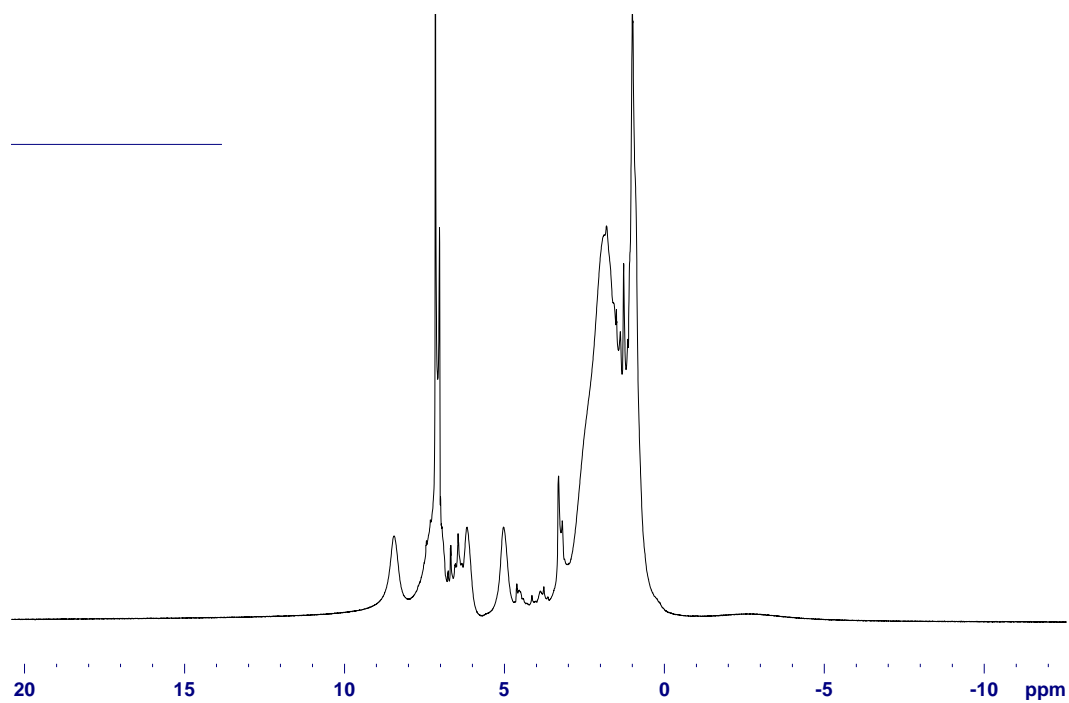


**Figure A3.1**  $^1\text{H}$  NMR spectrum of TiL in  $\text{C}_6\text{D}_6$  (500 MHz).

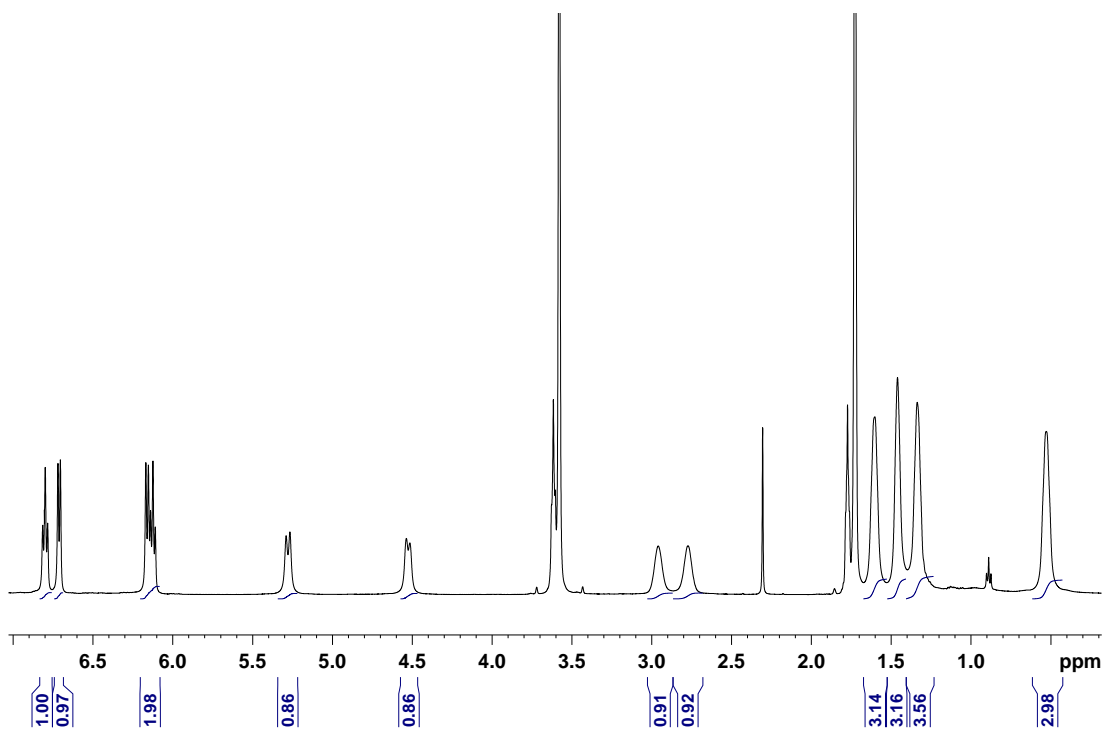


**Figure A3.2** <sup>1</sup>H NMR spectrum of **1** in THF-d<sub>8</sub> (500 MHz).

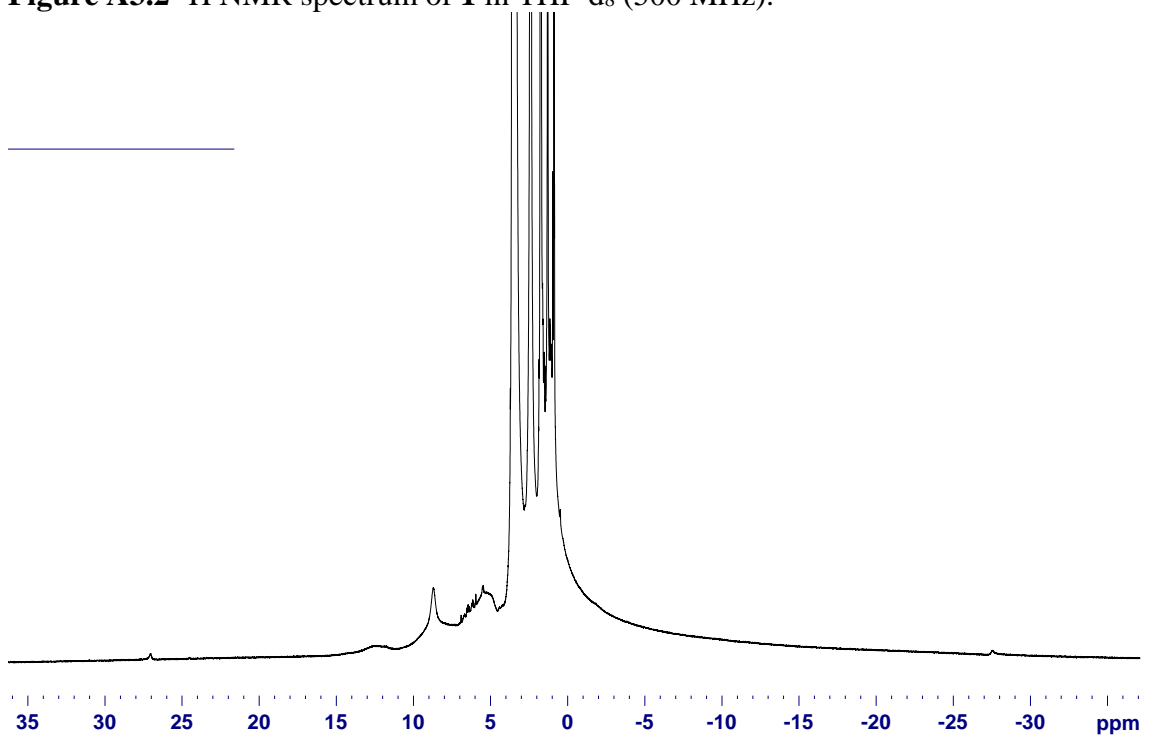


**Figure A3.3** <sup>1</sup>H NMR spectrum of **2** in THF-d<sub>8</sub> (500 MHz).



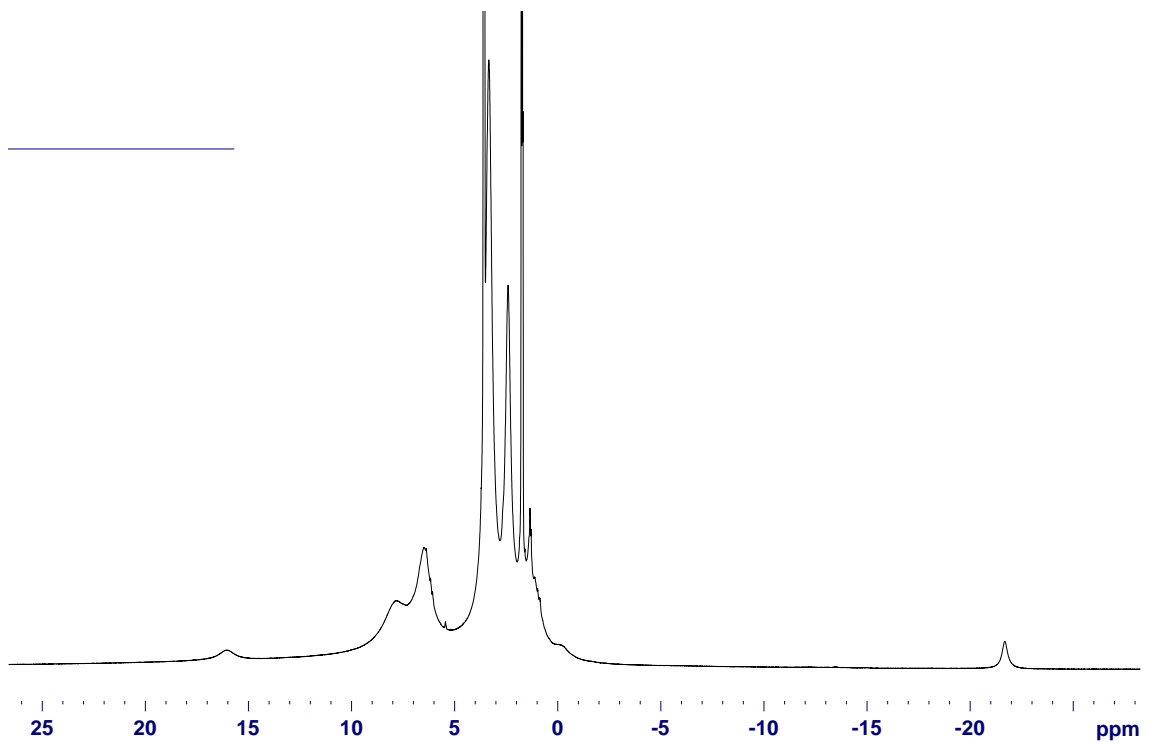


**Figure A3.4**  $^1\text{H}$  NMR spectrum of **3** in THF- $d_8$  (500 MHz).

**Table A3.1** Selected crystallographic details for neutral CoML complexes.

	1 - CoTiL	CoVL	CoCrL		CoCoL	(N <sub>2</sub> )CoAl L
Co-M (Å)	2.1979(8)	2.1234(4)	2.1454(11)	2.1349(11)	2.3231(6)	2.6202(9)
FSR	0.89	0.89	0.92	0.92	1.00	1.06
Co-N						1.841(3)
N-N						1.107(4)
Co-P	2.2444(11)	2.2315(7)	2.2083(16)	2.2093(16)	2.2878(11)	2.2408(8)
	2.2553(11)	2.2317(6)	2.2171(16)	2.2128(16)	2.2975(10)	2.2712(8)
	2.2704(11)	2.2434(6)	2.2213(15)	2.2183(17)	2.3025(10)	2.2859(9)
Co-P (ave)	2.26	2.33	2.22	2.21	2.30	2.27
M-Neq	1.947(3)	1.9442(18)	1.915(4)	1.924(4)	1.922(3)	1.872(2)
	1.954(3)	1.9543(18)	1.921(4)	1.925(4)	1.923(3)	1.878(2)
	1.955(3)	1.9694(17)	1.925(4)	1.926(4)	1.926(2)	1.879(2)
M-Neq (ave)	1.95	1.96	1.92	1.93	1.92	1.88
M-Nap	2.251(3)	2.2266(17)	2.226(4)	2.216(4)	2.167(2)	2.187(2)
Co to P3-plane	-0.128	-0.03	0.053	0	-0.155	0.42
M to N3-plane'	0.298	0.395	0.38	0.363	0.179	0.32
P-Co-P angle	119.63(4)	120.61(3)	119.08(6)	117.91(6)	119.11(4)	105.07(3)
	118.16(4)	120.01(2)	119.71(6)	120.64(6)	118.71(4)	111.90(3)
	121.25(4)	119.33(3)	121.04(6)	121.40(6)	120.82(4)	132.50(3)
Neq - M-Neq	117.50(13)	114.20(8)	113.51(18)	115.06(18)	119.18(12)	118.4(1)
	116.68(13)	117.03(8)	117.83(17)	116.53(19)	119.10(14)	116.1(1)
	118.93(13)	116.84(8)	117.21(18)	117.96(18)	119.17(14)	117.0(1)
Co-M-Nap	178.90(8)	177.67(5)	179.58(13)	178.67(11)	179.87(8)	177.92(7)

**Table A3.2** Selected crystallographic details for anionic CoML complexes.

	K(crypt-222)[(N <sub>2</sub> )CoVL]		K(crypt-222)[(N <sub>2</sub> )CoCrL]		K(crypt-222)[(N <sub>2</sub> )Co <sub>2</sub> L]	K(crypt-222)[(N <sub>2</sub> )CoAIL]
Co-M (Å)	2.6466(7)	2.6661(7)	2.5822(11)	2.5377(12)	2.6771(7)	2.507(2)
FSR	1.11	1.12	1.11	1.09	1.16	1.02
Co-N	1.796(3)	1.788(3)	1.792(5)	1.813(5)	1.770(4)	1.789(3)
N-N	1.130(4)	1.135(4)	1.135(6)	1.120(7)	1.114(4)	1.110(8)
Co-P	2.2024(9)	2.1859(10)	2.1907(15)	2.1988(14)	2.2505(10)	2.177(1)
	2.2049(A)	2.1968(10)	2.1918(14)	2.2057(14)	2.2515(10)	
	2.2121(10)	2.2094(10)	2.1965(14)	2.2188(15)	2.2651(11)	
Co-P (ave)	2.21	2.2	2.19	2.21	2.26	2.18
M-Neq	1.952(3)	1.946(3)	1.953(4)	1.975(4)	1.929(3)	1.898(3)
	1.954(3)	1.949(3)	1.974(4)	1.975(5)	1.931(3)	
	1.958(3)	1.957(3)	1.980(4)	1.979(4)	1.933(3)	
M-Neq (ave)	1.95	1.95	1.97	1.98	1.93	
M-Nap	2.212(2)	2.222(3)	2.202(4)	2.183(4)	2.135(3)	2.324(6)
Co to P3-plane	0.407	0.428	0.312	0.357	0.383	0.375
M to N3-plane'	0.356	0.343	0.34	0.328	0.249	0.426
P-Co-P angle	109.29(4)	107.59(4)	116.36(6)	122.21(6)	124.02(4)	117.10(2)
	124.97(4)	121.18(4)	117.64(6)	113.74(6)	112.75(4)	
	115.63(4)	120.04(4)	120.01(6)	116.31(6)	114.70(4)	
Neq - M-Neq	117.35(11)	116.39(12)	115.07(18)	118.3(2)	119.01(11)	115.11(8)
	117.03(11)	118.89(12)	107.07(18)	128.26(19)	118.38(12)	
	115.89(11)	115.65(12)	128.88(19)	105.13(19)	117.71(12)	
Co-M-Nap v(N <sub>2</sub> )	179.03(7)	178.37(8)	179.06(11)	178.91(12)	178.97(8)	180
		1971		1990	1994	1995
[CoM]0/-redox potential (V)		-2.48		-2.32	-2.12	-0.95

**Table A3.3** Redox potentials (V) for CoML species for samples collected in 0.4 M TBAPF<sub>6</sub> in THF at scan speed of 50 mV/s under Argon with the following exceptions: CoCrL collected at 10 mV/s with the 1<sup>st</sup> and 2<sup>nd</sup> oxidations and 2<sup>nd</sup> reductions listed under N<sub>2</sub>, CoCoL collected in 0.1 M TBAPF<sub>6</sub> in DME at 10mV/s, and CoAIL collected under N<sub>2</sub>.

	<b>2nd Oxidation</b>	<b>1st Oxidation</b>	<b>1st reduction</b>	<b>2nd reduction</b>
<b>CoTiL</b>	-0.21	-0.79	-3.2	
<b>CoVL</b>		-1.6	-2.5	
<b>CoCrL</b>	-0.42	-1.32	-2.32	-3.27
<b>CoCoL</b>			-2.11	-2.74
<b>CoAIL</b>			-0.95	

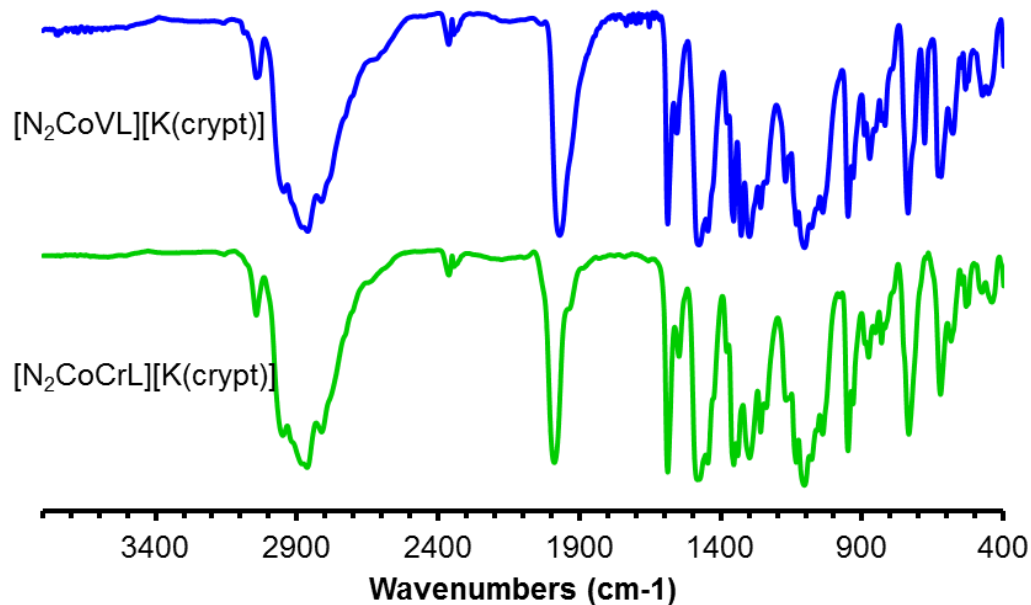


**Figure A3.5** IR spectra (KBr pellet) of **2** and **3**.

### Computational Details

**Table A3.4** Comparison of calculated and experimental bond lengths (Å) and angles (deg) for the CoTiL neutral species

Complexes	Experimental	CoTiL (M06-L)		CoTiL(PBE)*	
		Calculated	$\Delta(\text{calc-exp})$	Calculated	$\Delta(\text{calc-exp})$
<b>Co-Ti</b>	2.1979(8)	2.059	-0.139	2.196	-0.002
<b>Co-P</b>	2.2444(11)	2.199	-0.046	2.174	-0.070
	2.2553(11)	2.200	-0.055	2.176	-0.079
	2.2704(11)	2.209	-0.061	2.180	-0.090
<b>Ti-N<sub>eq</sub></b>	1.947(3)	2.009	0.062	1.999	0.055
	1.954(3)	2.013	0.058	2.002	0.046
	1.955(3)	2.016	0.060	2.000	0.044
<b>Ti-N<sub>ax</sub></b>	2.251(3)	2.339	0.088	2.315	0.064
<b><math>\Sigma(\text{P-Co-P})</math></b>	119.63(4)	117.60	-0.57	119.30	1.14
	118.16(4)	121.05	1.42	120.26	0.63
	121.25(4)	121.23	-0.03	120.27	-0.98
<b><math>\Sigma(\text{N-Ti-N})_{\text{eq}}</math></b>	117.50(13)	113.54	-3.14	115.06	-1.62
	116.68(13)	113.83	-3.67	115.70	-1.80
	118.93(13)	116.12	-2.81	116.04	-2.89
<b>CoP-TiN-N<sub>ax</sub></b>	178.90(8)	179.25	0.34	179.29	0.38

\*Note: The metal-metal bond distance was kept fixed and only the ligand was allowed to relax during the optimization process.

**Table A3.5** Comparison of Calculated (M06-L) and Experimental Bond Lengths (Å) and Angles (deg.) for N<sub>2</sub>-CoAIL anionic species

Complexes	N <sub>2</sub> -CoAIL <sup>-</sup>		
	Experimental	Calculated	$\Delta(\text{calc-exp})$
<b>Co-Al</b>	2.507(2)	2.486	-0.022
<b>Co-P</b>	2.177(1)	2.167	-0.010
	2.2712(8)	2.167	-0.104
	2.2859(9)	2.167	-0.119
<b>Al-N<sub>eq</sub></b>	1.878(2)	1.907	0.029
	1.879(2)	1.907	0.028
	1.898(3)	1.907	0.009
<b>Al-N<sub>ax</sub></b>	2.324(6)	2.348	0.023
<b><math>\Sigma(\text{P-Co-P})</math></b>	111.90(3)	116.65	4.75
	117.10(2)	116.71	-0.39
	132.50(3)	116.74	-15.77
<b><math>\Sigma(\text{N-Al-N})_{\text{eq}}</math></b>	115.11(8)	114.55	-0.57
	116.1(1)	114.59	-1.52
	117.0(1)	114.62	-2.39
<b>CoP-AlN-N<sub>ax</sub></b>	177.92(7)	179.99	2.06
<b>N<sub>1</sub>-N<sub>2</sub></b>	1.110(8)	1.130	0.019
<b>Co-N<sub>1</sub></b>	1.789(3)	1.794	0.005
<b>AlN-CoP-N<sub>1</sub></b>	-	179.98	-

**Table A3.6** Comparison of Calculated (M06-L) and Experimental Bond Lengths (Å) and Angles (deg.) for N<sub>2</sub>-CoVL anionic species.

Complexes	N <sub>2</sub> -CoVL <sup>-</sup>				
	Experimental		Calculated	Δ(calc-exp)	
Co-V	2.6466(7)	2.6661(7)	2.668	0.021	0.002
Co-P	2.2024(9)	2.1859(10)	2.181	-0.021	-0.005
	2.2049(A)	2.1968(10)	2.189	-0.016	-0.008
	2.2121(10)	2.2094(10)	2.202	-0.010	-0.007
V-N <sub>eq</sub>	1.952(3)	1.946(3)	1.957	0.005	0.011
	1.954(3)	1.949(3)	1.965	0.011	0.016
	1.958(3)	1.957(3)	1.974	0.016	0.017
V-N <sub>ax</sub>	2.212(2)	2.222(3)	2.239	0.027	0.017
Σ(P-Co-P)	109.29(4)	107.59(4)	107.42	-1.87	-0.17
	115.63(4)	120.04(4)	117.85	2.22	-2.20
	124.97(4)	121.18(4)	121.63	-3.34	0.45
Σ(N-V-N) <sub>eq</sub>	115.89(11)	115.65(12)	113.88	-2.01	-1.77
	117.03(11)	116.39(12)	117.87	0.84	1.48
	117.35(11)	118.89(12)	118.37	1.02	-0.52
Cop-V <sub>N</sub> -N <sub>ax</sub>	179.03(7)	178.37(8)	177.86	-1.18	-0.52
N <sub>1</sub> -N <sub>2</sub>	1.130(4)	1.135(4)	1.132	0.002	-0.003
Co-N <sub>1</sub>	1.796(3)	1.788(3)	1.799	0.003	0.011
V <sub>N</sub> -Cop-N <sub>1</sub>			175.761		

**Table A3.7** Comparison of Calculated (M06-L) and Experimental Bond Lengths (Å) and Angles (deg.) for N<sub>2</sub>-CoCrL anionic species.

Complexes	N <sub>2</sub> -CoCrL <sup>-</sup>				
	Experimental		Calculated	Δ(calc-exp)	
Co-Cr	2.5822(11)	2.5377(12)	2.5911	0.009	0.053
Co-P	2.1907(15)	2.1988(14)	2.1906	0.000	-0.008
	2.1918(14)	2.2057(14)	2.1897	-0.002	-0.016
	2.1965(14)	2.2188(15)	2.1935	-0.003	-0.025
Cr-N <sub>eq</sub>	1.953(4)	1.975(4)	1.9903	0.037	0.015
	1.974(4)	1.975(5)	1.9735	-0.001	-0.002
	1.980(4)	1.979(4)	2.0183	0.038	0.039
Cr-N <sub>ax</sub>	2.202(4)	2.183(4)	2.2129	0.011	0.030
Σ(P-Co-P)	116.36(6)	113.74(6)	115.99	-0.38	2.24
	117.64(6)	116.31(6)	117.24	-0.41	0.92
	120.01(6)	122.21(6)	118.90	-1.12	-3.32
Σ(N-Cr-N) <sub>eq</sub>	107.07(18)	105.13(19)	101.14	-5.93	-3.99
	115.07(18)	118.3(2)	117.30	2.23	-1.02
	128.88(19)	128.26(19)	131.55	2.67	3.29
Cop-Cr <sub>N</sub> -N <sub>ax</sub>	179.06(11)	178.91(12)	178.52	-0.54	-0.39
N <sub>1</sub> -N <sub>2</sub>	1.135(6)	1.120(7)	1.130	-0.006	0.009
Co-N <sub>1</sub>	1.792(5)	1.813(5)	1.807	0.015	-0.006
Cr <sub>N</sub> -Cop-N <sub>1</sub>			176.878		

**Table A3.8** Electronic energies at the M06-L/def2-TZVPD/SMD // M06-L/def2-TZVP level of theory. PBE electronic and free energies are included for CoTiL. Total energies (E, in a.u.) in gas phase, free energies (G, in a.u.) in gas phase, and  $\Delta G$  include the solvent effect (THF) and thermal corrections to the energy.

		Ti(M06-L)				
Complexes	Charge	Spin	E (gas phase)	$\Delta G^{THF}$	$\Delta G_{rel}$	
			a.u.	a.u.	kcal/mol	
CoTiL	0	0.0	<b>-4996.5948</b>	<b>-4995.8004</b>	<b>0.0</b>	
		1.5	-4996.5450	-4995.7526	30.0	
		2.5	-4996.5205	-4995.7334	42.0	
		3.5	-4996.4430	-4995.6582	89.2	

		Ti(PBE)			Ti (PBE/truncated-XRay)			
Charge	Spin	E (gas phase)	$\Delta G$ (gas phase)	$\Delta G_{rel}$	E (gas phase)	$\Delta G$ (gas phase)	$\Delta G_{rel}$	
		a.u.	a.u.	kcal/mol	a.u.	a.u.	kcal/mol	
CoTiL	0	0.0	<b>-4522.9744</b>	<b>-4522.4794</b>	<b>0.0</b>	<b>-4522.9719</b>	<b>-4522.4794</b>	<b>0.0</b>
		1.5	-4522.9188	-4522.4260	34.9	-4522.9183	-4522.4260	33.7
		2.5	-4522.8718	-4522.38124	64.4	-4522.8411	-4522.3812	82.1
		3.5	-4403.5873	-4403.0973	109.3	-4522.7545	-4403.0973	136.4

M=		Al			Ti				
Complexes	Charge	Spin	E (gas phase)	$\Delta G^{THF}$	$\Delta G_{rel}$	Spin	E (gas phase)	$\Delta G^{THF}$	$\Delta G_{rel}$
			a.u.	a.u.	kcal/mol		a.u.	a.u.	kcal/mol
N <sub>2</sub> -CoML	-1	0	<b>-4499.2214</b>	<b>-4498.4476</b>	<b>0.0</b>	0.5	<b>-5106.1896</b>	<b>-5105.4237</b>	<b>0.0</b>
		1.0	-4499.1537	-4498.3897	36.4	2.0	-5106.1422	-5105.3757	30.1
							4.0	-5106.0956	-5105.3440

M=		V			Cr				
Complexes	Charge	Spin	E (gas phase)	$\Delta G^{THF}$	$\Delta G_{rel}$	Spin	E (gas phase)	$\Delta G^{THF}$	$\Delta G_{rel}$
			a.u.	a.u.	kcal/mol		a.u.	a.u.	kcal/mol
N <sub>2</sub> -CoML	-1	0.0	-5200.6883	-5199.9188	16.3	0.5	-5301.1222	-5300.3546	26.8
		1.5	<b>-5200.7132</b>	<b>-5199.9447</b>	<b>0.0</b>	2.0	<b>-5301.1617</b>	<b>-5300.3973</b>	<b>0.0</b>
		2.5	-5200.6703	-5199.9130	19.9	4.0	-5301.1291	-5300.3790	11.5
		3.5	-5200.6241	-5199.8879	35.7				

**Table A3.9** Calculated Bond Lengths (Å) and N<sub>1</sub>-N<sub>2</sub> bond stretching frequencies (cm<sup>-1</sup>) for ground spin-state species. All species are in their anionic form, except free N<sub>2</sub>.

Species	N <sub>1</sub> -N <sub>2</sub> (cm <sup>-1</sup> )	Distances		
		Co-M	C <sub>OP</sub> -N <sub>1</sub>	N <sub>1</sub> -N <sub>2</sub>
<b>Free N<sub>2</sub></b>	2424	-	-	1.095
<b>Al/d<sup>10</sup>/u0</b>	2099	2.486	1.794	1.130
<b>Ti/d<sup>11</sup>/u1</b>	2087	2.562	1.805	1.131
<b>N<sub>2</sub>CoML V/d<sup>12</sup>/u2</b>	2085	2.668	1.799	1.132
<b>Cr/d<sup>13</sup>/u3</b>	2092	2.591	1.807	1.130
<b>Co/d<sup>16</sup>/u2</b>	2105	2.648	1.817	1.128

**Table A3.10** Calculated spin densities, CM5 charges, and NBO analysis at the metal centers and N<sub>2</sub> molecule for ground spin-state species.

Species	Spin Density		CM5 Charges				NBO		
	C <sub>OP</sub>	M <sub>N</sub>	C <sub>OP</sub>	M <sub>N</sub>	N <sub>1</sub>	N <sub>2</sub>	Co-M	C <sub>OP</sub> -N <sub>1</sub>	N <sub>1</sub> -N <sub>2</sub>
<b>Free N<sub>2</sub></b>	-	-	-	-	-	-	-	-	3.03
<b>Al/d<sup>10</sup>/u0</b>	0.00	0.00	0.26	0.40	-0.20	-0.15	0.30	0.98	2.58
<b>Ti/d<sup>11</sup>/u1</b>	-0.03	1.02	0.15	1.04	-0.21	-0.15	0.54	0.94	2.57
<b>N<sub>2</sub>CoML V/d<sup>12</sup>/u2</b>	-0.03	2.19	0.16	1.00	-0.21	-0.16	0.45	0.95	2.57
<b>Cr/d<sup>13</sup>/u3</b>	-0.29	3.36	0.15	0.99	-0.20	-0.15	0.51	0.93	2.58
<b>Co/d<sup>16</sup>/u2</b>	-0.89	2.28	0.20	0.62	-0.19	-0.13	0.23	0.86	2.59



➤ Spin density analysis

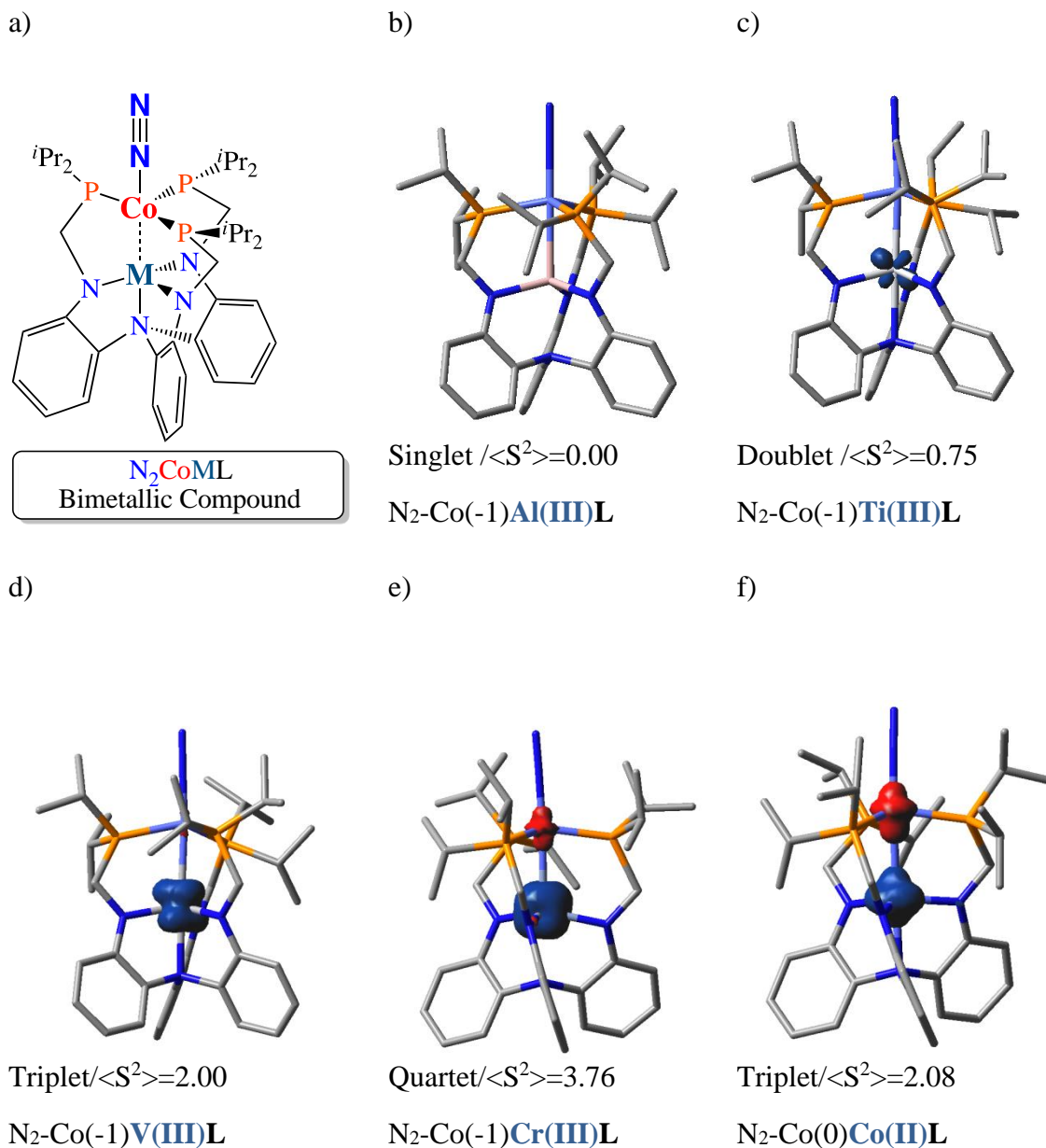


**Figure A3.6** Spin densities of N<sub>2</sub>-CoML anionic species. a) Schematic representation of the atom centers. b) For M=Al no unpaired electron was found; c) For M=Ti the  $\langle S^2 \rangle_{\text{calc}} = 0.75$ ; d) For M=V the  $\langle S^2 \rangle_{\text{calc}} = 2.00$ ; e) For M=Cr the  $\langle S^2 \rangle_{\text{calc}} = 3.76$ ; and f) For M=Co the  $\langle S^2 \rangle_{\text{calc}} = 2.08$ .<sup>1</sup>Blue density corresponds to alpha electron excess and red to beta electron excess, using isosurfaces = 0.04 a.u. Carbon atoms are in gray; nitrogen is in blue; and phosphorus in orange. Hydrogen atoms are not show for clarity of the structure.

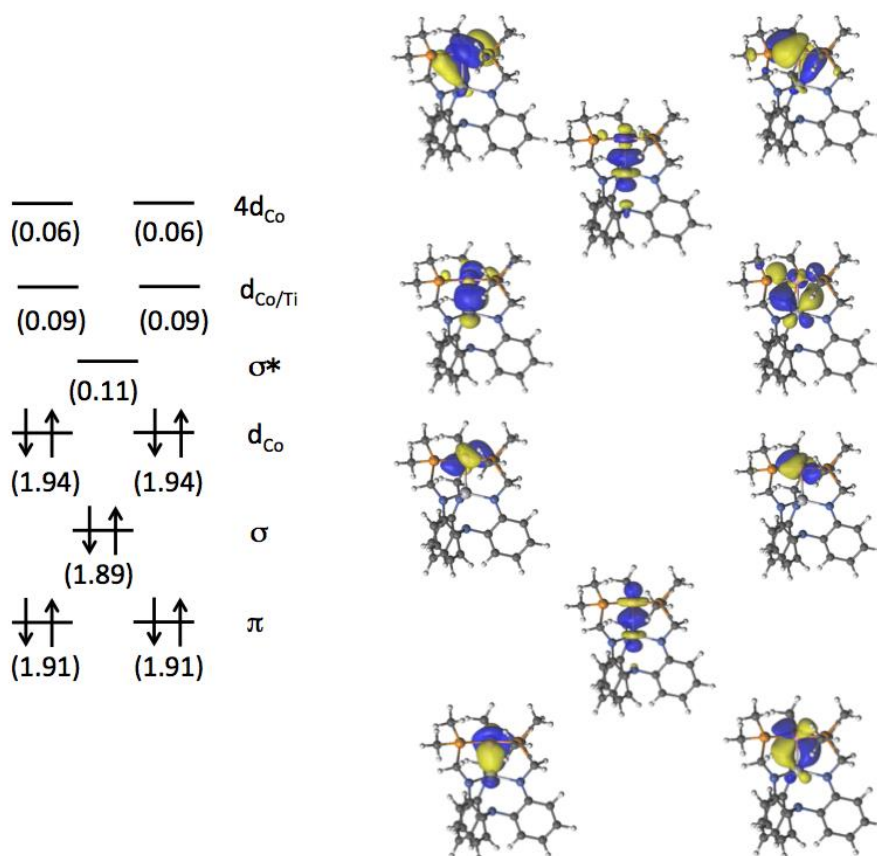


**Figure A3.7** Qualitative MO diagram showing the natural orbitals for CoTiL resulting from the CASSCF calculation. The complete active space of 10 *d*-electrons in 10 orbitals is shown, with the occupancies of the MOs. Only the dominating electronic configuration (83 %) is reported.

**Table A3.11** Detailed CASSCF orbital analysis of CoTiL (10,10) neutral species.

Orbital type	%C <sub>OP</sub>	%Ti <sub>N</sub>	total electrons	Electrons on C <sub>OP</sub>	Electrons on Ti <sub>N</sub>
d <sub>Co</sub>	100.00	0.00	1.94	1.94	0.00
□	86.02	13.98	1.91	1.65	0.27
□	70.93	29.07	1.89	1.34	0.55
□	86.07	13.93	1.91	1.65	0.27
□□	28.42	71.58	0.11	0.03	0.08
d <sub>Co/Ti</sub>	55.38	44.62	0.09	0.05	0.04
d <sub>Co/Ti</sub>	55.66	44.34	0.09	0.05	0.04
d <sub>Co</sub>	100.00	0.00	1.94	1.94	0.00
4d <sub>Co</sub>	93.71	6.29	0.06	0.05	0.00
4d <sub>Co</sub>	93.75	6.25	0.06	0.05	0.00
Total electrons			10.0	8.76	1.24
Oxidation State				0.24	2.76

**Table A3.12** Detailed CASSCF orbital analysis of CoTiL (10,10) neutral species. Energies in kcal/mol.

CoTiL (d <sup>10</sup> )	Spin state	<S <sup>2</sup> >pure	<S <sup>2</sup> >calc	DFT (PBE) (kcal/mol)	CASSCF (kcal/mol)	CASPT2 (kcal/mol)	Percent of main configuration
	<b>singlet</b>	<b>0.00</b>	<b>0.00</b>	<b>0.0</b>	<b>0.0</b>	<b>0.0</b>	<b>83%</b>
	triplet	2.00	2.00	33.7	35.4	67.0	90%
	quintet	6.00	6.00	82.1	80.9	100.3	95%
	septet	12.00	12.00	136.4	187.8	213.9	97%

\* The energetics correspond to the truncated structure with fixed metal-metal bond length.

❖ CASSCF molecular orbital analysis of the ground spin-state of N<sub>2</sub>-CoML species.

➤ N<sub>2</sub>CoTiL anion, d<sup>11</sup> system

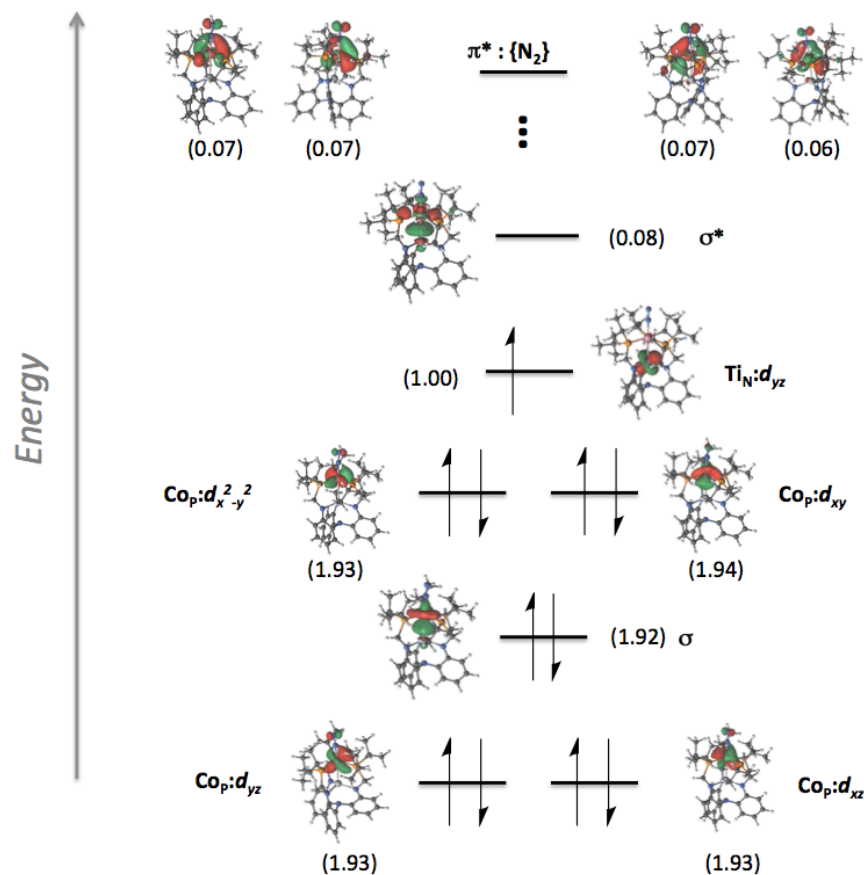


**Figure A3.8** Qualitative MO diagram showing the natural orbitals for N<sub>2</sub>-CoTiL resulting from CASSCF calculations. The complete active space of 11 *d*-electrons in 11 orbitals is shown, with the occupancies per MO. Only the dominating electronic configuration (84.7 %) is shown.

**Table A3.13** Detailed CASSCF orbital analysis of N<sub>2</sub>-CoTiL neutral species.

Orbital type	%Co <sub>P</sub>	%Ti <sub>N</sub>	Total electrons	Electrons on Co <sub>P</sub>	Electrons on Ti <sub>N</sub>	Electrons on N <sub>2</sub>	Electrons on P <sub>ligand</sub>
σ/Co	82.0	18.0	1.917	1.57	0.35	0.00	0.00
σ*	43.6	34.6	0.085	0.04	0.03	0.01	0.01
Ti	98.9	1.07	1.001	0.01	0.99	0.00	0.00
Co	93.8	-	1.932	1.81	-	0.12	0.00
Co	94.2	-	1.930	1.82	-	0.09	0.02
Co	96.9	-	1.936	1.88	-	0.06	0.00
Co	94.4	-	1.933	1.82	-	0.11	0.00
Co	47.2	1.7	0.063	0.03	0.00	0.01	0.02
Co	50.9	5.5	0.067	0.03	0.00	0.01	0.02
Co	53.6	2.2	0.067	0.04	0.00	0.01	0.02
Co	55.7	-	0.069	0.04	-	0.01	0.02
Total electrons				9.09	1.37	0.43	0.11
Oxidation State (O.S.)				-0.09	+2.63		
O.S. (including N <sub>2</sub> and ligand contribution)				-0.63	+2.63		

➤ N<sub>2</sub>CoVL anion, d<sup>12</sup> system

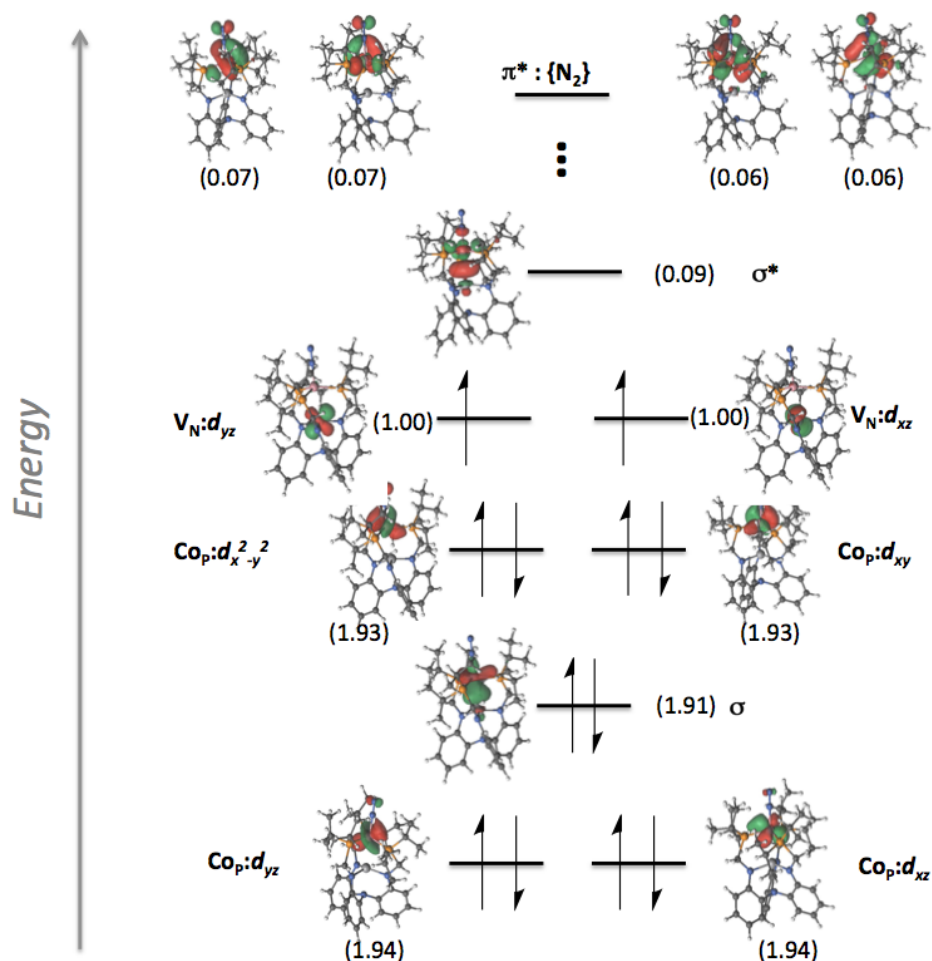


**Figure A3.9** Qualitative MO diagram showing the natural orbitals for N<sub>2</sub>-CoVL resulting from CASSCF calculations. The complete active space of 12 *d*-electrons in 12 orbitals is shown, with the occupancies per MO. Only the dominating electronic configuration (84.6 %) is shown.

**Table A3.14** Detailed CASSCF orbital analysis of N<sub>2</sub>-CoVL neutral species.

orbital type	%Co <sub>P</sub>	%V <sub>N</sub>	total electrons	Electrons on Co <sub>P</sub>	Electrons on V <sub>N</sub>	Electrons on N <sub>2</sub>	Electrons on P <sub>ligand</sub>
σ	79.8	18.9	1.911	1.52	0.36	0.00	0.02
σ*	48.1	28.3	0.092	0.04	0.03	0.01	0.01
V	-	100	1.001	-	1.00	0.00	0.00
V	-	100	1.001	-	1.00	0.00	0.00
Co	98.5	-	1.937	1.91	-	0.03	0.00
Co	94.2	-	1.937	1.82	-	0.09	0.02
Co	94.1	-	1.931	1.82	-	0.11	0.00
Co	93.9	-	1.929	1.81	-	0.12	0.00
Co	57.3	1.1	0.068	0.04	0.00	0.01	0.02
Co	48.0	-	0.061	0.03	-	0.01	0.02
Co	55.1	-	0.070	0.04	-	0.01	0.02
Co	50.2	3.4	0.061	0.03	0.00	0.01	0.02
Total electrons				9.07	2.39	0.40	0.13
Oxidation State (O.S.)				-0.07	+2.61		
O.S. (including N <sub>2</sub> and ligand contribution)				-0.60	+2.61		

➤ N<sub>2</sub>CoCrL anion, d<sup>13</sup> system

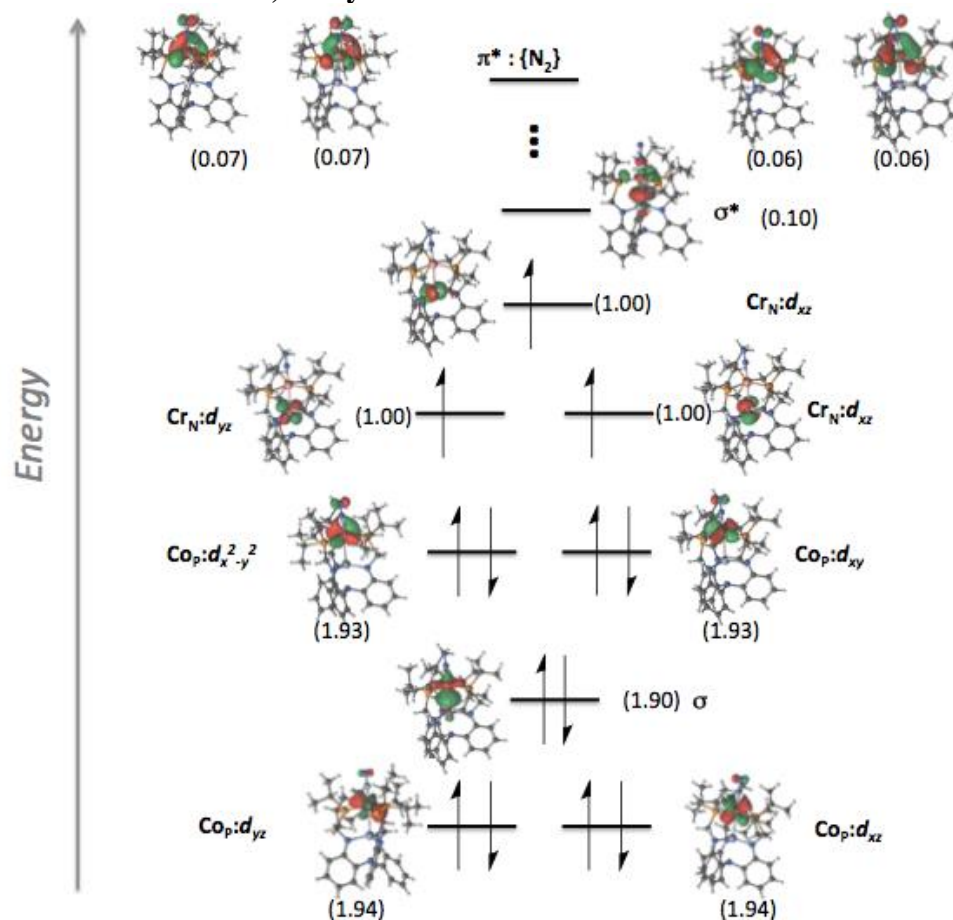


**Figure A3.10** Qualitative MO diagram showing the natural orbitals for N<sub>2</sub>-CoCrL resulting from CASSCF calculations. The complete active space of 13 *d*-electrons in 13 orbitals is shown, with the occupancies per MO. Only the dominating electronic configuration (84.4 %) is shown.



**Table A3.15** Detailed CASSCF orbital analysis of N<sub>2</sub>-CoCrL neutral species.

orbital type	%Co <sub>P</sub>	%Cr <sub>N</sub>	total electrons	Electrons on Co <sub>P</sub>	Electrons on Cr <sub>N</sub>	Electrons on N <sub>ligand</sub>	Electrons on P <sub>ligand</sub>
σ	79.2	20.8	1.905	1.51	0.40	0.00	0.00
σ*	46.2	31.0	0.098	0.05	0.03	0.01	0.01
Cr	-	100	1.001	-	1.00	0.00	0.00
Cr	-	100	1.000	-	1.00	0.00	0.00
Cr	-	100	1.001	-	1.00	0.00	0.00
Co	96.7	-	1.938	1.87	-	0.06	0.00
Co	95.4	-	1.939	1.85	-	0.09	0.00
Co	92.4	-	1.932	1.79	-	0.12	0.02
Co	93.8	-	1.930	1.81	-	0.09	0.03
Co	48.9	-	0.059	0.03	-	0.01	0.02
Co	54.1	0.80	0.067	0.04	0.00	0.01	0.02
Co	56.4	-	0.070	0.04	-	0.01	0.02
Co	51.4	-	0.061	0.03	-	0.01	0.02
Total electrons				9.01	3.43	0.41	0.14
Oxidation State (O.S.)				-0.01	+2.57		
O.S. (including N <sub>2</sub> and ligand contribution)				-0.56	+2.57		

➤ **N<sub>2</sub>Co<sub>2</sub>L anion, d<sup>16</sup> system**

**Table A3.16** Details of σ and σ\* CASSCF bond orbital analysis of N<sub>2</sub>-Co<sub>2</sub>L neutral species. This values were taken from a previous study published in ref. 25

orbital type	%Co <sub>P</sub>	%Co <sub>N</sub>	Total electrons	Electrons on Co <sub>P</sub>	Electrons on Co <sub>N</sub>
σ	36.6	63.4	1.29	0.47	0.82
σ*	48.9	51.1	0.69	0.34	0.35
Total electrons				9.00	8.00
Oxidation State				0.0	2.0

- ❖ Qualitative M06-L molecular orbital diagram analysis of the N<sub>2</sub>CoAIL anionic species.

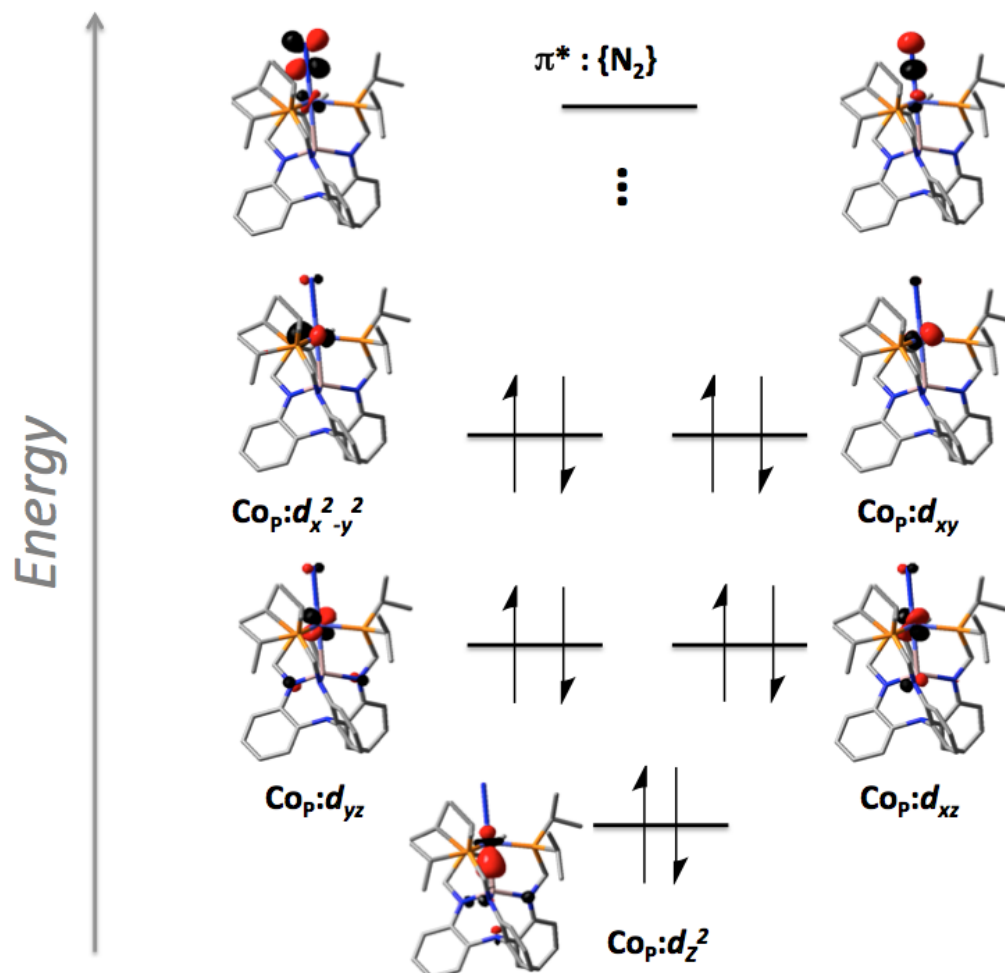


**Figure A3.11** Qualitative molecular orbital diagram for N<sub>2</sub>-CoAIL resulting from DFT(M06-L) calculations. Carbon atoms are in gray, nitrogen is in blue, and phosphorus in orange. Hydrogen atoms are not shown for clarity of the structure.

- ❖ Qualitative M06-L molecular orbital diagram analyses of the  $N_2Co_2L$  anionic species.

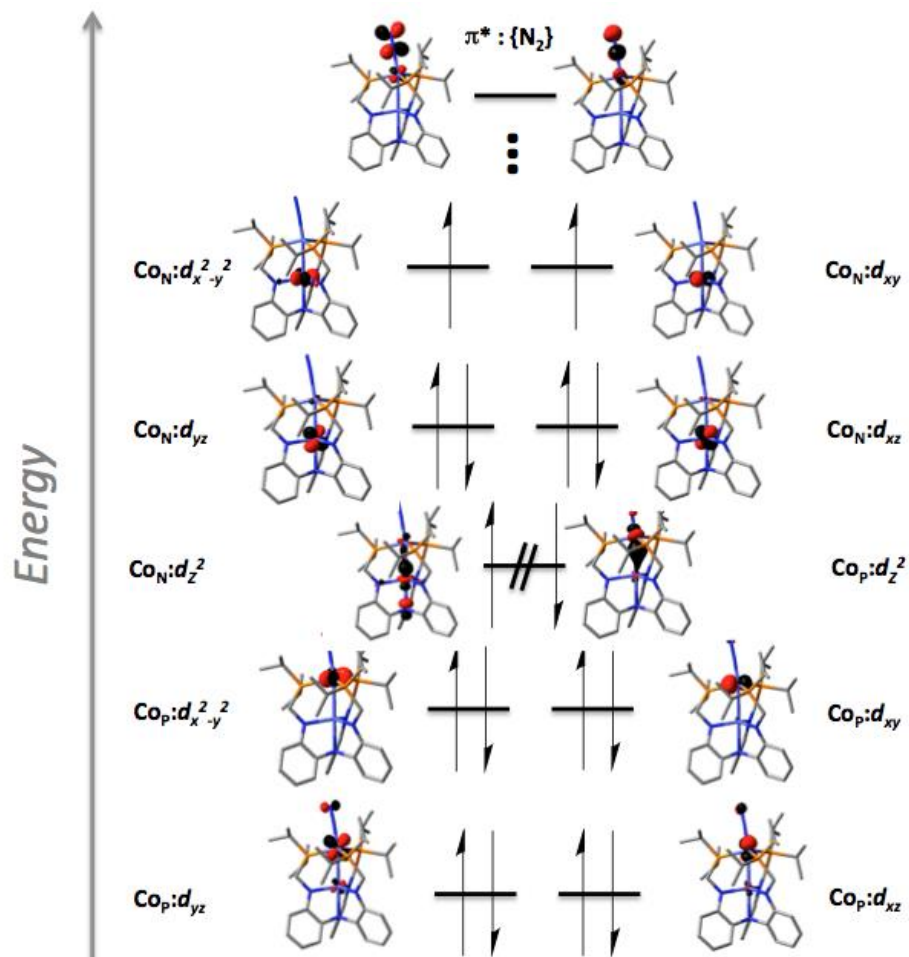


**Figure A3.12** Qualitative molecular orbital diagram for  $N_2-Co_2L$  resulting from DFT(M06-L) calculations. Carbon atoms are in gray, nitrogen is in blue, and phosphorus in orange. Hydrogen atoms are not show for clarity of the structure.

❖ **Summary of the N<sub>2</sub>CoML anionic species.**

**Table A3.17** Oxidation states of N<sub>2</sub>-CoML complexes with the percent of electron located on the upper Co atom in the  $\sigma$  bond.

N <sub>2</sub> CoML Species	<i>d</i> -count	Oxidation state		% of electron on the Co <sub>P</sub>
		Co <sub>P</sub>	M <sub>N</sub>	$\sigma$
Al	10	-1.0	3.0	100.0
Ti	11	-0.63	2.63	82.0
V	12	-0.60	2.61	79.8
Cr	13	-0.56	2.57	79.2
Co	16	0.0	2.0	36.6

## Appendix 4

Supporting information figures for Chapter 5

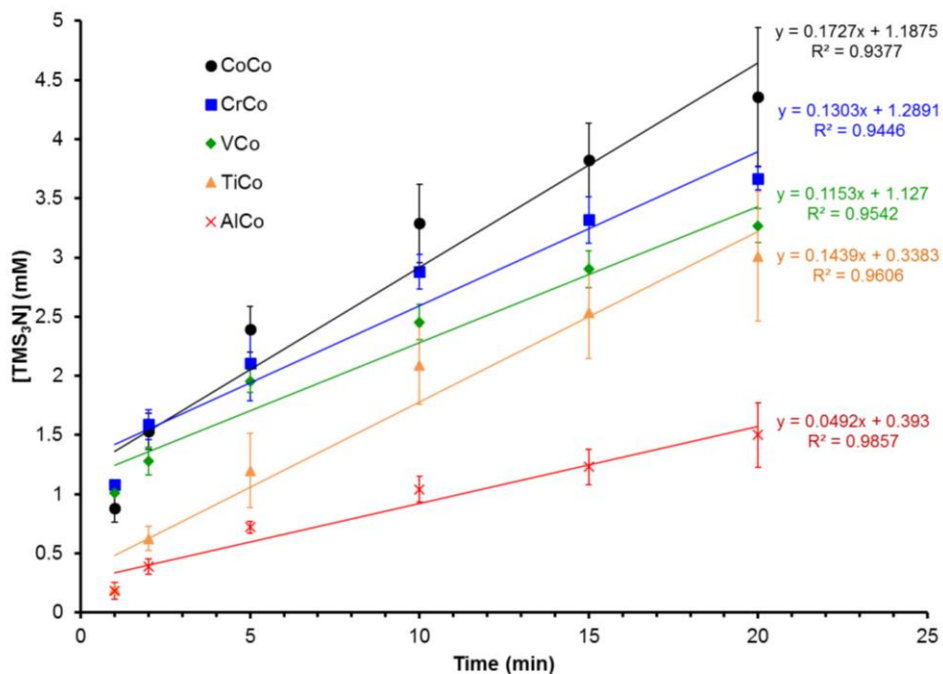


**Figure A4.1** Kinetic plot via method 1 for CoML complexes along with their linear fit for up to 20 minutes.

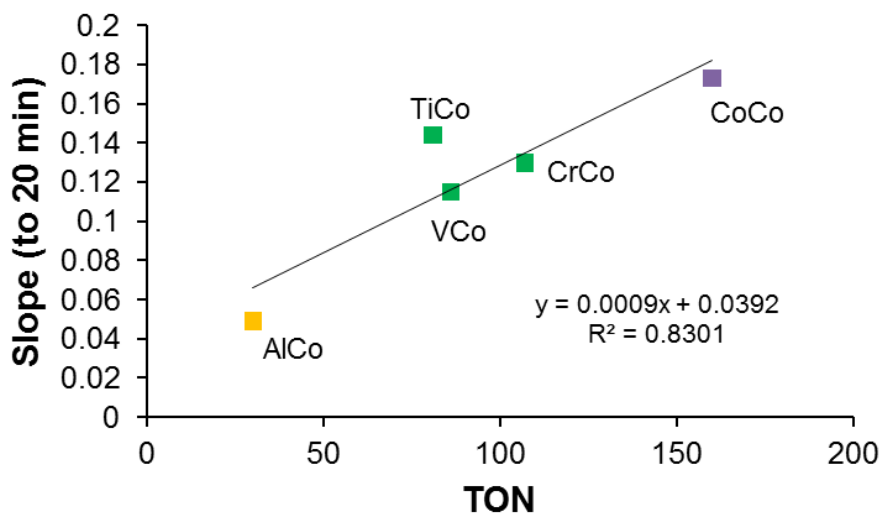


**Figure A4.2** Plot of the slope taken from the linear fit against the overall TON of the various CoML complexes to show the general correlation of initial rate and overall TON.

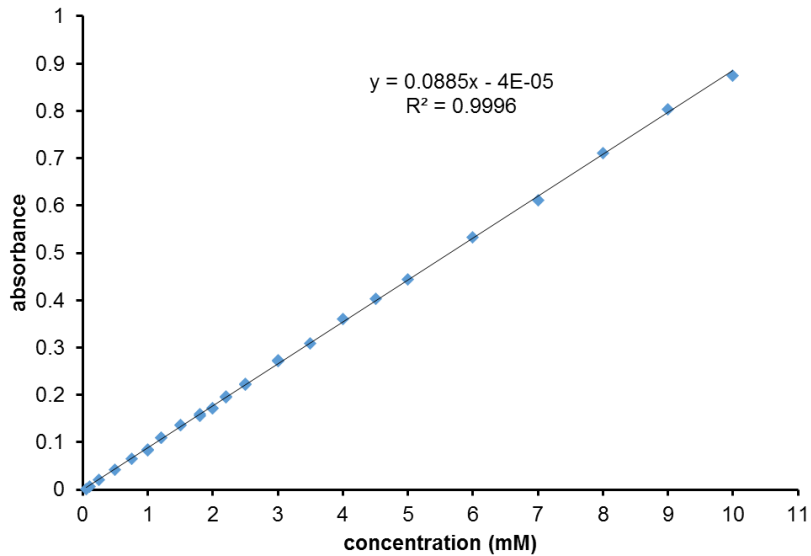


**Figure A4.3** Calibration curve for the indophenol method to quantify  $N(SiMe_3)_3$ , using an 80  $\mu L$  aliquot of a known  $N(SiMe_3)_3$  concentration solution and a 1 cm pathlength cuvette.

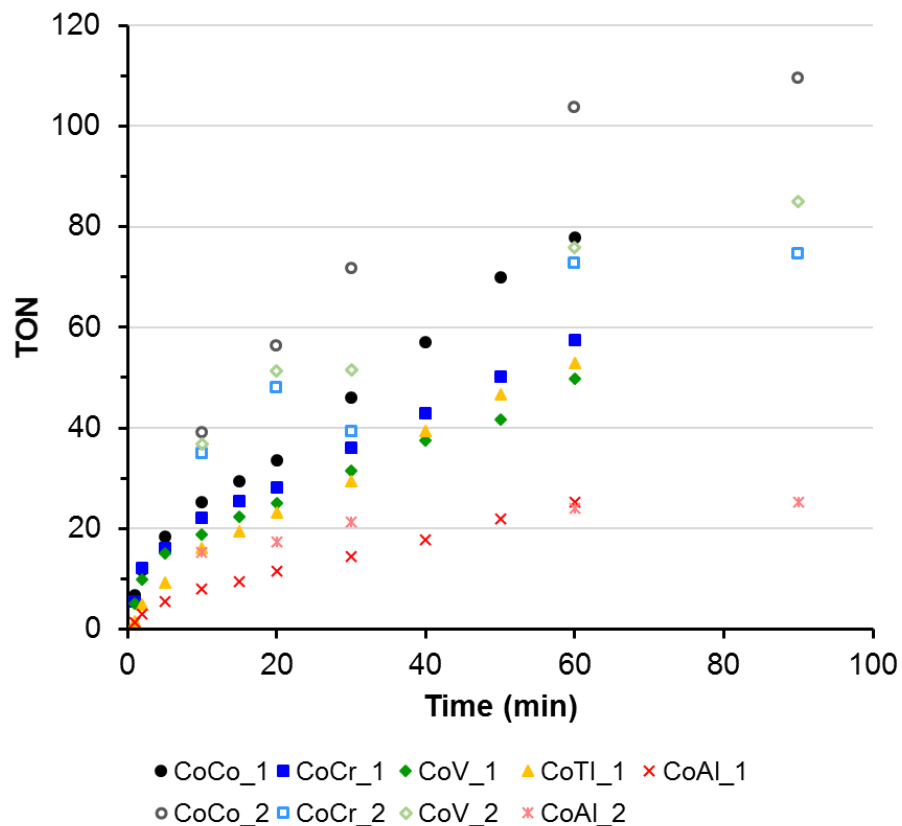


**Figure A4.4** Combined kinetic plot for method 1 (closed markers) and 2 (open markers) showing that both methods qualitatively provide the same kinetic trend.

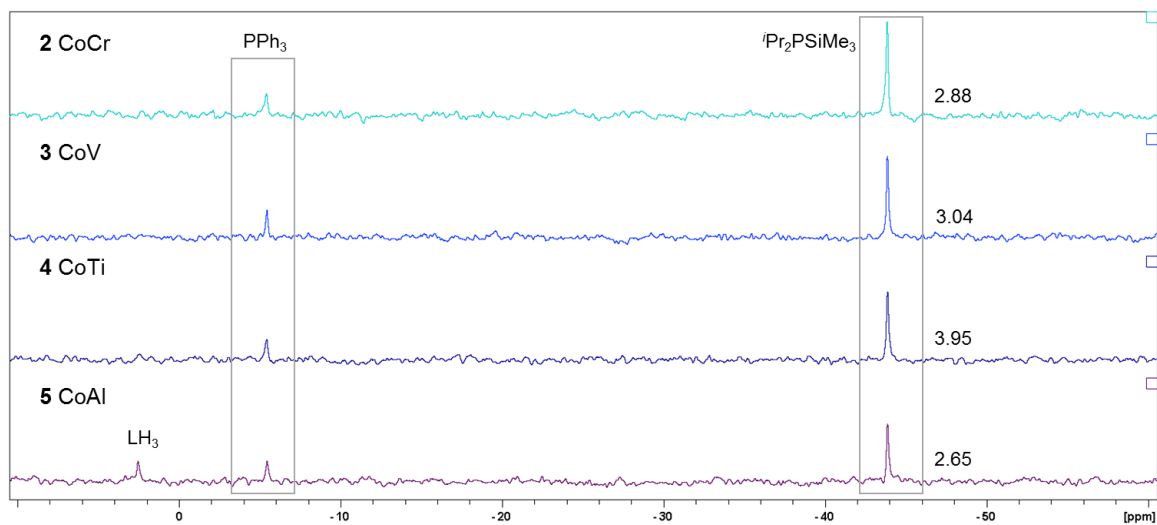


**Figure A4.5**  $^{31}\text{P}$  NMR spectra overlay of the *in-operando* studies of CoML catalysts with 10 equivalents of reagents. A  $\text{PPh}_3$  standard was added to each tube to obtain relative amounts of  $^i\text{Pr}_2\text{PSiMe}_3$  present in each reaction. The integrated value of  $^i\text{Pr}_2\text{PSiMe}_3$  is given relative to a  $\text{PPh}_3$  standard set to 1.

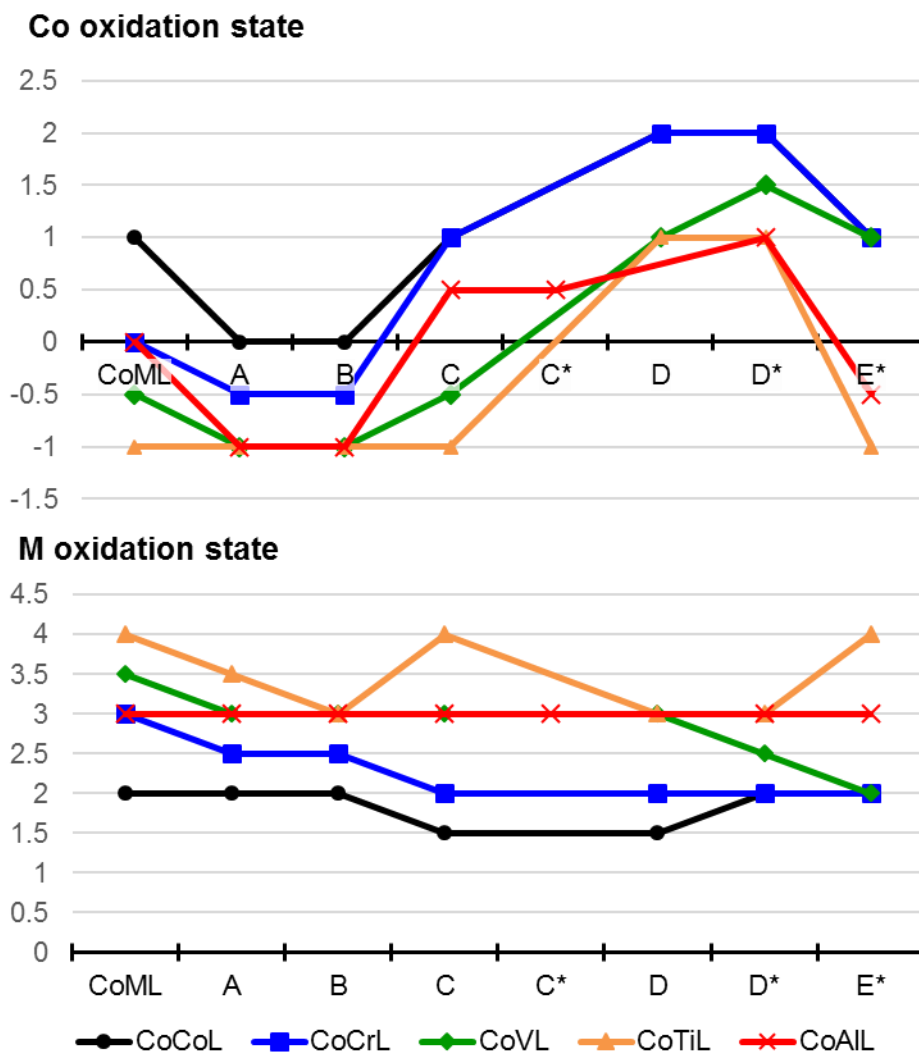


**Figure A4.6** Plot of the oxidation state for Co (top) and supporting metal M (bottom) based on the spin density located at each metal.



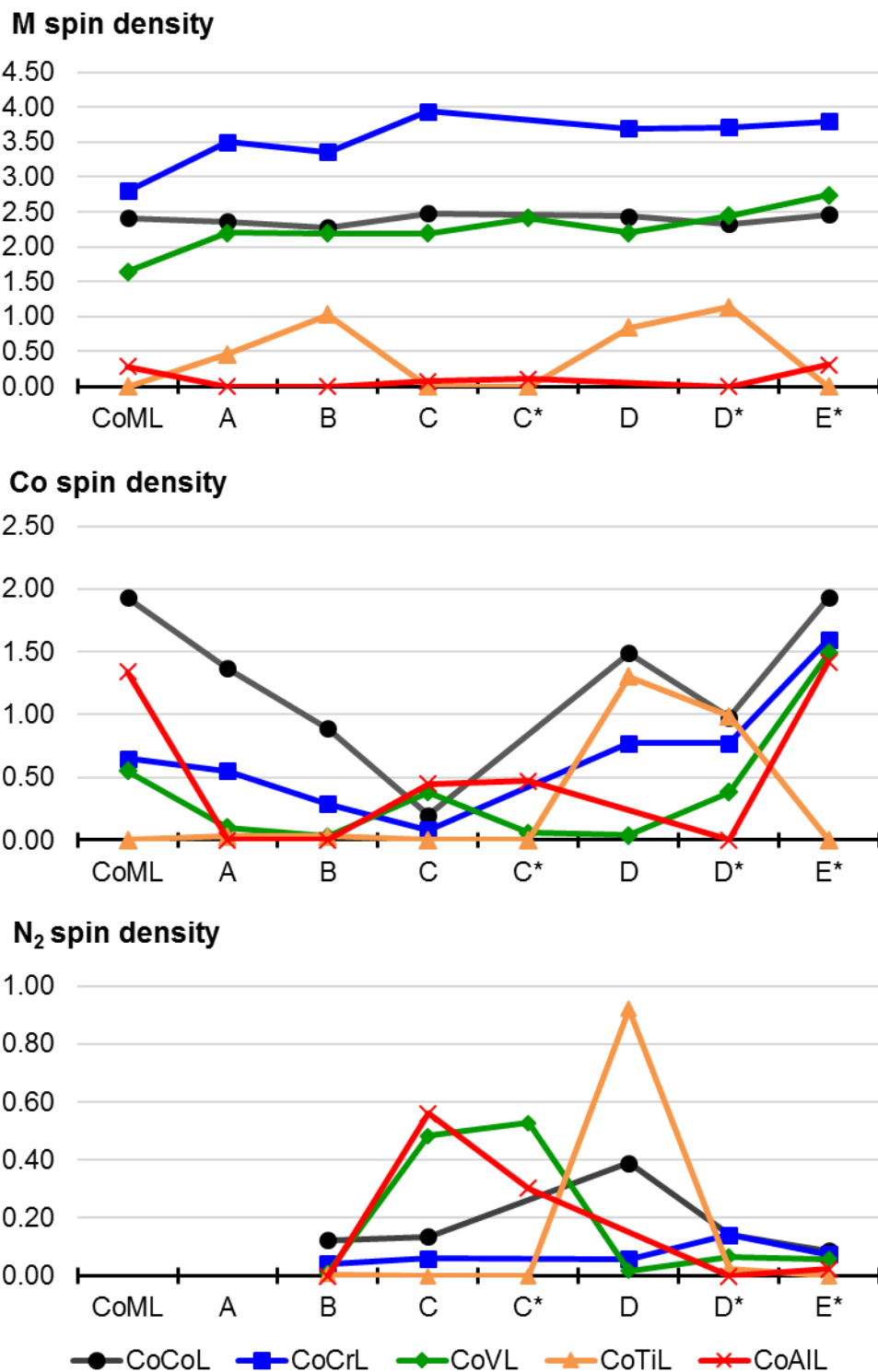


**Figure A4.7** Plot of the spin density located at supporting metal M (top), Co (middle) and N<sub>2</sub> (bottom) throughout the catalytic cycle. The absolute value of the spin density is displayed.

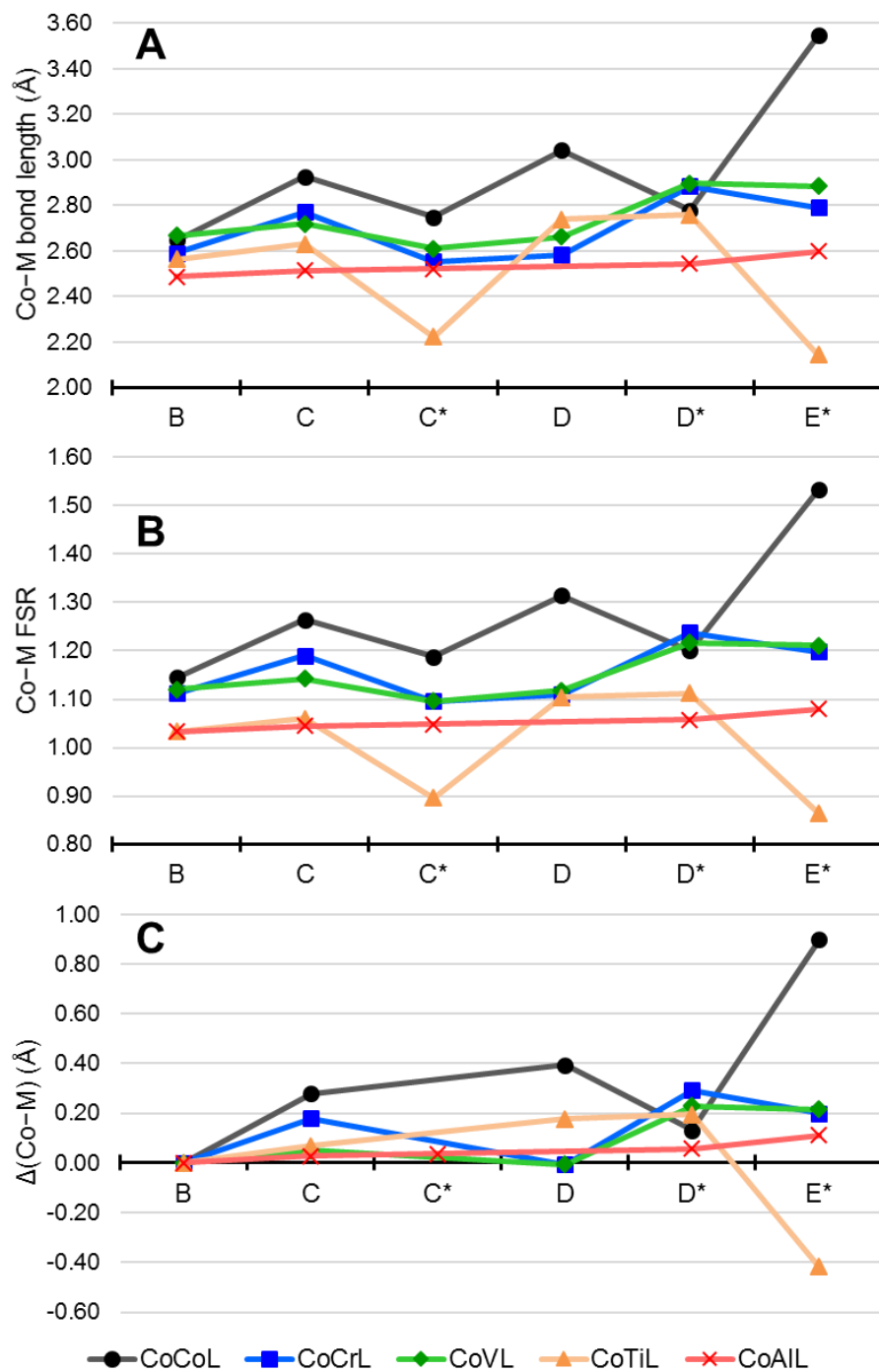


**Figure A4.8** A) Plot of the Co–M bond distance (Å) in intermediates B through E\* taken from the DFT geometry optimized structures B) FSR plot for the Co–M distance and C) Plot of the change in Co–M distance (Å) throughout the catalytic cycle, the difference is calculated as Co–M distance in intermediate B subtracted from the distance in each intermediate. Positive values indicate a longer Co–M distance.

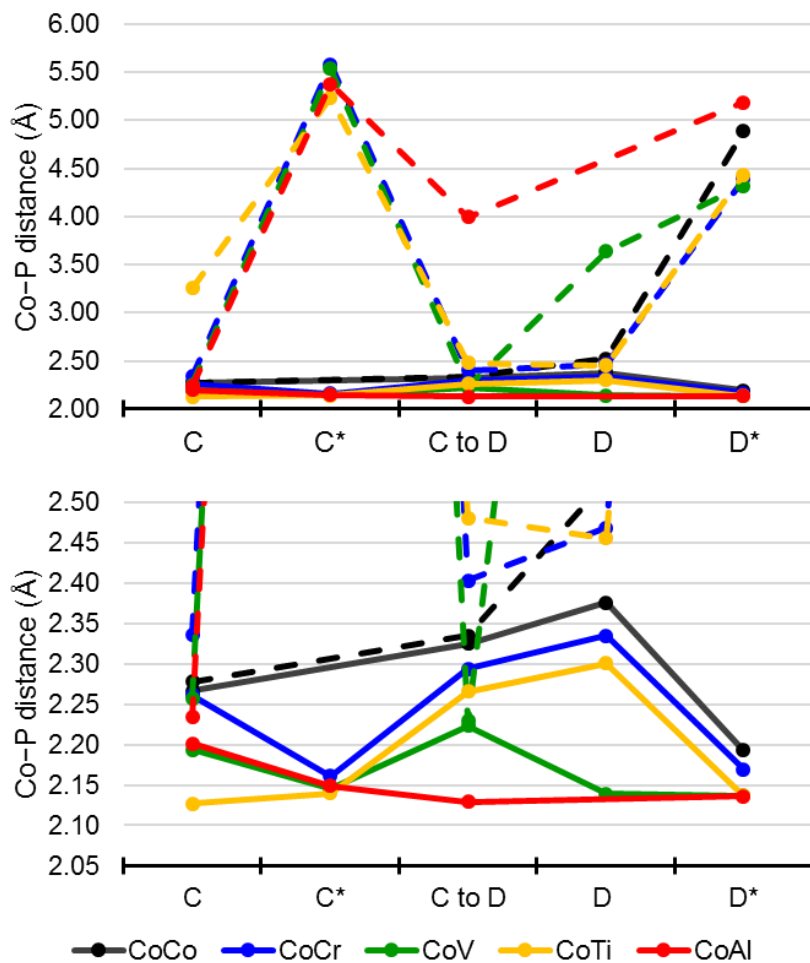


**Figure A4.9** Plot of the Co–P distances (Å) from the DFT optimized intermediates (top) with an enlargement of the shorter distances shown below. Solid lines represent the average distance of the two closest phosphines and dashed lines represent the longest Co–P distance.

**Table A4.1** Energy profile of the catalytic mechanism mediated by CoML catalysts with calculated intermediates and transition states for the bimetallic series. For each structure, the lowest spin state is indicated, along with  $\Delta G$  values (relative to the reactants: A, N<sub>2</sub> and six TMS radicals). Reaction barriers are shown in red within parenthesis.  $\Delta G$  are reported in kcal mol<sup>-1</sup>. *S* represents the total spin of the CoML species.

CoML	Al		Ti		V		Cr		Co	
Intermediate	$\Delta G$	S	$\Delta G$	S	$\Delta G$	S	$\Delta G$	S	$\Delta G$	S
<b>A</b>	0	0	0	1/2	0	1	0	3/2	0	3/2
<b>B</b>	-20.8	0	-5.8	1/2	-14	1	-13	3/2	-6.7	3/2
<b>B to C</b>	-9.5 (11.3)	1/2	4.9 (10.7)	1	-7.4 (6.6)	3/2	-3.1 (9.9)	1	1.9 (8.6)	1
<b>C</b>	-17.7	1/2	-6.2	0	-14.9	3/2	-19.1	2	-25.6	2
<b>C*</b>	-31.2	1/2	-19	0	-15.4	3/2	-15.2	2	-13.8	2
<b>C to D</b>	-10.9 (20.3)	0	11.9 (18.1)	1/2	1.4 (16.3)	1	-2.6 (16.5)	3/2	-9.3 (16.3)	3/2
<b>D</b>	N/A	N/A	-13.2	3/2	-35.9	1	-32.6	3/2	-30.7	3/2
<b>D*</b>	-39.5	0	-25.5	1/2	-46.7	1	-34.2	3/2	-41.3	3/2
<b>D to E</b>	-22.0 (17.5)	1/2	-24.5 (1.0)	1	-33.9 (12.8)	1/2	-33.1 (1.1)	3	-36.9 (4.4)	3
<b>E*</b>	-67.8	1/2	-68.3	0	-67.5	5/2	-76.4	3	-80.1	3
<b>F*</b>	-61.5	1/2	-69.9	0	-60.4	1/2	-53.6	2	-62.9	2
<b>G</b>	-78.4	1/2	-98.3	0	-82.3	1/2	-75.2	2	-81	2

**Table A4.2** List of electronic energies for CoAIL calculated at the M06-L/def2-TZVPD/SMD // M06-L/def2-TZVP level of theory. Total energies (E, in au) in gas phase and  $G_{\text{THF}}$  include the solvent effect (THF) and thermal corrections to the energy, of the stationary points involved in the first part of the mechanistic cycle.

Complexes	Charge	S	E (au)	$G_{\text{THF}}$ (au)	$\Delta G_{\text{SPIN}}$ (kcal/mol)	$\Delta G_{\text{THF-rx}}$ (kcal/mol)	$\langle S^2 \rangle_{\text{calc}}$
CoAIL	0	0.5	-4389.56488	-4388.76752	0.0	50.9	0.76
A	-1	0	-4389.61004	-4388.84856	0.0	0.0	0.00
	-1	1	-4389.59616	-4388.83408	9.1	9.1	0.00
B	-1	0	-4499.22137	-4498.44769	-0.2	-20.8	0.00
	-1	0	-4499.22129	-4498.44737	0.0	-20.6	0.00
	-1	1	-4499.15374	-4498.38895	36.7	16.1	2.00
TS(B to C)	-1	0.5	-4908.33150	-4907.45904	0.0	-9.5	0.75
C	-1	0.5	-4908.34358	-4907.47203	0.0	-17.7	0.75
	-1	1.5	-4908.30636	-4907.43768	21.6	3.9	3.75
C*	-1	0.5	-4908.32690	-4907.49365	-13.6	-31.2	0.75
TS(C to D)	-1	0	-5317.470907	-5316.49058	0.0	-10.9	0.00
D	-1	0	-5317.49983	-5316.52605	0.0	-33.2	0.00
	-1	1	-5317.48824	-5316.50914	10.6	-22.5	2.02
D*	-1	0	-5317.51121	-5316.53611	0.0	-39.5	0.00
	-1	1	-5317.48453	-5316.51436	13.7	-25.8	2.01
TS(D to E)	-1	0.5	-5726.61293	-5725.53759	0.0	-22.0	0.76
	-1	1.5	-5726.57939	-5725.52043	13.7	-11.2	3.75
E*	-1	0.5	-5726.69371	-5725.61064	0.0	-67.8	0.79
	-1	1.5	-5726.67238	-5725.59365	10.7	-57.2	3.75
F*	-1	0.5	-4389.52881	-5725.60057	0.0	-61.5	0.76
	-1	1.5	-4389.48809	-5725.56091	24.9	-36.6	3.75
G	-1	0	-4389.56488	-5725.62747	0.0	-78.4	0.76

**Table A4.3** List of electronic energies for CoTiL calculated at the M06-L/def2-TZVPD/SMD // M06-L/def2-TZVP level of theory. Total energies (E, in au) in gas phase and  $G_{\text{THF}}$  include the solvent effect (THF) and thermal corrections to the energy, of the stationary points involved in the first part of the mechanistic cycle.

Complexes	Charge	S	E (au)	$G_{\text{THF}}$ (au)	$\Delta G_{\text{SPIN}}$ (kcal/mol)	$\Delta G_{\text{THF-rx}}$ (kcal/mol)	$\langle S^2 \rangle_{\text{calc}}$
CoTiL	<b>0</b>	<b>0</b>	<b>-4996.5948</b>	<b>-4995.7997</b>	<b>0.0</b>	<b>31.0</b>	<b>0.00</b>
	0	1	-4996.5450	-4995.7518	30.1	61.0	2.00
	0	2	-4996.5205	-4995.7341	41.2	72.2	6.00
	0	3	-4996.4430	-4995.6567	89.7	120.7	12.00
A	<b>-1</b>	<b>0.5</b>	<b>-4996.6048</b>	<b>-4995.8490</b>	<b>0.0</b>	<b>0.0</b>	<b>0.75</b>
	-1	1.5	-4996.5608	-4995.8091	25.1	25.1	3.75
	-1	2.5	-4996.5333	-4995.7879	38.4	38.4	8.75
B	<b>-1</b>	<b>0.5</b>	<b>-5106.1896</b>	<b>-5105.4244</b>	<b>0.0</b>	<b>-5.8</b>	<b>0.75</b>
	-1	1.5	-5106.1422	-5105.3829	26.0	20.2	3.75
	-1	2.5	-5106.0956	-5105.3424	51.4	45.6	8.75
B to C	-1	0	-5515.2923	-5514.4285	5.1	10.0	0.00
	<b>-1</b>	<b>1</b>	<b>-5515.3013</b>	<b>-5514.4367</b>	<b>0.0</b>	<b>4.9</b>	<b>2.00</b>
	-1	2	-5515.2571	-5514.4005	22.7	27.5	6.00
C*	<b>-1</b>	<b>0</b>	<b>-5515.3349</b>	<b>-5514.4746</b>	<b>0.0</b>	<b>-19.0</b>	<b>0.00</b>
	-1	1	-5515.3110	-5514.4562	11.6	-7.4	2.00
	-1	2	-5515.2674	-5514.4163	36.6	17.6	6.00
	-1	3	N/A	N/A	N/A	N/A	N/A
C	<b>-1</b>	<b>0</b>	<b>-5515.3170</b>	<b>-5514.4542</b>	<b>0.0</b>	<b>-6.2</b>	<b>0.00</b>
	-1	1	-5515.3134	-5514.4483	3.7	-2.5	2.00
	-1	2	-5515.2798	-5514.4228	19.7	13.5	6.00
	-1	3	-5515.2531	-5514.4035	31.8	25.6	12.00
C to D	<b>-1</b>	<b>0.5</b>	<b>-5924.4281</b>	<b>-5923.4547</b>	<b>0.0</b>	<b>11.9</b>	<b>0.75</b>
	-1	1.5	-5924.4199	-5923.4491	3.5	15.4	3.76
	-1	2.5	-5924.3884	-5923.4280	16.7	28.7	8.75
D	-1	0.5	-5924.4653	-5923.4940	0.4	-12.8	1.84
	<b>-1</b>	<b>1.5</b>	<b>-5924.4650</b>	<b>-5923.4947</b>	<b>0.0</b>	<b>-13.2</b>	<b>3.77</b>
	-1	2.5	-5924.4416	-5923.4780	10.5	-2.7	8.75
D*	<b>-1</b>	<b>0.5</b>	<b>-5924.4803</b>	<b>-5923.5144</b>	<b>0.0</b>	<b>-25.5</b>	<b>0.75</b>
	-1	1.5	-5924.4608	-5923.4996	9.3	-16.2	3.75
	-1	2.5	-5924.4379	-5923.4816	20.6	-5.0	8.75
D to E	-1	0	-6333.6192	-6332.5442	0.0	-25.8	2.95
	<b>-1</b>	<b>1</b>	<b>-6333.6181</b>	<b>-6332.5421</b>	<b>1.3</b>	<b>-24.5</b>	<b>2.01</b>
	-1	2	-6333.6041	-6332.5358	5.2	-20.6	6.09
E*	<b>-1</b>	<b>0</b>	<b>-6333.6939</b>	<b>-6332.6119</b>	<b>0.0</b>	<b>-68.3</b>	<b>0.00</b>
	-1	1	-6333.6790	-6332.6036	5.2	-63.1	2.01
	-1	2	-6333.6599	-6332.5931	11.8	-56.5	6.00
	-1	3	-6333.6054	-6332.5440	42.6	-25.7	12.00
F*	<b>-1</b>	<b>0</b>	<b>-4996.5403</b>	<b>-6332.6144</b>	<b>0.0</b>	<b>-69.9</b>	<b>0.00</b>
	-1	1	-4996.4975	-6332.5780	22.8	-47.0	2.00
	-1	2	-4996.4647	-6332.5559	36.7	-33.2	6.00
	-1	3	-4996.4187	-6332.5005	71.5	1.6	12.00
G	<b>-1</b>	<b>0</b>	<b>-4996.5948</b>	<b>-6332.6596</b>	<b>-28.4</b>	<b>-98.3</b>	<b>0.00</b>
	-1	1	-4996.5450	-6332.6117	1.7	-68.2	2.00
	-1	2	-4996.5205	-6332.5940	12.8	-57.1	6.00
	-1	3	-4996.4430	-6332.5167	61.3	-8.6	12.00

**Table A4.4** List of electronic energies for CoVL calculated at the M06-L/def2-TZVPD/SMD // M06-L/def2-TZVP level of theory. Total energies (E, in au) in gas phase and  $G_{\text{THF}}$  include the solvent effect (THF) and thermal corrections to the energy, of the stationary points involved in the first part of the mechanistic cycle.

Complexes	Charge	S	E (au)	$G_{\text{THF}}$ (au)	$\Delta G_{\text{SPIN}}$ (kcal/mol)	$\Delta G_{\text{THF-rx}}$ (kcal/mol)	$\langle S^2 \rangle_{\text{calc}}$
CoVL	0	0.5	-5091.0750	-5090.2803	0.0	47.0	0.79
	0	1.5	-5091.0718	-5090.2792	0.7	47.7	3.75
	0	2.5	-5091.0545	-5090.2623	11.3	58.3	8.75
A	-1	0	-5091.0878	-5090.3324	14.3	14.3	0.12
	-1	1	-5091.1105	-5090.3552	0.0	0.0	2.00
	-1	2	-5091.0907	-5090.3337	13.5	13.5	6.00
	-1	3	-5091.0607	-5090.3148	25.4	25.4	12.00
B	-1	0	-5200.6883	-5199.9176	16.2	2.3	0.03
	-1	1	-5200.7132	-5199.9435	0.0	-14.0	2.00
	-1	2	-5200.6703	-5199.9120	19.7	5.8	6.00
	-1	3	-5200.6241	-5199.8847	36.9	22.9	12.00
B to C	-1	0.5	-5609.8288	-5608.9620	0.1	-7.2	1.09
	-1	1.5	-5609.8288	-5608.9622	0.0	-7.4	3.75
	-1	2.5	-5609.7854	-5608.9335	18.0	10.7	8.76
C*	-1	0.5	-5609.8299	-5608.9702	2.5	-12.4	0.81
	-1	1.5	-5609.8343	-5608.9750	-0.5	-15.4	3.75
	-1	2.5	-5609.7899	-5608.9350	24.6	9.7	8.75
C	-1	0.5	-5609.8388	-5608.9703	2.4	-12.4	1.09
	-1	1.5	-5609.8398	-5608.9742	0.0	-14.9	3.75
	-1	2.5	-5609.8022	-5608.9391	22.0	7.1	8.75
C to D	-1	0	-6018.9434	-6017.9710	4.1	5.5	1.08
	-1	1	-6018.9535	-6017.9776	0.0	1.4	2.07
	-1	2	-6018.9432	-6017.9722	3.4	4.8	6.14
	-1	3	-6018.9105	-6017.9551	14.1	15.5	12.12
D	-1	0	-6018.9908	-6018.0169	12.7	-23.2	6.93
	-1	1	-6019.0072	-6018.0371	0.0	-35.9	2.00
	-1	2	-6018.9895	-6018.0132	15.0	-21.0	6.01
	-1	3	-6018.9619	-6018.0041	20.7	-15.2	12.00
D*	-1	0	-6018.9812	-6018.0194	-26.2	-39.2	6.72
	-1	1	-6018.9995	-6018.0314	-33.8	-46.7	2.02
	-1	2	-6018.9802	-6018.0144	-23.1	-36.1	6.00
	-1	3	-6018.9564	-6018.0014	-15.0	-27.9	12.00
D to C	-1	0.5	-6428.1413	-6427.0631	0.0	-33.9	2.26
	-1	1.5	-6428.1367	-6427.0583	3.0	-30.9	3.94
	-1	2.5	-6428.1273	-6427.0398	14.6	-19.3	8.85
E*	-1	0.5	-6428.2020	-6427.1247	0.0	-72.5	3.16
	-1	1.5	-6428.1937	-6427.1149	6.1	-66.4	3.78
	-1	2.5	-6428.1879	-6427.1166	5.1	-67.5	8.75
F*	-1	0.5	-5091.0312	-6427.1053	0.0	-60.4	0.75
	-1	1.5	-5091.0252	-6427.1042	0.7	-59.7	3.75
	-1	2.5	-5091.0135	-6427.0886	10.5	-49.9	8.75
G	-1	0.5	-5091.0750	-6427.1403	-21.9	-82.3	0.79
	-1	1.5	-5091.0718	-6427.1392	-21.2	-81.6	3.75
	-1	2.5	-5091.0545	-6427.1223	-10.6	-71.0	8.75

**Table A4.5** List of electronic energies for CoCrL calculated at the M06-L/def2-TZVPD/SMD // M06-L/def2-TZVP level of theory. Total energies (E, in au) in gas phase and  $G_{\text{THF}}$  include the solvent effect (THF) and thermal corrections to the energy, of the stationary points involved in the first part of the mechanistic cycle.

Complexes	Charge	S	E (au)	$G_{\text{THF}}$ (au)	$\Delta G_{\text{SPIN}}$ (kcal/mol)	$\Delta G_{\text{THF-rx}}$ (kcal/mol)	$\langle S^2 \rangle_{\text{calc}}$
CoCrL	0	0	-5191.4827	-5190.6860	23.5	77.6	6.25
	0	1	-5191.5110	-5190.7195	2.5	56.6	2.12
	0	2	-5191.5089	-5190.7235	0.0	54.1	6.00
	0	3	-5191.4974	-5190.7171	4.0	58.1	12.00
A	-1	0.5	-5191.5346	-5190.7835	16.5	16.5	5.64
	-1	1.5	-5191.5611	-5190.8097	0.0	0.0	3.78
	-1	2.5	-5191.5429	-5190.7944	9.6	9.6	8.75
B	-1	0.5	-5301.1222	-5300.3537	26.8	13.8	0.77
	-1	1.5	-5301.1617	-5300.3964	0.0	-13.0	3.76
	-1	2.5	-5301.1291	-5300.3778	11.7	-1.3	8.75
B to C	-1	0	-5710.2351	-5709.3671	26.9	23.8	2.72
	-1	1	-5710.2732	-5709.4100	0.0	-3.1	3.35
	-1	2	-5710.2716	-5709.4076	1.5	-1.6	6.01
	-1	3	-5710.2545	-5709.3910	11.9	8.8	12.00
C*	-1	0	-5710.2298	-5709.3675	38.7	23.5	0.00
	-1	1	-5710.2718	-5709.4151	8.8	-6.4	2.74
	-1	2	-5710.2842	-5709.4292	0.0	-15.2	6.00
	-1	3	-5710.2411	-5709.3885	25.5	10.3	12.00
C	-1	0	-5710.2401	-5709.3721	39.7	20.7	0.00
	-1	1	-5710.2839	-5709.4175	11.2	-7.8	2.74
	-1	2	-5710.2877	-5709.4354	0.0	-19.1	6.00
	-1	3	-5710.2603	-5709.4107	15.5	-3.6	12.00
C to D	-1	0.5	-6119.3916	-6118.4242	8.9	6.3	3.26
	-1	1.5	-6119.3979	-6118.4384	0.0	-2.6	5.09
	-1	2.3	-6119.3972	-6118.4382	0.1	-2.5	9.08
D	-1	0.5	-6119.4436	-6118.4737	7.9	-24.7	7.83
	-1	1.5	-6119.4619	-6118.4863	0.0	-32.6	3.77
	-1	2.5	-6119.4440	-6118.4770	5.8	-26.8	8.76
D*	-1	0.5	-6119.4321	-6118.4717	10.7	-23.5	8.26
	-1	1.5	-6119.4529	-6118.4887	0.0	-34.2	3.85
	-1	2.5	-6119.4405	-6118.4857	1.9	-32.3	8.76
D* to E*	-1	0	-6528.5680	-6527.4983	15.1	-21.8	3.49
	-1	1	-6528.5932	-6527.5224	0.0	-36.9	3.82
	-1	2	-6528.5808	-6527.5093	8.2	-28.7	6.39
	-1	3	-6528.5836	-6527.5164	3.7	-33.1	12.12
E*	-1	0	-6528.6189	-6527.5474	25.7	-52.6	10.94
	-1	1	-6528.6587	-6527.5883	0.0	-78.2	4.08
	-1	2	-6528.6260	-6527.5577	19.2	-59.1	6.03
	-1	3	-6528.6502	-6527.5854	1.8	-76.4	12.00
F*	0	0	-5191.4521	-6527.5261	22.2	-39.2	7.28
	0	1	-5191.4719	-6527.5614	0.0	-61.4	3.28
	0	2	-5191.4630	-6527.5491	7.7	-53.6	6.00
	0	3	-5191.4541	-6527.5489	7.8	-53.5	12.00
G	0	0	-5191.4827	-5190.6860	23.5	-51.7	6.25
	0	1	-5191.5110	-5190.7195	2.5	-72.7	2.12
	0	2	-5191.5089	-5190.7235	0.0	-75.2	6.00
	0	3	-5191.4974	-5190.7171	4.0	-71.2	12.00



**Table A4.6** Calculated Bond Lengths (Å) and N<sub>1</sub>-N<sub>2</sub> bond stretching frequencies (cm<sup>-1</sup>). All species are in their anionic form, except neutral CoML and free N<sub>2</sub>.

Species		Spin-State	N <sub>1</sub> -N <sub>2</sub> (cm <sup>-1</sup> )	Distances		
				Co-M	Co <sub>p</sub> -N <sub>1</sub>	N <sub>1</sub> -N <sub>2</sub>
<b>Free N<sub>2</sub></b>	<b>M=</b>	-	2424	-	-	1.095
<b>CoML</b>	Al	Doublet	-	2.478	-	-
	Ti	Singlet	-	2.059	-	-
	V	Doublet	-	2.170	-	-
	Cr	Quintet	-	2.464	-	-
	Co	Sextet	-	2.522	-	-
<b>A</b>	Al	Singlet	-	2.358	-	-
	Ti	Doublet	-	2.118	-	-
	V	Triplet	-	2.394	-	-
	Cr	Quartet	-	2.399	-	-
	Co	Quintet	-	2.625	-	-
<b>B</b>	Al	Singlet	2099	2.486	1.794	1.130
	Ti	Doublet	2087	2.562	1.805	1.131
	V	Triplet	2085	2.668	1.799	1.132
	Cr	Quartet	2092	2.591	1.807	1.130
	Co	Triplet	2105	2.648	1.817	1.128
<b>B to C</b>	Al	Doublet	1861(-158)	2.507	1.785	1.156
	Ti	Triplet	1868(-168)	2.262	1.789	1.156
	V	Quartet	1880(-138)	2.702	1.784	1.155
	Cr	Triplet	1886(-139)	2.631	1.799	1.153
	Co	Quartet	1885(-223)	2.886	1.804	1.149
<b>C</b>	Al	Doublet	1622	2.513	1.785	1.221
	Ti	Triplet	1572	2.630	1.785	1.230
	V	Quartet	1545	2.719	1.779	1.236
	Cr	Quintet	1784	2.771	1.665	1.205
	Co	Quartet	1771	2.927	1.660	1.207
<b>C*</b>	Al	Doublet	1656	2.522	1.668	1.225
	Ti	Singlet	1567	2.223	1.699	1.241
	V	Quartet	1633	2.609	1.665	1.231
	Cr	Quintet	1663	2.552	1.665	1.225
	Co	Quartet	1702	2.749	1.647	1.217
<b>C to D</b>	Al	Singlet	1601(-194)	2.513	1.837	1.215
	Ti	Doublet	1391(-224)	2.557	1.874	1.242
	V	Triplet	1323(-281)	2.695	1.871	1.248
	Cr	Quartet	1471(-255)	2.791	1.773	1.242
	Co	Quintet	1545(-145)	2.937	1.755	1.230
<b>D</b>	Al	Singlet	N/A	N/A	N/A	N/A
	Ti	Quartet	1019	2.738	1.836	1.403
	V	Triplet	1115	2.661	1.691	1.370
	Cr	Quartet	1135	2.584	1.688	1.364
	Co	Quintet	1124	3.042	1.800	1.354
<b>D*</b>	Al	Singlet	1210	2.543	1.667	1.346
	Ti	Doublet	1181	2.758	1.681	1.352
	V	Triplet	1154	2.896	1.682	1.356
	Cr	Quartet	1160	2.883	1.686	1.352

	Co	Triplet	1176	2.779	1.675	1.349
<b>D* to E*</b>	Al	Doublet	1051(-265)	2.538	1.733	1.383
	Ti	Triplet	1053(-238)	2.724	1.795	1.394
	V	Doublet	1059(-205)	3.023	1.784	1.392
	Cr	Septet	1043(-168)	3.179	1.791	1.392
	Co	Sextet	1003(-170)	3.547	1.986	1.482
<b>E*</b>	Al	Doublet	991	2.597	1.997	1.490
	Ti	Singlet	990	2.144	2.026	1.491
	V	Sextet	991	3.155	1.986	1.494
	Cr	Septet	1004	3.523	1.986	1.485
	Co	Sextet	1003	3.547	1.986	1.482
<b>CoML*</b>	Al	Doublet	-	2.504	-	-
	Ti	Singlet	-	2.080	-	-
	V	Doublet	-	2.065	-	-
	Cr	Quintet	-	2.477	-	-
	Co	N/A	N/A	N/A	N/A	N/A

**Table A4.7** Calculated spin densities, CM5 charges and Bond order from the NBO analysis.

Species	M/d <sup>n</sup> /u <sup>e</sup>	Spin Density		CM5 Charges				NBO		
		Co <sub>P</sub>	M <sub>N</sub>	Co <sub>P</sub>	M <sub>N</sub>	N <sub>1</sub>	N <sub>2</sub>	Co-M	Co <sub>P</sub> -N <sub>1</sub>	N <sub>1</sub> -N <sub>2</sub>
<b>Free N<sub>2</sub></b>	M/d <sup>n</sup> /u <sup>e</sup>	-	-	-	-	-	-	-	-	-
<b>CoML</b>	Al/d <sup>9</sup> /u <sup>1</sup>	1.34	-0.28	0.12	0.44	-	-	0.31	-	-
	Ti/d <sup>10</sup> /u <sup>0</sup>	0.00	0.00	-0.03	1.06	-	-	1.38	-	-
	V/d <sup>11</sup> /u <sup>1</sup>	-0.55	1.64	0.02	1.00	-	-	1.24	-	-
	Cr/d <sup>12</sup> /u <sup>4</sup>	1.02	3.09	1.01	0.02	-	-	0.60	-	-
	Co/d <sup>15</sup> /u <sup>5</sup>	1.93	2.41	0.12	0.61	-	-	0.39	-	-
<b>A</b>	Al/d <sup>10</sup> /u <sup>0</sup>	0.00	0.00	0.10	0.38	-	-	0.31	-	-
	Ti/d <sup>11</sup> /u <sup>1</sup>	0.03	0.46	-0.05	1.03	-	-	1.38	-	-
	V/d <sup>12</sup> /u <sup>2</sup>	-0.10	2.20	-0.01	0.96	-	-	0.72	-	-
	Cr/d <sup>13</sup> /u <sup>3</sup>	-0.55	3.50	-0.02	0.96	-	-	0.73	-	-
	Co/d <sup>16</sup> /u <sup>4</sup>	1.37	2.36	0.05	0.57	-	-	0.30	-	-
<b>B</b>	Al/d <sup>10</sup> /u <sup>0</sup>	0.00	0.00	0.26	0.40	-0.20	-0.15	0.30	0.98	2.58
	Ti/d <sup>11</sup> /u <sup>1</sup>	-0.03	1.03	0.15	1.04	-0.21	-0.15	0.55	0.94	2.57
	V/d <sup>12</sup> /u <sup>2</sup>	-0.03	2.19	0.16	1.00	-0.21	-0.16	0.48	0.95	2.57
	Cr/d <sup>13</sup> /u <sup>3</sup>	-0.29	3.36	0.15	0.99	-0.20	-0.15	0.58	0.94	2.58
	Co/d <sup>16</sup> /u <sup>2</sup>	-0.89	2.28	0.20	0.61	-0.19	-0.13	0.25	0.90	2.59
<b>B to C</b>	Al/d <sup>10</sup> /u <sup>1</sup>	0.40	-0.05	0.25	0.41	-0.25	-0.14	0.30	1.05	2.28
	Ti/d <sup>11</sup> /u <sup>2</sup>	0.94	0.38	0.16	1.06	-0.25	-0.14	0.51	1.02	2.30
	V/d <sup>12</sup> /u <sup>3</sup>	0.39	2.15	0.18	1.01	-0.25	-0.14	0.45	1.03	2.30
	Cr/d <sup>13</sup> /u <sup>2</sup>	-0.72	3.46	0.16	0.99	-0.24	-0.13	0.56	1.00	2.32
	Co/d <sup>16</sup> /u <sup>3</sup>	1.19	2.45	0.22	0.58	-0.24	-0.13	0.17	0.92	2.36
<b>C</b>	Al/d <sup>10</sup> /u <sup>1</sup>	0.45	-0.07	0.26	0.41	-0.29	-0.27	0.30	1.16	1.89
	Ti/d <sup>11</sup> /u <sup>0</sup>	0.00	0.00	0.17	0.98	-0.35	-0.30	1.01	1.28	1.72
	V/d <sup>12</sup> /u <sup>3</sup>	0.38	2.19	0.19	1.00	-0.30	-0.29	0.45	1.17	1.82
	Cr/d <sup>13</sup> /u <sup>4</sup>	0.08	3.94	0.24	0.87	-0.31	-0.25	0.30	1.47	1.82

	Co/d <sup>16</sup> /u3	0.20	2.48	0.28	0.59	-0.32	-0.25	0.13	1.51	1.81
C*	Al/d <sup>10</sup> /u1	0.47	0.11	0.29	0.43	-0.35	-0.28	0.35	1.45	1.77
	Ti/d <sup>11</sup> /u0	0.00	0.00	0.16	1.03	-0.36	-0.30	1.18	1.26	1.71
	V/d <sup>12</sup> /u3	0.06	2.41	0.20	0.96	-0.35	-0.28	0.52	1.37	1.75
	Cr/d <sup>13</sup> /u4	-0.19	3.59	0.20	0.96	-0.34	-0.27	0.56	1.37	1.78
C to D	Al/d <sup>10</sup> /u0	0.00	0.00	0.24	0.41	-0.28	-0.21	0.29	1.01	1.77
	Ti/d <sup>11</sup> /u1	-0.28	1.04	0.12	1.04	-0.31	-0.23	0.59	0.96	1.68
	V/d <sup>12</sup> /u2	-0.14	2.20	0.14	1.01	-0.32	-0.24	0.47	0.99	1.65
	Cr/d <sup>13</sup> /u3	-1.14	3.90	0.20	0.91	-0.34	-0.23	0.41	1.19	1.69
	Co/d <sup>16</sup> /u4	1.22	2.45	0.25	0.59	-0.33	-0.23	0.15	1.22	1.75
D	Al/d <sup>10</sup> /u0	N/A	N/A	N/A	N/A	N/A	N/A	N/A	N/A	N/A
	Ti/d <sup>11</sup> /u3	1.30	0.84	0.16	1.05	-0.43	-0.38	0.47	1.28	1.15
	V/d <sup>12</sup> /u2	-0.04	2.20	0.22	0.98	-0.44	-0.35	0.49	1.41	1.20
	Cr/d <sup>13</sup> /u3	-0.77	3.70	0.21	0.94	-0.43	-0.36	0.47	1.46	1.25
	Co/d <sup>16</sup> /u4	1.49	2.44	0.22	0.59	-0.40	-0.33	0.14	1.21	1.31
D*	Al/d <sup>10</sup> /u0	0.00	0.00	0.28	0.41	-0.43	-0.33	0.36	1.55	1.26
	Ti/d <sup>11</sup> /u1	0.99	1.14	0.20	0.99	-0.43	-0.34	0.55	1.36	1.31
	V/d <sup>12</sup> /u2	-0.38	2.45	0.21	0.95	-0.43	-0.34	0.49	1.43	1.24
	Cr/d <sup>13</sup> /u3	-0.77	3.71	0.21	0.94	-0.43	-0.34	0.47	1.45	1.25
	Co/d <sup>16</sup> /u2	-0.98	2.33	0.28	0.61	-0.44	-0.34	0.19	1.52	1.24
D to E*	Al/d <sup>10</sup> /u1	0.58	-0.06	0.28	0.41	-0.41	-0.36	0.35	1.25	1.17
	Ti/d <sup>11</sup> /u2	1.07	0.82	0.20	1.00	-0.40	-0.35	0.58	1.13	1.14
	V/d <sup>12</sup> /u1	-1.22	2.61	0.22	0.96	-0.40	-0.35	0.42	1.14	1.14
	Cr/d <sup>13</sup> /u6	-1.72	4.05	0.24	0.92	-0.40	-0.35	0.21	1.09	1.15
	Co/d <sup>16</sup> /u5	1.67	2.54	0.28	0.63	-0.41	-0.35	0.05	1.14	1.16
E*	Al/d <sup>10</sup> /u1	1.42	-0.31	0.21	0.44	-0.45	-0.39	0.37	0.56	1.00
	Ti/d <sup>11</sup> /u0	0.00	0.00	0.06	0.98	-0.43	-0.38	1.41	0.47	0.99
	V/d <sup>12</sup> /u5	2.15	2.87	0.21	0.91	-0.46	-0.39	0.30	0.53	0.99
	Cr/d <sup>13</sup> /u6	1.96	4.05	0.23	0.91	-0.47	-0.39	0.11	0.53	1.00
	Co/d <sup>16</sup> /u5	1.93	2.46	0.25	0.62	-0.47	-0.39	0.07	0.54	1.00
CoML*	Al/d <sup>9</sup> /u1	1.35	-0.23	0.13	0.46	-	-	0.35	-	-
	Ti/d <sup>11</sup> /u0	0.00	0.00	-0.04	1.06	-	-	1.40	-	-
	V/d <sup>12</sup> /u1	-0.15	1.27	-0.03	0.98	-	-	1.47	-	-
	Cr/d <sup>13</sup> /u4	1.19	3.09	0.01	0.99	-	-	0.71	-	-